

Abstract

Title of Dissertation: A Study of Cold Gas and Star Formation
in Low-Mass Blue-Sequence E/S0s

Hsin-Han Lisa Wei, Doctor of Philosophy, 2010

Dissertation directed by: Professor Stuart Vogel
Department of Astronomy

We present a study of cold gas and star formation in low-mass blue-sequence E/S0 galaxies — a population that is morphologically early-type, but resides on the blue sequence in color vs. stellar mass space alongside spirals. A subset of these blue-sequence E/S0s may provide an evolutionary link between traditional red and dead early-type galaxies and star-forming spirals via disk (re)growth. In this dissertation, we use data from the Green Bank Telescope (GBT), the Combined Array for Research in Millimeter-wave Astronomy (CARMA), the *Spitzer Space Telescope*, and the *Galaxy Evolution Explorer* (*GALEX*) to examine the potential for morphological transformation of low-mass blue-sequence E/S0s.

In considering the HI content of these galaxies, we find that, normalized to stellar mass, the atomic gas masses for 12 of the 14 blue-sequence E/S0s range from 0.1 to $\gtrsim 1.0$. These gas-to-stellar mass ratios are comparable to those of spiral and irregular galaxies, and have a similar dependence on stellar mass. Assuming that the HI is accessible for star formation, we find that 9 of 14 blue-sequence E/S0s can increase in stellar mass by 10–60% in 3 Gyr with current HI reservoirs alone. We present evidence that star formation in these galaxies is bursty and likely involves externally triggered gas inflows.

For a sub-sample of eight E/S0s (four blue-, two mid-, and two red-sequence) whose CARMA CO(1–0), *Spitzer* MIPS 24 μm , and *GALEX* FUV emission dis-

tributions are spatially resolved on a 750 pc scale, we find roughly linear relationships between molecular-gas and star-formation surface densities within all galaxies, with power law indices $N = 0.6\text{--}1.9$ (median 1.2). Adding 11 more blue-sequence E/S0s whose CO(1–0) emission is not as well resolved, we find that most of our E/S0s have 1–8 kpc aperture-averaged molecular-gas surface densities overlapping the range spanned by the disks and centers of spiral galaxies. While many of our E/S0s fall on the same Schmidt-Kennicutt relation as local spirals, $\sim 80\%$ are offset towards apparently higher molecular-gas star formation efficiency. We discuss possible interpretations of the apparently elevated efficiencies.

We examine star formation in blue- and red-sequence E/S0s as traced by the $8\ \mu\text{m}$ PAH emission. We find the $8\ \mu\text{m}$ PAH/ $3.6\ \mu\text{m}$ emission ratios for most of our blue-sequence E/S0s to be similar to those of local spirals. Ratio images of the two tracers reveal ring-like and non-axisymmetric structures in some of our E/S0s, suggestive of internally and/or externally triggered gas inflow and centrally concentrated star formation. Comparison between the CO(1–0) and $8\ \mu\text{m}$ PAH emission distributions shows good agreement globally, although the $8\ \mu\text{m}$ PAH/ $3.6\ \mu\text{m}$ emission ratio appears to better trace non-axisymmetric structures observed in CO. Similar to CO observations of spiral galaxies, we find detectable CO emission in our E/S0s to be centrally concentrated, ranging from $0.1\text{--}0.6r_{25}$ (median $0.3r_{25}$). We also find that the aperture-averaged $8\ \mu\text{m}$ PAH to $3.6\ \mu\text{m}$ stellar emission ratio correlates with the atomic and molecular gas mass fractions.

**A Study of Cold Gas and Star Formation
in Low-Mass Blue-Sequence E/S0s**

by

Hsin-Han Lisa Wei

Dissertation submitted to the Faculty of the Graduate School of the
University of Maryland at College Park in partial fulfillment
of the requirements for the degree of
Doctor of Philosophy
2010

Advisory Committee:

Professor Stuart Vogel, chair
Professor Andrew Baker
Professor Alberto Bolatto
Professor Robert Hudson
Professor Sheila Kannappan
Professor Sylvain Veilleux

© Hsin-Han Lisa Wei 2010

Preface

Some of the work presented in this dissertation has been published, and the rest has either been submitted or is in preparation for submission. Chapter Two has been published in *The Astrophysical Journal* as *Gas Mass Fractions and Star Formation in Blue-Sequence E/S0 Galaxies* (Wei, Kannappan, Vogel, & Baker 2010a). The results of this paper were also presented as a poster at the 2009 Galaxy Wars Conference in Johnson City, Tennessee and as an oral presentation at the 2010 winter American Astronomical Society Meeting in Washington, D.C.

Chapter Four was accepted for publication to *The Astrophysical Journal Letters* in November of 2010 (L. Wei, S. Vogel, S. Kannappan, S. Baker, D. Stark, & S. Laine). Much of this work was given as an oral presentation in a Tuesday UVa/NRAO Astronomy Lunch Series talk in May 2010.

We are currently preparing Chapter Five for submission to *The Astrophysical Journal* (L. Wei, A. Baker, S. Kannappan, S. Laine, A. Moffett, M. Regan, & S. Vogel), with an abridged version of Chapter Three as an Appendix in the paper. Parts of this chapter were presented at The Fourth North American ALMA Science Center Conference in Charlottesville, Virginia in September of 2009.

Appendix B was released as *CARMA Memorandum Series #45: Bandpass Calibration for CARMA* (L. Wei, D. Woody, P. Teuben, M. La Vigne, & S. Vogel) in July of 2008.

Dedicated to: My Parents

Acknowledgements

I would like to acknowledge the many people who made a difference in my life over the past few years, without whom this thesis would not have been possible. First and foremost is my “three-headed monster of an adviser” — Stuart Vogel, Sheila Kannappan, and Andrew Baker, I’ve learned different things from each of my advisers that helped shape who I am as a scientist. Stuart, who is always patient, encouraging, and generous with his time, taught me perseverance through times of frustration. Stuart also taught me that you can always reduce your data one more time. Sheila, who is the driving force behind this thesis, taught me to think outside the box and understand the big picture behind the data. Andrew, who is meticulous in all things, taught me to be detail-orientated and to always be statistically significant. I thank you all for challenging me to think deeper, push harder, and be a better researcher. Thanks to my other collaborators — Seppo Laine, Amanda Moffett, Mike Regan, David Stark, and Dave Woody for their scientific and technical contributions to this thesis.

I am also indebted to the many fantastic professors at UMD — Andy Harris, Cole Miller, Lee Mundy, and Sylvain Veilleux for being always willing to chat about science and answer my questions. I cannot express my gratitude to Alberto “El Supremo” Bolatto for sharing his wisdom, for his constant encouragement, for being my sounding board for all things scientific, and for being a steady source of amusement. I hope he doesn’t step on me after he reads this.

To the LMA/CARMA crew — Stephen White, Peter Teuben, Marc Pound, and Kevin Rauch: thanks for putting up with my constant questions and teaching me so much about interferometry. To Misty La Vigne, Ashley Zauderer, Jin Koda, Andrew West, Scott Schnee, Dominik Riechers, Stuartt Corder, Nikolaus Volgenau, James Lamb, and Dave Hawkins: all the system crashes, antenna collisions, and power outages were better because you were there with me. I also really appreciate Cecil Patrick, Terry Sepsey, Kurt Giovanine, and Mike Cooper for making CARMA my home away from home.

I would like to acknowledge the old and wise UMD grads who were always willing to share their wisdom, knowledge, and gossip with me: Stacy Teng, Matthew Knight, Nicholas Chapman, Michael McDonald, Vanessa Lauburg, Mike Gill, and Rahul Shetty. To the young’uns: Hannah Krug, Jithin George, Megan DeCesar, and Shaye Storm — thanks for making me laugh and forcing me to not take myself so seriously.

This is getting long, but I need to thank my Mandalay family for being a big part of my life — especially Aung, who is just awesome, and Stevie, for all the kitty therapy she gave me on bad days.

To my husband, who always believed in me even when I was full of doubt — thank you for putting up with all my crazy in the past eight months. And last, but closest to my heart, I must acknowledge my parents, who always encouraged me to pursue my dreams. Your selflessness leaves me without words.

Contents

List of Tables	x
List of Figures	xi
1 Introduction	1
1.1 Historical Galaxy Classification	1
1.1.1 The Hubble Sequence	1
1.1.2 Galaxy Bimodality	2
1.2 Hierarchical Galaxy Evolution	3
1.3 Requirements for Morphological Evolution	5
1.3.1 Cold Gas Reservoir	5
1.3.2 Molecular Gas	6
1.3.3 Star Formation	7
1.4 Low-Mass Blue-Sequence E/S0s	8
1.5 Tracers of Gas, Stars, and Star Formation	12
1.6 The Structure of this Dissertation	14
2 Atomic Gas Mass Fraction and Star Formation	17
2.1 Introduction	17
2.2 Sample and Data	22
2.2.1 Sample	22
2.2.2 HI Data	24
2.3 Gas Reservoirs	33
2.3.1 Comparison of Gas Reservoirs in NFGS Galaxies	33
2.3.2 Comparison with Sage & Welch E/S0 Sample	40
2.4 Star Formation and Stellar Mass Growth	41
2.4.1 Two Limiting Scenarios for Growth in the Stellar Component	43
2.4.2 Estimates of Stellar Mass Growth Over Time	44
2.5 Availability of Gas for Star Formation	47
2.5.1 Timescale for Gas Exhaustion and Inflow	47
2.5.2 Evidence for Episodic Gas Inflow	56

2.6	Summary	61
3	CARMA Observations of E/S0s	72
3.1	Introduction	72
3.2	Sample and Data	74
3.3	Observations & Data Reduction	76
3.4	Comparison of Interferometric and Single-Dish CO Fluxes	80
3.5	Description of Individual Galaxies	82
3.5.1	IC 1141	82
3.5.2	NGC 3032	86
3.5.3	NGC 3773	91
3.5.4	NGC 3870	94
3.5.5	NGC 4117	97
3.5.6	NGC 5173	101
3.5.7	NGC 5338	105
3.5.8	UGC 12265N	109
3.5.9	UGC 6003	114
3.5.10	UGC 6570	117
3.5.11	UGC 6805	121
3.5.12	UGC 7020A	124
3.6	Summary	128
4	The Relationship Between Molecular Gas and Star Formation	129
4.1	Introduction	129
4.2	Sample & Data	131
4.3	The Resolved Star Formation Relation at 750 pc Resolution	135
4.4	The Global Star Formation Relation	137
4.5	Discussion	140
5	Star Formation as Traced by 8 μm PAH Emission	144
5.1	Introduction	144
5.2	Sample, Observations, and Data Reduction	146
5.2.1	<i>Spitzer</i> IRAC Data	148
5.2.2	Supplementary Data	150
5.2.3	Radial Profiles	150
5.3	8 μ m PAH Emission and Stellar Emission	151
5.3.1	Tracers of the Stellar and Star Formation Distributions	151
5.3.2	Maps of Stellar and PAH Emission	152
5.3.3	Stellar and PAH Radial Profiles	164
5.3.4	Structure in the PAH Emission	177
5.4	8 μ m PAH Emission vs. CO(1–0) Emission	182

5.4.1	Comparison of Spatial Distributions of PAH and CO(1–0) Emission	182
5.4.2	Radial Distributions of PAH and CO(1–0) Emission	188
5.4.3	Correlations Between PAH, Gas, and Star Formation	191
5.5	Conclusions	194
6	Summary and Future Work	196
6.1	Overview	196
6.2	Future Work	199
A	Notes on GBT Observations	201
A.0.1	GBT Flux Measurements and Comparison with Literature Fluxes	201
A.0.2	GBT HI Profiles of Sub- M_b E/S0s	203
B	Bandpass Calibration for CARMA	206
B.1	Introduction	206
B.2	The Signal Path	207
B.3	Astronomical Bandpass Calibration	208
B.3.1	Observations	208
B.3.2	Reduction: Bandpass of 500 MHz Band	212
B.3.3	Reduction: Bandpass of One 500 MHz + Two Narrower Bands	213
B.4	Calibrating the Bandpass with the Noise Source	214
B.4.1	Visibilities	214
B.4.2	Bandpass Calibration	215
B.4.3	Writing an Observing Script	217
B.4.4	Reduction	218
B.4.5	Phase Calibration	221
B.5	Calibration in the 62 MHz – CARMA Hybrid Mode	222
B.5.1	The Hybrid Method	222
B.5.2	Writing a Hybrid Observing Script	223
B.5.3	Reduction	227
C	Glossary	233
	Bibliography	235

List of Tables

2.1	Values of M_* and $M_{\text{HI+He}}/M_*$ for the sub- M_b sample.	37
2.2	Fits of $M_{\text{HI+He}}/M_*$ vs. M_*	39
2.3	Timescales for sub- M_b E/S0s	49
2.4	HI Data for the NFGS	64
2.4	HI Data for the NFGS	65
2.4	HI Data for the NFGS	66
2.4	HI Data for the NFGS	67
2.4	HI Data for the NFGS	68
2.4	HI Data for the NFGS	69
2.5	New HI data	70
2.5	New HI data	71
3.1	Properties of CARMA-observed galaxies	76
3.2	CARMA observation parameters	79
3.3	CARMA map parameters	79
4.1	Aperture-averaged properties for CARMA & IRAM 30 m E/S0s . . .	132
4.2	Star formation relation fit parameters	139
5.1	IRAC image properties	148
5.2	Galaxy properties derived from IRAC data	177
B.1	Calibrator integration times	211
B.2	CARMA system information	211

List of Figures

1.1	Hubble tuning fork	2
1.2	$u - r$ color vs. absolute magnitude	4
1.3	$U - R$ color vs. stellar mass	9
1.4	Images of E/S0s	10
2.1	$U - R$ color vs. stellar mass – HI sample	25
2.2	GBT HI spectra of red-sequence E/S0s	27
2.3	GBT spectra of blue- and mid-sequence E/S0s	28
2.4	$U - R$ color vs. R -band luminosity	32
2.5	$M_{\text{HI+He}}$ vs. M_*	34
2.6	Atomic gas-to-stellar mass ratio	36
2.7	$M_{\text{HI+He}}/L_B$ vs. L_B	42
2.8	Fractional stellar mass growth	46
2.9	Gas exhaustion time	51
2.10	$\Delta(B - R)_{\text{corr}}$ distribution	57
2.11	Expected SSFR vs. $\Delta(B - R)_{\text{corr}}$	59
3.1	$U - R$ color vs. stellar mass – CARMA sample	75
3.2	CARMA vs. single-dish flux comparison	81
3.3	IC 1141 channel maps	83
3.3	IC 1141 channel maps, continued	84
3.4	Multiwavelength view of IC 1141	85
3.5	NGC 3032 channel maps	88
3.5	NGC 3032 channel maps, continued	89
3.6	Multiwavelength view of NGC 3032	90
3.7	NGC 3773 channel maps	92
3.8	Multiwavelength view of NGC 3773	93
3.9	NGC 3870 channel maps	95
3.10	Multiwavelength view of NGC 3870	96
3.11	NGC 4117 channel maps	98
3.11	NGC 4117 channel maps, continued	99
3.12	Multiwavelength view of NGC 4117	100

3.13	NGC 5173 channel maps	102
3.13	NGC 5173 channel maps, continued	103
3.14	Multiwavelength view of NGC 5173	104
3.15	NGC 5338 channel maps	106
3.15	NGC 5338 channel maps, continued	107
3.16	Multiwavelength view of NGC 5173	108
3.17	UGC 12265N channel maps	110
3.17	UGC 12265N channel maps, continued	111
3.17	UGC 12265N channel maps, continued	112
3.18	Multiwavelength view of UGC 12265N	113
3.19	UGC 6003 channel maps	115
3.20	Multiwavelength view of UGC 6003	116
3.21	UGC 6570 channel maps	118
3.21	UGC 6570 channel maps, continued	119
3.22	Multiwavelength view of UGC 6570	120
3.23	UGC 6805 channel maps	122
3.24	Multiwavelength view of UGC 6805	123
3.25	UGC 7020A channel maps	125
3.25	UGC 7020A channel maps, continued	126
3.26	Multiwavelength view of UGC 7020A	127
4.1	$U - R$ color vs. stellar mass – CO Sample	133
4.2	Σ_{SFR} vs. Σ_{H_2} at 750 pc resolution.	136
4.3	Aperture-averaged Σ_{SFR} vs. Σ_{H_2}	138
5.1	$U - R$ color vs. stellar mass – IRAC Sample	147
5.2	IRAC images of 3.6 μm and 8 μm PAH emission	153
5.2	IRAC images of 3.6 μm and 8 μm PAH emission, continued	154
5.2	IRAC images of 3.6 μm and 8 μm PAH emission, continued	155
5.2	IRAC images of 3.6 μm and 8 μm PAH emission, continued	156
5.2	IRAC images of 3.6 μm and 8 μm PAH emission, continued	157
5.2	IRAC images of 3.6 μm and 8 μm PAH emission, continued	158
5.2	IRAC images of 3.6 μm and 8 μm PAH emission, continued	159
5.2	IRAC images of 3.6 μm and 8 μm PAH emission, continued	160
5.2	IRAC images of 3.6 μm and 8 μm PAH emission, continued	161
5.2	IRAC images of 3.6 μm and 8 μm PAH emission, continued	162
5.2	IRAC images of 3.6 μm and 8 μm PAH emission, continued	163
5.3	Radial profiles and $I_{8.0\text{PAH}}/I_{3.6}$ ratio images	166
5.3	Radial profiles and $I_{8.0\text{PAH}}/I_{3.6}$ ratio images, continued	167
5.3	Radial profiles and $I_{8.0\text{PAH}}/I_{3.6}$ ratio images, continued	168
5.3	Radial profiles and $I_{8.0\text{PAH}}/I_{3.6}$ ratio images, continued	169

5.3	Radial profiles and $I_{8.0\text{PAH}}/I_{3.6}$ ratio images, continued	170
5.3	Radial profiles and $I_{8.0\text{PAH}}/I_{3.6}$ ratio images, continued	171
5.3	Radial profiles and $I_{8.0\text{PAH}}/I_{3.6}$ ratio images, continued	172
5.3	Radial profiles and $I_{8.0\text{PAH}}/I_{3.6}$ ratio images, continued	173
5.3	Radial profiles and $I_{8.0\text{PAH}}/I_{3.6}$ ratio images, continued	174
5.3	Radial profiles and $I_{8.0\text{PAH}}/I_{3.6}$ ratio images, continued	175
5.3	Radial profiles and $I_{8.0\text{PAH}}/I_{3.6}$ ratio images, continued	176
5.4	Comparison of $8\ \mu\text{m}$ PAH and CO(1–0) emission	184
5.4	Comparison of $8\ \mu\text{m}$ PAH and CO(1–0) emission	185
5.5	Comparison of $I_{8.0\text{PAH}}/I_{3.6}$ ratio maps with CO(1–0) emission	186
5.5	Comparison of $I_{8.0\text{PAH}}/I_{3.6}$ ratio maps with CO(1–0) emission	187
5.6	Radial profiles of CO(1–0) and $8\ \mu\text{m}$ PAH emission	189
5.6	Radial profiles of CO(1–0) and $8\ \mu\text{m}$ PAH emission	190
5.7	Aperture-averaged $I_{8.0\text{PAH}}/I_{3.6}$ vs. SSFR	193
5.8	Aperture-averaged $I_{8.0\text{PAH}}/I_{3.6}$ vs. gas mass fractions	193
A.1	HI flux comparison	205
B.1	Signal path through the CARMA system	209
B.2	500 MHz amplitude & phase — noise source	228
B.3	500 MHz amplitude & phase — 3C273	229
B.4	31 MHz amplitude & phase — noise source	230
B.5	31 MHz amplitude & phase — 3C273	231
B.6	31 MHz amplitude & phase — 3C273 check	232

Chapter 1

Introduction

1.1 Historical Galaxy Classification

1.1.1 The Hubble Sequence

After demonstrating that spiral nebulae are extragalactic objects based on Cepheid variable distances, Edwin Hubble classified these galaxies by morphology. Because of their smooth, spherical, and uncomplicated appearance, Hubble considered elliptical galaxies (E) to be “early-type” galaxies. Spiral galaxies, on the other hand, appeared to be much more complex structurally, and so Hubble defined these as “late-type” galaxies (Hubble 1926). This led to the mistaken assumption of a temporal evolutionary sequence (E→Sa→Sb→Sc), characterized by the “Hubble Tuning Fork” (Figure 1.1), which also showed the spiral galaxies branching off into barred (SB) and unbarred (S) galaxies¹. Later studies, however, determined that the stellar population in late-type galaxies is in fact much younger than that of early-type galaxies, refuting the direction of the perceived evolutionary sequence. The nomen-

¹Hubble meant to use “early” and “late” to describe the progression from simple to complex structures, and explicitly rejected the temporal connotations of those words (Hubble 1926).

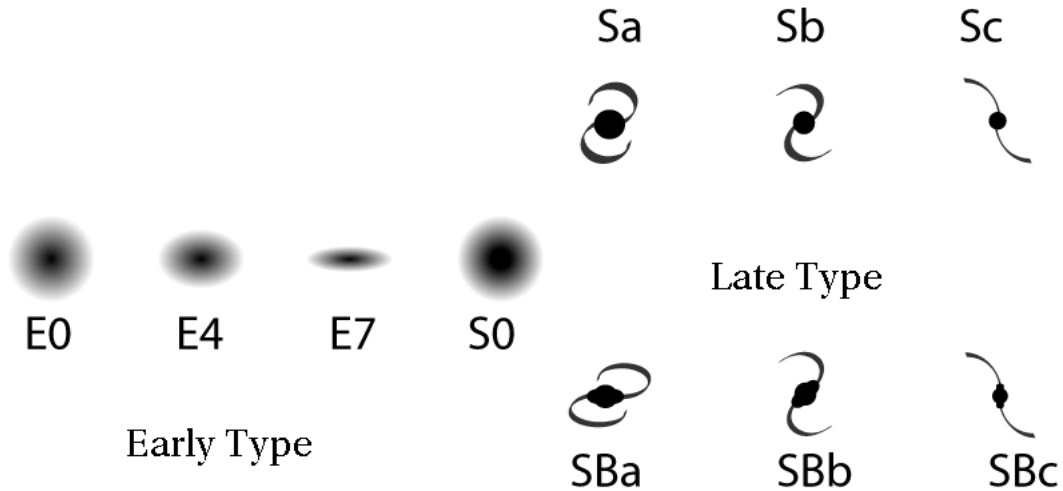


Figure 1.1: (Figure Credit: <http://www.astro.lsa.umich.edu>) The Hubble Tuning Fork, which illustrates Hubble’s classification scheme for galaxies. Ellipticals and lenticulars (left) are referred to as early types, while spirals are referred to as late types.

clature of “early” and “late” types, however, remains widely used today to describe elliptical and spiral galaxies, even though galaxy evolution appears to be primarily occurring in the other direction, from late to early type.

1.1.2 Galaxy Bimodality

The differences between early- and late-type galaxies can be characterized by the bimodal distribution of many galaxy properties, much of which appears to be related to the bimodality mass ($M_b \sim 3 \times 10^{10} M_\odot$). In color vs. magnitude space, there appear to be two distinct galaxy populations: the “red sequence”, which dominates the galaxy population above M_b , and the “blue sequence”,² which dominates the galaxy population below M_b (Bell et al. 2003; Baldry et al. 2004). The two sequences

²Sometimes referred to as the “blue cloud”.

are clearly separated in color vs. absolute magnitude parameter space (Figure 1.2; Baldry et al. 2004) as well as vs. stellar mass parameter space (see §1.4). Morphologically, blue-sequence galaxies are typically disk-dominated late-type galaxies, while red-sequence galaxies tend to be spheroidal, early-type galaxies (Kauffmann et al. 2003; Blanton et al. 2005). The lower-mass blue-sequence galaxies generally have younger populations and more active star formation than the high-mass red-sequence galaxies (e.g., Kauffmann et al. 2003), suggesting that the more massive galaxies formed the bulk of their stars at higher redshifts (i.e., “downsizing”). These differences appear to be related to the environments of the host galaxies, as blue-sequence galaxies tend to reside in low-density environments, while red-sequence galaxies tend to reside in high-density environments (e.g., Blanton et al. 2005).

1.2 Hierarchical Galaxy Evolution

The currently accepted paradigm of galaxy formation and evolution is based on the hierarchical buildup from smaller systems through the successive merging of dark halos (White & Rees 1978; White & Frenk 1991) and the galaxies within those halos (e.g., Kauffmann et al. 1993; Cole et al. 1994; Somerville & Primack 1999; Bower et al. 2006). In these models, galaxies evolve within the Hubble sequence through a series of violent and quiet phases, with major mergers forming dynamically hot E/S0 systems and quiescent periods allowing the regrowth of dynamically cold stellar disks (e.g., Steinmetz & Navarro 2002; Governato et al. 2007).

The idea of transformation from late to early type via major mergers of similar-mass disk galaxies dates back to at least Toomre & Toomre (1972); this process is still widely recognized today as a source of classical ellipticals. Additionally, recent simulations find that unequal mass or gas-rich mergers of galaxies result in S0s

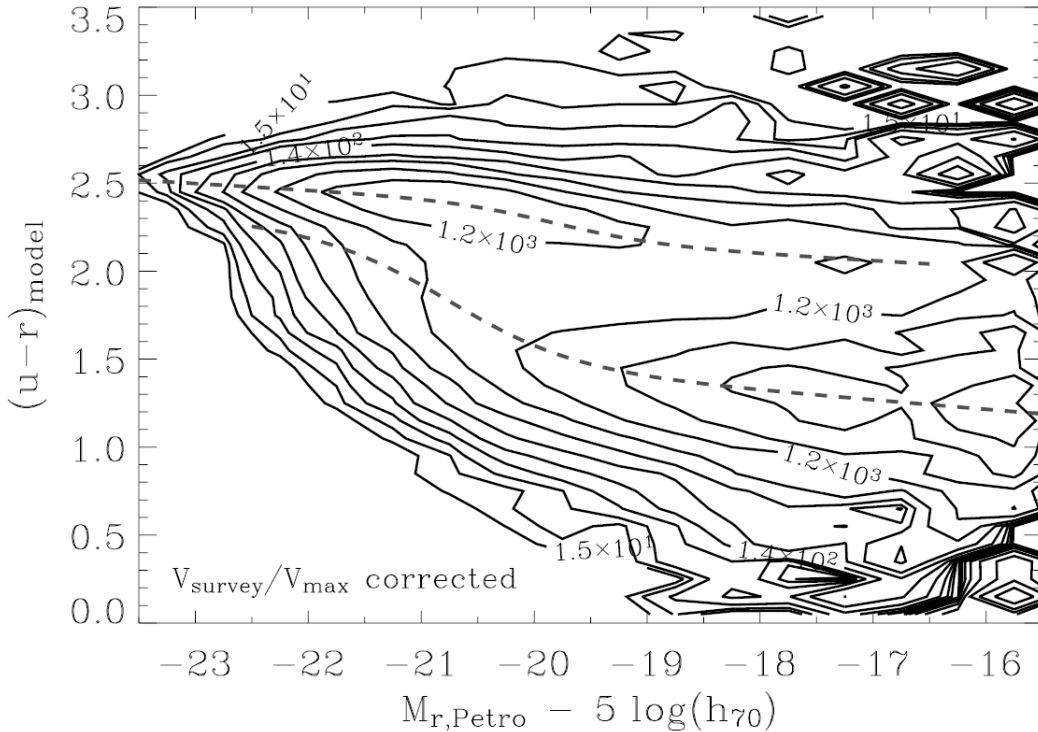


Figure 1.2: **(Figure Credit: Baldry et al. 2004)** $u-r$ color vs. absolute magnitude contours for galaxies in the Sloan Digital Sky Survey, revealing a bimodal distribution of galaxies.

and hybrid galaxies with properties of both early and late types (Bekki 1998; Naab et al. 2006; Bournaud et al. 2005; Hopkins et al. 2009). Observationally, there is substantial evidence confirming that early-type galaxies can form through major mergers (e.g., Schweizer & Seitzer 1992; van Dokkum 2005; Dasyra et al. 2006b). In agreement with the simulations, Emsellem et al. (2007) argue that larger, slow-rotating elliptical galaxies form from dry major mergers while fainter, fast-rotating ellipticals and S0s seem to form from minor mergers or very gas-rich major mergers.

What about evolution in the other direction, from early to late type? Simulations suggest that galaxy evolution in this direction involves the regrowth of stellar

disks (Steinmetz & Navarro 2002; Governato et al. 2007) from gas disks that either survived a gas-rich major merger (Hopkins et al. 2009; Stewart et al. 2009) or are rebuilt via cold-mode gas accretion (e.g., Dekel & Birnboim 2006). As disk (re)growth is a relatively quiescent process, however, observational evidence has been elusive.

1.3 Requirements for Morphological Evolution

Morphological transformation from early to late type requires that several conditions be met. We discuss these conditions and what is currently known about early-type galaxies below.

1.3.1 Cold Gas Reservoir

First, the transformation from early- to late-type requires a substantial reservoir of cold gas — the raw material for disk regrowth. Historically, early-type galaxies were thought to be gas-poor (Faber & Gallagher 1976; Knapp et al. 1978). Subsequent surveys, however, found that the ratio of gas mass to blue luminosity (M_{HI}/L_B) in early-type galaxies ranges from upper limits of $M_{\text{HI}}/L_B \sim 0.009 M_{\odot}/L_{\odot}$ to measured $M_{\text{HI}}/L_B \sim 2.7 M_{\odot}/L_{\odot}$ (Hawarden et al. 1981; Knapp et al. 1985; Wardle & Knapp 1986; Sadler et al. 2000; Oosterloo et al. 2002); at the high end, the early-type galaxies have atomic gas reservoirs (normalized to stellar mass) comparable to spirals. The 70% HI detection rate by Morganti et al. (2006) suggests that atomic gas reservoirs are actually relatively common in field early-type galaxies. The large range in cold gas content hints that there may be distinct sub-populations of early-type galaxies — the conventional red and dead early types, and a population that is still accreting gas and forming stars.

In addition to the *presence* of cold gas, the distribution of the gas in an equi-

librium configuration (i.e., disks) is important in assessing the potential for disk regrowth. Atomic gas accreted from small companions via dynamical friction, losing momentum/kinetic energy from gravitational interactions with the dark matter halo, is often not in equilibrium. The HI is typically distributed in tidal tails and streams (e.g., Hibbard et al. 2001) soon after a merger/interaction, and requires time to settle into regularly-rotating disks and rings that are conducive for disk growth.

The existence of giant HI disks and rings (Morganti et al. 1997; Serra et al. 2007), as predicted by simulations of mergers between gas-rich galaxies (Barnes 2002; Hopkins et al. 2009), makes it possible for stellar disks to form from already-present gas disks. The HI structures around some early-types galaxies are known to have regular velocity fields, with a continuity between ionized and neutral gas (van Gorkom et al. 1986; Schweizer et al. 1989; Schiminovich et al. 1995; Morganti et al. 2006). Hibbard & van Gorkom (1996) find a rotationally supported HI disk in the elliptical galaxy NGC 520, which, if star formation is triggered in the disk, may transform it into a late-type galaxy. All these observations suggest that the gas disks around some, possibly most, early-type galaxies have reached an equilibrium arrangement suitable for disk growth.

1.3.2 Molecular Gas

While a substantial atomic gas reservoir is necessary for morphological transformation, it is molecular gas that appears to be most intimately connected to star formation in spiral galaxies (e.g., Kennicutt 1998; Wong & Blitz 2002; Bigiel et al. 2008). The fact that large single-dish surveys of CO emission in FIR-bright early-type galaxies (Wiklind & Henkel 1989; Lees et al. 1991; Wiklind et al. 1995) typically have higher detection rates than volume or flux-limited surveys (Knapp & Rupen

1996; Welch & Sage 2003; Sage et al. 2007; Combes et al. 2007) suggests that this is also the case for early-type galaxies. These surveys find molecular gas masses ranging from 10^7 to $10^9 M_\odot$ in 28–78% of early-type galaxies (with higher detection rates for FIR-bright galaxies; Lees et al. 1991; Knapp & Rupen 1996; Welch & Sage 2003; Sage et al. 2007; Combes et al. 2007).

Spatially-resolved studies of molecular gas in early-type galaxies, however, are sparse, as interferometric observations are time-consuming and difficult to obtain. There have been some single-galaxy studies of early types that find the molecular gas to be very centrally concentrated, often with ring morphologies (Wiklind & Henkel 1992; Inoue et al. 1996; Wiklind et al. 1997; Okuda et al. 2005). More recent efforts by Young et al. have more than doubled the number of interferometric observations of early-type galaxies, finding evidence that the molecular gas in some of these galaxies was acquired from external sources (Young et al. 2008), as well as good spatial correlation between molecular gas and star formation (Young et al. 2009).

1.3.3 Star Formation

In addition to the presence of cold atomic and molecular gas disks in equilibrium configurations, there must be a non-negligible amount of on-going star formation for morphological change to occur in early-type galaxies. Recent work finds that 20–30% of field early-type galaxies are either actively star-forming (Schawinski et al. 2009) or have had recent (<1 Gyr) star formation (Yi et al. 2005). The level of star formation in early-type galaxies is typically low, ranging from 0.02 to $0.2 M_\odot \text{yr}^{-1}$ for the local, typically massive ($M_B < -18$) S0s from the Spectrographic Areal Unit for Research on Optical Nebulae survey (SAURON; Temi et al. 2009a) and 1 to $10 M_\odot \text{yr}^{-1}$ for the most infrared-luminous S0s (Temi et al. 2009b).

In a single-dish survey of CO emission in SAURON E/S0s, Combes et al. (2007)

find that their galaxies follow the $N = 1.4$ disk-averaged power law between molecular-gas and star-formation surface densities, characteristic of spirals (Kennicutt 1998). Using multiple star-formation tracers, Crocker et al. (2010) find a similar result for a sample of 12 E/S0s, although possibly at lower total-gas star formation efficiencies than spirals. Shapiro et al. (2010) update the Combes et al. results with spatially resolved maps, localizing both CO emission and star formation in the central regions of the E/S0s.

Considering the body of work on early-type galaxies, there appear to be at least some galaxies that satisfy requirements for evolution towards later-type morphologies. The focus of these studies, however, is on high-mass early-type galaxies ($M_* > 3 \times 10^{10} M_\odot$), for which there is no clearly defined population that appears to be transitioning from early to late type. Additionally, most studies predict that the majority of these galaxies will eventually exhaust their gas reservoirs and evolve passively.

1.4 Low-Mass Blue-Sequence E/S0s

Kannappan, Guie, & Baker (2009, hereafter KGB) have recently identified a population of galaxies that are morphologically early type, but reside alongside spiral galaxies on the blue sequence in color vs. stellar mass parameter space (Figure 1.3). These blue-sequence E/S0s fall between spirals and red-sequence E/S0s in scaling relations (stellar mass M_* vs. radius and vs. velocity dispersion σ), implying that blue-sequence E/S0s may form a transitional population between the two groups (KGB).

Unlike red-sequence E/S0s, whose mass function peaks at high masses, blue-sequence E/S0s increase in numbers for $M_* < 3 \times 10^{10} M_\odot$ (KGB). Their abundance

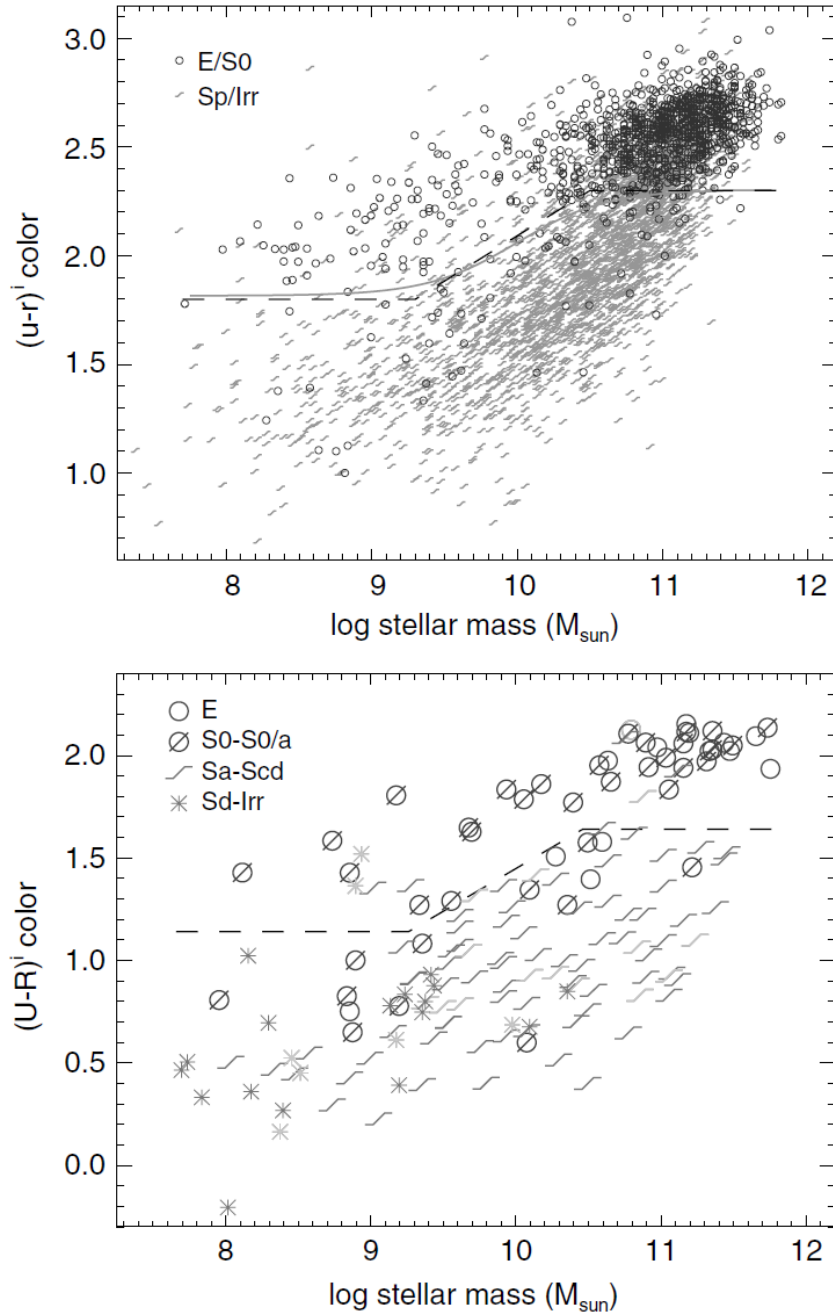


Figure 1.3: **(Figure Credit: KGB)** $U - R$ color vs. stellar mass for (a) a sample of galaxies from HyperLeda/SDSS/2MASS and (b) the Nearby Field Galaxy Survey (Jansen et al. 2000b). Symbols denote morphological type. The red sequence, the main locus of high-mass and/or cluster E/S0s, lies above the dashed line, while the blue sequence, typically populated by spiral galaxies, lies below. Note the presence of a population of galaxies with early-type morphology in the region of color vs. stellar mass space populated by spirals.

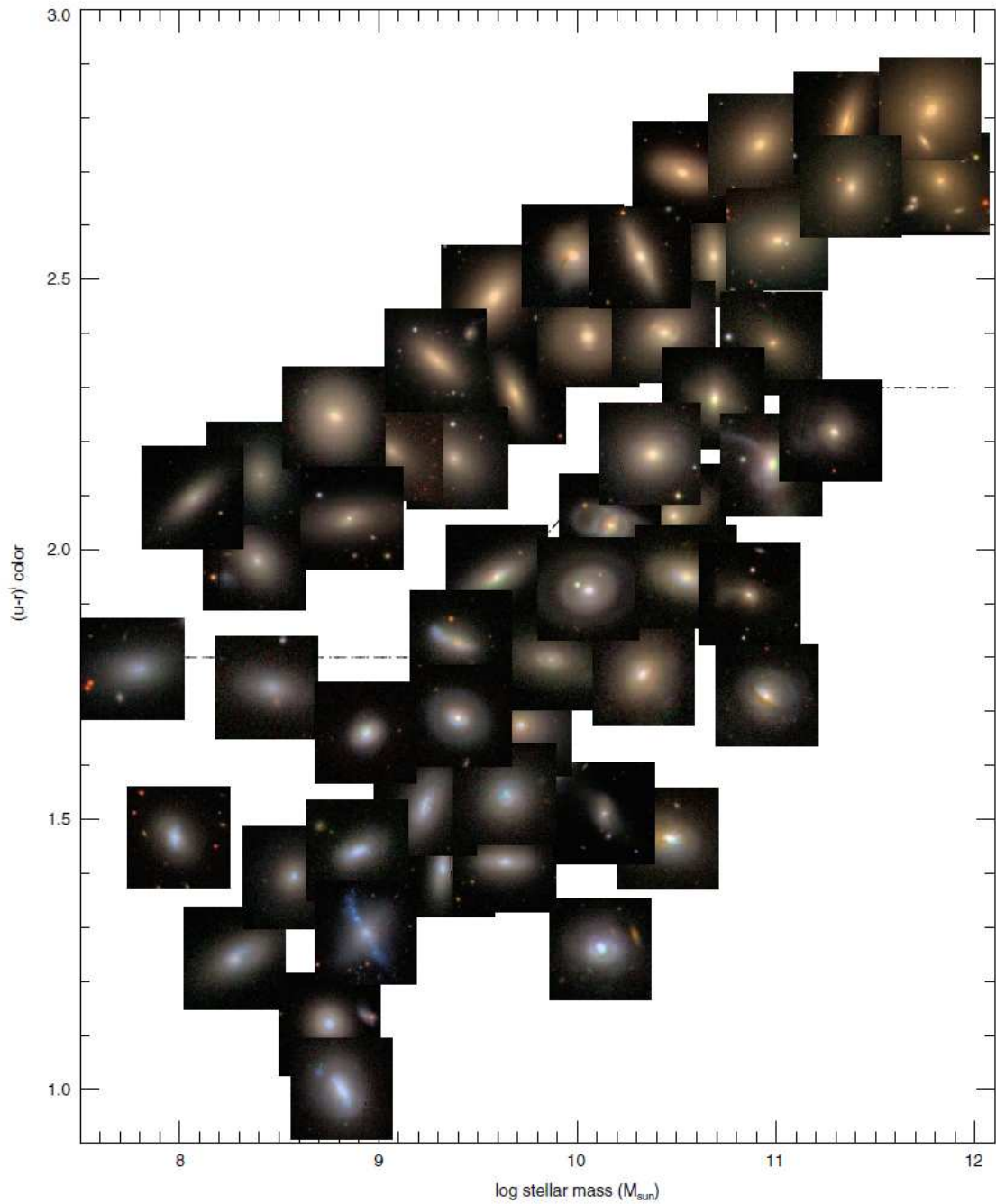


Figure 1.4: **(Figure Credit: KGB)** Composite-color images from SDSS of blue- and red-sequence E/S0s from the NFGS and HyperLeda/SDSS/2MASS sample presented in $(u - r)^i$ color vs. stellar mass space.

increases sharply to 20–30% of E/S0s below $M_* \lesssim 5 \times 10^9 M_\odot$, which is the same transition mass below which galaxies become notably more gas-rich (Kannappan & Wei 2008, based on Kannappan 2004). Most high-mass blue-sequence E/S0s are clearly recent major merger remnants or disturbed satellites of larger galaxies, and as such destined to fade onto the red sequence, consistent with recent studies of blue, high-mass E/S0s (Schawinski et al. 2009). At intermediate masses between 10^{10} and $10^{11} M_\odot$, KGB find that blue-sequence E/S0s include examples of both major mergers that are likely to fade onto the red sequence after exhausting their gas and also settled galaxies that may be evolving toward later-type morphologies. The former dominate at higher masses, and the latter at lower masses within this intermediate mass range.

These low-mass blue-sequence E/S0s show signs of disk (re)building such as blue outer disks as well as blue centers (Figure 1.4) that may reflect diskly “pseudobulge” growth involving instabilities and/or satellite interactions (KGB). As non-classical bulges, pseudobulges have exponential surface brightness profiles, blue colors, and rotationally supported dynamics (Kormendy & Kennicutt 2004). Pseudobulges seem to form within and together with large disks, as the size of the two components correlate (Courteau et al. 1996), so the presence of a pseudobulge may imply the existence of a large disk. Further supporting this disk-building picture, KGB find evidence for kinematically distinct disks (i.e., counterrotating or polar) in a sub-population of blue-sequence E/S0s. KGB also find concentration indices in blue-sequence E/S0s to be similar to those identified by Kauffmann et al. (2006) as being optimal for peak (total-gas) star formation efficiency, suggesting that many blue-sequence E/S0s are in a “sweet spot” for star formation in their evolutionary life cycle that may enable large-scale disk building.

Simulations of hierarchical galaxy formation/evolution (e.g., Steinmetz & Navarro

2002) predict that there should be galaxies that are actively re(growing) stellar disks and transitioning from early to late type. Observational evidence for these transitional galaxies has been scarce. The subset of blue-sequence E/S0s with low-to-intermediate masses may represent the missing link between early- and late-type galaxies expected by these simulations.

1.5 Tracers of Gas, Stars, and Star Formation

We discussed in §1.3 conditions required for morphological transformation such as a large atomic gas reservoir, molecular gas, and active star formation. Here we describe the measurements that must be made in order to quantify these characteristics in galaxies.

Atomic Hydrogen : We estimate the amount of atomic hydrogen (HI) present from 21 cm radiation observed in the radio regime of the electromagnetic spectrum. The ground state of atomic hydrogen is split into two hyperfine levels; the configuration where the spin of the electron and proton are parallel has higher energy than the configuration where the spins are anti-parallel. When the atom flips from the parallel to the anti-parallel state, a photon with wavelength 21.105 cm (corresponding to a frequency of 1420.405 MHz) is emitted. Based on the probability of such a transition, one can estimate the HI mass of a galaxy based on the observed 21 cm flux.

Molecular Hydrogen : Because molecular hydrogen (H_2) does not have a dipole moment, it is difficult to directly estimate the amount of H_2 in a galaxy. Molecular hydrogen gas masses are often indirectly estimated based on the emission from carbon monoxide (CO) through its rotational (J) transitions. The most commonly used CO lines for estimating H_2 in galaxies are at 2.6 and 1.3 mm in the

radio regime (115 and 230 GHz), corresponding to the $J=1-0$ and $J=2-1$ transitions. Collisions with H_2 molecules in molecular clouds keeps the CO excited, as the lifetimes of rotationally excited levels of CO are relatively short. Thus one can estimate the amount of H_2 present based on the strength of the CO emission. Because ^{12}CO is optically thick, the conversion from CO to H_2 (X_{CO}) is empirically determined by estimating the virial mass of a molecular cloud in the Milky Way based on the size and velocity dispersion of that cloud (e.g., Solomon et al. 1987). In lower-mass systems, the value of X_{CO} is somewhat uncertain and controversial (e.g., Maloney & Black 1988; Pak et al. 1998; Pelupessy & Papadopoulos 2009) as CO molecules are destroyed by hard radiation fields in lower dust and metallicity environments.

Stars : On the Rayleigh-Jeans tail of the stellar blackbody curve, the emission scales linearly with temperature, so the low-mass stars with lower effective temperatures contribute a significant fraction of the emission in the near-infrared. Emission from the stellar photospheres of low-mass K and M stars can be observed at $3.6 \mu m$ (Pahre et al. 2004a). The bulk of a galaxy's stellar mass can be directly traced by emission around the K -band ($\sim 2.2 \mu m$). The other advantage of observing the stellar mass distribution at infrared wavelengths is that it is virtually unaffected by extinction compared to optical wavelengths. An improved estimate of the stellar mass of a galaxy can be obtained by fitting the spectral energy distribution with stellar population models.

Star Formation : In H II regions, hydrogen is ionized by emission from the most massive (O and early-type B) stars with wavelength shortward of 912 \AA . As the lifetimes of these stars are quite short (\sim few million years), $H\alpha$ emission at 6562.81 \AA , originating from the recombination of ionized hydrogen with electrons and transitioning from the $n=3$ to $n=2$ state is a good tracer of very recent star

formation. While only O and very early B stars produce ionizing photons, the longer-lived later-type B stars produce copious UV photons longward of the 912Å Lyman limit. Thus UV observations trace star formation averaged over $\sim 10^8$ years. Both estimate recent star formation directly, but may be strongly affected by extinction by dust absorption. Thus it is important to consider tracers of obscured star formation as well.

In the infrared at $24\ \mu\text{m}$, the emission is dominated by the re-radiation of dust-absorbed UV/optical light from young, massive stars. This is a good tracer of obscured star formation and is complementary to the $\text{H}\alpha$ /UV tracers, and a linear combination of optical/UV and infrared tracers is often used to estimate the total star formation rate in a galaxy (e.g., Bigiel et al. 2008; Kennicutt et al. 2009). At shorter wavelengths (e.g., $8\ \mu\text{m}$), the infrared emission is attributed to polycyclic aromatic hydrocarbons (PAHs) — small dust grains that are heated by UV/optical photons from young stars. PAHs are sensitive to the local radiation field strength and metallicity, and thus may be a less reliable tracer of obscured star formation than $24\ \mu\text{m}$ emission (Calzetti et al. 2007 and references therein).

1.6 The Structure of this Dissertation

The goal of this dissertation is to study the potential for morphological evolution of low-mass blue-sequence E/S0s from the perspective of cold gas and star formation.

In Chapter 2, we approach the question of morphological evolution from the point of view of atomic gas reservoirs. KGB addressed this question with limited archival data for the Nearby Field Galaxy Survey (NFGS, Jansen et al. 2000b), finding preliminary evidence for gas reservoirs (normalized to stellar mass) comparable to those of spiral galaxies. In this chapter we present more complete, higher-quality

data for all NFGS E/S0s with $M_* < 4 \times 10^{10} M_\odot$ and a sampling of more massive E/S0s. We compare the atomic gas masses (normalized to M_*) of blue-sequence E/S0s with those of other galaxies, and we examine the possible fractional growth in M_* given current rates of star formation. We discuss preliminary evidence from our work and that of others that suggests efficient conversion is plausible.

In Chapter 3, we examine the distribution of molecular gas in 12 E/S0s (primarily on the blue sequence) as traced by CO(1–0) emission. We present CO(1–0) channel maps, velocity-integrated emission maps, and velocity fields obtained from the Combined Array for Research in Millimeter-wave Astronomy (CARMA). We discuss the galaxies individually and compare the molecular gas distribution with optical and infrared tracers.

In Chapter 4, we consider the relationship between molecular gas and star formation surface densities (Σ_{H_2} , Σ_{SFR}) for a sub-sample of E/S0s predominantly on the blue sequence. For galaxies whose CARMA CO(1–0), *Spitzer* MIPS 24 μm , and *GALEX* FUV emission distributions are spatially resolved on a 750 pc scale, we consider the pixel-to-pixel relationship between Σ_{H_2} and Σ_{SFR} for our E/S0s and compare with that for local spirals from Bigiel et al. (2008). We also consider the molecular Schmidt-Kennicutt relation (Σ_{SFR} vs. Σ_{H_2}) on a global scale for additional blue-sequence E/S0s whose CO(1–0) emission is not as well resolved. We compare our results with those of normal disk and starburst galaxies from Kennicutt (1998) and SAURON E/S0s from Shapiro et al. (2010).

In Chapter 5, we use the 8 μm PAH emission observed by the *Spitzer* InfraRed Array Camera as a star-formation tracer for a larger sample of E/S0s on both sequences to investigate the nature of star formation in early-type galaxies, with emphasis on lower-mass E/S0s. We consider the spatial distributions of 8 μm PAH

and $3.6\ \mu\text{m}$ stellar emission, and compare our E/S0s with spiral disks from Regan et al. (2006) and SAURON E/S0s from Shapiro et al. (2010). For select galaxies with resolved CO maps, we examine the relationship between $8\ \mu\text{m}$ PAH emission and CO emission. Finally, we consider the correlation between global $8\ \mu\text{m}$ PAH emission and measures of star formation as well as global atomic and molecular gas masses.

We summarize our results and discuss possible future work in Chapter 6.

Chapter 2

Atomic Gas Mass Fraction and Star Formation

2.1 Introduction

Current models of galaxy formation and evolution favor hierarchical growth of galaxies from smaller systems (e.g., White & Frenk 1991; Somerville & Primack 1999; Bower et al. 2006). Within the paradigm of hierarchical galaxy formation, galaxies evolve along the Hubble sequence, transforming back and forth between E/S0 and spiral/irregular morphology through a series of quiescent and violent phases.

Recognition that galaxies can transform from late to early type dates back at least to Toomre & Toomre (1972), who proposed that elliptical galaxies can form from mergers of similar mass late-type galaxies. Recent simulations find that while similar mass (1:1–3:1) mergers of disk galaxies result in classical ellipticals, unequal mass (4.5:1–10:1) or gas-rich mergers of galaxies result in S0s and hybrid galaxies with properties of both early and late types (Bekki 1998; Naab et al. 2006; Bournaud et al. 2005). Substantial observational evidence confirms that early-type galaxies

can form through major mergers (e.g., Schweizer & Seitzer 1992; van Dokkum 2005; Dasyra et al. 2006a,c). In agreement with the simulations, Emsellem et al. (2007) argue that larger, slow-rotating elliptical galaxies form from dry major mergers while fainter, fast-rotating ellipticals and S0s seem to form from minor mergers or very gas-rich major mergers.

Can galaxies evolve in the other direction, from early to late type? Simulations suggest that galaxy evolution in this direction involves the regrowth of stellar disks (Steinmetz & Navarro 2002; Governato et al. 2007). Morphological transformation from early to late type requires that several conditions be met, which recent studies have found satisfied in some early-type galaxies.

First, the transformation from early- to late-type requires a substantial reservoir of cold gas — the raw material for disk regrowth. Historically, early-type galaxies were thought to be gas-poor (Faber & Gallagher 1976; Knapp et al. 1978). Subsequent surveys, however, found that the ratio of gas mass to blue luminosity (M_{HI}/L_B) in early-type galaxies ranges from upper limits of $M_{\text{HI}}/L_B \sim 0.009 M_{\odot}/L_{\odot}$ to measured $M_{\text{HI}}/L_B \sim 2.7 M_{\odot}/L_{\odot}$ for large atomic gas reservoirs similar to those of spiral galaxies (Hawarden et al. 1981; Knapp et al. 1985; Wardle & Knapp 1986; Sadler et al. 2000; Oosterloo et al. 2002). The 70% HI detection rate by Morganti et al. (2006) suggests that atomic gas reservoirs are actually relatively common in field early-type galaxies. Recent surveys also find molecular gas (10^7 – $10^9 M_{\odot}$) in 28–78% of early-type galaxies, depending on the survey (Lees et al. 1991; Knapp & Rupen 1996; Welch & Sage 2003; Sage et al. 2007; Combes et al. 2007). The large range in cold gas content hints that there may be distinct sub-populations of early-type galaxies — the conventional red and dead early types, and a population that is still accreting gas and forming stars.

In addition to the *presence* of cold gas, the distribution of the gas is important in

assessing the potential for disk regrowth. The existence of giant HI disks and rings (Morganti et al. 1997; Serra et al. 2007), as predicted by simulations of mergers between gas-rich galaxies (Barnes 2002), makes it possible for stellar disks to form from already-present gas disks. The HI structures around some early-type galaxies are known to have regular velocity fields, with a continuity between ionized and neutral gas (van Gorkom et al. 1986; Schweizer et al. 1989; Schiminovich et al. 1995; Morganti et al. 2006). Hibbard & van Gorkom (1996) find a rotationally supported HI disk in the elliptical galaxy NGC 520, which, if star formation is triggered in the disk, may generate a late-type galaxy. Kiloparsec-scale disks of regularly rotating molecular gas have also been found in the center of some early-type galaxies (Young 2002, 2005; Young et al. 2008; Crocker et al. 2008). All these observations suggest that the gas disks around some, possibly most early-type galaxies have reached an equilibrium arrangement suitable for disk growth.

While the presence of cold gas disks in an equilibrium configuration is necessary for stellar disk growth, it does not imply that star formation is actually occurring. A key question is whether E/S0 galaxies with such disks are currently evolving morphologically, and whether such galaxies constitute a significant fraction of the early-type galaxy population. To answer these questions, one must be able to distinguish between old, gas-poor early-type galaxies and those undergoing morphological transformation via disk regrowth.

Kannappan, Guie, & Baker (2009, hereafter KGB) have recently identified a population of E/S0s that reside alongside spiral galaxies on the blue sequence in color vs. stellar mass parameter space. They argue that among these “blue-sequence E/S0s,” a subset with low-to-intermediate masses may represent the missing link — i.e., galaxies that are actively (re)growing stellar disks and plausibly transitioning from early to late type. KGB find that these blue-sequence E/S0s fall between

spirals and red-sequence E/S0s in scaling relations (stellar mass M_* vs. radius and vs. velocity dispersion σ), implying that blue-sequence E/S0s might form a transitional population between the two groups. Compared to conventional red-sequence E/S0s, blue-sequence E/S0s consistently have bluer outer disks, and often bluer centers as well — suggesting on-going star formation in both disks and disk bulges (i.e., pseudobulges). Further supporting this disk-building picture, KGB find evidence for kinematically distinct disks (i.e., counterrotating or polar) in a notable sub-population of blue-sequence E/S0s.

Unlike red-sequence E/S0s, whose mass function peaks at high masses, blue-sequence E/S0s are rare for $M_* > 1\text{--}2 \times 10^{11} M_\odot$, and are common only for $M_* < 3 \times 10^{10} M_\odot$ (KGB). Their abundance increases sharply to 20–30% below $M_* \lesssim 5 \times 10^9 M_\odot$, coincident with the mass threshold below which galaxies become notably more gas-rich (Kannappan & Wei 2008, based on Kannappan 2004). At intermediate masses between 10^{10} and $10^{11} M_\odot$, KGB find that blue-sequence E/S0s include examples of both major mergers that are likely to fade onto the red sequence after exhausting their gas, and settled galaxies that may be evolving toward later-type morphologies. The former dominate at higher masses, and the latter at lower masses.

One outstanding question that remains is the extent of disk growth possible in low-to-intermediate mass blue-sequence E/S0s. In this Chapter, we approach this question from the point of view of atomic gas reservoirs. KGB addressed this question with limited archival data for the Nearby Field Galaxy Survey (NFGS, Jansen et al. 2000b), finding preliminary evidence for gas reservoirs comparable to those of spiral galaxies. In this Chapter we present more complete, higher-quality data for all NFGS E/S0s with $M_* < 4 \times 10^{10} M_\odot$ and a sampling of more massive E/S0s. We compare the atomic gas masses (normalized to M_*) of blue-sequence

E/S0s with those of other galaxies, and we examine the possible fractional growth in M_* given current rates of star formation. The question of how efficiently the atomic gas might flow inward and condense into molecular gas is beyond the scope of this Chapter; however, we discuss preliminary evidence from our own and others' work that suggests efficient conversion is plausible (elaborated in a forthcoming paper: Kannappan et al. 2010, hereafter K10).

Section 2.2 describes our statistically representative sample of red- and blue-sequence E/S0s from the NFGS, and presents new Green Bank Telescope¹ (GBT) data for the galaxies with $M_* < 4 \times 10^{10} M_\odot$, which are expected to show the most disk growth (KGB). We also present a tabulation of HI data for the full NFGS. Section 2.3 compares atomic gas masses of blue-sequence E/S0s with those of red-sequence E/S0s and galaxies of later-type morphology within the NFGS. We also compare to the sample of Sage & Welch (2006). Section 2.4 examines the fractional stellar mass growth possible for blue-sequence E/S0s given the current star formation rate, in two limiting scenarios — constant (i.e., allowing gas infall) and exponentially declining (i.e., closed box) star formation. In Section 2.5, we discuss gas exhaustion and gas inflow timescales, and we examine evidence for bursty star formation in blue-sequence E/S0s, which likely implies efficient conversion of HI to H₂. We conclude with a discussion of the evolutionary fates of blue-sequence E/S0s.

Appendix A details features of our new HI data for interesting individual galaxies. In this Chapter, we assume $H_0 = 70 \text{ km s}^{-1} \text{ Mpc}^{-1}$.

¹The National Radio Astronomy Observatory is a facility of the National Science Foundation operated under cooperative agreement by Associated Universities, Inc.

2.2 Sample and Data

2.2.1 Sample

NFGS Sample and Data

To understand the role of blue-sequence E/S0s in the morphological evolution of galaxies, we need to examine these galaxies alongside different types of galaxies in various stages of evolution. The NFGS provides an ideal parent sample for such study, spanning the natural diversity of galaxies in the local universe in terms of mass, luminosity, and morphological type. Jansen et al. (2000b) selected the NFGS galaxies from the CfA redshift catalog, which they binned by absolute magnitude and sub-binned by morphological type. After applying a luminosity-dependent minimum redshift to avoid galaxies of a large angular size, Jansen et al. (2000b) chose every N th galaxy from each bin, scaling N to approximate the local galaxy luminosity function. The resulting NFGS spans the full range of morphological types and eight magnitudes in luminosity, providing a distribution of galaxies that is statistically consistent with that of the local universe.

Archival NFGS data include UBR photometry (Jansen et al. 2000a), integrated spectrophotometry (Jansen et al. 2000b), and ionized gas and stellar kinematic data (Kannappan & Fabricant 2001; Kannappan et al. 2002). All NFGS galaxies also have JHK photometry from 2MASS (Skrutskie et al. 2006).

Stellar masses are estimated by fitting stellar population models to $UBRJHK$ photometry and integrated spectrophotometry as described in KGB (updating Kannappan & Gawiser 2007; see also Kannappan & Wei 2008), following the “diet” Salpeter IMF of Bell et al. (2003). This limits the “full NFGS sample” to 176 galaxies for which stellar masses are available. For consistency with the red/blue sequence

dividing line of KGB, we use $U - R$ colors with those authors’ extinction corrections and k -corrections. Total magnitudes are also extinction corrected. We also use star formation rates calculated by KGB from extinction-corrected $H\alpha$ spectral line data, integrated by scanning the slit across each galaxy and calibrated against IRAS-based star formation rates (SFRs) following Kewley et al. (2002)².

Sub- M_b E/S0 Sample

We consider a subsample of NFGS E/S0 galaxies for detailed study of the M_* regime where KGB report abundant blue-sequence E/S0s. Our focus sample includes all 14 blue-sequence E/S0s with $M_* \leq 4 \times 10^{10} M_\odot$, with the limit chosen where the blue-sequence E/S0s tail off (Figure 2.1). To make a fair comparison, we include all 11 NFGS red-sequence E/S0s with $M_* \leq 4 \times 10^{10} M_\odot$. We also include two galaxies that lie on the dividing line between the red and blue sequences, which we will refer to as “mid-sequence” E/S0s following the naming convention of KGB. Our cutoff mass is very close to the bimodality mass ($M_b \sim 3 \times 10^{10} M_\odot$) discussed in KGB, so henceforth we refer to this sample as the “sub- M_b ” E/S0s.

The sample mass limit $M_* \lesssim M_b$ excludes a large population of high-mass red-sequence E/S0s; this is appropriate because many properties scale with stellar mass, and including the high-mass galaxies would bias statistical comparison. Figure 2.1 shows the sub- M_b sample in $U - R$ color vs. stellar mass parameter space, illustrating similar mass distributions with good coverage of both the red and blue sequences. KGB divide the two sequences with the dashed line in Figure 2.1, which is chosen with respect to the locus that hugs the upper boundary of the distribution of most late-type galaxies. The line levels out at $U - R$ values of 1.14 and 1.64, in agreement

²The Kewley et al. (2002) SFRs were scaled to the same “diet” Salpeter IMF used in the stellar mass estimation by KGB.

with Baldry et al. (2004). The rest of the NFGS (spirals and irregulars) is plotted in the background in the same figure for comparison. Because the full NFGS was selected to be broadly representative of the local universe, we expect our sub- M_b E/S0 sample to encompass a wide range of evolutionary stages as well.

2.2.2 HI Data

We present the compilation of HI data for the full NFGS in Table 2.4.

HyperLeda and Literature

HI fluxes are available for most of the NFGS from the HyperLeda database (Paturel et al. 2003), which consists of data compiled from the literature. Because the HyperLeda database is compiled from observations made at different telescopes by different observers, Paturel et al. homogenize the HI data to account for differences in observational parameters such as beamsize, spectral resolution, and flux scale.

For NFGS galaxies lacking HI data in HyperLeda, we gather data from the literature when possible. We obtain upper limits for three galaxies from Huchtmeier & Richter (1989), four HI fluxes and one upper limit from the Cornell EGG HI Digital Archive (Springob et al. 2005), and six upper limits and one flux measurement from the HI Parkes All Sky Survey (HIPASS, Barnes et al. 2001). Because these measurements are often upper limits or taken at telescopes not included in the homogenization effort of Paturel et al. (2003), the fluxes for these galaxies are not homogenized to the HyperLeda dataset.

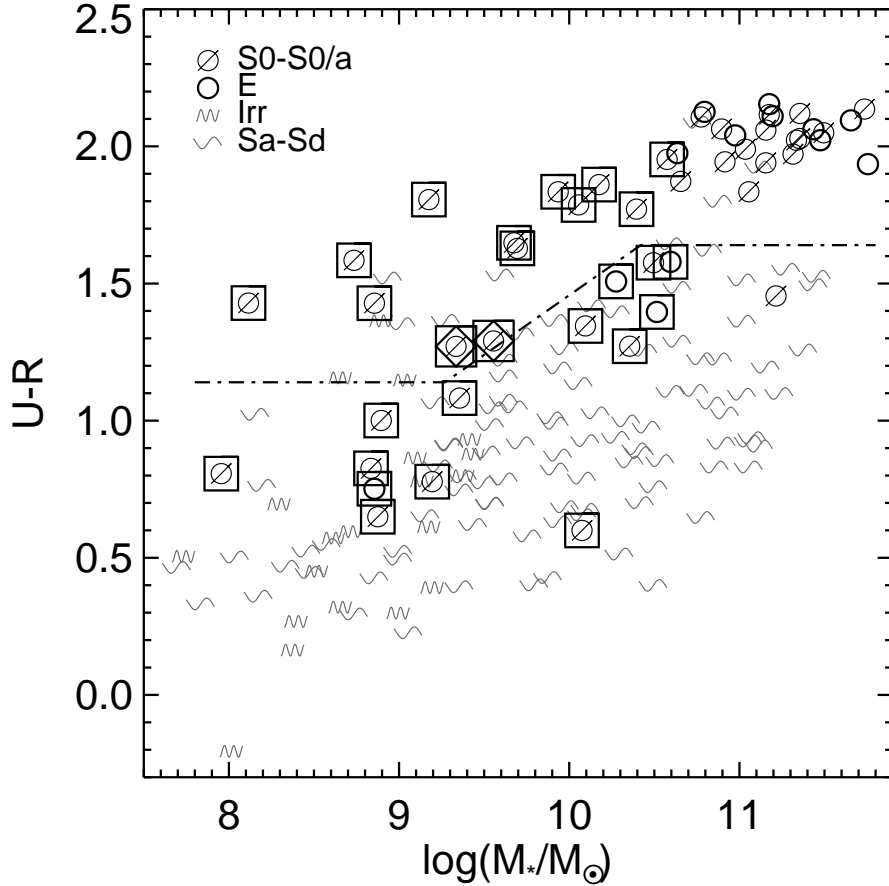


Figure 2.1: $U - R$ color vs. stellar mass for galaxies in the Nearby Field Galaxies Survey (NFGS, Jansen et al. 2000b). Symbols denote morphological type classified by eye using monochrome B or g band images (KGB). The red sequence, the main locus of high-mass and/or cluster E/S0s, lies above the dashed line, while the blue-sequence, typically populated by spiral galaxies, lies below. Note the presence of a population of galaxies with early-type morphology in the region of color vs. stellar mass space populated by spirals. For consistency with the red/blue sequence dividing line of KGB, we use $U - R$ colors with those authors’ extinction corrections and k-corrections. The sub- M_b E/S0 sample of galaxies are boxed, with the two mid-sequence E/S0s on the borderline between the red and blue sequences also enclosed in diamonds. Note that in this Chapter “sub- M_b ” means $M_* < 4 \times 10^{10} M_\odot$, i.e., we use a cutoff slightly above $M_b = 3 \times 10^{10} M_\odot$, due to our original sample selection.

New GBT HI Observations

Good quality literature data are lacking for many early-type galaxies in the NFGS, so we have obtained GBT HI observations for many of these galaxies, with priority for our sample of sub- M_b E/S0s. The observations were obtained with the GBT Spectrometer in L-band, with 50 MHz bandwidth, one spectral window, and nine sampling levels, in ten minute on-off source pairs (five minutes per position) during March and October of 2007. The total on-source time for each galaxy was determined during the observing runs based on the strength of the HI emission relative to the noise.

The spectra were reduced using GBTIDL (Marganian et al. 2006). Individual 30 second records with large harmonic radio frequency interference (RFI) were flagged, and persistent RFI spikes near the velocity range of the galaxy were interpolated across in a few cases. The scans were accumulated and averaged for all data for an individual galaxy, and a polynomial of order ≤ 5 was fitted over a range of ~ 20 MHz to subtract the baseline. Hanning and fourth order boxcar smoothing, with decimation, were then applied to all the baseline-subtracted data, resulting in channel resolution of 0.0244 MHz (~ 5 km s $^{-1}$). Flux calibration is derived from simultaneous observations of an internal noise diode whose intensity is stable.

Figures 2.2 and 2.3 present the spectra of red-, blue-, and mid-sequence E/S0s obtained with the GBT, and Table 2.5 lists the observational parameters and measured quantities. Col. (6) lists the total on-source time in seconds; Col. (7) is the heliocentric recession velocity measured at the mid-point of 20% flux after excluding companions (V_{\odot} , see §2.2.2). Cols. (8) and (9) are the HI line widths measured at the 20% and 50% level (W_{20}, W_{50}). Col. (10) gives the velocity-integrated flux and error ($f_{\text{HI}}, \sigma_{f_{\text{HI}}}$), both in Jy km s $^{-1}$, and Col. (11) gives the dispersion of the baseline channels measured in a line-free part of the spectrum (σ_{chan}) in mJy.

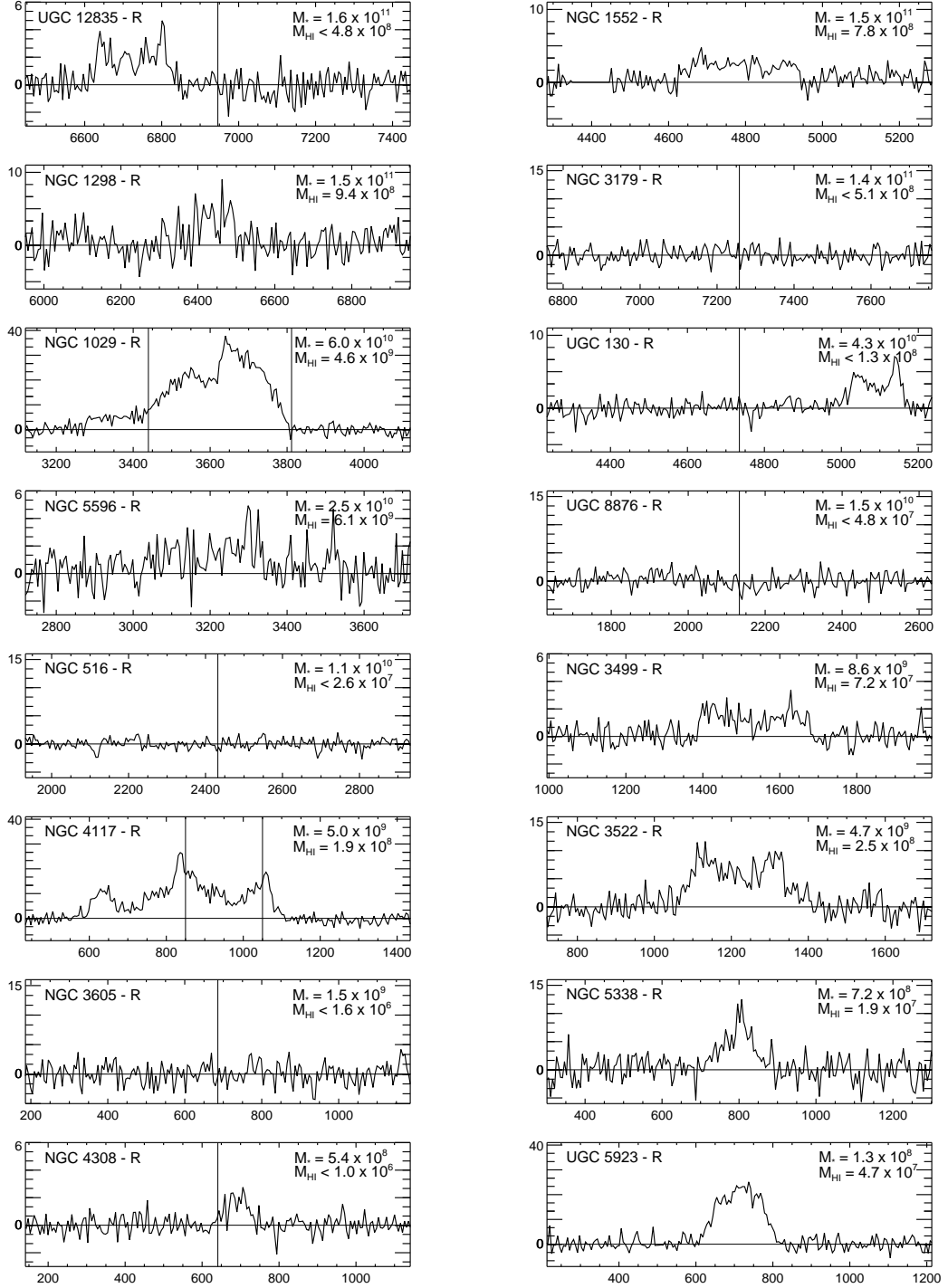


Figure 2.2: HI spectra of red-sequence E/S0s from the NFGS observed with the GBT. The galaxies are ordered left to right, top to bottom by decreasing stellar mass. Double vertical lines indicate the ranges of ionized-gas rotation (or stellar rotation, if ionized gas data are not available) between which we measure the HI flux to exclude companion flux. Please see Appendix A for more details on individual galaxies. Single vertical lines mark the optical velocities for the target galaxies with HI upper limits. NGC 4308 is considered a non-detection because the measured HI velocity coincides exactly with the optical velocity of a nearby companion. Assigning the gas to NGC 4308 would not change any results since the measured HI flux would still be extremely low for this galaxy’s stellar mass.

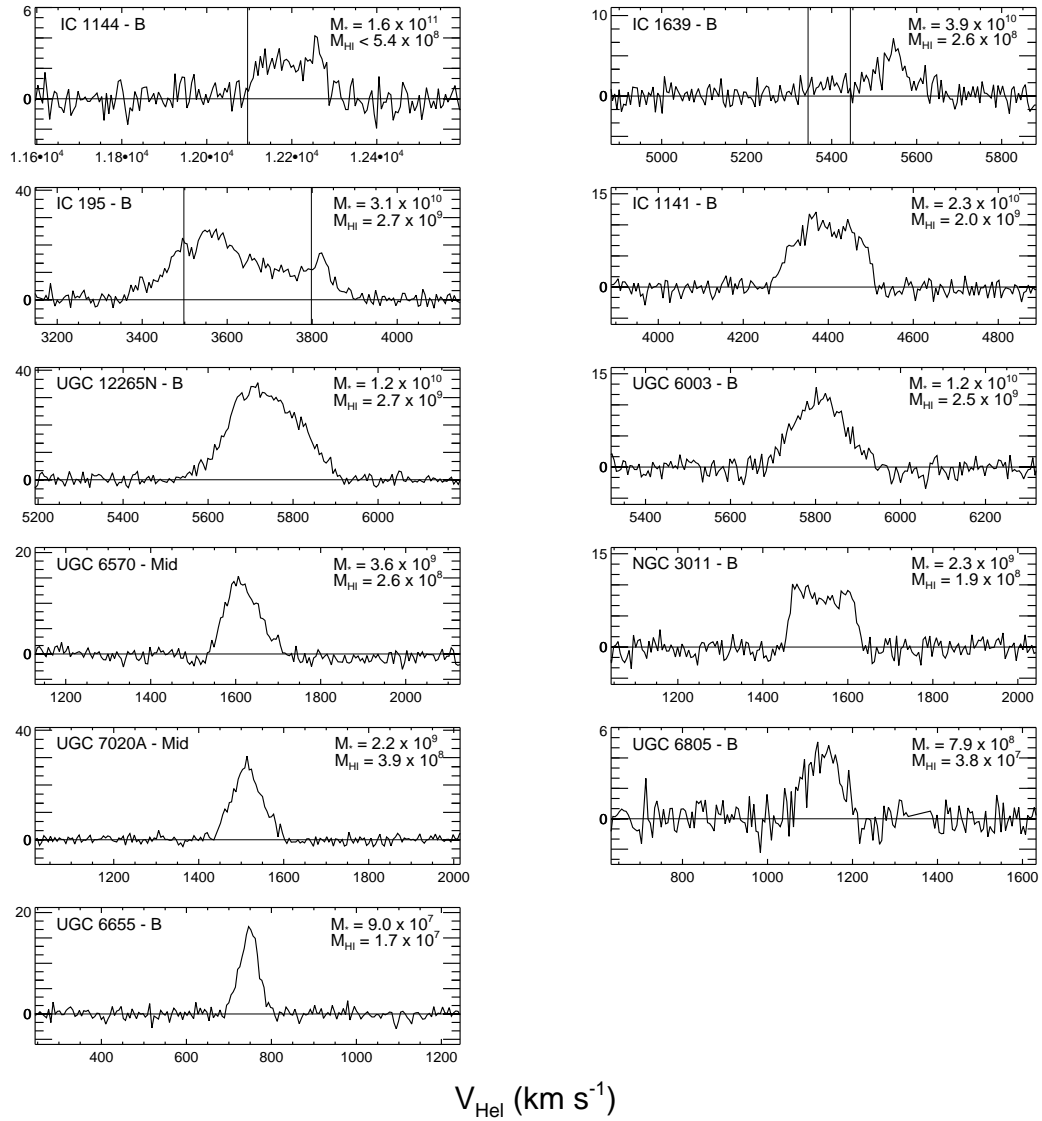


Figure 2.3: HI spectra of blue- and mid-sequence E/S0s from the NFGS observed with the GBT. The galaxies are ordered left to right, top to bottom by decreasing stellar mass. Double vertical lines indicate the ranges of ionized-gas rotation (or stellar rotation, if ionized gas data are not available) between which we measure the HI flux to exclude companion flux. Please see Appendix A for more details on individual galaxies. A single vertical line marks the optical velocity for the galaxy (IC 1144) with an HI upper limit. IC 1144 is not in the sub- M_b sample because of its large stellar mass ($M_* = 1.6 \times 10^{11} M_\odot$).

We estimate the error of our flux measurements following Schneider et al. (1986, 1990), who derived the following analytical expression for uncertainty in total HI flux ($\sigma_{f_{\text{HI}}}$):

$$\sigma_{f_{\text{HI}}} = 2\sigma_{\text{chan}} \sqrt{1.2W_{20}\Delta V} \text{ Jy km s}^{-1} \quad (2.1)$$

where σ_{chan} is the rms dispersion of the baseline in Jy and ΔV is the velocity resolution of the spectrum in km s^{-1} . The errors in the measured heliocentric velocity ($\sigma_{V_{\odot}}$) and velocity widths ($\sigma_{W_{50}}, \sigma_{W_{20}}$) are estimated following Fouque et al. (1990), using:

$$\sigma_{V_{\odot}} = 4\sqrt{\Delta V P} (\text{S/N})^{-1} \text{ km s}^{-1} \quad (2.2)$$

$$\sigma_{W_{50}} = 2\sigma_{V_{\odot}} \text{ km s}^{-1} \quad (2.3)$$

$$\sigma_{W_{20}} = 3\sigma_{V_{\odot}} \text{ km s}^{-1} \quad (2.4)$$

where P is the steepness of the profile, $(W_{20} - W_{50})/2$, and S/N is the ratio of the peak signal to σ_{chan} .

We cannot homogenize our HI fluxes to the HyperLeda system of Paturel et al. (2003), because these authors do not include the GBT in their homogenization calculations. However, because of the large beam of the GBT at 21cm ($\sim 9'$) compared to the small optical sizes of our galaxies ($\sim 2'$), no beam-filling correction is needed. Also, flux calibration of GBT HI spectral line data is extremely stable and accurate, so large offsets in the flux scale between our GBT data and the HyperLeda data are unlikely. In fact, comparison between our new GBT HI data and existing HI data from HyperLeda for 11 galaxies show that over half have GBT fluxes within 20%

of published HI fluxes, even though the HyperLeda data are of poorer quality in all cases. We discuss the HI fluxes and line profiles of individual galaxies in further detail in Appendix A.

Companions

We check for companions to our GBT galaxies by setting the search radius in the NASA/IPAC Extragalactic Database (NED) to match the beam of the GBT. For galaxies with known or obvious companions, we measure the HI flux twice: the first time we measure the flux within the velocity ranges from ionized-gas rotation curves (or stellar rotation curves, if ionized gas is not available), and the second time we include all flux in the beam within a reasonable velocity range near the galaxy ($\pm 300 \text{ km s}^{-1}$). We mark the ionized-gas/stellar velocity range used to measure fluxes for the first method in Figures 2.2 and 2.3 with double vertical lines. We present both measurements in Table 2.5: the first row contains values measured in the ionized-gas/stellar velocity range, while the second row includes companion flux (if any) within $\pm 300 \text{ km s}^{-1}$.

The first method most likely underestimates HI content for the two galaxies (IC 1639, IC 195) for which we must determine the velocity range from stellar rotation curves, as those rotation curves are still rising at the last measured point. The ionized-gas rotation curves used for the other galaxies, on the other hand, are flat, so the underestimation of HI flux for those galaxies should be small. The second method likely overestimates a galaxy's HI reservoir, since cold gas from a companion may not be readily accessible for star formation in the target galaxy. *We only use fluxes measured with the first method in our analysis, as conservative estimates of HI gas mass.* We discuss how our results may change if we include companion gas in §2.5.1.

Kinematics

We estimate the observed maximum rotation speed, V_M^{syni} for each galaxy following Paturel et al. (2003):

$$\log 2V_M^{\text{syni}} = a \log W(r, l) + b \quad (2.5)$$

where a and b are specified for a given velocity width W measured at % level l and velocity resolution r , enabling galaxies from disparate HI datasets to be compared. For our GBT data, we adopt the recommended values of $a = 1.071$ and $b = -0.21$ to convert our W_{50} widths into V_M^{syni} (Table 2.4, Col. (7)).

We find the difference between heliocentric measurements of the HI velocity and the optical velocity for NFGS galaxies to be small, centered around 0 km s^{-1} , with a standard deviation of 33 km s^{-1} .

Atomic Gas Masses

Of the 200 galaxies in the NFGS, we have HI information for 170: new GBT observations for 27 galaxies, HyperLeda HI data for 128 galaxies, and other literature data for 15 galaxies. The 30 galaxies with no HI information are distributed reasonably evenly between morphological types (53% early, 40% late, and 7% Pec/Im) as well as sequences (43% blue, 43% red, and 14% unknown because no stellar mass estimate is available). We plot $U - R$ color as a function of R -band luminosity in Figure 2.4 to show the distribution of the NFGS sample with HI information. There is a somewhat higher frequency of missing data among the brightest galaxies (also the most distant, Jansen et al. 2000b).

The HI gas masses given in Col. (9) of Table 2.4 are calculated from f_{HI} following Haynes & Giovanelli (1984):

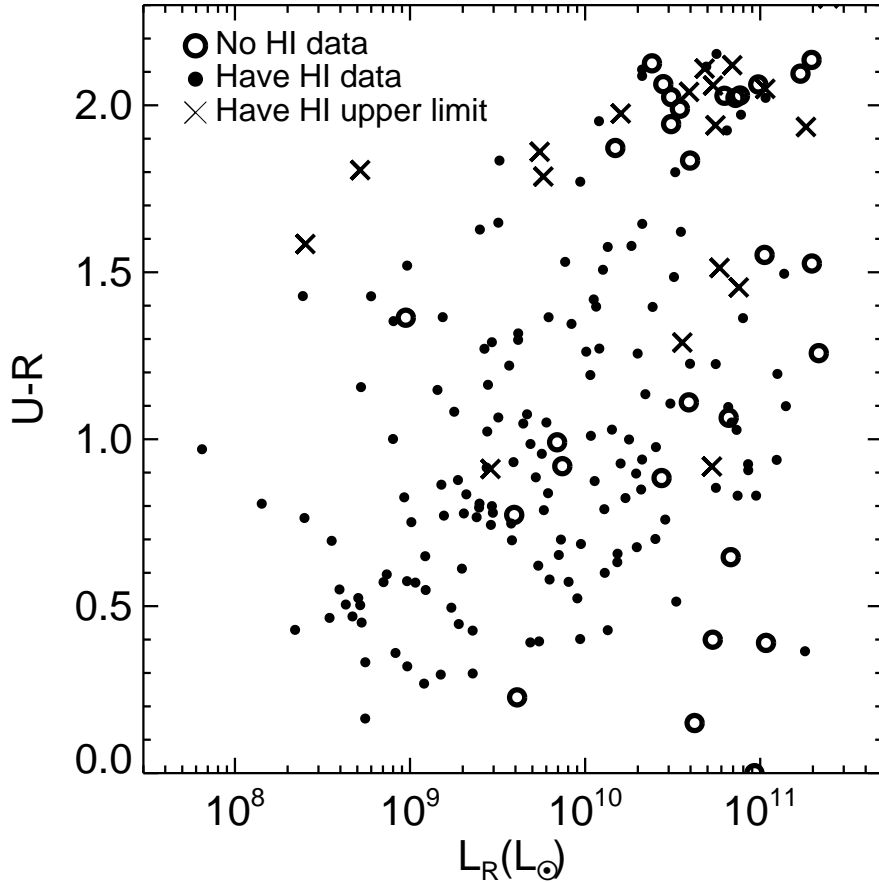


Figure 2.4: $U - R$ color as a function of R -band luminosity, both extinction corrected, for galaxies in the NFGS. HI detections are shown as dots, HI upper limits are represented by \times 's, and galaxies with no HI data are shown as open circles.

$$M_{\text{HI}} = 2.36 \times 10^5 f_{\text{HI}} \left(\frac{v_{\text{vlgvc}}}{H_0} \right)^2 M_{\odot} \quad (2.6)$$

where v_{vlgvc} is the Local Group and Virgocentric flow corrected recessional velocity from Jansen et al. (2000b), which we use to be consistent with the stellar mass estimates. We multiply the HI gas mass by a factor of 1.4 to account for the presence of helium.

Upper Limits to HI Masses

To calculate upper limits, we measure the rms dispersion of the baseline, σ_{chan} , in a signal-free part of the spectrum within the velocity range from ionized-gas (or stellar) rotation curves. We then estimate σ_{up} following:

$$\sigma_{\text{up}} = \sigma_{\text{chan}} \Delta V \sqrt{N} \quad (2.7)$$

where N is the number of channels in the velocity range we measured from, and ΔV is the width of each channel in units of km s^{-1} . We estimate the HI mass upper limit using $3\sigma_{\text{up}}$ as the HI flux and following Equation 2.6.

2.3 Gas Reservoirs

2.3.1 Comparison of Gas Reservoirs in NFGS Galaxies

All of our sub- M_b blue-sequence E/S0s, as well as both mid-sequence E/S0s, are detected in HI and have atomic gas masses ($M_{\text{HI+He}}$) ranging from 10^7 to almost $10^{10} M_{\odot}$. In contrast, four of our eleven sub- M_b red-sequence E/S0s were not detected, although we integrated down to upper limits of 10^6 – $10^7 M_{\odot}$. The remaining seven galaxies have atomic gas masses ranging from 10^7 – $10^9 M_{\odot}$.

We plot the distribution of atomic gas mass as a function of stellar mass for the sub- M_b blue- and red-sequence E/S0s, mid-sequence E/S0s, and other NFGS galaxies in Figure 2.5. We find that, at a given M_* , blue-sequence E/S0s tend to have larger gas masses than red-sequence E/S0s. This result confirms the preliminary results of KGB, for HI data that are much more complete in terms of sampling sub- M_b E/S0s. Since almost half of the red-sequence E/S0s are actually upper limits, the separation between the gas masses of blue- and red-sequence E/S0s is actually

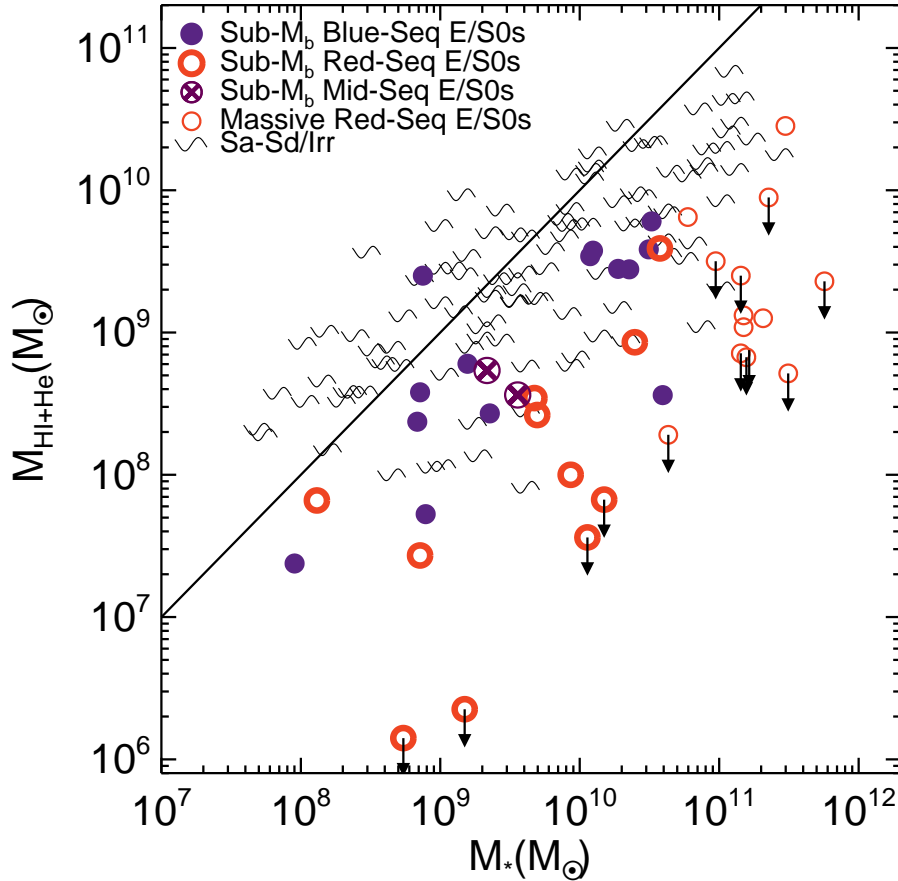


Figure 2.5: Distribution of atomic gas mass (HI + He) for galaxies in the NFGS, as a function of stellar mass. Solid line indicates 1:1 ratio; downward arrows indicate upper limits.

larger than it appears in Figure 2.5.

Even more intriguing is the location of blue-sequence E/S0s *in between* spiral/irregular galaxies and red-sequence E/S0s in the $M_{\text{HI+He}}$ vs. M_* relation shown in Figure 2.5. In fact, there is considerable overlap between blue-sequence E/S0s and spiral/irregular galaxies. This supports the KGB suggestion that blue-sequence E/S0s form a transitional class between spirals/irregular galaxies and traditional red-sequence E/S0s, as originally inferred from the fact that blue-sequence E/S0s also lie between spiral/irregular galaxies and red-sequence E/S0s in the M_* -radius

and M_* - σ relations.

Since we are interested in the potential for morphological transformation in blue-sequence E/S0s, it is informative to consider $M_{\text{HI+He}}/M_*$ — the mass of the atomic gas relative to the current stellar mass of a galaxy. We plot the distribution of atomic gas-to-stellar mass ratios for sub- M_b E/S0s on both sequences in Figure 2.6a and list their values in Table 2.1. A Kolmogorov-Smirnov test on the distributions of $M_{\text{HI+He}}/M_*$ for sub- M_b red- and blue-sequence E/S0s rejects at the 99% level the possibility that these galaxies derive from the same parent population.

While most of the sub- M_b blue-sequence E/S0s and both the mid-sequence E/S0s have $M_{\text{HI+He}}/M_*$ in the range of 0.1 to 1.0, all but two of the sub- M_b red-sequence E/S0s have $M_{\text{HI+He}}/M_* < 0.1$. Following Binney & Merrifield (1998) Figure 4.51, the formation of new stars in an extended disk constituting 25% of original total stellar mass will change the typical S0 galaxy to an Sa galaxy. This suggests that at least half of the sub- M_b blue-sequence E/S0s *do* have large enough gas reservoirs for major morphological transformation *if* all the gas is converted into stars in the disk. We discuss in later sections whether the gas is actually forming stars. But for now, we can say that at least half of our sub- M_b blue-sequence E/S0s do have the *potential* to transform their morphologies simply based on their atomic gas masses. In contrast, sub- M_b red-sequence E/S0s lack sufficient atomic gas to do the same, with rare exceptions.

Interesting Outliers

Figure 2.6a shows that while sub- M_b red-sequence E/S0s tend to have lower values of $M_{\text{HI+He}}/M_*$, sub- M_b blue-sequence E/S0s tend to have higher values. There are, however, a couple of outliers that do not seem to follow this trend. The most prominent of the outliers are the red-sequence E/S0 with a large gas reservoir,

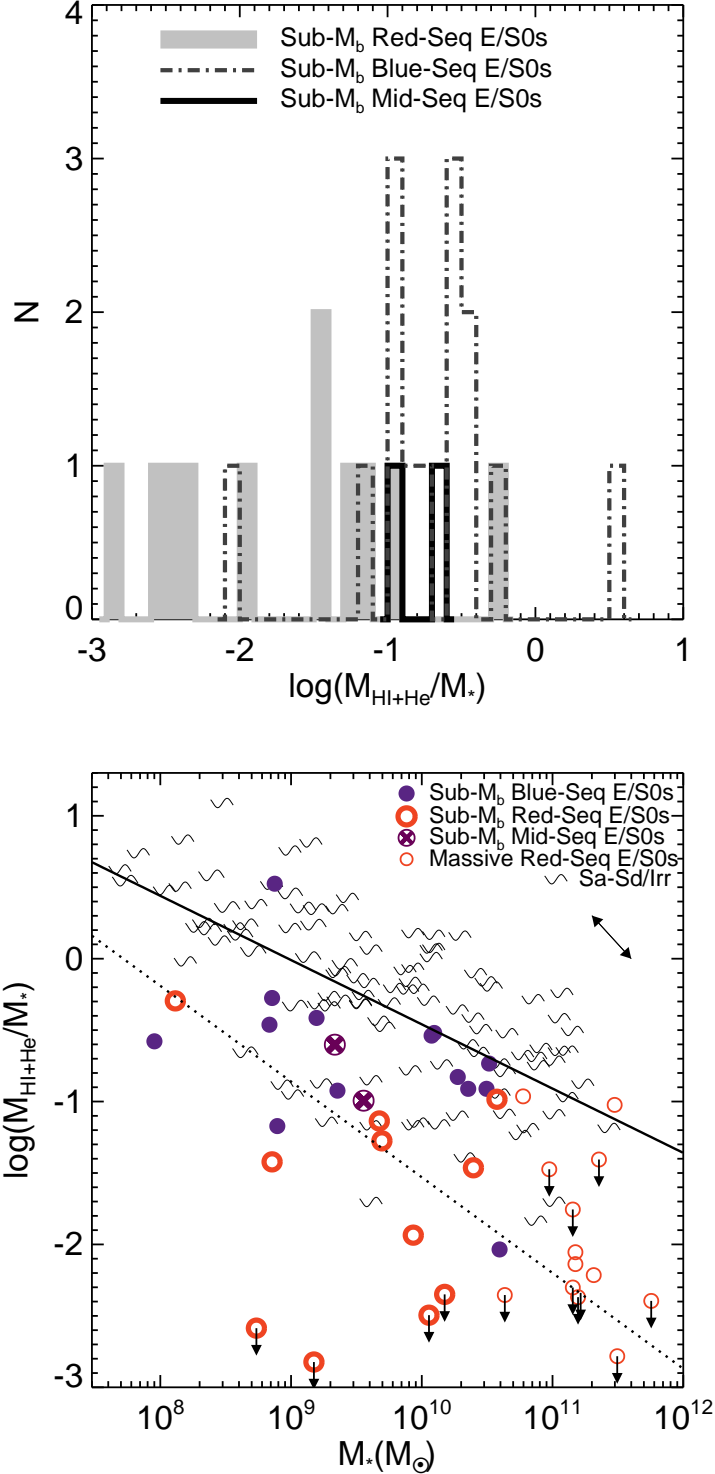


Figure 2.6: (a) Histogram of the distribution of atomic gas-to-stellar mass ratio for red-, blue-, and mid-sequence E/S0s in the sub- M_b E/S0 sample. (b) Atomic gas-to-stellar mass ratio as a function of stellar mass for galaxies in the NFGS. The arrow in the upper right indicates a factor of two error in stellar mass in either direction (increasing or decreasing). Downward arrows indicate upper limits. The solid/dashed line is the forward fit of $M_{\text{HI+He}}/M_*$ as a function of M_* for late/early-type galaxies in the NFGS.

Table 2.1. Values of M_* and $M_{\text{HI+He}}/M_*$ for the sub- M_b sample.

Galaxy Name	M_* (M_\odot)	$M_{\text{HI+He}}/M_*$
IC 1639	3.9×10^{10}	0.01
IC 195	3.1×10^9	0.12
NGC 3011	2.3×10^9	0.12
UGC 6003	1.2×10^{10}	0.29
IC 692	7.2×10^8	0.53
UGC 6637	1.6×10^9	0.38
UGC 6655	9.0×10^7	0.26
UGC 6805	7.9×10^8	0.07
NGC 5173	1.9×10^{10}	0.15
UGC 9562	7.5×10^8	3.35
IC 1141	2.3×10^{10}	0.12
NGC 7077	6.8×10^8	0.34
NGC 7360	3.3×10^{10}	0.18
UGC 12265N	1.2×10^{10}	0.30
UGC 6570	3.6×10^9	0.10
UGC 7020A	2.2×10^9	0.25
NGC 516	1.1×10^{10}	<0.003
UGC 5923	1.3×10^8	0.51
NGC 3499	8.6×10^9	0.01
NGC 3522	4.7×10^9	0.07
NGC 3605	1.5×10^9	<0.002
NGC 4117	5.0×10^9	0.05
NGC 4308	5.4×10^8	<0.003
NGC 5338	7.2×10^8	0.04
UGC 8876	1.5×10^{10}	<0.004
NGC 5596	2.5×10^{10}	0.03
NGC 6123	3.8×10^{10}	0.10

Note. — Values of M_* and $M_{\text{HI+He}}/M_*$ for blue-, mid-, and red-sequence E/S0s in the sub- M_b sample. Typical uncertainty in $M_{\text{HI+He}}/M_*$ is $\lesssim 10\%$.

UGC 5923 ($\log M_{\text{HI+He}}/M_* = -0.3$), and the blue-sequence E/S0 with a very small gas reservoir, IC 1639 ($\log M_{\text{HI+He}}/M_* = -2.0$). Taking the stellar masses of these galaxies into consideration, however, provides plausible explanations for their gas-to-stellar mass ratios.

UGC 5923, the gas-rich red-sequence E/S0, has the lowest stellar mass of all red-sequence E/S0s in the NFGS with $M_* = 1.3 \times 10^8 M_\odot$, so it is not surprising that this galaxy has a fractionally large gas reservoir, despite its red color. $\text{H}\alpha$ emission indicates that there is some low-level star formation in UGC 5923, but not enough to push the galaxy towards the blue sequence. This galaxy does, however, appear dusty and has the highest internal extinction of all sub- M_b red-sequence E/S0s, which suggests that it could also be forming stars *now* behind an obscuring dust screen. But for dust, this object might well follow the trend of the blue-sequence E/S0s in Figure 2.6.

IC 1639, the gas-poor blue-sequence E/S0, is on the other end of the stellar mass scale as the galaxy with the largest stellar mass in the sub- M_b E/S0 sample ($M_* = 3.9 \times 10^{10} M_\odot$). KGB argue that blue-sequence E/S0s at these higher stellar masses are more often associated with violent encounters than disk building. It is possible that this galaxy underwent an interaction with its larger companion in the not-so-distant past, which triggered a burst of star formation (hence its blue color) and quickly exhausted its gas reservoir.

$M_{\text{HI+He}}/M_*$ as a Function of Stellar Mass

The outliers described in the previous section indicate the importance of taking stellar mass into account when considering the gas-to-stellar mass ratio. Hence we plot $M_{\text{HI+He}}/M_*$ as a function of M_* (Figure 2.6b) for all galaxies in the NFGS.

We fit the trend of decreasing atomic gas-to-stellar mass ratio with increasing

Table 2.2. Fits of $M_{\text{HI+He}}/M_*$ vs. M_*

NFGS population	Fit Type	Slope	Intercept	Scatter
Blue Sequence:				
	forward	-0.45 ± 0.05	4.09	0.45
	bisector	-0.72	6.70	
Spiral/Irregular:				
	forward	-0.45 ± 0.05	4.04	0.44
	bisector	-0.70	6.49	
Red Sequence:				
	forward	-0.67 ± 0.12	5.23	0.58
	bisector	-1.46	13.0	
E/S0:				
	forward	-0.67 ± 0.12	5.17	0.59
	bisector	-1.57	13.9	

Note. — Fits of $\log(M_{\text{HI+He}}/M_*) = m \log(M_*) + b$ for all galaxies in the NFGS with HI data, grouped by either sequence or morphological type. The forward fits were done using Buckley-James survival method in the ASURV package (Lavalley et al. 1992). The bisector fit is the mathematical bisector of the forward and backward fits using the same survival method, and so lacks estimates of the uncertainty and scatter.

stellar mass in Figure 2.6b with a line in the form of $\log(M_{\text{HI+He}}/M_*) = m \log(M_*) + b$ for all NFGS galaxies with HI data, using survival analysis (the ASURV package: Lavalley et al. 1992) to include galaxies with $M_{\text{HI+He}}$ upper limits. Table 2.2 lists the coefficients for the different fits (forward, bisector) for different populations (Blue Sequence, Red Sequence, Spiral/Irregulars, and E/S0s).

As mentioned earlier, most of the sub- M_b blue-sequence E/S0s have $M_{\text{HI+He}}/M_*$ in the range of 0.1 to 1.0, while all but two of the sub- M_b red-sequence E/S0s have $M_{\text{HI+He}}/M_* < 0.1$. The separation between the two populations is even more striking in Figure 2.6b, and re-emphasizes the difference in potential for morphological transformation between sub- M_b blue- and red-sequence E/S0s.

2.3.2 Comparison with Sage & Welch E/S0 Sample

We compare the masses of gas reservoirs in our sample of sub- M_b E/S0s with an ongoing survey of cold gas (HI and CO) in a volume-limited sample of nearby E/S0s by Sage & Welch (2006) and Sage et al. (2007). Sage & Welch (2006) report that E/S0s contain less than $\sim 10\%$ of the cold gas mass (HI + He + H₂) predicted for gas return by analytical stellar evolution models (Ciotti et al. 1991). In particular, Ciotti et al. (1991) predict that $M_{\text{gas}} \sim L_B$ in solar units, while Sage & Welch (2006) conclude that $M_{\text{gas}} \lesssim 0.1 L_B$ for S0s and suggest that this also applies to ellipticals based on preliminary data (Sage et al. 2007).

We plot M_{gas}/L_B vs. L_B in Figure 2.7, showing $M_{\text{gas}} \sim 0.1 L_B$ as a dashed line. We divide M_{gas} by L_B rather than M_* to facilitate comparison with Sage & Welch (2006); although the larger scatter compared to Figure 2.6b suggests that L_B does not work as well in tracing the stellar mass as M_* , M_* is not available for the E/S0s from Sage & Welch (2006) and Sage et al. (2007).

While there are a few E/S0 galaxies from Sage & Welch (2006) and Sage et al. (2007) with values of $M_{\text{gas}}/L_B > 0.1$, the majority of their E/S0s have much smaller values of M_{gas}/L_B . In contrast, all but two of our sub- M_b blue-sequence E/S0s fall above the $0.1 M_{\text{gas}}/L_B$ cutoff, as do both of the mid-sequence and a few red-sequence E/S0s. Note that our data points do not include molecular gas as opposed to the Sage & Welch (2006) data points, so the values of M_{gas}/L_B for our galaxies reflect only the neutral atomic ISM, and the actual values could be even higher. This result suggests that the sub- M_b blue-sequence E/S0s in our sample have some of the most massive fractional gas reservoirs among early-type galaxies, in comparison to red-sequence E/S0s in our sample as well as E/S0s from the literature.

The differences in how galaxies in the two samples are selected may explain the

disparity in M_{gas}/L_B between them. The Sage & Welch (2006) sample, selected from the Nearby Galaxies Catalog, inherits the parent sample’s biases against optically small galaxies (diameter $< 1'.5\text{--}2'$) and HI-poor systems (Welch & Sage 2003). Hence, it is likely that the Sage & Welch (2006) E/S0s are more massive and therefore more likely to be on the red sequence than our sample of E/S0s. The distribution of L_B for the two different samples in Figure 2.7 hints at this, with our sample of sub- M_b E/S0s predominantly at lower L_B and the Sage & Welch (2006) sample dominating at higher values. Note that the L_B of blue-sequence E/S0s in our sub- M_b sample may be systematically enhanced by star formation, decreasing M_{gas}/L_B , so the difference in M_{gas}/M_* between our sub- M_b E/S0s and the Sage & Welch (2006) galaxies may be even larger.

Although our sub- M_b blue-sequence E/S0s have larger gas mass reservoirs than seen by Sage & Welch, we still find much smaller reservoirs than those predicted for gas return by the analytical stellar evolution models discussed in Sage & Welch (2006), ranging from 10% to 30% of the predicted values. Our findings support Sage & Welch’s conclusion that stellar mass loss is not the primary source of HI in E/S0s.

2.4 Star Formation and Stellar Mass Growth

Now that we have established that sub- M_b blue-sequence E/S0s typically have substantial fractional atomic gas reservoirs and therefore potential for morphological transformation, we consider the question of whether this gas is being converted into stars at a rate that can lead to morphological transformation in a reasonable amount of time. Although we lack information about the spatial distribution of the atomic gas, we can make some simplifying assumptions and create limiting scenarios for the evolutionary trajectory of blue-sequence E/S0s given the current rate of star

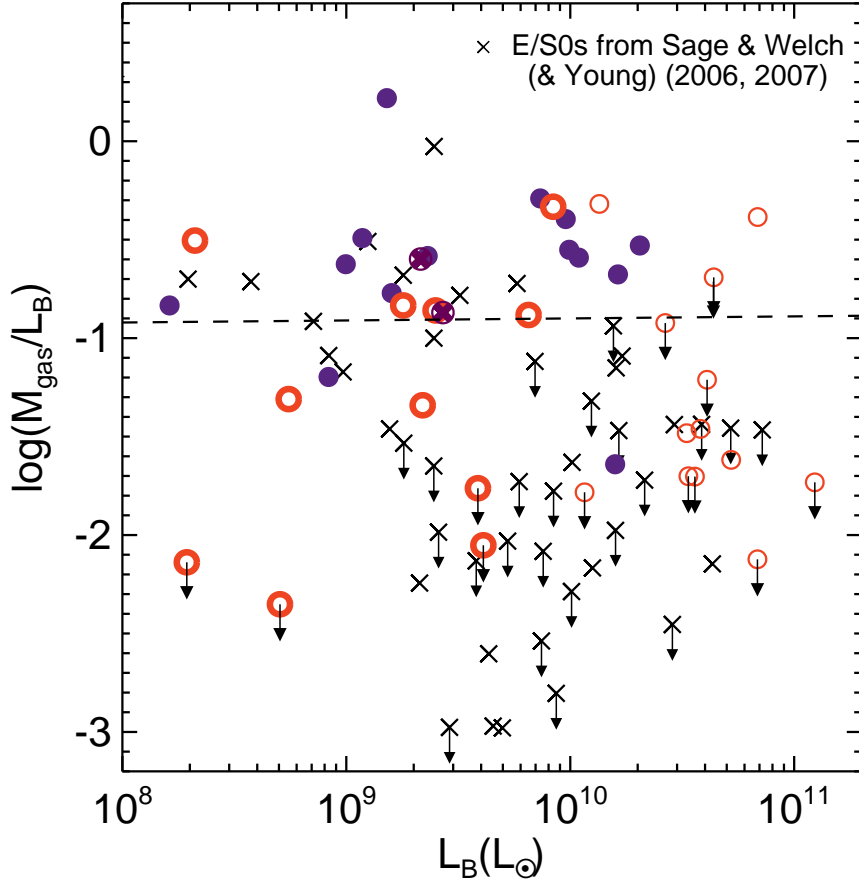


Figure 2.7: Ratio of gas mass to B -band luminosity (in solar units) vs. B -band luminosity. The B -band luminosities are corrected for foreground and internal extinction. M_{gas} values for E/SOs from Sage & Welch (2006, 2007; \times 's) account for HI, He, and H_2 , while M_{gas} values for blue-, red-, and mid-sequence E/SOs from this Chapter (filled and empty circles, same symbols as Figures 2.5 and 2.6b) account for only HI and He. The cold gas cutoff at $M_{\text{gas}} \sim 0.1 L_B$ found by Sage & Welch (2006) is shown as a dashed line. Downward arrows indicate upper limits.

formation.

2.4.1 Two Limiting Scenarios for Growth in the Stellar Component

To construct truly realistic scenarios for the evolutionary path of our galaxies, we would have to account for all sinks and sources of gas. The sink terms are the rates at which gas is converted into stars and ionized and/or expelled due to stellar winds and supernovae. The source terms include the rate at which fresh gas is brought in from external sources (minor mergers, interactions, etc.) and at which gas is returned by stellar evolution. A detailed accounting of all these processes, however, is beyond the scope of this Chapter. While there are many theoretical studies of the hierarchical assembly of galaxies (many of which include estimates of the frequency of mergers), simulations still lack the resolution to predict the frequency of very minor mergers and interactions. We discuss current simulations in more detail in §2.5.1.

We consider here the range of plausible evolutionary trajectories for our blue-sequence E/S0s by presenting two simplified, but limiting, scenarios. We should note that we assume that the atomic gas is distributed in such a way that it can be made available for star formation (e.g., via conversion to molecular gas) at a rate comparable to the current star formation rate. This may not always be the case, but we argue that this is a plausible assumption in §2.5.1 and §2.5.2.

In the first scenario, we assume that the current star formation rate remains constant over time, which is an assumption many population synthesis models make. Preserving a constant star formation rate requires an increasing star formation efficiency for a closed box, or open-box inflows. This scenario provides a reasonable upper limit on the possible growth in stellar mass per unit time and a lower limit

on the amount of time it takes for that mass to form.

The second scenario represents the other limit: an exponentially declining star formation rate (i.e., closed box with no gas return). For each galaxy, we start out with the current cold gas reservoir ($M_{\text{HI+He},0}$) and star formation rate (SFR_0). As time progresses, the star formation rate declines exponentially following $\text{SFR}(t) = \text{SFR}_0 e^{-t/\tau}$ as gas is converted into stars, where $\tau = M_{\text{HI+He},0}/\text{SFR}_0$ (e.g., Li et al. 2006). This scenario defines the lower limit on the amount of gas converted to stars within a fixed time, as the star formation rate is declining exponentially.

Because we lack information regarding the frequency of internal/external gas replenishment, these two scenarios (exponentially declining SFR with no new gas, and constant SFR allowing gas infall) represent simplified limits that likely bracket the actual amount of growth in the stellar component in these galaxies.

2.4.2 Estimates of Stellar Mass Growth Over Time

Given the two limiting scenarios described in the previous section, how much growth in stellar mass is possible for the different galaxies? We plot the ratio of new stellar mass formed relative to the current stellar mass as a function of current stellar mass 1, 2, 3, and 4 Gyr in the future in Figures 2.8a–d, respectively. Here we note that 11 E/S0s from the sub- M_b sample (two on the blue sequence and nine on the red sequence) do not appear in Figure 2.8. These galaxies have spectra that are integrated over the galaxy, but no H α emission was detected, so these galaxies do not appear in any of the figures using star formation rates. Future work with *GALEX* and *Spitzer* data will provide better estimates of the star formation rates in these galaxies.

For each galaxy, a vertical line in Figure 2.8 represents the range of possible fractional increase in stellar mass, with the lower end representing the exponentially

declining SFR scenario and the upper end representing the constant SFR scenario. We mark the vertical line with a horizontal dash to note the stellar mass fraction at which the original gas reservoir run out. Any growth in the stellar component indicated by the line above the horizontal dash requires inflow of gas, which we allow in the constant star formation scenario. Galaxies that have not converted all of the original gas mass in the constant star formation rate scenario after the time specified for each figure do not have a horizontal dash. Since these two scenarios are the limiting cases, it is likely that the actual amount of stellar mass growth is somewhere in between the two ends of the line.

Figure 2.8b shows that many of the sub- M_b blue-sequence E/S0s (dark solid lines) have the potential to increase their stellar masses by a large fraction in just 2 Gyr, with seven of the fourteen sub- M_b blue-sequence E/S0s crossing or above the 10% line. In 3 Gyr, the time by which most sub- M_b blue-sequence E/S0s have exhausted their gas reservoirs (2.5.1), nine of the fourteen sub- M_b blue-sequence E/S0s will cross or be above the 10% line. The remaining five blue-sequence E/S0s have lower SFRs, so they are below the 10% line after 3 Gyr has passed. In fact, the SFRs for NGC 7360, IC 1639, and IC 195 are so low they do not form $>0.1\%$ of their current stellar masses within 3 or even 4 Gyr, so they do not appear on any of the panels in Figure 2.8. This large spread in the fractional stellar mass growth in blue-sequence E/S0s reflects the spread in star formation rates, which in turn may be indicative of differences in burst stages of the galaxies within this population. We discuss this in more depth in §2.5.2.

The two mid-sequence E/S0s in our sample also have potential for substantial morphological transformation. UGC 7020A ($M_* \sim 2.2 \times 10^9$) can form new stellar mass in the range of 20–40% of its current stellar mass within 3 Gyr, and UGC 6570 ($M_* \sim 3.6 \times 10^9$) can form new stellar mass $\sim 10\%$ over the same period.

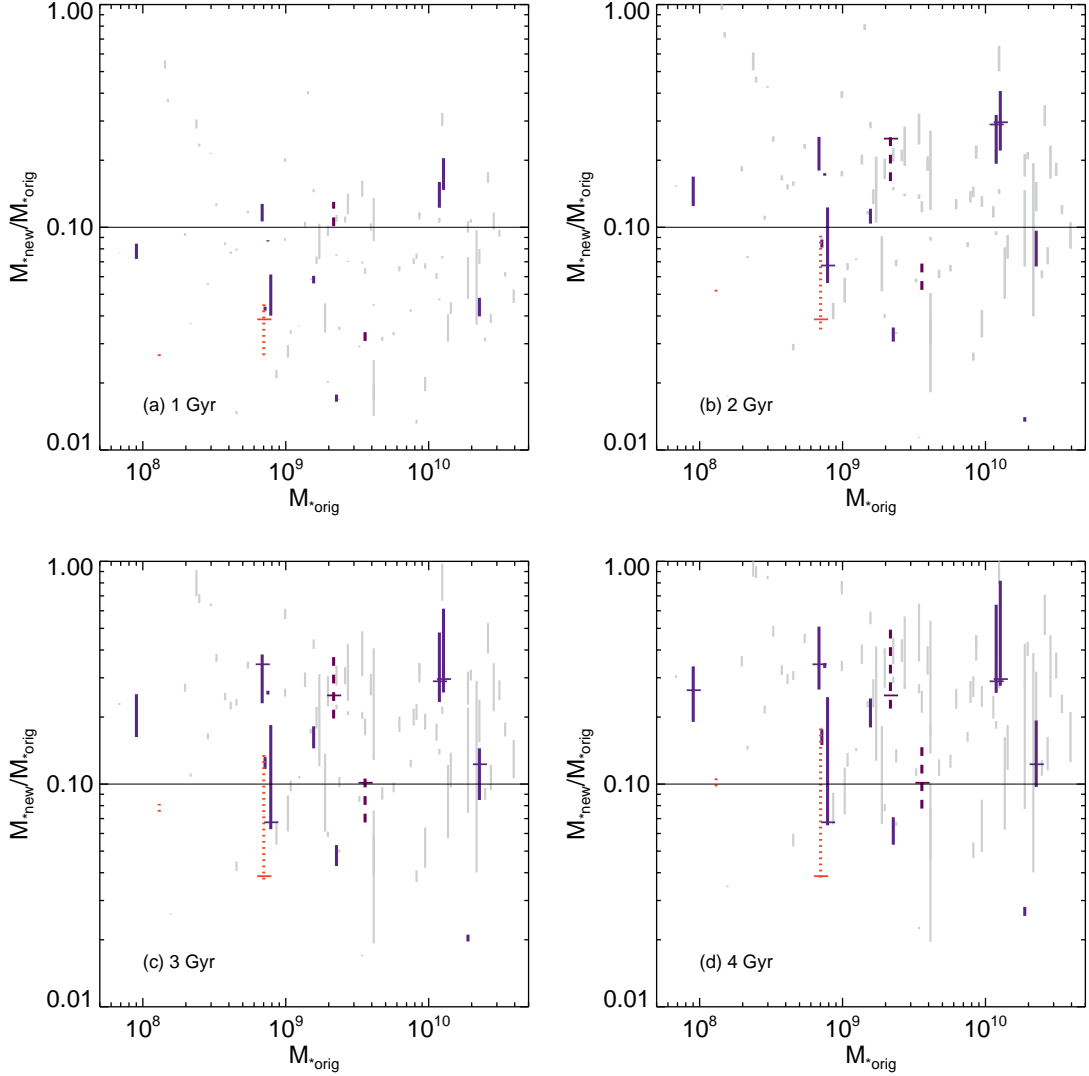


Figure 2.8: The fractional stellar mass formed 1, 2, 3, and 4 Gyr in the future. For each galaxy, the two different scenarios are represented by the lower (exponentially declining SFR) and upper (constant SFR) end of a vertical line. The horizontal dash marks where the original gas reservoir runs out for each galaxy. The solid horizontal line indicates 10% fractional stellar mass growth. Dark solid vertical lines represent sub- M_b blue-sequence E/S0s, short vertical dashes are sub- M_b red-sequence E/S0s, long vertical dashes are mid-sequence E/S0s, and solid grey lines are spiral/irregular galaxies.

The low-mass red-sequence E/S0 with a surprisingly large gas mass reservoir discussed earlier, UGC 5923 ($M_* \sim 1.3 \times 10^8$), has a relatively low star formation rate, but can still form new stellar mass $>10\%$ of its current stellar mass within 3 Gyr. NGC 5338 ($M_* \sim 7.2 \times 10^8$) has a very small gas reservoir but might form significant stellar mass if there is replenishment of gas. The rest of the sub- M_b red-sequence E/S0s have such low SFRs that they are below the 1% line (i.e., off the plot) in all four panels of Figure 2.8.

We plot the same lines of fractional stellar mass growth for spiral and irregular galaxies with $M_* \leq 4 \times 10^{10} M_\odot$ in grey in Figures 2.8a–d for comparison. For sub- M_b blue-sequence E/S0s, the ratio of new stellar mass formed in 1–3 Gyr to original stellar mass is comparable to that of the spiral/irregular distribution (Figure 2.8a–c). This suggests that, as a population, sub- M_b blue-sequence E/S0s have potential for growth in the stellar component similar to that of spiral/irregular galaxies in the near term future (~ 1 –3 Gyr). The horizontal dashes marking where the original gas reservoirs runs out, however, suggest that the inflow of fresh gas is important to the long-term evolution of our galaxies (Figure 2.8c, d).

2.5 Availability of Gas for Star Formation

2.5.1 Timescale for Gas Exhaustion and Inflow

Without maps of the distribution of HI, we cannot say for certain that the atomic gas is distributed in such a fashion that it is readily available for star formation. In §2.5.1 and §2.5.1 below, we argue that regardless of the distribution of the atomic gas (extra-planar, in the disk, or in companions), the timescale for inward travel of gas is most likely shorter than the duration of star formation in blue-sequence E/S0s. This suggests that assuming that the atomic gas reservoir is readily available

for star formation is reasonable given internal or external mechanisms to drive gas inflow. In §2.5.2 we will discuss evidence for frequent, externally driven inflow in the sub- M_b blue-sequence E/S0 population.

Gas Exhaustion Time

The timescale that can be directly estimated from the atomic gas mass and star formation rate of a galaxy is the (atomic) gas exhaustion time ($\tau = M_{\text{HI+He}}/\text{SFR}$) — the amount of time it would take to convert all the gas into stars, assuming the current star formation rate remains constant. This is the same τ as the one used in the exponentially declining star formation rate calculation for the second scenario in §2.4.1, although by definition the gas reservoir will never be exhausted in this scenario since the SFR decreases exponentially in parallel with decreasing gas mass. *Most* of the gas mass, however, will be converted into stellar mass within the timescale τ , so this is an interesting timescale to consider for both scenarios.

Table 2.3 lists the gas exhaustion times for galaxies in the sub- M_b E/S0 sample that have star formation rates. The large spread in gas exhaustion times may be reflective of the diversity of evolutionary states within the blue-sequence E/S0 population, which we explore further in §2.5.2. Note that the range of gas exhaustion timescales we find includes shorter timescales than found by KGB because of preferential incompleteness at low HI masses in the archival data used by KGB.

For a more informative picture, we plot the fraction of sub- M_b galaxies that will *not* have exhausted their original atomic gas reservoirs at a given future time in Figure 2.9. We include the mid-sequence E/S0s with the blue-sequence E/S0s in this figure as they seem to behave similarly. While the fraction of star-forming spiral/irregular galaxies seems to have a gradual, smooth decline in this figure, the blue-sequence E/S0s have a sharp drop-off at ~ 3 Gyr. In agreement with Figure

Table 2.3. Timescales for sub- M_b E/S0s

Galaxy	Seq.	τ (Gyr)	$t_{\text{dyn,HI}}$ (Gyr)	$t_{\text{dyn,GBT}}$ (Gyr)
NGC 3011	B	6.7	0.06	1.0
UGC 6003	B	1.8	0.12	2.5
IC 692	B	12.1	0.15	1.3
UGC 6637	B	6.4	0.17	1.6
UGC 6655	B	3.1	0.09	1.0
UGC 6805	B	1.1	0.06	1.1
NGC 5173	B	21.1	0.17	0.7
UGC 9562	B	38.3	0.10	1.6
IC 1141	B	2.5	0.07	1.3
NGC 7077	B	2.7	0.17	1.1
NGC 7360	B	168.5	0.15	1.1
UGC 12265N	B	1.4	0.17	2.4
UGC 6570	Mid	2.7	0.22	0.9
UGC 7020A	Mid	1.9	0.28	1.0
UGC 5923	R	18.7	0.04	0.7
NGC 5338	R	0.8	0.40	0.4

Note. — Col. (3): Gas exhaustion time, $\tau = M_{\text{HI+He}}/\text{SFR}$, in Gyr. Col. (4): Inward travel time of gas from the edge of the HI disk, following $t_{\text{dyn}} = \pi r_{\text{HI}}/2v_c$ (Binney & Tremaine 2008). We estimate r_{HI} using a typical ratio of HI to blue optical diameter of 2.11 for early type galaxies from Noordermeer et al. (2005), and v_c is the inclination-corrected maximum rotation speed of the HI from $V_M^{\text{sin}i}$. Col. (5): Inward travel time of gas from the edge of the GBT beam, following $t_{\text{dyn}} = \sqrt{\pi^2 r_{\text{beam}}^3/4GM_{\text{tot}}}$ (Binney & Tremaine 2008), where M_{tot} is the stellar mass of the galaxy multiplied by 10 to account for dark matter and r_{beam} is the distance from the edge of the GBT beam to the center of each galaxy.

2.8a–d, Figure 2.9 suggests that sub- M_b spiral/irregular galaxies typically continue forming new stars long after star formation in sub- M_b blue-sequence E/S0s is extinguished by the exhaustion of the original gas reservoir.

There is no drop-off for the sub- M_b red-sequence E/S0s, as we have SFRs for only two of the eleven galaxies. The fact that most of the sub- M_b red-sequence E/S0s have extremely low star formation rates, however, supports the conclusion that the near-term evolutionary trajectories of blue- and red-sequence E/S0s will be quite different.

Inward Travel of Gas

In §2.3 and §2.4, we have demonstrated that blue-sequence E/S0s have substantial fractional atomic gas reservoirs that, if readily available for star formation, can translate into significant growth in stellar mass and consequent morphological transformation. The key uncertainty is whether this gas is or can be made available for star formation on a reasonable timescale compared to the gas exhaustion timescale just discussed.

The GBT spectra, at 21 cm, have a resolution of only $\sim 9'$, which (for our sample) translates to an uncertain radius of 10–110 kpc in the location of atomic gas, depending on the distance to the galaxy. Without maps with sufficient angular resolution (e.g., VLA HI maps), we do not know whether the cold atomic gas is accessible for conversion into H_2 for star formation or not. Broadly, there are three possible distributions for the HI gas: on a trajectory falling into the galaxy, in an HI disk that is a part of the galaxy (the most plausible configuration for reasons discussed below), or in companions.

Infalling Gas: If the gas is somewhere outside the galaxy on its way inward, we expect it to travel inwards to the galaxy on a dynamical timescale. The $9'$ GBT

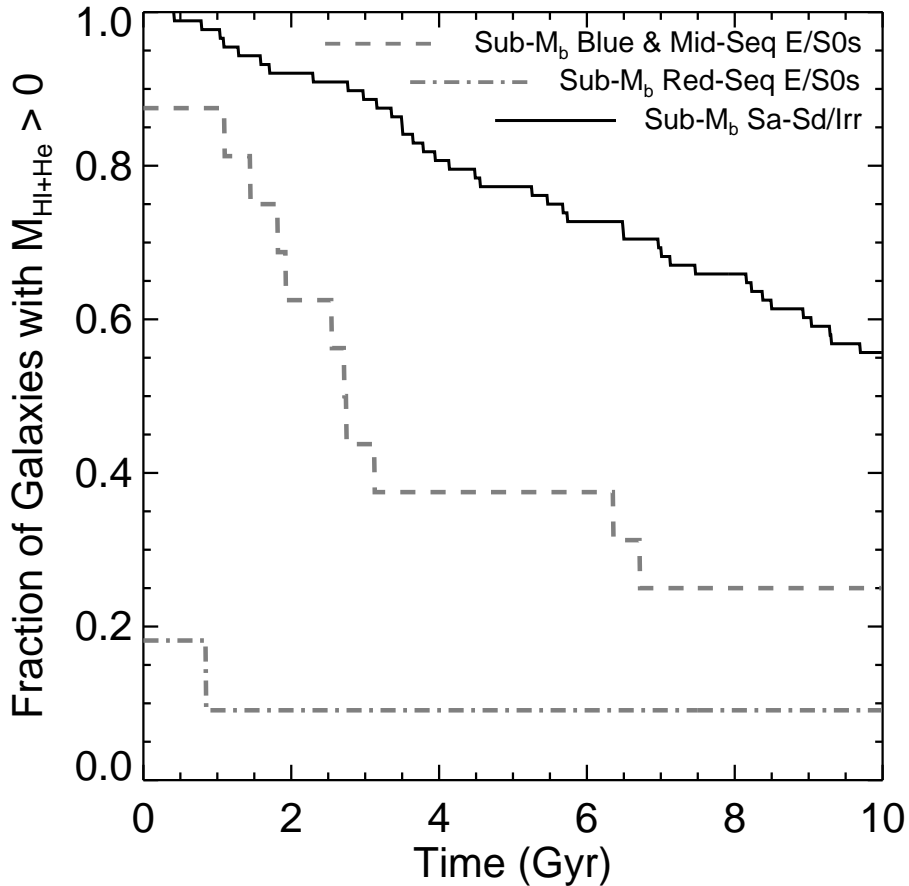


Figure 2.9: Fractions of galaxies that have not exhausted their atomic gas reservoirs as a function of time in a constant star formation rate scenario. Fractions begin below 1.0 because some E/S0s have no detected star formation.

beam at 1.4 GHz corresponds to radii of 10–110 kpc from the centers of galaxies in the sub- M_b E/S0 sample, with a median of 34 kpc. We list the dynamical timescale for inward travel of gas from the edge of the beam for each galaxy in the sub- M_b sample in Col. (5) of Table 2.3. The dynamical timescale estimates for inward travel of gas range from 0.4 to 2.5 Gyr, with a median of 1.1 Gyr. These timescale estimates are smaller than the gas exhaustion times for all but two of the galaxies. These two galaxies happen to be the most distant of all sub- M_b E/S0s in Table

2.3, so the edge of the GBT beam corresponds to >100 kpc. Therefore it is not surprising that these galaxies have long timescales for infall from the edge of the beam that are greater than their gas exhaustion times.

Assuming that the gas is at the edge of the beam is the most extreme case; it is much more likely that the gas is much closer to the galaxy, which would reduce the infall time as $r^{3/2}$. For example, the dynamical time for inflow of gas from the predicted HI radius (2–17 kpc, scaling from the blue optical radius using an assumed ratio of 2.11; Noordermeer et al. 2005) is much shorter than the gas exhaustion time in all cases, ranging from 50–400 Myr, with a median of 150 Myr (Table 2.3, Col. (4)). Fraternali & Binney (2008) find evidence for the infall of extra-planar gas onto star-forming spiral galaxies on short timescales — at rates comparable to their star formation rates (\sim few $M_{\odot} \text{ yr}^{-1}$), which supports our estimates above.

The dynamical timescales we estimate here are for inward travel of gas all the way to the center of the galaxy. However, the gas is capable of forming stars far from the centers of galaxies, depending on parameters such as local surface density and mid-plane pressure (e.g., Blitz & Rosolowsky 2004; Leroy et al. 2008). Thus the distance infalling gas has to travel to reach star forming regions and the corresponding infall timescale may be even shorter than our estimates above.

Disk Gas: Comparison between ionized-gas rotation curves and the new GBT HI profiles suggests that most of the atomic gas is likely distributed in rotating disks for all the GBT galaxies. We identify four particularly interesting cases. The ionized gas data show marginal or no rotation for UGC 6805, UGC 7020A, and UGC 6003, but their HI profiles have the appropriate widths for rotation given their stellar masses (e.g., based on the M_{*} -rotation velocity relation in KGB). There is no ionized gas detection at all for NGC 3522, so the HI profile for this galaxy indicates the presence of a previously unknown gas disk.

If the gas is in a stable orbit in the disk of a galaxy, it will not necessarily travel inwards towards star forming regions on a short timescale compared to the gas exhaustion time. Depending on the density of the gas, the gas disk may or may not collapse to form stars. A dense disk of gas could dovetail nicely with either of our star formation scenarios above — it will collapse and form a stellar disk at the rate of the global SFR. If, however, the HI disk is too diffuse and spread out in an extended disk, the gas will continue in circular orbit in a dormant fashion unless it is perturbed by internal instabilities or events such as minor mergers or interactions.

Recent simulations find that the frequency of mergers increases as the ratio of masses between the progenitors ($\xi < 1$) decreases (e.g., Stewart et al. 2008; Fakhouri & Ma 2008 and references therein). At the finest resolution currently available with the Millennium Simulation, Fakhouri & Ma (2008) find minor merger rates of 0.2 to 0.7 mergers per halo per Gyr at $z = 0$ for $\xi = 1:30$ to $1:100$, respectively. These minor merger rates correspond to one merger every 5 Gyr on the high mass end (1:30) and one per 1.4 Gyr on the low mass end (1:100). The minor merger rate at the high mass end (1:30) is perhaps a bit long relative to the gas exhaustion times for our galaxies, but minor mergers with progenitor mass ratios down to 1:100 and even smaller may still be capable of inducing gas inflow and star formation. Due to the lack of resolution, however, Fakhouri & Ma (2008) do not consider progenitor mass ratios smaller than 1:100, where mergers are extrapolated to occur on timescales shorter than 1 Gyr.

There is also observational evidence suggesting that tidal interactions with small companions occur relatively frequently in field galaxies, bringing fresh infall of gas. At least 25% of field galaxies observed in HI in several surveys show asymmetric features, indicating that they have recently undergone or are undergoing tidal interactions (Sancisi 1992; Verheijen & Sancisi 2001; van der Hulst et al. 2001).

Moreover, if one takes lopsided structure (azimuthal distortions in the stellar disk) and kinematics as evidence of interaction, the fraction would increase to more than 50% of field galaxies (Zaritsky & Rix 1997).

The frequency of minor mergers, taking into account recent studies of how gaseous disks could survive mergers and interactions (Hopkins et al. 2009; Stewart et al. 2009), suggests that if some of the galaxies in our sub- M_b E/S0 sample have large, diffuse, and extended HI disks, they may not lie dormant for too long before a minor merger or interaction induces the gas to flow inwards and triggers star formation. Once a minor merger or interaction occurs, we expect the gas to travel inwards on the order of a dynamical timescale or shorter (Barnes 2001). As we discussed above, these are short timescales relative to the frequency of minor mergers in simulations, and so we take the merger rate as the limiting factor in this case, not the subsequent inward travel time.

Here we have considered only external mechanisms that could drive the disk gas inwards, but secular mechanisms that are internally driven (e.g., cloud-cloud collisions that provide an effective viscosity, bars that may be able to form independently of external perturbations, resonances, instabilities, etc.) likely also play a role in the inflow of disk gas. Because these mechanisms do not require external triggers, including the effects of internal mechanisms will shorten the gas inflow timescales we estimate from minor mergers/interactions alone.

Companion Gas: As described in §2.2.2, we adopt a conservative approach and limit the HI flux measurement to the velocity range indicated by the primary ionized-gas (or stellar) rotation curve for galaxies with known companions. Since we restrict the flux measurements, our fluxes are most likely underestimates.

Of the four sub- M_b E/S0s with known companions in NED (UGC 12265N, IC 195, IC 1639, and NGC 4117), only UGC 12265N has a non-negligible SFR

and appears in the plots in §2.4. The other three will increase their atomic gas-to-stellar mass ratios by factors of 1.6–3.7 if we include the companion gas (IC 195: 0.12 \rightarrow 0.20, IC 1639: 0.01 \rightarrow 0.03, NGC 4117: 0.05 \rightarrow 0.12), but do not change the results of §2.3 significantly. Because these three galaxies have no detected star formation, the fractional stellar mass growth over time remains negligible.

Including the companion gas, the atomic gas-to-stellar mass ratio for UGC 12265N would quadruple from 0.3 to 1.2, giving it the second highest value of $M_{\text{HI+He}}/M_*$ for sub- M_b blue-sequence E/S0s. The amount of growth over time (Figure 2.8) would not change by much; the upper limit would remain the same, but the lower limit would increase since τ is larger with the extra gas. If the atomic gas is readily accessible for star formation, the gas exhaustion timescale would then increase from 1.4 Gyr to 5.6 Gyr.

Following Equation 4 of Lin & Tremaine (1983), we estimate the timescale for a merger via dynamical friction between UGC 12265N and its companion (UGC 12265S) 12 kpc away (neglecting the unknown line-of-sight distance) to be ~ 70 Myr³. This is shorter than its gas exhaustion timescale, which suggests that much of the companion gas is available for star formation in the near future and the amount of growth in the stellar component for this galaxy is greater than our conservative estimates in the previous sections.

Given the 1:2 progenitor mass ratio for this system, the resultant burst of star formation is likely to be more extreme than the scenarios discussed in §2.4.1, enhancing the star formation rate by a factor of two or more (e.g., Li et al. 2008;

³ $t_{\text{merge}} = \frac{10^{10} \text{yr}}{\ln \Lambda} \left[\frac{r_s(0)}{52 \text{kpc}} \right]^2 \left[\frac{10^{10} M_\odot}{m_s} \right] \left[\frac{v_c}{\sqrt{(2) \cdot 100 \text{km s}^{-1}}} \right]$, where r_s and m_s is the distance to and the mass of the satellite. We assume that $\ln \Lambda = 3.3$, $v_c = 250 \text{km s}^{-1}$, and the companion is half as massive as UGC 12265N. If the companion is more massive than our assumption, the merger time would decrease by the same factor. If the companion is less massive and/or further away, the timescale for merger would increase as m_s^{-1} and r_s^2 .

Darg et al. 2009). Whether the merger between UGC 12265N and its companion and the subsequent star formation will result in late-type morphology is unclear. A burst of central star formation may leave UGC 12265N with early-type morphology (e.g., Dasyra et al. 2006b), but the gas-richness of this pair suggests that a disk-dominated remnant may be more likely (KGB; Hopkins et al. 2009; Stewart et al. 2009).

2.5.2 Evidence for Episodic Gas Inflow

In §2.5.1 above, we presented the possibility of minor mergers and/or interactions acting as a trigger which induces gas inflow and star formation. Here we examine observational evidence that inflow events, most likely triggered externally, are in fact occurring in blue-sequence E/S0s.

In addition to having bluer inner and outer disk colors than red-sequence E/S0s, half of the blue-sequence E/S0s in the NFGS have centers (within 50% light radii) that are *bluer* than their outer disks (50–75% light radii) (KGB). Figure 2.10 plots the distribution of a related quantity, $\Delta(B - R)_{\text{corr}}$, for sub- M_b NFGS galaxies. $\Delta(B - R)_{\text{corr}}$ is the color gradient of a galaxy “corrected” for the mean color difference of galaxies of the same L_B (Kannappan et al. 2004), since larger galaxies may have central colors diluted by preexisting red bars or bulges. Figure 2.10 shows that all but one of the sub- M_b blue-sequence E/S0s and both mid-sequence E/S0s are on the more blue-centered end of the distribution for spiral/irregular galaxies.

In the broader NFGS, larger values of $\Delta(B - R)_{\text{corr}}$ reflect central star formation enhancements and correlate strongly with morphological peculiarities and the presence of nearby companions (Kannappan et al. 2004), suggesting a triggered gas inflow scenario. Kewley et al. (2006a) also find evidence for gas inflows in interacting blue-centered galaxies based on radial trends in gas metallicity. These results are

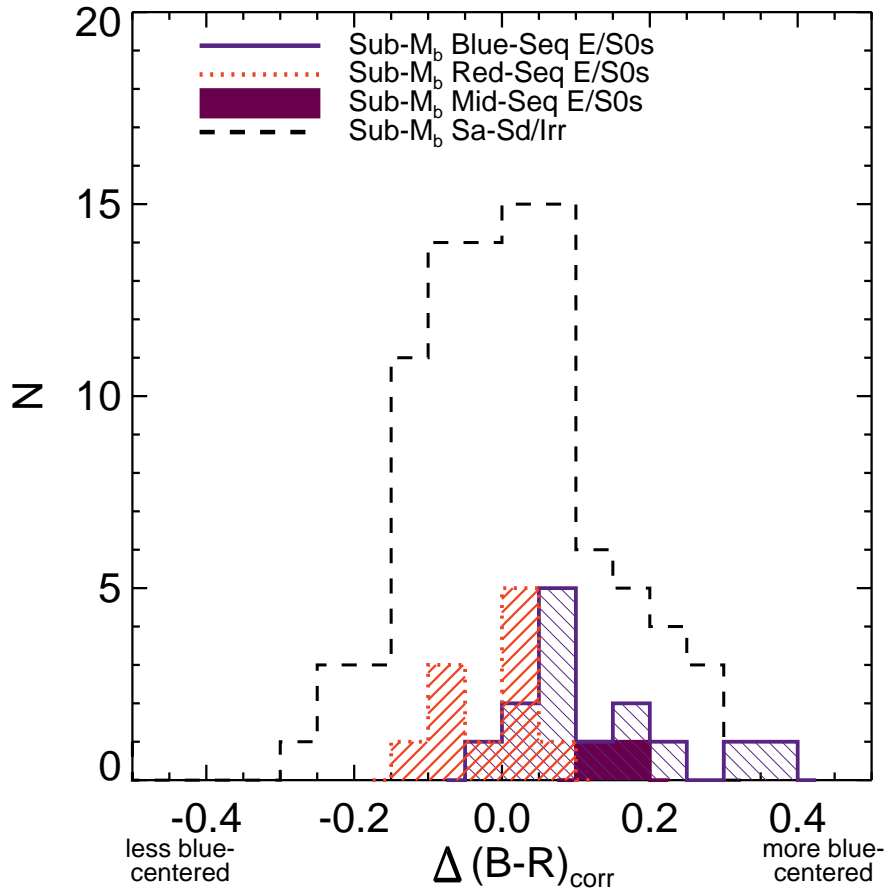


Figure 2.10: Distribution of $\Delta(B - R)_{\text{corr}}$ for sub- M_b NFGS galaxies, where $\Delta(B - R)_{\text{corr}}$ is the outer disk color (between 50–75% light radii) minus the central color (within 50% light radii), corrected for the typical color gradient of a galaxy at that galaxy’s blue luminosity (see Kannappan et al. 2004).

consistent with preliminary evidence for a relationship between $\Delta(B - R)_{\text{corr}}$ and molecular-to-atomic gas mass ratios in S0–Sb galaxies, to be reported in Kannappan et al. (2010) and Stark et al. (2010), which implies that HI can in fact flow inwards and become H_2 , fueling central star formation.

If the range of blue-centeredness we see in the sub- M_b blue-sequence E/S0s indicates different burst stages resulting from episodic gas inflow, then perhaps the specific star formation rate (SSFR) in these galaxies should scatter about some av-

erage SSFR expected based on the median 3 Gyr gas exhaustion timescale and the atomic gas mass of each galaxy. We consider the difference between this expected SSFR ($\text{SSFR}_{\text{expected}} = \text{SFR}_{\text{expected}}/M_* \equiv (M_{\text{HI+He}}/3 \text{ Gyr})/M_*$) and the observed SSFR as a function of $\Delta(B - R)_{\text{corr}}$ (Figure 2.11). The error bars for $\Delta(B - R)_{\text{corr}}$ are formal errors, and do not include systematic uncertainties from $\Delta(B - R)$ not being corrected for dust and/or from delays between the bluest stellar population colors and the peak of star formation. Such uncertainties may cause some of the significant scatter seen in this figure. Nonetheless, there is a suggestive trend with the more blue-centered galaxies having enhanced SSFRs, and the less blue-centered galaxies having reduced SSFRs.

The Spearman rank correlation coefficient for the data in Figure 2.11 is -0.39 , with the probability of a null correlation at 19%. However, if we exclude IC 692 ($\text{SSFR}_{\text{expected}} - \text{SSFR}_{\text{observed}} = 0.13$) from the calculation, the correlation coefficient becomes -0.64 , with a probability of a null correlation decreasing to 3%. Given the error bars, we infer that the relationship is likely real. This supports the inflow-driven burst picture, although follow-up on the apparent outliers would be informative.

The correlation between blue-centeredness and several properties — morphological peculiarities, the presence of companions, increasing molecular-to-atomic gas mass ratios, and enhanced SSFRs — suggests that the inflow of gas in sub- M_b blue-sequence E/S0s may be episodic and triggered externally. Episodic inflows of gas in sub- M_b blue-sequence E/S0s would imply that these galaxies are in various stages of bursty star formation, which is in agreement with the large ranges of prospective stellar mass growth (§2.4.2) and gas exhaustion times (§2.5.1) we see for this population.

This result also suggests that our focus on HI rather than molecular gas (to be

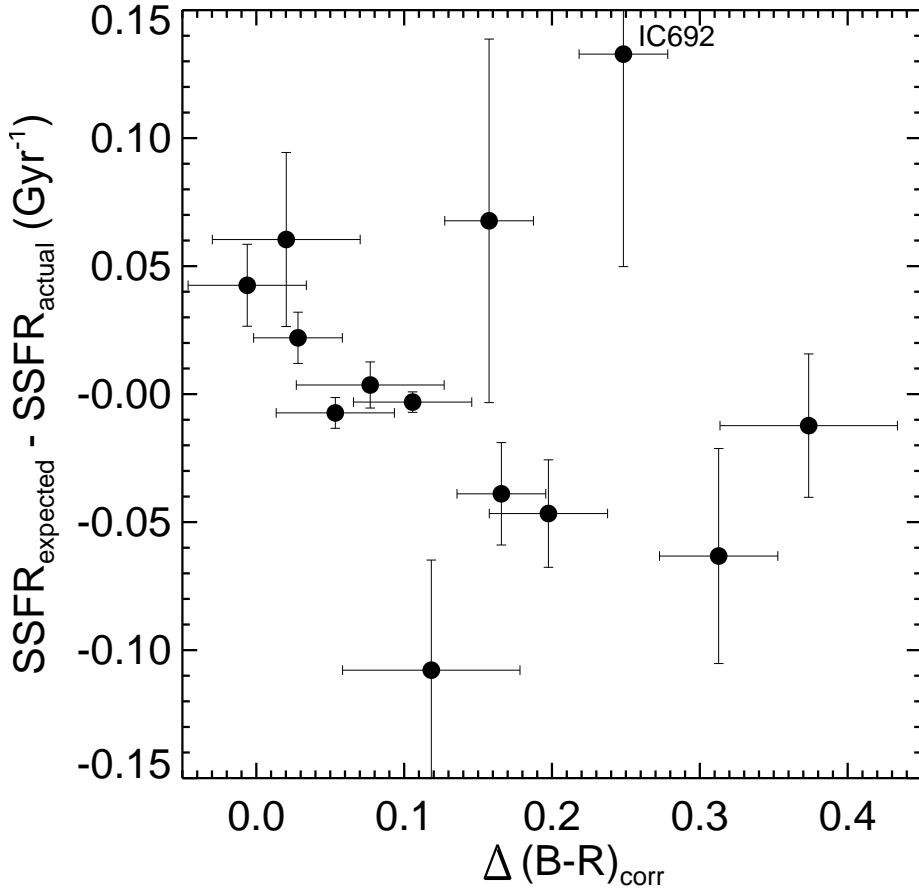


Figure 2.11: Difference between expected specific star formation rate ($\text{SSFR}_{\text{expected}} \equiv \frac{M_{\text{HI+He}}/3 \text{ Gyr}}{M_*}$) and observed specific star formation rate for sub- M_b blue- and mid-sequence E/S0s as a function of blue-centeredness. One of our blue-sequence E/S0s, UGC 9562, is excluded from this figure because it is a polar ring galaxy and not expected to behave normally with respect to inflow (KGB).

discussed in Wei et al., in prep.) does not render our estimates of stellar mass growth and gas exhaustion time in §2.4.2 and 2.5.1 highly inaccurate. Although stars typically form from molecular gas, the estimates of inflow and minor merger/interaction timescales suggest that the transition from HI to H₂ may occur quickly enough that the potential for morphological transformation can be realized even after material already in the molecular phase has been consumed or otherwise dispersed. These in-

flow events may also play an important role in bridging between the sub- M_b red- and blue-sequence E/S0 populations, triggering star formation in sub- M_b red-sequence E/S0s such as the gas-rich UGC 5923 (discussed in §2.3.1) and moving E/S0s onto the blue sequence.

Observations of the SAURON E/S0 sample (de Zeeuw et al. 2002; Emsellem et al. 2004) have found that many intermediate-mass early-type galaxies seem to contain a disk-like stellar component (e.g., Emsellem et al. 2007; Krajnović et al. 2008) — possibly the remnant of a burst of star formation induced by the inflow of gas as discussed in this section. It is possible that some of our sub- M_b blue-sequence E/S0s are in an active, post gas-infall star-forming phase but will eventually become passive early-type galaxies like those observed by Krajnović et al. (2008).

Some of the differences between the SAURON E/S0s and our blue-sequence E/S0s, however, likely arise from the differences between the two samples. While there are some E/S0s below the bimodality mass $M_b \sim 3 \times 10^{10} M_\odot$ in the SAURON sample, these are in the minority; in contrast, the disk-building sub-population of blue-sequence E/S0s becomes numerically important only below this mass, and more notably below the threshold mass at $5 \times 10^9 M_\odot$ (KGB). It is also possible that the accretion of fresh gas from external sources, as discussed in §2.5.1, will reignite star formation in some red-sequence E/S0s (in both samples) and continue building disks (KGB; Cortese & Hughes 2009). The high frequency of blue-sequence E/S0s below the threshold mass ($\sim 5\%$ of the general galaxy population and $\sim 25\%$ of E/S0s, KGB) would be difficult to explain by quenching mergers alone, but could be explained if these systems' star-forming phase is either long or episodic.

2.6 Summary

Kannappan, Guie, & Baker (2009) have recently identified a population of morphological E/S0s on the blue sequence in color vs. stellar mass space, where spiral galaxies typically reside. Blue-sequence E/S0s increase in numbers below the bimodality mass ($M_b \sim 3 \times 10^{10} M_\odot$) and especially below the gas richness threshold mass ($\sim 5 \times 10^9 M_\odot$). These sub- M_b blue-sequence E/S0s are characterized by fairly regular morphology, and many appear to be rebuilding disks (KGB). Blue-sequence E/S0s also fall between red-sequence E/S0s and spirals in the M_* -radius and M_* - σ relations, suggesting that they may be a transitional population (KGB).

In this Chapter, we examined the atomic gas content of blue-sequence E/S0s below $\sim M_b$ to determine whether they have large enough gas reservoirs to transform to later-type morphology. In a representative sample drawn from the Nearby Field Galaxy Survey, we find that blue-sequence E/S0s have substantial atomic gas masses in the range of 10^7 – $10^{10} M_\odot$, comparable to the gas masses of spiral and irregular galaxies in the same stellar mass range. Blue- and red-sequence E/S0s have distinctly different atomic gas-to-stellar mass ratios, with most blue-sequence E/S0s in the range of 0.1–1.0 and most red-sequence E/S0s < 0.1 . This suggests significantly greater potential for morphological transformation in blue-sequence E/S0s than red-sequence E/S0s.

Combining these atomic gas masses with current rates of star formation, we find that many of the sub- M_b blue-sequence E/S0s can form new stars in the range of 10–60% of their current stellar masses within 3 Gyr, in both constant (i.e., allowing gas infall) and exponentially declining (i.e., closed box) star formation scenarios, provided that the atomic gas reservoir is available for star formation. In the constant star formation scenario, we find that about half of the sub- M_b blue-sequence E/S0

systems will exhaust their gas reservoirs in $\lesssim 3$ Gyr if no fresh gas infall is permitted.

Because of the lack of spatial resolution in our HI data, we cannot say for certain that the gas is readily available for star formation. We find evidence, however, which indicates that fresh gas may be brought inwards and made available for star formation on timescales shorter than the gas exhaustion timescale. We estimate the dynamical timescale for infall of extra-planar gas to be on average < 1 Gyr, shorter than the gas exhaustion time for most of our galaxies. The frequency of inflow for gas trapped in diffuse disks may be dominated by the rate of minor mergers/interactions, which simulations find to occur every 1.4 Gyr or less for progenitor mass ratios of 1:100 or smaller (Fakhouri & Ma 2008). As evidence of such events, we find that sub- M_b blue-sequence E/S0s are more often blue-centered than the general galaxy population, where blue-centeredness is measured relative to the typical color gradient of galaxies at a given luminosity. Kannappan et al. (2004) find blue-centeredness to correlate with morphological peculiarities and companions, which supports the externally triggered gas inflow scenario. For blue-sequence E/S0s, we find a relationship between blue-centeredness and variations in specific star formation rates relative to typical reference values, suggesting that such inflows may be episodic and trigger bursts of star formation. In summary, this work clearly confirms that blue-sequence E/S0s have both the gas reservoirs and the potential for sustained star formation necessary for significant disk growth, consistent with evolution toward later-type morphology if the spatial distribution of the gas is extended.

While our sample of 27 blue- and red-sequence E/S0s is sufficient for the analysis presented in this Chapter, it is important to extend our work to a larger sample of sub- M_b E/S0s for more robust statistics. The multi-wavelength RESOLVE Survey underway (Kannappan & Wei 2008) would be an ideal data set for such a study. Active follow-up of our current sample includes obtaining IRAM CO(1–0) and CO(2–1)

spectra to quantify the molecular gas content in these galaxies, which may be a large fraction of the gas mass content and further extend the potential for morphological transformation in blue-sequence E/S0s. We are also obtaining VLA HI maps (supplementing the CARMA CO(1–0) maps described in Chapter 3) to resolve the distributions of the atomic and molecular gas in blue-sequence E/S0s. HI maps will allow us to look for extended gas disks, small companions, and/or signs of interactions. The CO(1–0) maps are well-suited to reveal inner disk “pseudobulges” growing in tandem with extended disks, as would be expected during the formation of late-type galaxies.

Table 2.4. HI Data for the NFGS

ID	Galaxy Name	UGC	Morph.	Sequence	$V_{\odot}(\sigma_{V_{\odot}})$ (km s ⁻¹)	$V_M^{\text{sin}i}(\sigma_{V_M^{\text{sin}i}})$ (km s ⁻¹)	$f_{\text{HI}}(\sigma_{f_{\text{HI}}})$ (Jy km s ⁻¹)	M_{HI} (M_{\odot})	sub- M_b Sample	E/S0	Reference
(1)	(2)	(3)	(4)	(5)	(6)	(7)	(8)	(9)	(10)	(11)	(11)
1	A00113p3037	130	cE	R			<0.12	<1.36×10 ⁸			GBT
2	A00289p0556	313	Sd	B	2085(7)	48(2)	0.78(0.13)	1.65±0.27 × 10 ⁸			LE
3	NGC193	408	L-	R	4220?		<2.0	<1.80×10 ⁹			HR
4	A00389m0159	439	Sa	B	5299(7)	55(3)	4.94(1.28)	6.54±1.69 × 10 ⁹			LE
5	A00442p3224	484	Sb	B	4857(8)	197(6)	13.12(4.83)	1.56±0.57 × 10 ¹⁰			LE
6	A00510p1225	545	Sc	B	18339(8)	175(9)	1.03(0.33)	1.66±0.53 × 10 ¹⁰			LE
7	NGC315	597	E	R	4921		<1.33	<1.63×10 ⁹			HR
8	A00570p1504	615	Sab	B	5507(3)	164(12)	1.72(0.21)	2.53±0.31 × 10 ⁹			CEGG
9	A01047p1625	685	Im	B	156(4)	32(1)	11.32(2.04)	5.07±0.91 × 10 ⁷			LE
10	NGC382	688	E	R							LE
11	IC1639	750	cE	B	5381(12)	22(10)	0.70(0.08)	9.55±1.09 × 10 ⁸	×		GBT
12	A01123m0046	793	Sc	B			<1.98	<1.01×10 ¹⁰			HI
13	A01187m0048	892	Sa	B	5228(5)	32(2)	2.37(0.33)	3.04±0.42 × 10 ⁹	×		CEGG
14	NGC516	946	L	R			<0.09	<2.59×10 ⁷			GBT
15	A01300p1804	1104	Im	B	684(4)	44(2)	7.62(0.97)	2.35±0.30 × 10 ⁸			LE
16	A01344p2838	1154	Sbc	B	7758(7)	124(5)	5.03(2.38)	1.47±0.70 × 10 ¹⁰			LE
17	A01346p0438	1155	Sbc	B	3181(8)	85(4)	2.50(0.42)	1.18±0.20 × 10 ⁹			LE
18	A01374p1539B	1176	Im	B	632(3)	16(0.4)	23.23(2.24)	5.98±0.58 × 10 ⁸			LE
19	NGC695	1315	Sc	B	9729(6)	148(5)	3.93(0.84)	1.84±0.39 × 10 ¹⁰			LE
20	NGC784	1501	Sm	B	198(4)	41(1)	45.50(4.39)	2.87±0.28 × 10 ⁸			LE
21	A02008p2350	1551	Sdm	B	2671(5)	47(2)	11.53(1.11)	4.15±0.40 × 10 ⁹			LE
22	IC195	1555	S0/a	B	3648(2)	104(7)	6.85(0.16)	4.39±0.10 × 10 ⁹	×		GBT
23	IC197	1564	Sbc	B	6316(6)	122(9)	8.26(0.86)	1.55±0.16 × 10 ¹⁰			CEGG
24	IC1776	1579	Sc	B	3410(6)	48(2)	12.19(3.16)	6.64±1.72 × 10 ⁹			LE
25	A02056p1444	1630	Sb	B	4437(3)	133(10)	6.39(0.67)	5.94±0.62 × 10 ⁹			CEGG
26	NGC825	1636	Sa	R	3397(5)	217(10)	5.89(1.52)	3.20±0.83 × 10 ⁹			LE
27	NGC927	1908	Sc	B	8266(10)	94(4)	4.43(1.15)	1.43±0.37 × 10 ¹⁰			LE
28	A02257m0134	1945	Sdm	B	1768(8)	49(3)	2.30(0.2)	3.25±0.28 × 10 ⁸			LE
29	NGC984	2059	Sa	R	4355(7)	278(18)	10.62(4.59)	1.00±0.43 × 10 ¹⁰			LE
30	NGC1029	2149	S0/a	R	3620(28)	127(9)	8.32(0.15)	5.19±0.09 × 10 ⁹			GBT
31	A02464p1807	2296	cE	B			<6.9	3.39×10 ¹⁰			HR
32	A02493m0122	2345	Sm	B	1506(5)	40(2)	19.68(2.5)	2.03±0.26 × 10 ⁹			LE
33	NGC1298	2683	?E	R	6452(3)	36(2)	0.48(0.09)	9.43±1.77 × 10 ⁸			GBT
34	A03202m0205	2704	Sa	B			<1.92	<6.03×10 ⁹			HI
35	NGC1552	3015	L	R	4784(8)	129(9)	0.7(0.09)	7.76±1 × 10 ⁸			GBT

Table 2.4 (cont'd)

ID	Galaxy Name	UGC	Morph.	Sequence	$V_{\odot}(\sigma_{V_{\odot}})$ (km s^{-1})	$V_{\text{M}}^{\text{sin}i}(\sigma_{V_{\text{M}}^{\text{sin}i}})$ (km s^{-1})	$f_{\text{HI}}(\sigma_{f_{\text{HI}}})$ (Jy km s^{-1})	M_{HI} (M_{\odot})	sub- M_b E/S0 Sample	Reference
(1)	(2)	(3)	(4)	(5)	(6)	(7)	(8)	(9)	(10)	(11)
36	NGC2692	4675	Sa	R	4026(12)	75(4)	3.03(0.42)	$2.37 \pm 0.33 \times 10^9$		LE
37	A08567p5242	4713	Sb	B	9036(7)	249(9)	3.09(0.27)	$1.27 \pm 0.11 \times 10^{10}$		LE
38	A09045p3328	4787	Sdm	B	552(8)	53(1)	6.00(1.02)	$1.07 \pm 0.18 \times 10^8$		LE
39	NGC2780	4843	Sab	B	1962(7)	130(10)	0.25(0.06)	$5.83 \pm 1.40 \times 10^7$		LE
40	A09125p5303	4879	Im	R						LE
41	NGC2799	4909	Sm	B	1755(25)	146(13)	7.55(2.5)	$1.70 \pm 0.56 \times 10^9$		LE
42	NGC2824	4933	L	R						LE
43	NGC2844	4971	Sa	B	1489(6)	145(5)	6.46(0.82)	$9.75 \pm 1.24 \times 10^8$		LE
44	NGC3011	5259	S0/a	B	1543(2)	76(5)	1.24(0.08)	$1.93 \pm 0.12 \times 10^8$		LE
45	NGC3009	5264	Sc	B	4564(12)	194(13)	2.95(0.34)	$3.42 \pm 0.39 \times 10^9$	×	GBT
46	IC2520	5335	Pec	B	1238(8)	85(8)	6.00(1.69)	$6.31 \pm 1.78 \times 10^8$		LE
47	A09557p4758	5354	Sm	B	1171(4)	76(3)	17.14(1.48)	$1.85 \pm 0.16 \times 10^9$		LE
48	NGC3075	5360	Sc	B	3582(8)	124(4)	15.07(7.12)	$1.00 \pm 0.47 \times 10^{10}$		LE
49	A09579p0439	5378	Sb	B	4161(10)	117(4)	6.05(2.86)	$5.31 \pm 2.51 \times 10^9$		LE
50	NGC3104	5414	Im	B	603(3)	41(2)	17.78(1.36)	$4.33 \pm 0.33 \times 10^8$		LE
51	A10042p4716	5451	Im	R	629(9)	52(2)	2.84(0.64)	$7.17 \pm 1.62 \times 10^7$		LE
52	NGC3165	5512	Im	R	1333(4)	61(2)	3.45(0.78)	$3.63 \pm 0.82 \times 10^8$		LE
53	A10114p0716	5522	Sc	B	1220(4)	90(2)	27.92(2.98)	$2.62 \pm 0.28 \times 10^9$		LE
54	NGC3179	5555	L	R			<0.19	< 5.10×10^8		GBT
55	A10171p3853	5577	Sm	B	2028(9)	45(2)	3.30(0.93)	$8.61 \pm 2.43 \times 10^8$		LE
56	NGC3213	5590	Sbc	B	1346(5)	67(4)	1.47(0.35)	$2.01 \pm 0.48 \times 10^8$		LE
57	NGC3264	5719	Sdm	B	940(7)	60(2)	14.93(1.44)	$1.16 \pm 0.11 \times 10^9$		LE
58	NGC3279	5741	Sc	B	1393(6)	156(4)	3.55(0.96)	$4.81 \pm 1.3 \times 10^8$		LE
59	A10321p4649	5744	Sc	B						LE
60	A10337p1358	5760	Scd	B	3010(6)	139(5)	3.78(0.33)	$1.86 \pm 0.16 \times 10^9$		LE
61	IC2591	5763	Sbc	B	6797(10)	160(5)	8.75(4.13)	$2.04 \pm 0.96 \times 10^{10}$		LE
62	A10365p4812	5791	Sc	B	857(5)	67(3)	3.72(1.05)	$2.34 \pm 0.66 \times 10^8$		LE
63	A10368p4811	5798	Sc	B	1519(6)	72(5)	5.37(1.52)	$9.36 \pm 2.65 \times 10^8$		LE
64	NGC3326	5799	Sb	B	8153(8)	100(6)	2.77(0.88)	$8.97 \pm 2.85 \times 10^9$		LE
65	A10389p3859	5819	Sbc	B						LE
66	A10431p3514	5870	Sa	B	1992(6)	100(7)	4.59(1.3)	$1.24 \pm 0.35 \times 10^9$		LE
67	A10448p0731	5892	Sb	B			<1.53	< 4.97×10^9		HI
68	A10465p0711	5923	S0/a	R	713(4)	65(5)	3.12(0.16)	$4.71 \pm 0.24 \times 10^7$	×	GBT
69	A10504p0454	6003	S0/a	B	5819(5)	67(5)	1.47(0.09)	$2.46 \pm 0.15 \times 10^9$	×	GBT
70	NGC3454	6026	Sc	B	1109(5)	91(3)	5.62(1.26)	$5.62 \pm 1.26 \times 10^8$		LE

Table 2.4 (cont'd)

ID	Galaxy Name	UGC	Morph.	Sequence	$V_{\odot}(\sigma_{V_{\odot}})$ (km s^{-1})	$V_{\text{M}}^{\text{Sini}}(\sigma_{V_{\text{M}}^{\text{Sini}}})$ (km s^{-1})	$f_{\text{HI}}(\sigma_{f_{\text{HI}}})$ (Jy km s^{-1})	M_{HI} (M_{\odot})	sub- M_b E/S0 Sample	Reference
(1)	(2)	(3)	(4)	(5)	(6)	(7)	(8)	(9)	(10)	(11)
71	A10592p1652	6104	Sbc	B	2947(5)	110(2)	7.41(1.26)	$3.59 \pm 0.61 \times 10^9$		LE
72	NGC3499	6115	S0/a	R	1495(12)	119(9)	0.39(0.06)	$7.15 \pm 1.10 \times 10^7$	×	GBT
73	NGC3510	6126	Sd	B	704(3)	79(2)	33.57(2.9)	$7.26 \pm 0.63 \times 10^8$		LE
74	Mrk421	6132W	Pec							LE
75	NGC3522	6159	L-	R	1221(8)	112(8)	2.00(0.16)	$2.47 \pm 0.20 \times 10^8$	×	GBT
76	A11040p5130	6162	Sc	B	2208(5)	95(4)	12.65(1.74)	$4.04 \pm 0.56 \times 10^9$		LE
77	IC673	6200	Sa	B	3859(8)	151(5)	17.14(8.09)	$1.31 \pm 0.62 \times 10^{10}$		LE
78	A11068p4705	6201	L-	R						LE
79	A11072p1302	6206	Sc	B						LE
80	NGC3605	6295	L-	R					×	GBT
81	A11142p1804	6296	Sc	R	976(6)	82(3)	<0.11	$< 1.61 \times 10^6$		LE
82	NGC3633	6351	Sa	B	2599(6)	150(5)	2.10(0.72)	$8.28 \pm 2.84 \times 10^7$		LE
83	IC692	6438	E	B	1163(8)	35(3)	2.50(0.71)	$1.07 \pm 0.17 \times 10^9$		LE
84	A11238p5401	6446	Sd	B	645(4)	57(2)	28.71(3.65)	$2.71 \pm 0.77 \times 10^8$	×	LE
85	A11310p3254	6545	Sb	B	2630(6)	66(7)	1.00(0.28)	$1.13 \pm 0.14 \times 10^9$		LE
86	IC708	6549	?E	R				$4.20 \pm 1.18 \times 10^8$		LE
87	A11332p3536	6570	S0/a	Mid	1628(2)	49(3)	1.35(0.05)	$2.60 \pm 0.1 \times 10^8$	×	GBT
88	A11336p5829	6575	Sc	B	1216(5)	95(3)	13.12(1.27)	$1.68 \pm 0.16 \times 10^9$		LE
89	NGC3795A	6616	Scd	B	1148(5)	45(2)	11.86(1.63)	$1.39 \pm 0.19 \times 10^9$		LE
90	A11372p2012	6625	Sc	B						LE
91	NGC3795	6629	Sc	B	1212(6)	103(4)	7.21(0.62)	$7.72 \pm 0.66 \times 10^8$		LE
92	A11378p2840	6637	L-	B	1836(6)	61(5)	1.84(0.87)	$4.31 \pm 2.04 \times 10^8$	×	LE
93	A11392p1615	6655	L	B	744(2)	26(2)	0.92(0.04)	$1.70 \pm 0.07 \times 10^7$	×	GBT
94	NGC3846	6706	Sm	B	1451(8)	66(3)	6.34(0.87)	$1.00 \pm 0.14 \times 10^9$		LE
95	NGC3850	6733	Sc	B	1149(8)	69(3)	7.91(1.34)	$9.43 \pm 1.60 \times 10^8$		LE
96	A11476p4220	6805	L	B	1132(6)	49(3)	0.39(0.05)	$3.78 \pm 0.48 \times 10^7$	×	GBT
97	NGC3913	6813	Sd	B	954(3)	19(1)	10.52(1.12)	$9.06 \pm 0.96 \times 10^8$		LE
98	IC746	6898	Sb	B	5028(3)	123(4)	6.95(1.1)	$9.31 \pm 1.47 \times 10^9$		LE
99	A11531p0132	6903	Sc	B	1892(6)	78(3)	15.35(2.44)	$3.54 \pm 0.56 \times 10^9$		LE
100	NGC3978	6910	Sbc	B	9962(8)	77(3)	3.33(0.71)	$1.64 \pm 0.35 \times 10^{10}$		LE
101	A11547p4933	6930	Sc	B	778(5)	50(2)	27.41(4.06)	$1.53 \pm 0.23 \times 10^9$		LE
102	A11547p5813	6931	Sm	B	1195(8)	49(2)	4.63(0.89)	$5.62 \pm 1.08 \times 10^8$		LE
103	NGC4034	7006	Sc	B	2367(8)	91(6)	3.21(0.28)	$1.19 \pm 0.10 \times 10^9$		LE
104	A11592p6237	7009	Im	B	1120(12)	74(6)	6.00(1.02)	$6.79 \pm 1.15 \times 10^8$		LE
105	A12001p6439	7020A	L	Mid	1515(1)	39(3)	2.30(0.05)	$3.86 \pm 0.08 \times 10^8$	×	GBT

Table 2.4 (cont'd)

ID	Galaxy Name	UGC	Morph.	Sequence	$V_{\odot}(\sigma_{V_{\odot}})$ (km s^{-1})	$V_{\text{M}}^{\text{sin}i}(\sigma_{V_{\text{M}}^{\text{sin}i}})$ (km s^{-1})	$f_{\text{HI}}(\sigma_{f_{\text{HI}}})$ (Jy km s^{-1})	M_{HI} (M_{\odot})	sub- M_b E/S0 Sample	Reference
(1)	(2)	(3)	(4)	(5)	(6)	(7)	(8)	(9)	(10)	(11)
106	NGC4117	7112	L	R	934(2)	122(9)	5.10(0.20)	$4.36 \pm 0.17 \times 10^8$	×	GBT
107	NGC4120	7121	Sc	B	2246(7)	92(4)	10.42(0.9)	$3.53 \pm 0.30 \times 10^9$		LE
108	A12064p4201	7129	Sab	R	947(9)	60(6)	1.22(0.25)	$9.69 \pm 1.99 \times 10^7$		LE
109	NGC4141	7147	Sc	R	1902(7)	70(3)	6.89(0.60)	$1.90 \pm 0.17 \times 10^9$		LE
110	NGC4159	7174	Sdm	B	1753(12)	77(5)	5.68(2.09)	$1.29 \pm 0.47 \times 10^9$		LE
111	NGC4204	7261	Sdm	B	858(9)	36(1)	24.10(4.61)	$5.80 \pm 1.11 \times 10^8$		LE
112	NGC4238	7308	Sc	B	2765(6)	113(6)	5.78(0.50)	$2.78 \pm 0.24 \times 10^9$		LE
113	NGC4248	7335	Sdm	R	484(14)	29(3)	4.63(1.31)	$8.05 \pm 2.28 \times 10^7$		LE
114	A12167p4938	7358	Sc	B	3658(6)	132(5)	5.27(1.01)	$4.04 \pm 0.78 \times 10^9$		LE
115	NGC4272	7378	L	B	535(4)	77(3)	26.18(3.6)	$5.38 \pm 0.74 \times 10^8$		LE
116	NGC4288	7399	Sm	B			<0.06	$<1.01 \times 10^6$		LE
117	NGC4308	7426	L	R	1138(6)	28(1)	7.21(2.04)	$9.43 \pm 2.67 \times 10^8$	×	GBT
118	A12195p3222	7428	Sdm							LE
119	A12195p7535		cE							LE
120	A12263p4331	7608	Im		536(5)	24(1)	20.42(2.39)	$3.80 \pm 0.45 \times 10^8$		LE
121	A12295p4007	7678	Sd	B	682(9)	24(1)	5.03(1.42)	$1.49 \pm 0.42 \times 10^8$		LE
122	A12300p4259	7690	Sdm	B	538(11)	35(2)	14.52(2.46)	$2.73 \pm 0.46 \times 10^8$		LE
123	A12304p3754	7699	Sd	B	500(7)	81(3)	20.04(2.34)	$2.67 \pm 0.31 \times 10^8$		LE
124	NGC4509	7704	Sm	B	937(8)	38(4)	3.89(1.84)	$2.72 \pm 1.28 \times 10^8$		LE
125	A12331p7230	7761	Sb	B						LE
126	A12446p5155	7950	Im	B	498(4)	35(1)	5.89(0.63)	$1.37 \pm 0.15 \times 10^8$		LE
127	NGC4758	8014	Sbc	B	1243(6)	79(3)	8.59(1.46)	$1.24 \pm 0.21 \times 10^9$		LE
128	NGC4795	8037	Sa	R	2812(5)	155(7)	1.70(0.23)	$7.88 \pm 1.07 \times 10^8$		LE
129	NGC4807	8049	L+	R						LE
130	NGC4841B	8073	E							LE
131	NGC4926	8142	L	R	2534(4)	93(3)	12.19(1.94)	$4.98 \pm 0.79 \times 10^9$		LE
132	NGC4961	8185	Sbc	B	815(4)	81(4)	8.51(0.99)	$4.44 \pm 0.52 \times 10^8$		LE
133	A13065p5420	8231	Sb	B						LE
134	IC4213	8280	Scd	B						LE
135	A13194p4232	8400	Scd	B						LE
136	NGC5117	8411	Sc	B	2392(4)	96(3)	9.25(1.47)	$3.51 \pm 0.56 \times 10^9$		LE
137	NGC5173	8468	E	B	2428(6)	81(7)	4.99(1.06)	$2.00 \pm 0.42 \times 10^9$	×	LE
138	A13281p3153	8498	Sab	B	7320(8)	290(19)	11.43(5.40)	$3.19 \pm 1.51 \times 10^{10}$		LE
139	NGC5208	8519	L	R			<2.72	$<6.36 \times 10^9$		HI
140	NGC5230	8573	Sc	B	6856(6)	65(2)	8.75(1.39)	$2.12 \pm 0.34 \times 10^{10}$		LE

Table 2.4 (cont'd)

ID	Galaxy Name	UGC	Morph.	Sequence	$V_{\odot}(\sigma_{V_{\odot}})$ (km s^{-1})	$V_{\text{M}}^{\text{ini}}(\sigma_{V_{\text{M}}^{\text{ini}}})$ (km s^{-1})	$f_{\text{HI}}(\sigma_{f_{\text{HI}}})$ (Jy km s^{-1})	M_{HI} (M_{\odot})	sub- M_b E/S0 Sample	Reference
(1)	(2)	(3)	(4)	(5)	(6)	(7)	(8)	(9)	(10)	(11)
141	A13361p3323	8630	Sm	B	2438(7)	83(3)	6.70(0.58)	$2.48 \pm 0.22 \times 10^9$		LE
142	NGC5267	8655	Sb	B		70(4)	0.78(0.16)	$1.47 \pm 0.30 \times 10^9$		LE
143	A13422p3526	8693	Sbc	B	2438(8)	106(4)	8.36(3.95)	$3.41 \pm 1.61 \times 10^9$		LE
144	NGC5338	8800	L	R	801(9)	20(1)	0.77(0.12)	$1.93 \pm 0.3 \times 10^7$	×	GBT
145	NGC5356	8831	Sb	B	1372(5)	122(4)	4.39(0.84)	$6.75 \pm 1.29 \times 10^8$	×	LE
146	A13550p4613	8876	S0/a	R			<0.15	$< 4.78 \times 10^7$		GBT
147	NGC5407	8930	L	R						LE
148	NGC5425	8933	Sc	B	2072(8)	103(5)	6.64(0.78)	$2.01 \pm 0.24 \times 10^9$		LE
149	A14016p3559	8984	L	R						LE
150	NGC5470	9020	Sb	B	1026(8)	109(4)	7.69(1.47)	$6.75 \pm 1.29 \times 10^8$		LE
151	NGC5491	9072A	Sc	B	5888(7)	214(3)	6.17(1.05)	$1.10 \pm 0.19 \times 10^{10}$		LE
152	NGC5532	9137	L	R						LE
153	NGC5541	9139	Sc	B						LE
154	NGC5596	9208	L	R	3220(24)	94(7)	0.52(0.14)	$3.17 \pm 0.85 \times 10^8$	×	GBT
155	NGC5608	9219	Sm	B	664(6)	46(2)	9.33(1.09)	$4.19 \pm 0.49 \times 10^8$		LE
156	A14305p1149	9356	Sc	B	2226(6)	103(3)	15.92(2.53)	$5.18 \pm 0.82 \times 10^9$		LE
157	NGC5684	9402	L	R						LE
158	NGC5762	9535	Sa	B	1792(8)	80(3)	7.48(1.77)	$1.71 \pm 0.40 \times 10^9$		LE
159	A14489p3547	9560	Pec	B	1218(4)	80(4)	4.47(0.95)	$5.99 \pm 1.27 \times 10^8$		LE
160	A14492p3545	9562	L+	B	1257(3)	76(3)	11.97(2.29)	$1.79 \pm 0.34 \times 10^9$	×	LE
161	IC1066	9573	Sab	B	1576(6)	90(3)	7.69(2.93)	$1.43 \pm 0.54 \times 10^9$		LE
162	A14594p4454	9660	Sc	B	608(9)	29(2)	6.00(1.69)	$2.75 \pm 0.78 \times 10^8$		LE
163	A15016p1037		cE							LE
164	IC1100	9729	Scd	B						LE
165	NGC5874	9736	Sbc	B	3128(5)	139(5)	6.82(1.08)	$4.12 \pm 0.65 \times 10^9$		LE
166	NGC5875A	9741	Sc	B						LE
167	NGC5888	9771	Sb	B						LE
168	IC1124	9869	Sab	B						LE
169	NGC5940	9876	Sab	B	5313(8)	160(11)	3.48(0.90)	$5.19 \pm 1.34 \times 10^9$		LE
170	A15314p6744	9896	Sc		10214(6)	78(3)	1.58(0.25)	$7.90 \pm 1.25 \times 10^9$		LE
171	NGC5993	10007	Sb	B	6466(6)	115(4)	4.34(0.42)	$9.72 \pm 0.94 \times 10^9$		LE
172	IC1141	10051	S0/a	B	9562(9)	76(6)	5.83(1.65)	$2.67 \pm 0.75 \times 10^{10}$		LE
173	IC1144	10069	S0/a	B	4389(3)	93(7)	1.82(0.07)	$1.98 \pm 0.08 \times 10^9$	×	GBT
174	NGC6007	10079	Sbc	B			<0.07	$< 5.37 \times 10^8$		GBT
175	A15523p1645	10086	Sc	B	10544(5)	184(3)	8.99(2.65)	$4.89 \pm 1.44 \times 10^{10}$		LE
							<2.06	$< 6.53 \times 10^8$		LE

Table 2.4 (cont'd)

ID	Galaxy Name	UGC	Morph.	Sequence	$V_{\odot}(\sigma_{V_{\odot}})$ (km s^{-1})	$V_M^{\text{Sini}}(\sigma_{V_M^{\text{Sini}}})$ (km s^{-1})	$f_{\text{HI}}(\sigma_{f_{\text{HI}}})$ (Jy km s^{-1})	M_{HI} (M_{\odot})	sub- M_b E/S0 Sample	Reference
(1)	(2)	(3)	(4)	(5)	(6)	(7)	(8)	(9)	(10)	(11)
176	A15542p4800	10097	L	R			<2.10	<2.26×10 ⁹		HI
177	NGC6020	10100	?E	R				2.78±0.79 × 10 ⁹	×	HI
178	NGC6123	10333	S0/a	R	3964(12)	34(3)	3.01(0.85)	6.86±1.94 × 10 ⁹		LE
179	NGC6131	10356	Sc	B	5061(12)	93(7)	4.85(1.37)			LE
180	NGC6185	10444	Sa	B						LE
181	NGC7077	11755	S0/a	B	1148(6)	47(2)	2.00(0.41)	1.69±0.35 × 10 ⁸	×	LE
182	NGC7194	11888	?E	R	8105(?)	106(?)	6.17(0.58)	2.02±1.90 × 10 ⁹		HI
183	A22306p0750	12074	Sc	B	1989(7)	70(3)	1.90(0.32)	4.15±0.70 × 10 ⁸		LE
184	NGC7328	12118	Sab	B	2824(6)	143(4)	10.33(1.75)	4.33±0.73 × 10 ⁹		LE
185	NGC7360	12167	E	B	4685(7)	157(8)	3.96(1.87)	4.31±2.04 × 10 ⁹	×	LE
186	A22426p0610	12178	Sdm	B	1931(4)	103(7)	22.18(1.92)	4.46±0.39 × 10 ⁹		LE
187	A22551p1931N	12265N	L	B	5717(2)	103(7)	6.64(0.13)	1.07±0.02 × 10 ¹⁰	×	GBT
188	NGC7436	12269	E	R						LE
189	NGC7460	12312	Sb	B	3190(6)	90(3)	1.16(0.46)	6.28±2.49 × 10 ⁸		LE
190	NGC7537	12442	Sbc	B	2678(3)	142(3)	24.55(2.62)	8.74±0.93 × 10 ⁹		LE
191	NGC7548	12455	L	R	7991(6)	83(4)	0.29(0.07)	9.02±2.18 × 10 ⁸		LE
192	A23176p1541	12519	Sd	B	4378(5)	145(5)	4.23(0.32)	4.07±0.31 × 10 ⁹		LE
193	NGC7620	12520	Scd	B	9583(6)	108(3)	6.70(1.06)	3.11±0.49 × 10 ¹⁰		LE
194	A23264p1703	12620	L	R	6849		<0.16	<3.69×10 ⁸		CEGG
195	IC1504	12734	Sb	B	6274(6)	204(7)	7.28(0.63)	1.39±0.12 × 10 ¹⁰		LE
196	NGC7752	12779	Sd	B	5044(8)	170(10)	8.67(1.95)	1.06±0.24 × 10 ¹⁰		LE
197	A23514p2813	12835	E	R			<0.20	<4.79×10 ⁸		GBT
198	A23542p1633	12856	Im	B	1776(5)	66(2)	11.53(1.11)	2.02±0.19 × 10 ⁹		LE
199	A04345m0225	3104	L		9739(8)	87(6)	1.37(0.39)	4.99±1.42 × 10 ⁹		LE
200	NGC1517	2970	Sc		3483(3)	79(3)	10.71(0.93)	6.04±0.52 × 10 ⁹		LE

Note. — Col. (1): NFGS ID number. Col. (2): NGC number, IC number, or IAU anonymous notation. Col. (3): UGC number. Col. (4): Morphological type in the NFGS database. Col. (5): Sequence association (red, blue, or mid) if M_* and $U - R$ color are available, see Figure 2.1. Col. (6): Heliocentric optical velocity measured from HI in km s^{-1} . Col. (7): Observed maximum rotation speed in km s^{-1} . Col. (8): Velocity-integrated HI flux in Jy km s^{-1} . Col. (9): HI gas mass calculated from f_{HI} following Haynes & Giovanelli (1984). Col. (10): Reference for HI data. GBT: new GBT observations presented in this paper, LE: HyperLeda (Paturel et al. 2003), HR: *A General Catalog of HI Observations of Galaxies*, (Huchtmeier & Richter 1989), CEGG: Cornell EGG HI Digital Archive (Springob et al. 2005), HI: HIPASS (Barnes et al. 2001).

Table 2.5. New HI data

ID	Galaxy Name	UGC	α_{2000} (J2000)	δ_{2000} (J2000)	t_{int} (s)	$V_{\odot}(\sigma_{V_{\odot}})$ (km s^{-1})	$W_{20}(\sigma_{W_{20}})$ (km s^{-1})	$W_{50}(\sigma_{W_{50}})$ (km s^{-1})	$f_{\text{HI}}(\sigma_{f_{\text{HI}}})$ (Jy km s^{-1})	σ_{chan} (mJy)
(1)	(2)	(3)	(4)	(5)	(6)	(7)	(8)	(9)	(10)	(11)
1	A00113+3037	130	00:13:56.9	+30:52:59	2970				<0.12	0.93
11	IC1639	750	01:11:46.5	-00:39:52	2700	5381(12)	83(35)	54(23)	0.19(0.05)	1.00
						5523(12)	253(36)	80(24)	0.70(0.08)	1.00
14	NGC516	946	01:24:08.1	+09:33:06	4440				<0.09	0.80
22	IC195	1555	02:03:44.6	+14:42:33	1140	3648(2)	264(7)	229(4)	4.28(0.12)	1.46
30	NGC1029	2149	02:39:36.5	+10:47:36	870	3631(3)	474(10)	393(7)	6.85(0.16)	1.46
						3620(28)	340(83)	267(55)	7.41(0.14)	1.56
						3609(30)	365(91)	277(60)	8.32(0.15)	1.56
33	NGC1298	2683	03:20:13.1	-02:06:51	840	6452(3)	91(10)	86(6)	0.48(0.09)	1.87
35	NGC1552	2683	04:20:17.7	-00:41:34	3180	4784(8)	318(24)	281(16)	0.70(0.09)	0.98
44	NGC3011	5259	09:49:41.2	+32:13:15	2100	1543(2)	179(7)	170(5)	1.24(0.08)	1.25
54	NGC3179	5555	10:17:57.2	+41:06:51	1740				<0.19	1.31
68	A10465+0711	5923	10:49:07.6	+06:55:02	870	713(4)	188(11)	149(7)	3.12(0.16)	2.31
69	A10504+0454	6003	10:53:03.8	+04:37:54	1740	5819(5)	234(16)	152(11)	1.47(0.09)	1.17
72	NGC3499	6115	11:03:11.0	+56:13:18	6990	1495(12)	370(35)	261(23)	0.39(0.06)	0.58
75	NGC3522	6159	11:06:40.4	+20:05:08	900	1221(8)	308(24)	246(16)	2.00(0.16)	1.82
80	NGC3605	6295	11:16:46.6	+18:01:02	900				<0.11	1.33
87	A11332+3536	6570	11:35:49.1	+35:20:06	3600	1628(2)	155(7)	113(4)	1.35(0.05)	0.82
93	A11392+1615	6655	11:41:50.6	+15:58:25	3600	744(2)	86(5)	63(3)	0.92(0.04)	0.97
96	A11476+4220	6805	11:50:12.3	+42:04:28	3600	1132(6)	137(17)	114(11)	0.39(0.05)	0.90
105	A12001+6439	7020A	12:02:37.6	+64:22:35	2100	1515(1)	136(4)	91(3)	2.30(0.05)	0.91
106	NGC4117	7112	12:07:46.1	+43:07:35	900	950(2)	197(6)	197(4)	2.20(0.13)	1.80
						839(2)	480(7)	450(5)	5.10(0.2)	1.80
117	NGC4308 ^a	7426	12:21:56.9	+30:04:27	8070				<0.06	0.61
						702(5)	69(15)	56(10)	0.13(0.03)	0.61
144	NGC5338	8800	13:53:26.5	+05:12:28	900	801(9)	110(27)	48(18)	0.77(0.12)	2.23
146	A13550+4613	8876	13:56:58.0	+45:58:24	2100				<0.15	1.24
154	NGC5596	9208	14:22:28.7	+37:07:20	1920	3220(24)	385(73)	209(49)	0.52(0.14)	1.40
172	IC1141	10051	15:49:46.9	+12:23:57	4140	4389(3)	237(8)	207(5)	1.82(0.07)	0.92
173	IC1144 ^b	10069	15:51:21.7	+43:25:03	5700				<0.07	0.62
						12206(6)	215(19)	175(13)	0.47(0.05)	0.62
187	A22551+1931N ^c	12265N	22:57:36.0	+19:47:26	1140				1.66(0.13)	1.44
197	A23514+2813	12835	23:53:56.7	+28:29:34	4080	5717(2)	315(7)	227(5)	6.64(0.13)	1.44
						6728(5)	204(16)	182(10)	<0.20	0.79
									0.43(0.06)	0.79

Table 2.5 (cont'd)

ID	Galaxy Name	UGC	α_{2000} (J2000)	δ_{2000} (J2000)	t_{int} (s)	$V_{\odot}(\sigma_{V_{\odot}})$ (km s^{-1})	$W_{20}(\sigma_{W_{20}})$ (km s^{-1})	$W_{50}(\sigma_{W_{50}})$ (km s^{-1})	$f_{HI}(\sigma_{f_{HI}})$ (Jy km s^{-1})	σ_{chan} (mJy)
(1)	(2)	(3)	(4)	(5)	(6)	(7)	(8)	(9)	(10)	(11)

Note. — For galaxies with large companions in the GBT beam, we measure the HI flux twice. The first row contains values measured in the ionized-gas/stellar velocity range, or upper limits if the galaxy is undetected. The second row includes companion flux (if any) within $\pm 300 \text{ km s}^{-1}$ of the target galaxy. Please see §2.2.2 for more details. Col. (1): NFGS ID number. Col. (2): NGC number, IC number, or IAU anonymous notation. Col. (3): UGC number. Col. (4): RA of GBT pointing center in *hh:mm:ss.s* (J2000). Col. (5): DEC of GBT pointing center in *dd:mm:ss* (J2000). Col. (6): Time on-source in seconds. Col. (7): Heliocentric optical velocity measured from HI in km s^{-1} . Col. (8): Velocity width measured at the 20% level in km s^{-1} . Col. (9): Velocity width measured at the 50% level in km s^{-1} . Col. (10): Velocity-integrated HI flux in Jy km s^{-1} . Col. (11): Channel-to-channel RMS of the HI spectrum in mJy.

^aThe companion flux noted for this galaxy may in fact belong to NGC 4308, although the offset between the optical and measured HI velocity suggests that the flux belongs to a nearby companion.

^bThe measured HI velocity suggests that the flux belongs to a nearby companion.

^cPreliminary VLA HI data (Wei et al., in prep.) suggest that UGC 12265N contains about 1/4 of total HI within the GBT beam, so we use this fraction of the total HI flux for our analysis.

Chapter 3

CARMA Observations of E/S0s

3.1 Introduction

Until recently, early-type galaxies were considered to be red and dead — dried out remnants of major mergers that quickly exhausted/expelled their gas in a burst of star formation. Studies over the past couple of decades, however, have revealed several sub-populations that may have active star formation. Recent work finds that 20–30% of field early-type galaxies are either actively star forming (Kannappan et al. 2009; Schawinski et al. 2009) or have had recent (< 1 Gyr ago) star formation (Yi et al. 2005).

Where there is star formation, there must be gas to *fuel* the star formation. Surveys of atomic gas have found significant amounts of atomic gas (up to $M_{HI}/L_B \sim 2.7 M_\odot/L_\odot$) in a large percentage of early-type galaxies, up to 70% depending on the survey (Hawarden et al. 1981; Knapp et al. 1985; Wardle & Knapp 1986; Sadler et al. 2000; Oosterloo et al. 2002; Morganti et al. 2006; Wei et al. 2010a). These results suggest that at least some sub-population of early-type galaxies has sufficiently large gas reservoirs to sustain star formation over long periods of time (Chapter 2, Wei et al. 2010a).

It is molecular gas, however, that appears to be most intimately connected to star formation in spiral galaxies (e.g., Kennicutt 1998; Wong & Blitz 2002; Bigiel et al. 2008). The fact that large single-dish surveys of FIR-bright early-type galaxies (Wiklind & Henkel 1989; Lees et al. 1991; Wiklind et al. 1995) typically have higher CO-detection rates than volume or flux-limited CO surveys (Knapp & Rupen 1996; Welch & Sage 2003; Sage et al. 2007; Combes et al. 2007) suggests that this is also the case for early-type galaxies.

Spatially resolved studies of molecular gas in early-type galaxies, however, are sparse as interferometric observations are time-consuming and difficult to obtain. There have been some single-galaxy studies of early types that find the molecular gas to be very centrally concentrated, often with ring morphologies (Wiklind & Henkel 1992; Inoue et al. 1996; Wiklind et al. 1997; Okuda et al. 2005). More recent efforts by Young et al. have more than doubled the number of interferometric observations of early-type galaxies relative to Young (2002), finding evidence suggesting that the molecular gas in some of these galaxies was acquired from external sources (Young et al. 2008), as well as good spatial correlation between molecular gas and star formation (Young et al. 2009).

The galaxies observed by Young et al. are typically massive ($M_* > 10^{10} M_\odot$) and contain only low-level, residual star formation. Recent work, however, has identified a population of low-to-intermediate mass galaxies that are morphologically early-type, but occupy the blue sequence in color vs. stellar mass space, alongside spiral galaxies (Kannappan, Guie, & Baker 2009, hereafter KGB). While high-mass blue-sequence E/S0s often appear to be young major merger/interaction remnants, in which star formation will quickly taper off and allow them to resemble the E/S0s observed by Young et al., many blue-sequence E/S0s with lower stellar masses appear to be fairly regular and settled and show signs of recent central star formation

and disk (re)building — an interesting population to investigate the nature of gas and star formation in early-type galaxies.

In this Chapter, we focus on the galaxies mapped with the Combined Array for Research in Millimeter-wave Astronomy (CARMA). We present CO(1–0) channel maps, velocity-integrated emission maps, and velocity fields for each galaxy along with individual galaxy notes.

3.2 Sample and Data

Our parent sample of 32 galaxies consists of all E/S0s (14 blue-, 2 mid-, and 11 red-sequence) with $M_* \leq 4 \times 10^{10} M_\odot$ from the Nearby Field Galaxy Survey (NFGS, Jansen et al. 2000b), and an additional five blue-sequence E/S0s in the same mass range with HI maps available from the literature. The cutoff mass of $4 \times 10^{10} M_\odot$ is chosen to reflect the mass above which the fraction of blue-sequence E/S0s tails off (Figure 3.1).

Within this parent sample of 32 galaxies, we selected the FIR-bright sources to maximize detectability with CARMA. External factors such as weather, LST pressure, and array configuration schedule also affected target selection and time allocation.

Although these factors bias our sample towards the more strongly star-forming low-mass E/S0s, we are probing the population of E/S0s that is most unambiguously transitional and active in terms of evolution (KGB). Of the parent sample, 23 E/S0s were observed with CARMA in CO(1–0), with 12 detections and 11 non-detections (Figure 3.1). The detections include 8 of the 17 observed blue-sequence E/S0s, both mid-sequence E/S0s, and two of the four observed red-sequence E/S0s.

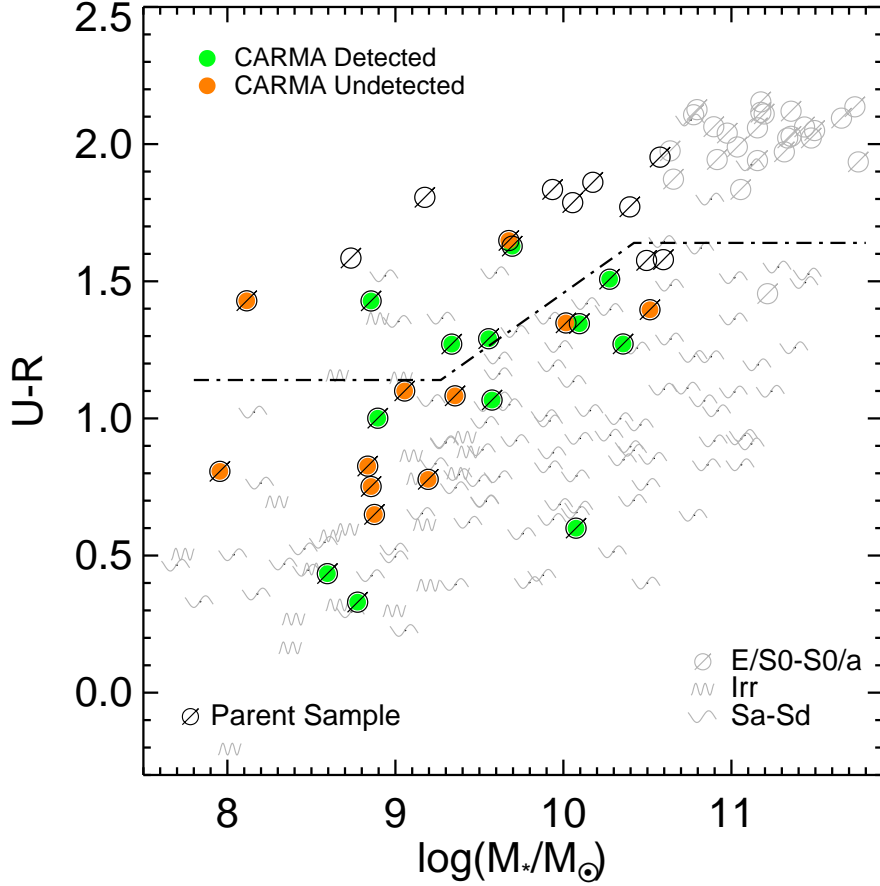


Figure 3.1: $U - R$ color vs. stellar mass for galaxies in the Nearby Field Galaxy Survey (Jansen et al. 2000b), plus five additional E/S0s from the literature. Symbols denote morphological type based on monochrome B or g band images (KGB). The red sequence (the main locus of high-mass and/or cluster E/S0s) lies above the dashed line, while the blue-sequence (typically populated by spiral galaxies) lies below. Dark symbols denote the 32 galaxies in the parent sample with $M_* \lesssim 4 \times 10^{10} M_\odot$; the remaining NFGS galaxies are shown in light grey. Our CARMA sample galaxies are denoted by filled circles; green indicates a CO detection while orange indicates a non-detection.

Table 3.1. Properties of CARMA-observed galaxies

Galaxy	α_{2000} (J2000)	δ_{2000} (J2000)	Morph.	Seq.	M_* ($\text{Log } M_\odot$)	v_\odot (km s^{-1})	D (Mpc)	L_B ($\text{Log } L_\odot$)	R_{25} (kpc)
(1)	(2)	(3)	(4)	(5)	(6)	(7)	(8)	(9)	(10)
IC 1141	15:49:46.9	+12:23:57	S0/a	Blue	10.4	4389	68.0	10.00	6.8
NGC 3032	09:52:08.2	+29:14:10	L	Blue	9.6	1546	25.2	9.75	4.6
NGC 3773	11:38:12.9	+12:06:43	L	Blue	8.6	985	10.5	9.20	1.6
NGC 3870	11:45:56.6	+50:11:59	L	Blue	8.8	758	14.5	9.12	2.1
NGC 4117	12:07:46.1	+43:07:35	L	Red	9.7	950	19.0	9.25	5.0
NGC 5173	13:28:25.3	+46:35:30	E	Blue	10.3	2428	41.2	10.04	7.0
NGC 5338	13:53:26.5	+05:12:28	L	Red	8.9	801	10.3	8.74	2.8
UGC 12265N	22:57:36.0	+19:47:26	L	Blue	10.1	5717	82.8	9.87	6.7
UGC 6003	10:53:03.8	+04:37:54	S0/a	Blue	10.1	5819	84.2	10.21	7.8
UGC 6570	11:35:49.1	+35:20:06	S0/a	Mid	9.6	1628	28.6	9.43	4.9
UGC 6805	11:50:12.3	+42:04:28	L	Blue	8.9	1132	20.3	8.92	2.0
UGC 7020A	12:02:37.6	+64:22:35	L	Mid	9.3	1515	26.7	9.33	4.4
IC 692	11:25:53.5	+09:59:15	E	Blue	8.9	1163	21.4	9.07	2.5
NGC 3011	09:49:41.2	+32:13:16	S0/a	Blue	9.4	1543	25.7	9.20	3.1
NGC 3073	10:00:52.1	+55:37:08	L	Blue	9.1	1217	21.1	9.19	3.3
NGC 3419	10:51:17.7	+13:56:46	L	Blue	10.0	3055	45.2	10.01	6.7
NGC 3522	11:06:40.4	+20:05:08	L-	Red	9.7	1221	22.9	9.40	5.1
NGC 7077	21:29:59.6	+02:24:51	S0/a	Blue	8.8	1148	18.9	9.00	2.4
NGC 7360	22:43:33.9	+04:09:04	E	Blue	10.5	4685	67.9	10.31	12.0
UGC 5923	10:49:07.6	+06:55:02	S0/a	Red	8.1	713	8.0	8.32	1.5
UGC 6637	11:40:24.8	+28:22:26	L-	Blue	9.2	1836	31.5	9.36	4.1
UGC 6655	11:41:50.6	+15:58:26	L	Blue	8.0	744	8.8	8.21	1.1
UGC 9562	14:51:14.4	+35:32:32	L+	Blue	8.9	1257	25.2	9.18	3.4

Note. — Morphology, sequence association, and M_* are from KGB. Heliocentric velocity (v_\odot , cz) is from HI spectra (Wei et al. 2010a), except for NGC 516 which is undetected in HI. Distance, L_B , and R_{25} are from Jansen et al. (2000a).

3.3 Observations & Data Reduction

Observations with CARMA (Bock et al. 2006) were obtained between Dec 2006 and Oct 2009 with the 15-element array at Cedar Flat, California, comprising of six 10-meter antennas from the Owens Valley Radio Observatory (OVRO) and nine 6-meter antennas from the Berkeley Illinois Maryland Association (BIMA). Data were obtained in the C, D, and (for one galaxy), E configurations, which have maximum baselines of 350 to 8 meters, respectively. Typical system temperatures ranged between 200-500 K, with a few tracks between 500-1000 K due to bad weather.

Before 2010, CARMA had three correlator bands that could be configured in-

dependently in various spectral line and wideband modes. Most of our galaxies were observed using two overlapping correlator bands, each 62 MHz wide, which resulted in velocity coverage of $\sim 300 \text{ km s}^{-1}$ and channel resolution of $\sim 2.5 \text{ km s}^{-1}$. Since our observations began during the commissioning phase for CARMA, we decided to take a conservative approach and observe the target and calibrator in the same correlator mode. For good S/N on the calibrator, the third band was set in 500 MHz mode and centered on our two spectral line bands. For the two galaxies (NGC 4117, UGC 12265N) with larger velocity extent, all three bands were set as overlapping 62 MHz bands for broader velocity coverage of $\sim 450 \text{ km s}^{-1}$. For the NGC 4117 calibrator observations, the correlator was switched to three overlapping 500 MHz bands for better signal-to-noise via the “Hybrid Mode”, but we chose to retain 62 MHz bandwidth for observations of UGC 12265N as its phase calibrator is the extremely bright quasar 3C454.3. With the exception of UGC 12265N, phase, bandpass, and flux calibrators were all observed with the 500 MHz mode. Total times on-source in each configuration for each galaxy are listed in Table 3.2.

CARMA data are reduced using tasks in the MIRIAD package (Sault et al. 1995). We first flag the data for bad channels, antennas, weather, and pointing (errors $> 10''$). All narrow-band data are Hanning smoothed before bandpass calibration on the noise source and a bright quasar (typically 0927+390, 3C273, or 3C454.3). We perform phase calibration at ~ 20 minute intervals, and absolute flux calibration is done using either a planet (when available) or MWC 349. Channels are then decimated and averaged, resulting in channel widths of 10 km s^{-1} .

We combine the tracks for each galaxy, using natural weighting with an additional weighting in inverse proportion to the noise as estimated using the system temperature, and invert the visibility data. Although all our observations are single-pointing only, the final images are mosaicked to account for the different primary

beam sizes of the 6- and 10-meter antennas. We use `MOSSDI2` to perform a Steer CLEAN (Steer et al. 1984) on the mosaicked cubes down to a cutoff of two sigma in the residual image. The clean beam is determined by fitting a gaussian to the dirty beam. The clean beam is then convolved with the clean components to form the final map cube. The typical clean beam ranges from 2–4''; we list the parameters for the final data cubes in Table 3.3.

Integrated-intensity and velocity maps are made from the cubes for each galaxy, limiting the channels in velocity based on the velocity extent of the HI emission. For galaxies showing fairly regular rotation (IC 1141, NGC 3032, NGC 3870, NGC 4117, NGC 5173, UGC 12265N, & UGC 6805) we fit their CO velocity maps with model rotation curves and create a mask from an adaptive window around the model velocity field using the MIRIAD task `ROTCURMASK` and the velocity dispersion map. The masks typically have a window of 25-35 km s^{-1} around the model velocity (visually checked to ensure inclusion of emission $> 2\sigma_{\text{chan}}$), with a median of 30 km s^{-1} . The masks are applied to the data cubes to further limit the noise, and we re-make the integrated intensity, velocity, and velocity dispersion maps from the masked cubes. A special case is UGC 7020A; the warped velocity distribution of this galaxy makes fitting a model impossible, but we can still make a mask to limit the noise using the velocity and velocity dispersion maps. For galaxies without regular rotation (NGC 3773, NGC 5338, UGC 6003, and UGC 6570), the integrated-intensity maps were masked only in velocity based on the HI velocity profile.

Table 3.2. CARMA observation parameters

Galaxy	C	D	E	Total	Bandpass Cal.	Flux Cal.	Phase Cal.
(1)	(hrs) (2)	(hrs) (3)	(hrs) (4)	(hrs) (5)	(6)	(7)	(8)
IC 1141	4.5	4.8		9.3	3C345	Mars	1549+390
NGC 3032	5.3	2.3		7.6	3C273, 3C84	Mars	0927+390, 0854+015
NGC 3773	4.25	10.8	3.3	18.35	3C273, 3C84	Mars	3C273
NGC 3870		12.2		12.2	3C273, 3C84	Mars	0927+390, 0958+655
NGC 4117	9.7	8.2		17.9	3C273, 3C84	Mars, MWC349	0927+390, 1146+399, 1310+323
NGC 5173	6.5	6.6		13.1	3C273, 3C345	Mars, MWC349	1310+323
NGC 5338	8.0	14.0		22.0	3C273	Mars, MWC349	3C279
UGC 12265N	11.4	5.5		16.9	3C454.3	Uranus, MWC349	3C454.3
UGC 6003	5.5	2.3		7.8	3C273, 3C111	Mars	1058+015
UGC 6570	5.5	2.2		7.7	3C273	MWC349	0927+390, 1159+292
UGC 6805	5.6	5.0		10.6	0927+390	Mars	0927+390, 1310+323
UGC 7020A	15.0	12.4		27.4	3C273, 3C345	Mars	1642+689
IC 692	4.0			4.0	0927+390	Mars	1058+015
NGC 3011	4.0			4.0	3C84	Mars	0854+201
NGC 3073	5.3			5.3	3C111	Mars	0927+390
NGC 3419	2.3			2.3	3C273	Mars	1058+015
NGC 3522	5.3			5.3	3C273	Mars	1159+292
NGC 7077	3.6			3.6	2148+069	MWC349	2158+069
NGC 7360	4.3			4.3	2232+117	Uranus	2232+117
UGC 5923	6.6			6.6	3C273, 3C111	Mars	1058+015
UGC 6637	3.5			3.5	3C273	MWC349	1159+292
UGC 6655	3.6	4.0		7.6	3C273	Mars	3C273, 3C279
UGC 9562	8.0			8.0	3C273	MWC349	1613+349

Note. — Col.(2)–(4) indicate the on-source time in each CARMA array configuration.

Table 3.3. CARMA map parameters

Galaxy	Corr. Velo. Range	Beam	B_{maj} PA	Chan. Width	σ_{chan}	$\sigma_{\Sigma\text{H}_2}$	Masking
	(km s^{-1})	($''$)	($^\circ$)	(km s^{-1})	(mJy beam^{-1})	($M_\odot \text{ pc}^{-2}$)	Method
IC 1141	4315–4500	3.35×2.60	–80.0	10	10	6	CO Rotation
NGC 3032	1450–1660	2.89×2.18	–78.3	10	17	13	CO Rotation
NGC 3773	943–1033	3.43×3.08	84.1	10	7	22	HI Velocity
NGC 3870	675–815	4.07×3.76	63.9	10	11	3	CO Rotation
NGC 4117	8215–1105	2.86×2.46	–88.5	10	8	5	CO Rotation
NGC 5173	2280–2525	3.13×2.65	87.7	10	7	3	CO Rotation
NGC 5338	723–873	3.02×2.92	50.6	10	7	4	HI Velocity
UGC 12265N	5542–5852	2.85×2.29	85.6	10	6	4	CO Rotation
UGC 6003	5721–5881	2.38×1.87	–76.7	10	7	7	HI Velocity
UGC 6570	1514–1684	2.25×1.41	88.8	10	13	20	CO Rotation
UGC 6805	1043–1203	2.08×1.64	–66.9	10	8	10	HI Velocity
UGC 7020A	1443–1603	2.94×2.38	–81.0	10	8	5	CO Rotation
IC 692	1035–1285	4.45×3.39	–70.5	10	16	14	
NGC 3011	1420–1670	4.05×3.59	73.2	10	9	8	
NGC 3073	1091–1341	4.71×3.59	63.3	10	26	21	
NGC 3419	2905–3160	5.59×3.50	56.6	10	18	12	
NGC 3522	1095–1345	4.44×3.46	57.0	10	17	14	
NGC 7077	1002–1262	6.93×4.11	11.5	10	24	11	
NGC 7360	4546–4806	5.63×4.11	20.9	10	10	5	
UGC 5923	585–835	4.32×3.46	46.6	10	14	12	
UGC 6637	1707–1967	4.08×3.72	77.9	10	12	11	
UGC 6655	620–870	2.35×2.04	–75.3	10	8	21	
UGC 9562	1119–1369	4.20×3.69	72.4	10	10	8	

Note. — $\sigma_{\Sigma\text{H}_2}$ assumes a CO-to-H₂ factor (X_{CO}) of $2 \times 10^{20} \text{ cm}^{-2} (\text{K km s}^{-1})^{-1}$.

3.4 Comparison of Interferometric and Single-Dish CO Fluxes

As interferometric observations may resolve out or fail to detect the more extended emission, we compare total fluxes from our CARMA CO(1–0) maps against available single-dish CO(1–0) data. Figure 3.2 shows that the fluxes agree reasonably well, with any discrepancies explained by differences in data quality or single-dish beam size. We discuss individual galaxies below.

NGC 3032: Sage & Wrobel (1989) measured a CO(1–0) flux of 92 ± 10 Jy km s⁻¹ with the NRAO 12 m for this galaxy, compared to our CARMA-derived flux of 76 ± 3 Jy km s⁻¹. This suggests that our CARMA observations are resolving out 17% of the extended flux from this galaxy.

NGC 3870: Welch & Sage (2003) measured a CO(1–0) flux of 10 ± 1 Jy km s⁻¹ for the central pointing with the IRAM 30 m. We do not include additional pointings from Welch & Sage (2003) for comparison as we only detect emission within the central 10'' of the galaxy. This agrees relatively well with our CARMA CO(1–0) flux of 6 ± 3 Jy km s⁻¹, as our detection is very noisy.

NGC 5173: the CO(1–0) spectrum for this galaxy (Lisa Young, private comm.) from the IRAM 30 m has very low signal-to-noise, which could explain the discrepancy in flux estimates.

NGC 5338: Leroy et al. (2005) measured a CO(1–0) flux of 33 ± 6 Jy km s⁻¹ with the ARO 12 m; although the CARMA flux (23 ± 2 Jy km s⁻¹) is less, the difference is not significant given the large uncertainties in the single-dish flux.

UGC 6805: Kannappan et al. (2010) measured a CO(1–0) flux of 8.2 ± 0.5 Jy km s⁻¹ with the IRAM 30 m. Our CARMA map shows flux extending beyond the edge of the 22'' IRAM 30 m primary beam, implying that the 30 m beam misses

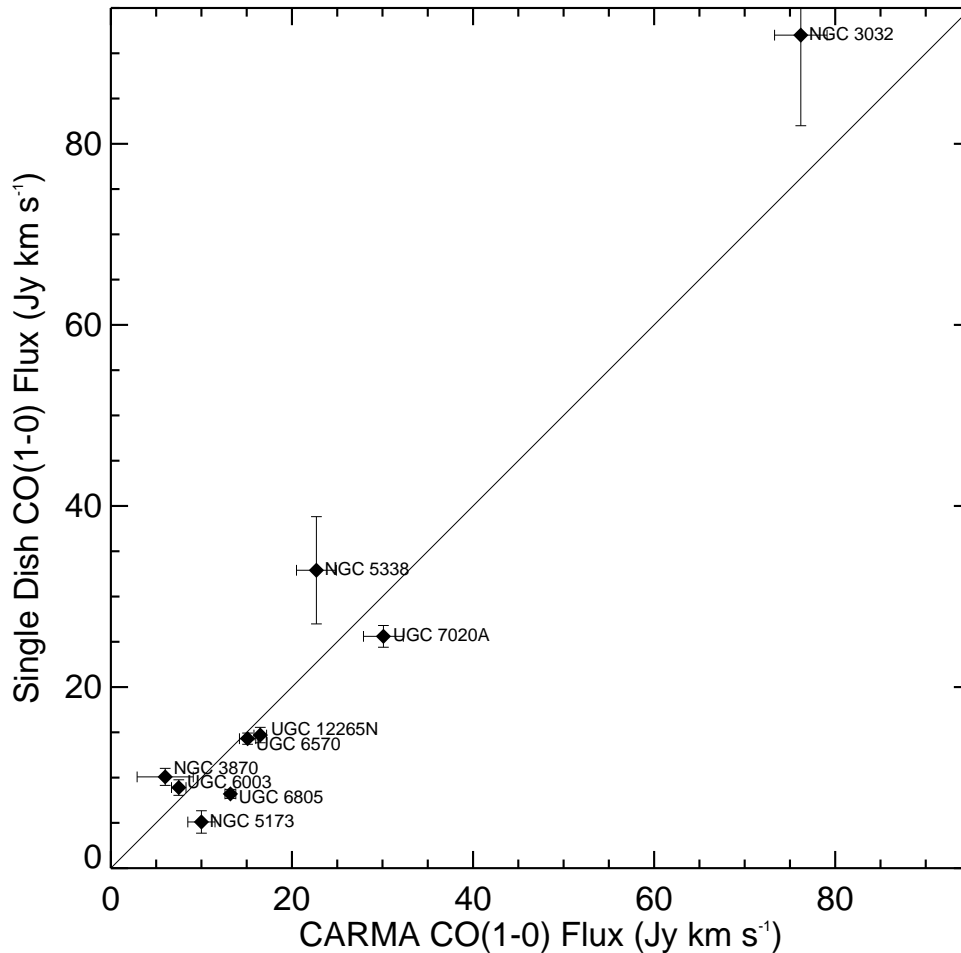


Figure 3.2: Comparison of CARMA CO(1–0) fluxes with single dish CO(1–0) fluxes (from Sage & Wrobel 1989; Welch & Sage 2003; Leroy et al. 2005; Kannappan et al. 2010).

some of the CO emission and accounting for the lower 30 m flux.

UGC 7020A: Kannappan et al. (2010) measured a CO(1–0) flux of 26 ± 1 Jy km s^{-1} with the IRAM 30 m. Our CARMA map shows flux extending beyond the edge of the 22'' IRAM 30 m primary beam, implying that the 30 m beam misses some of the CO emission and accounting for the lower 30 m flux.

3.5 Description of Individual Galaxies

In this Section we present CO(1–0) maps of the 12 galaxies (in alphabetical order) detected by CARMA in our sample, along with complementary optical and infrared imaging. For each galaxy, we include channel maps of the CO(1–0) emission, spaced at 10 km s^{-1} , and a four-panel figure which presents (a) the SDSS r -band image, (b) the *Spitzer* IRAC $8\mu\text{m}$ emission, with stellar emission subtracted following Pahre et al. (2004b) (see Chapter 5), (c) velocity-integrated CO(1–0) emission, and (d) the CO(1–0) velocity field. All the images are on the same spatial scale.

3.5.1 IC 1141

IC 1141 is an S0/a galaxy on the high-mass end of the blue sequence distribution ($M_* = 2.8 \times 10^{10} M_\odot$) from the NFGS. The CO emission reveals parts of spiral arms (lowest-level contour in Figure 3.4c) that are well correlated with the arms seen in $8\mu\text{m}$ PAH as well as r -band emission (Figure 3.4b, a), although the extent of the arms are not as well defined in the optical image. The integrated velocity map for this galaxy (Figure 3.4d) indicates that the gas in the arms of the galaxy rotates along with the rest of the gas disk. Jansen et al. (2000b) identify IC 1141 as an AGN host based on optical line diagnostics.

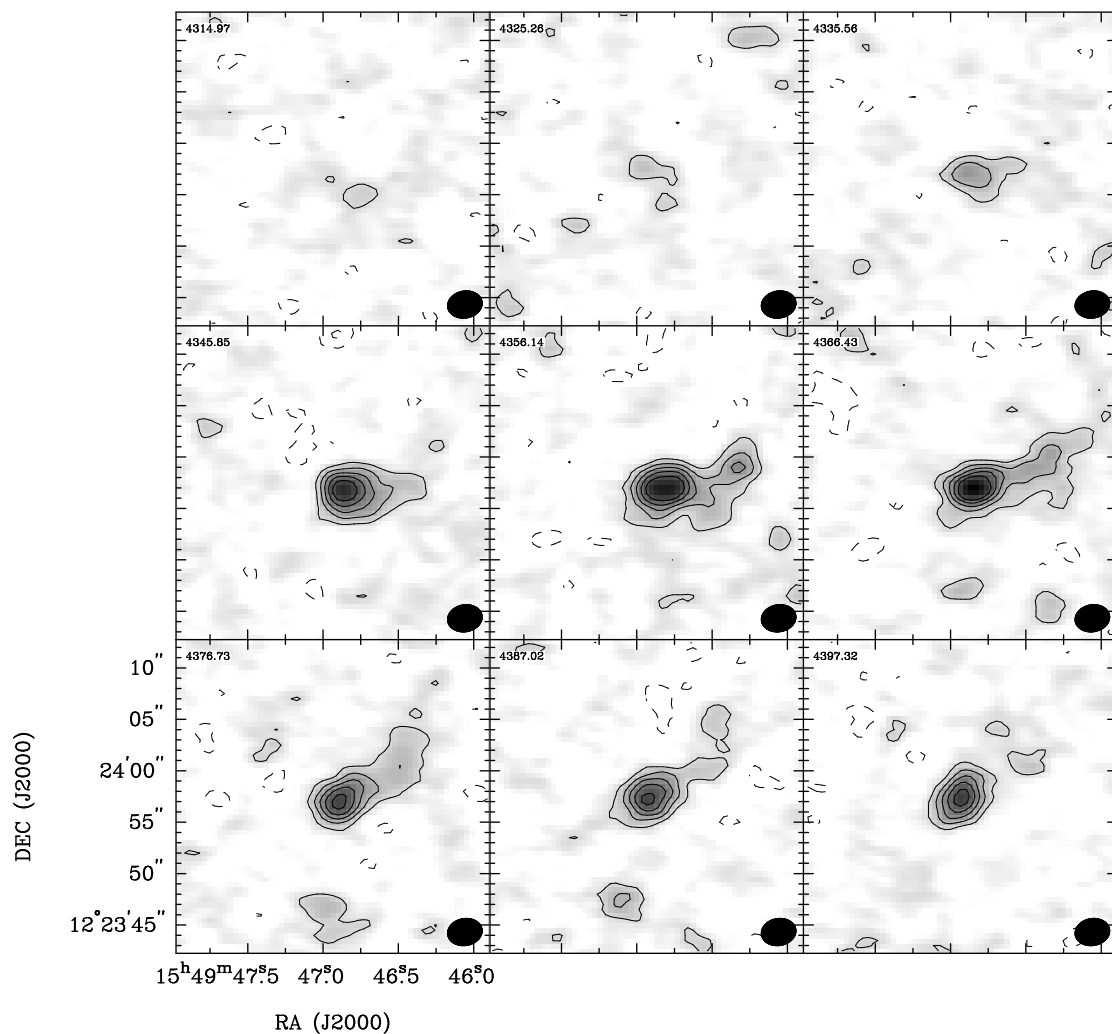


Figure 3.3: Channel maps of CO(1–0) emission (contours and greyscale) for IC 1141. Contour levels are -3 , -1.5 , 1.5 , 3 , 4.5 , 6 , 7.5 times the rms in each channel ($13.5 \text{ mJy beam}^{-1}$). Heliocentric velocity of each panel in km s^{-1} is indicated in the upper left; the beam is shown in the lower right corner.

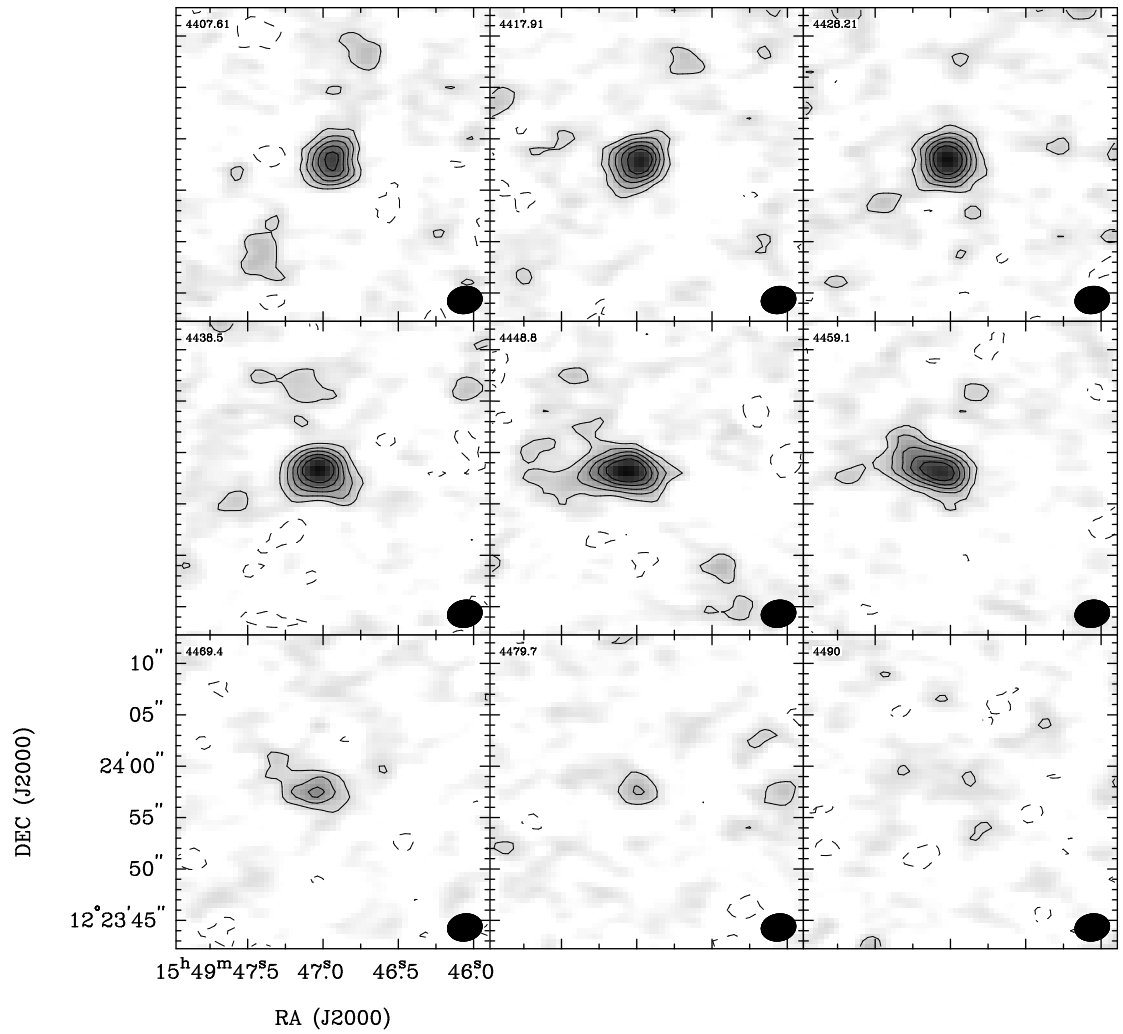


Figure 3.3: More CO(1-0) channel maps of IC 1141.

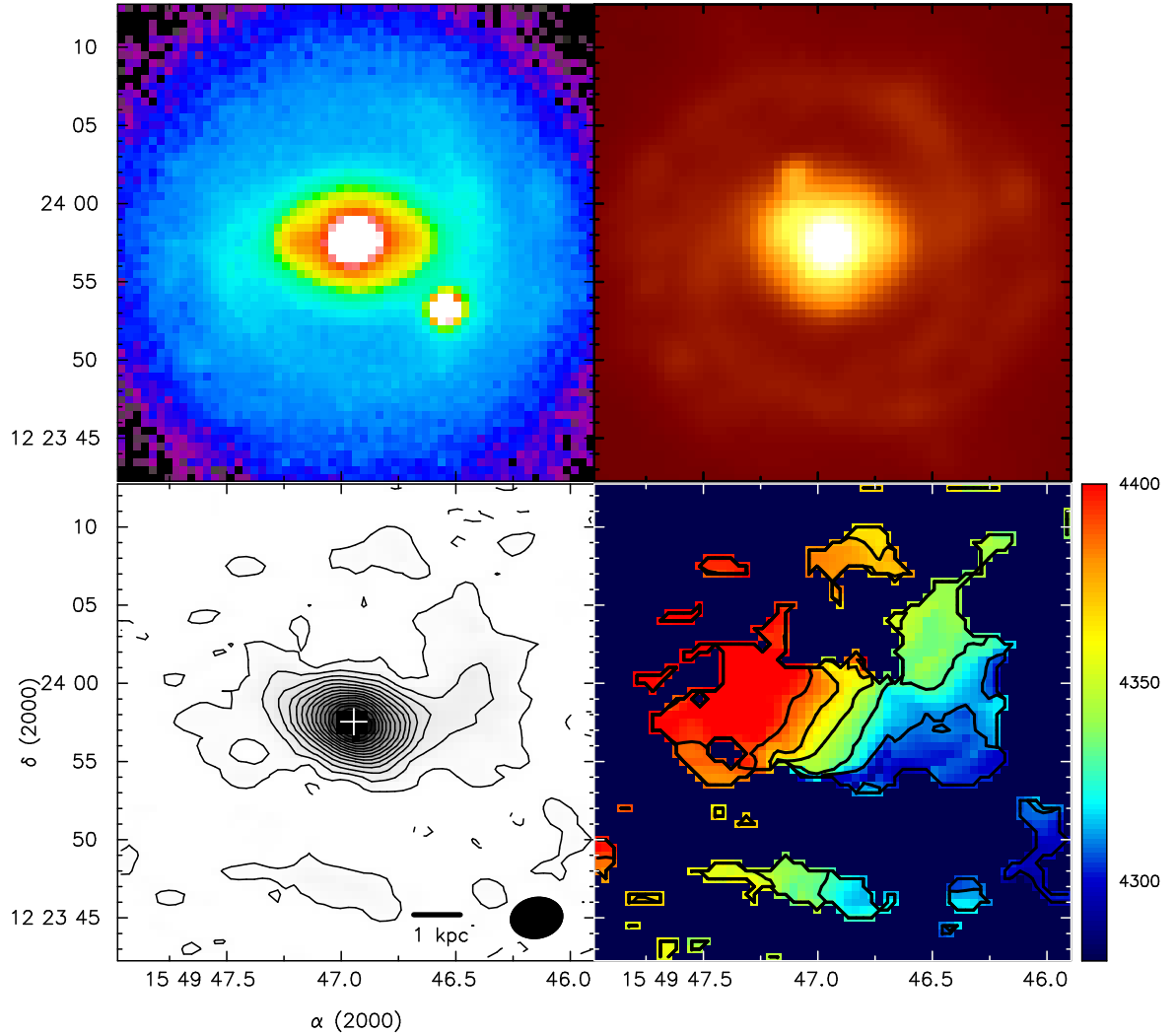


Figure 3.4: IC 1141: (a) SDSS r -band image. (b) *Spitzer* IRAC $8\mu\text{m}$ image, with stellar emission subtracted following Pahre et al. (2004b). (c) Velocity-integrated CO(1-0) emission in IC 1141 (contours and greyscale). Contour levels start at 1.5σ and are spaced in steps of 3σ ($\sigma = 0.3 \text{ Jy km s}^{-1}$); the cross marks the optical nucleus from SDSS. (d) CO(1-0) velocity field, with contours ranging from 4290 to 4390 km s^{-1} at intervals of 20 km s^{-1} .

3.5.2 NGC 3032

NGC 3032 is one of our five non-NFGS galaxies. It is also in the SAURON survey of early-type galaxies, classified as a fast rotator by Emsellem et al. (2007). BIMA CO(1–0) observations of this galaxy by Young et al. (2008) find a circular disk of CO extending out to about $14''$, slightly more extended than our CARMA observations indicate ($12''$ based on the CO radial profile), which suggests that we may have missed some of the more extended, diffuse emission. Young et al. (2008) found the CO, along with ionized gas traced by $H\beta$ and [OIII] emission, to be counterrotating relative to the stars observed by SAURON, implying the molecular gas is of an external origin obtained via accretion from either the intergalactic medium or another galaxy. Schweizer & Seitzer (1988) interpret the “ripples” they observe in optical images of NGC 3032 as evidence for past merger(s), although the settled nature of the molecular gas suggests that any mergers/interactions must have occurred in the past (Young et al. 2008).

Our CARMA map reveals a previously unknown central depression in the CO (Figure 3.6c), which was not detected in the BIMA observations by Young et al. (2008) due to the coarser resolution of the BIMA data. Based on radial profiles, the central depression is $6''$ in diameter, which corresponds well to the “dark dusty ring” or “tightly wrapped arms” described by Young et al. (2008) in the unsharp-masked *Hubble Space Telescope* (*HST*) WFPC2 image of the dust emission. Based on a color map made from WFPC2 F606W and NICMOS2 F160W imaging from the *HST*, Regan & Mulchaey (1999) identified NGC 3032 as a “loosely wound nuclear spiral”. Erwin & Sparke (2003) also find prominent arms and dust lanes among bright point sources in their unsharp-masked WFPC2 F606W image.

The CARMA CO(1–0) velocity field (Figure 3.6d) for NGC 3032 agrees well

with that found by Young et al. (2008) with BIMA, with the same butterfly-wing structure in the channel maps (Figure 3.5a).

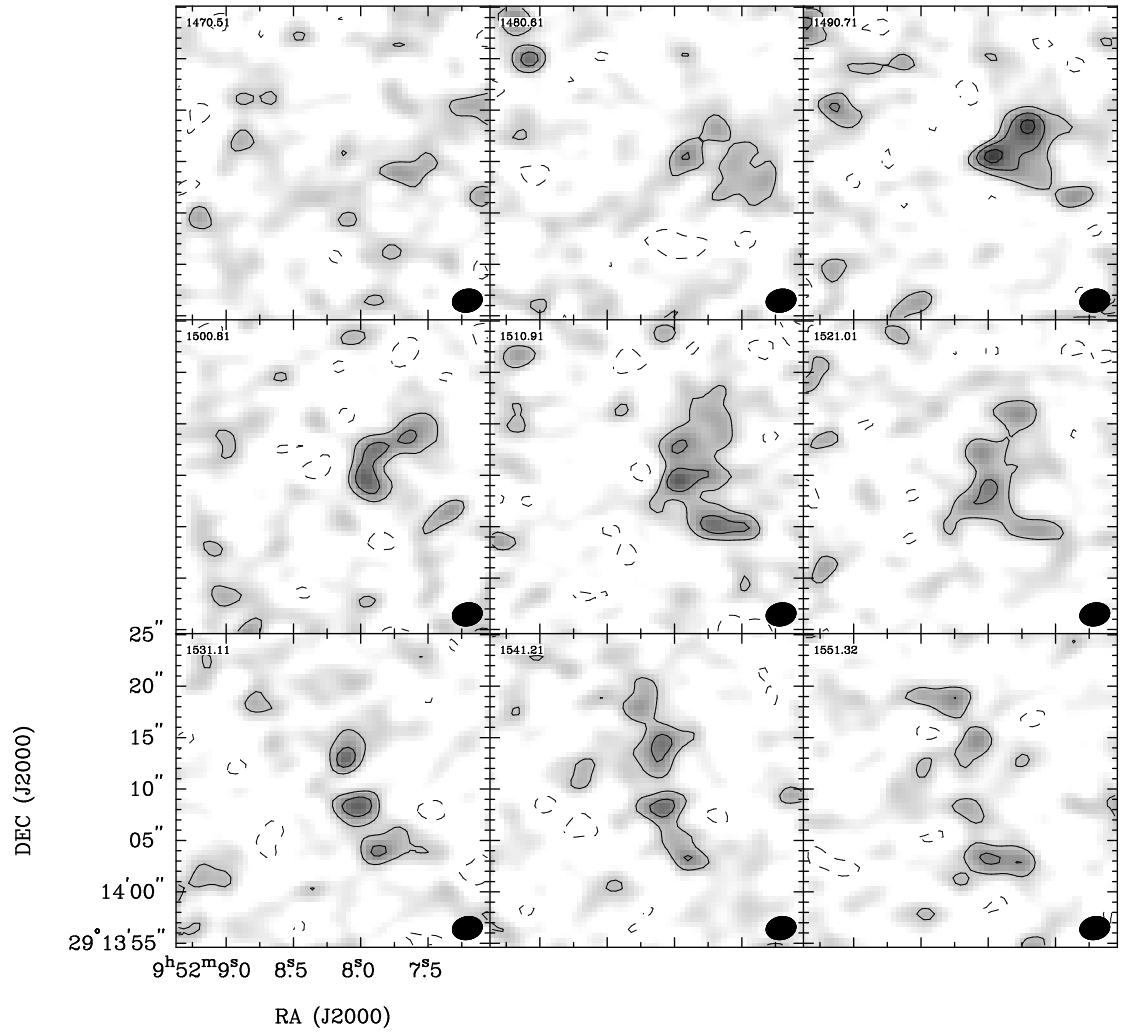


Figure 3.5: Channel maps of CO(1–0) emission (contours and greyscale) for NGC 3032. Contour levels are -3 , -1.5 , 1.5 , 3 , 4.5 times the rms in each channel ($13.7 \text{ mJy beam}^{-1}$). Heliocentric velocity of each panel in km s^{-1} is indicated in the upper left; the beam is shown in the lower right corner.

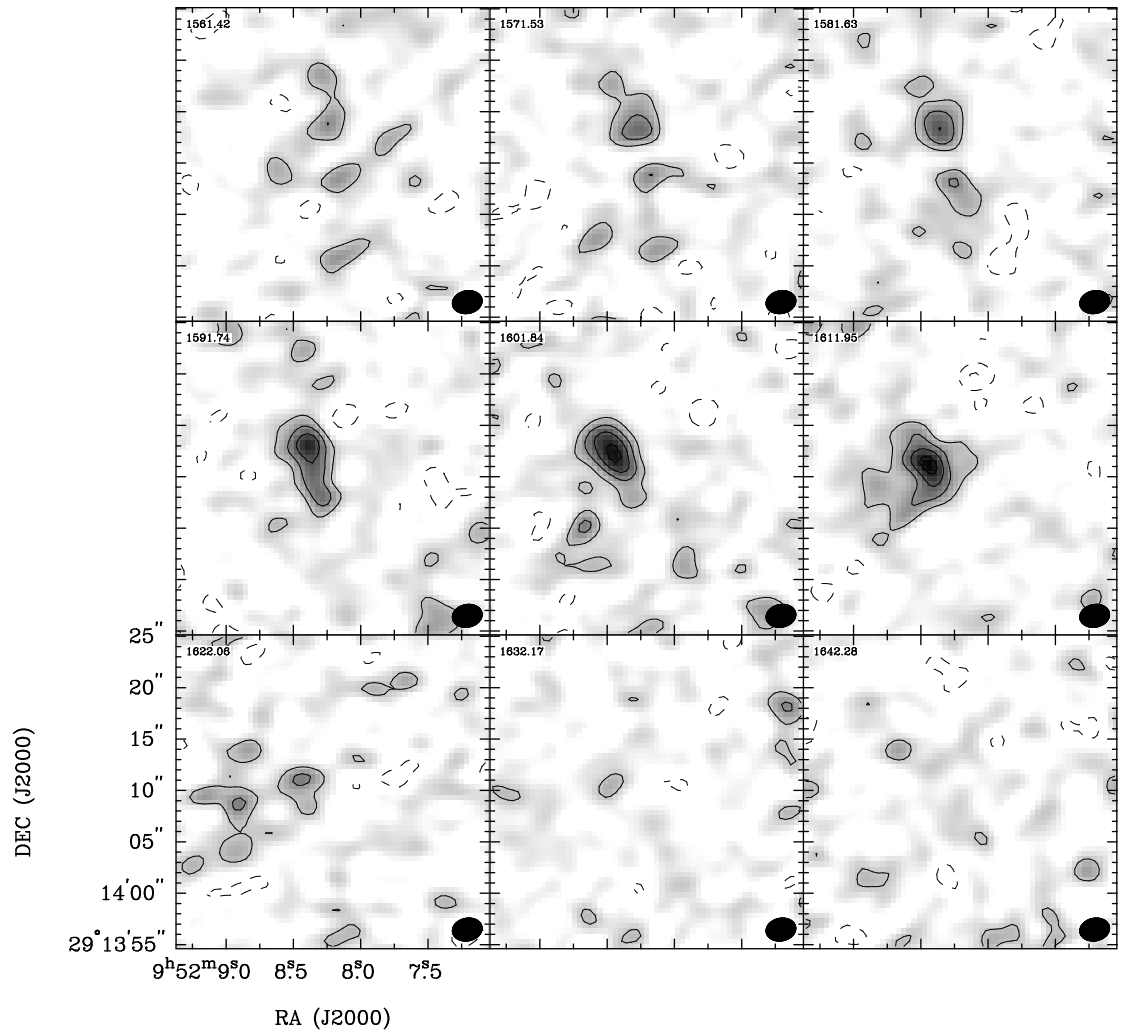


Figure 3.5: More CO(1-0) channel maps of NGC 3032.

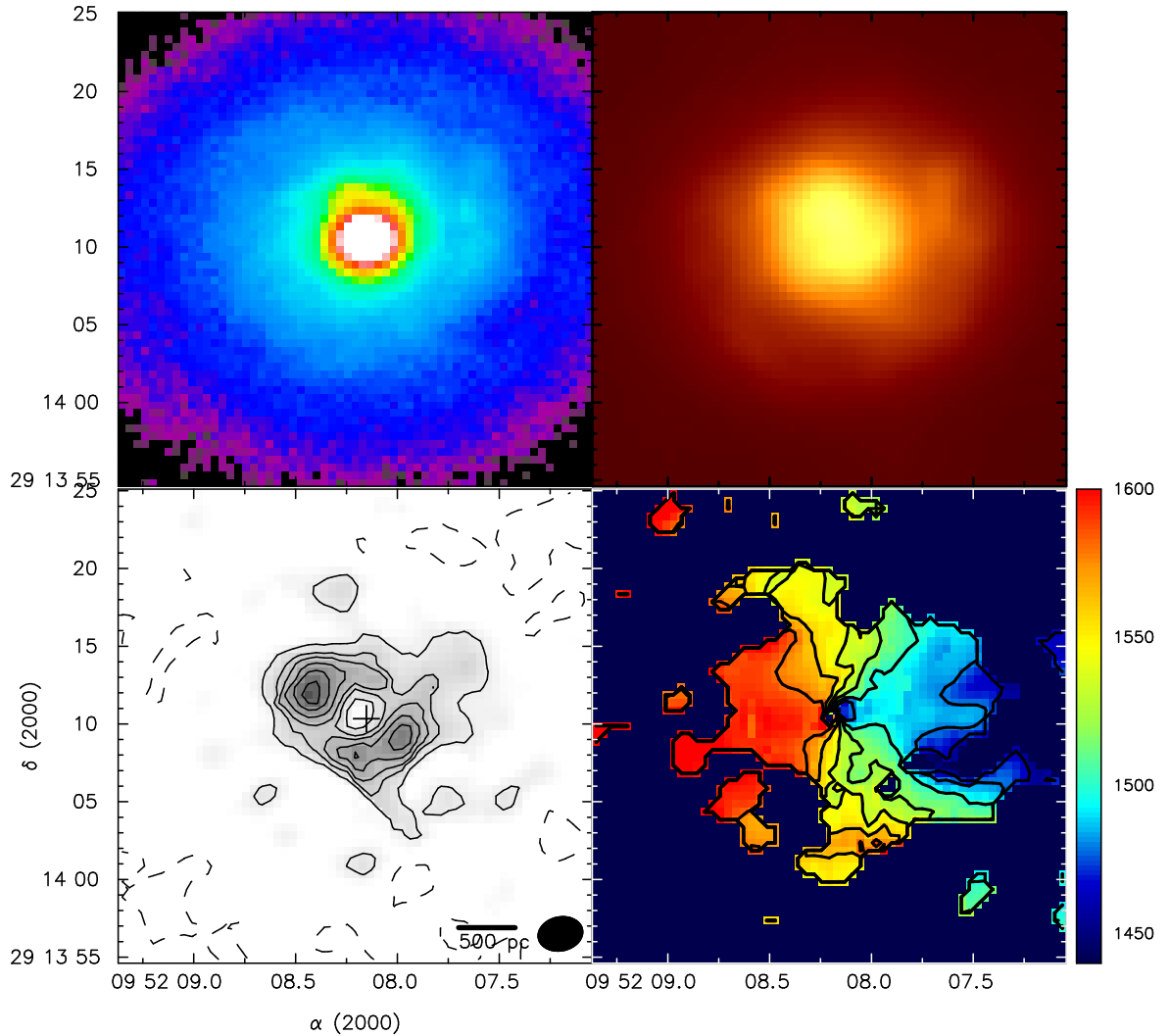


Figure 3.6: NGC 3032: (a) SDSS r -band image. (b) *Spitzer* IRAC $8\mu\text{m}$ image, with stellar emission subtracted following Pahre et al. (2004b). (c) Velocity-integrated CO(1–0) emission (contours and greyscale). Contour levels start at 1.5σ and are spaced in steps of 1.5σ ($\sigma = 0.55 \text{ Jy km s}^{-1}$); the cross marks the optical nucleus from SDSS. (d) CO(1–0) velocity field, with contours ranging from 1460 to 1580 km s^{-1} at intervals of 20 km s^{-1} .

3.5.3 NGC 3773

NGC 3773 is another non-NFGS galaxy, a target of the *Spitzer* Infrared Nearby Galaxies Survey (SINGS; Kennicutt et al. 2003) of 75 local galaxies. Optical and $8\mu\text{m}$ PAH images (Figure 3.8a, b) reveal the presence of two nuclei in this galaxy, suggesting that it may be a recent merger. In their study of dwarf galaxies in transition, Dellenbusch et al. (2008) observe prominent asymmetric dust features in their deep *R*-band image, which supports the merger/interaction scenario.

The CARMA map (Figure 3.8c) reveals *three* peaks in the CO(1–0) emission. The center peak, near the SDSS optical center (white cross), is well aligned with one of the optical/infrared nuclei. The left peak is offset from the optical/infrared by $\sim 2.5''$, and there is only a faint infrared (and no optical) counterpart for the right peak. The CO velocity map (Figure 3.8d) shows little rotation for the left and center CO emission peaks, implying that the gas is relatively face-on, while the gas in the right peak is much more regularly rotating. The mismatch in velocity and lack of optical/infrared counterparts suggests that the right blob seen in the CO emission may have been acquired from an external source.

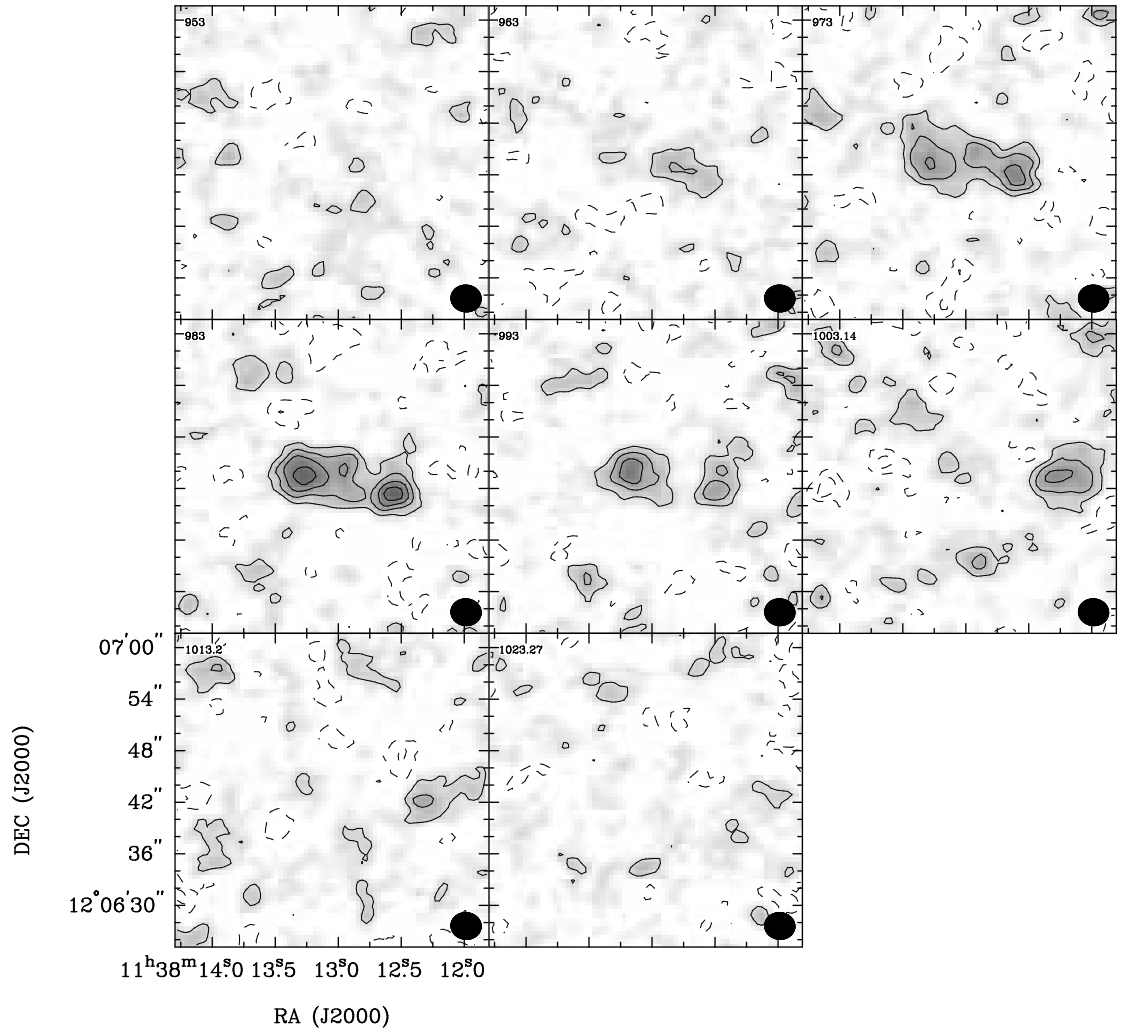


Figure 3.7: Channel maps of CO(1-0) emission (contours and greyscale) for NGC 3773. Contour levels are -3 , -1.5 , 1.5 , 3 , 4.5 , 6 times the rms in each channel (7 mJy beam^{-1}). Heliocentric velocity of each panel in km s^{-1} is indicated in the upper left; the beam is shown in the lower right corner.

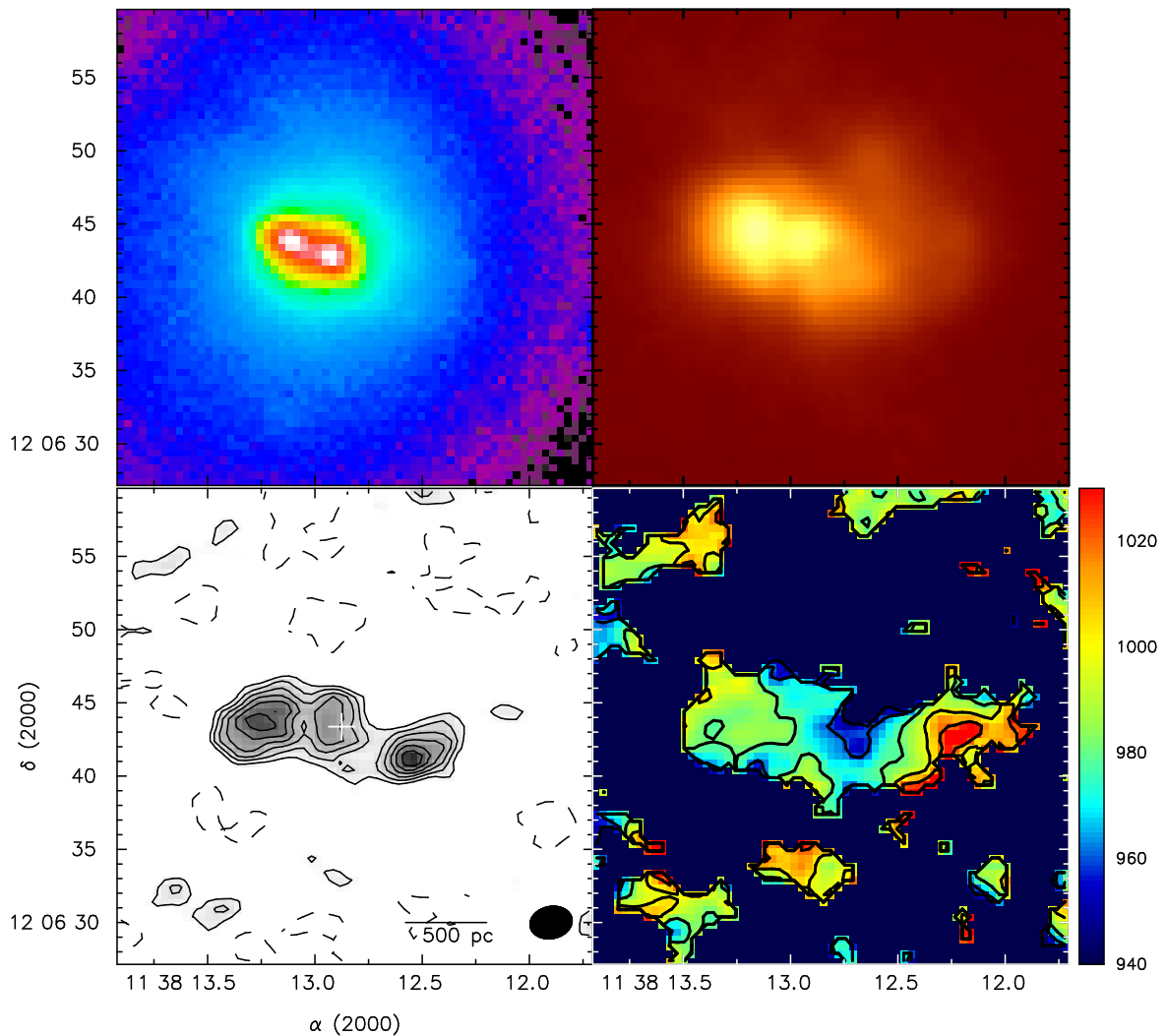


Figure 3.8: NGC 3773: (a) SDSS r -band image. (b) *Spitzer* IRAC $8\mu\text{m}$ image, with stellar emission subtracted following Pahre et al. (2004b). (c) Velocity-integrated CO(1-0) emission (contours and greyscale). Contour levels start at 1.5σ and are spaced in steps of 0.5σ ($\sigma = 0.3 \text{ Jy km s}^{-1}$); the cross marks the optical nucleus from SDSS. (d) CO(1-0) velocity field, with contours ranging from 940 to 1020 km s^{-1} at intervals of 20 km s^{-1} .

3.5.4 NGC 3870

NGC 3870 is one of the non-NFGS galaxies. It is a blue-sequence S0 galaxy in the Ursa Major group. The CO(1–0) emission is very weak, hence the channel maps (Figure 3.9) are noisy. Masking the channels based on the velocity map helps bring out the signal more in the velocity-integrated map (Figure 3.10). There is a clump of CO emission in the north-eastern corner of the map that may be associated with an optical (about 21" away from the center of the galaxy first identified by Barbieri et al. (1979)), but the signal-to-noise is too weak to say whether the CO is detected there. The same feature can be seen in the 8 μ m image. There are no known companions for NGC 3870.

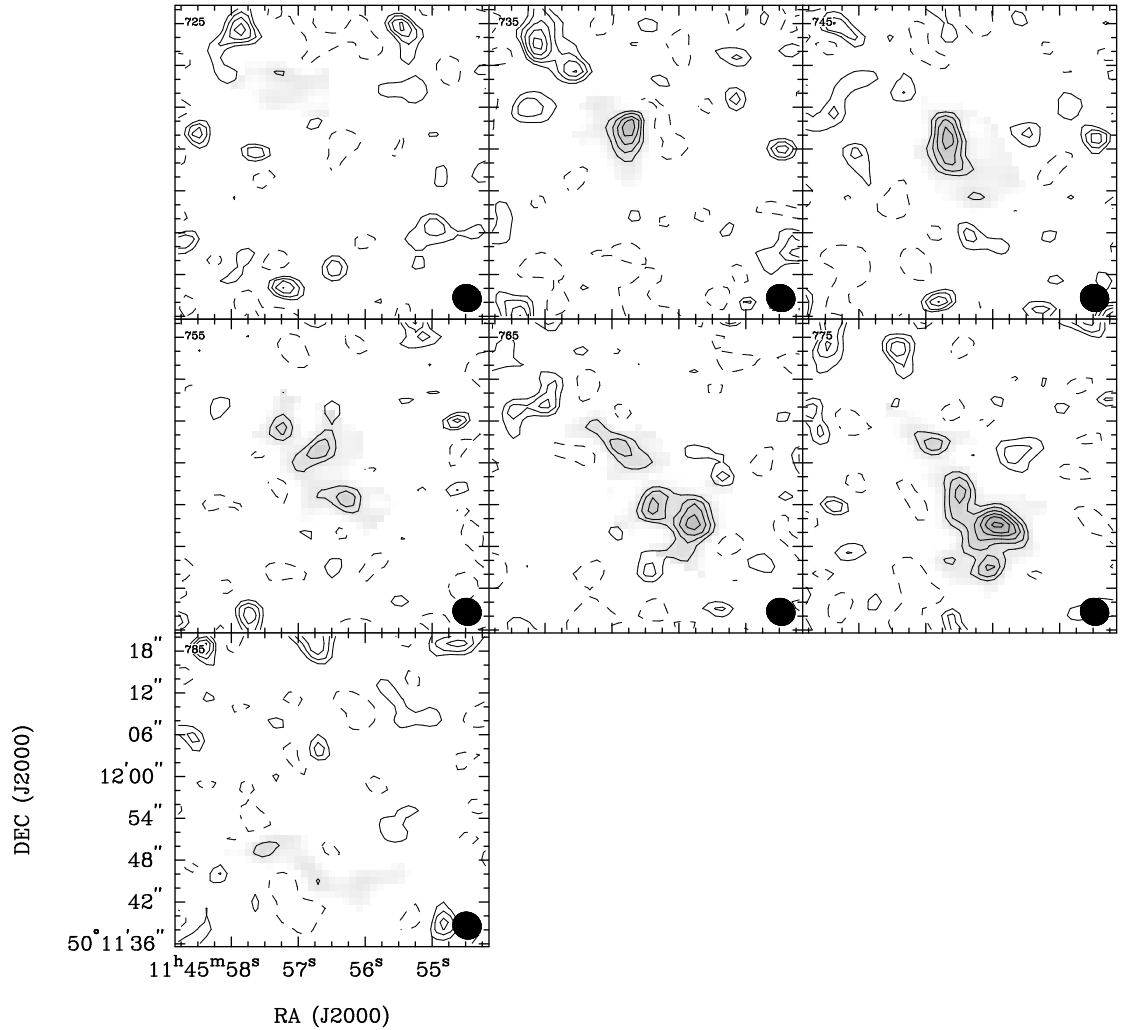


Figure 3.9: Channel maps of CO(1–0) emission for NGC 3870. Because of the extremely low S/N of this source, the greyscale only highlights emission from the galaxy (based on rotation-curve masking) while the contours include the noise. Contour levels are $-1, 1, 2, 2.5, 3, 3.5, 4$ times the noise in each channel (13 mJy beam^{-1}). Heliocentric velocity of each panel in km s^{-1} is indicated in the upper left; the beam is shown in the lower right corner.

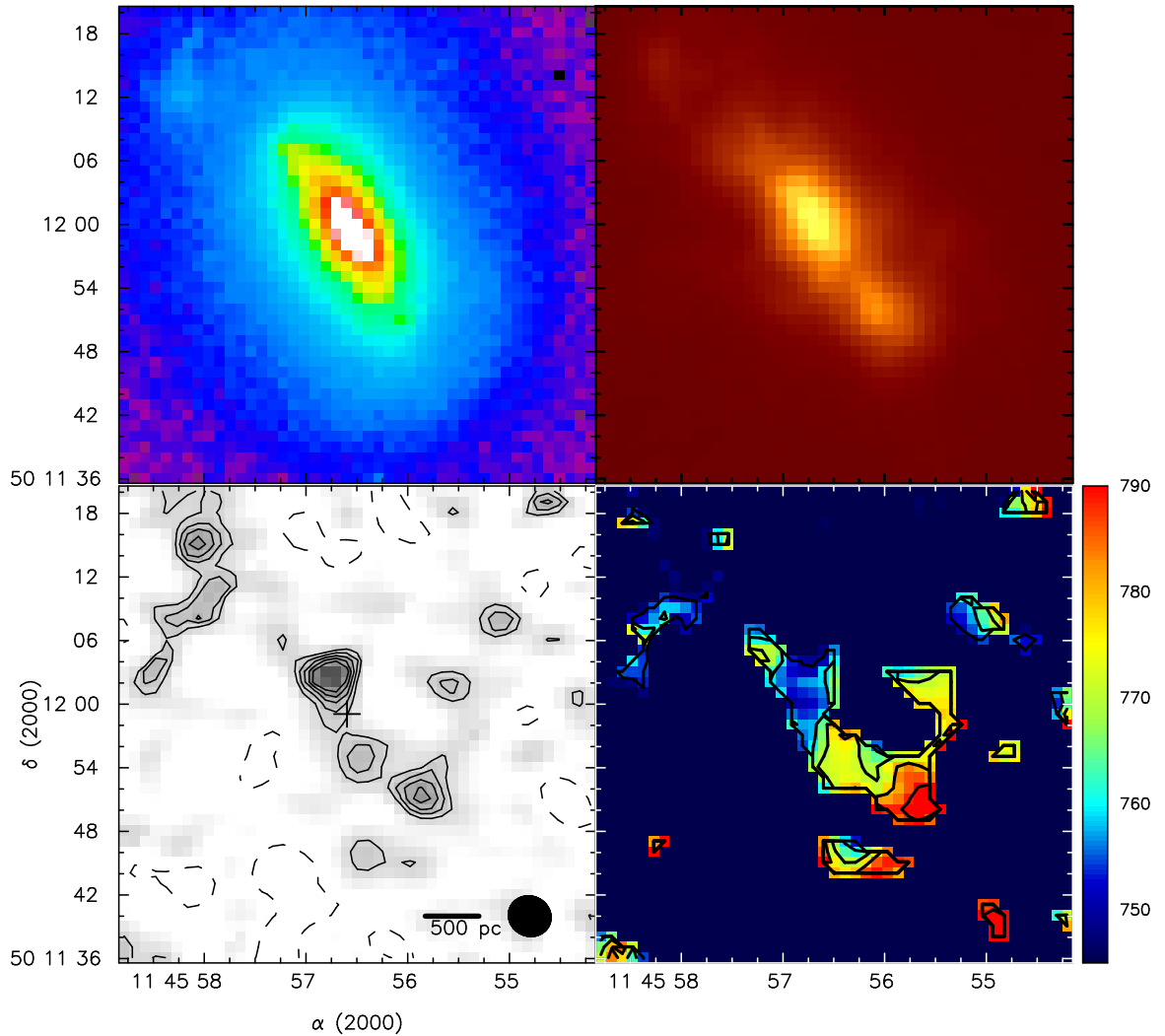


Figure 3.10: NGC 3870: (a) SDSS r -band image. (b) *Spitzer* IRAC $8\mu\text{m}$ image, with stellar emission subtracted following Pahre et al. (2004b). (c) Velocity-integrated CO(1–0) emission (contours and greyscale). Contour levels start at 2σ and are spaced in steps of 0.5σ ($\sigma = 0.32 \text{ Jy km s}^{-1}$); the cross marks the optical nucleus from SDSS. (d) CO(1–0) velocity field, with contours ranging from 750 to 790 km s^{-1} at intervals of 10 km s^{-1} .

3.5.5 NGC 4117

NGC 4117 is a red-sequence S0 galaxy possibly in the process of merging with a nearby companion (NGC 4118, 1'.5 away). The single-dish HI spectrum for the two galaxies (Chapter 2, Wei et al. 2010a) shows three overlapping peaks. The galaxy is highly inclined, which results in beam-smearing in the center of the galaxy, but its velocity field (Figure 3.12d) shows fairly regular rotation.

NGC 4117 is identified as an optical Seyfert 2 by emission line data. Mundell et al. (2009) find an increase in 8.4 GHz nuclear flux density over a timescale of seven years. Based on a color map made from WFPC2 F606W and NICMOS2 F160W imaging from the *HST*, Martini et al. (2003) classified NGC 4117 as a “loosely wound nuclear spiral”.

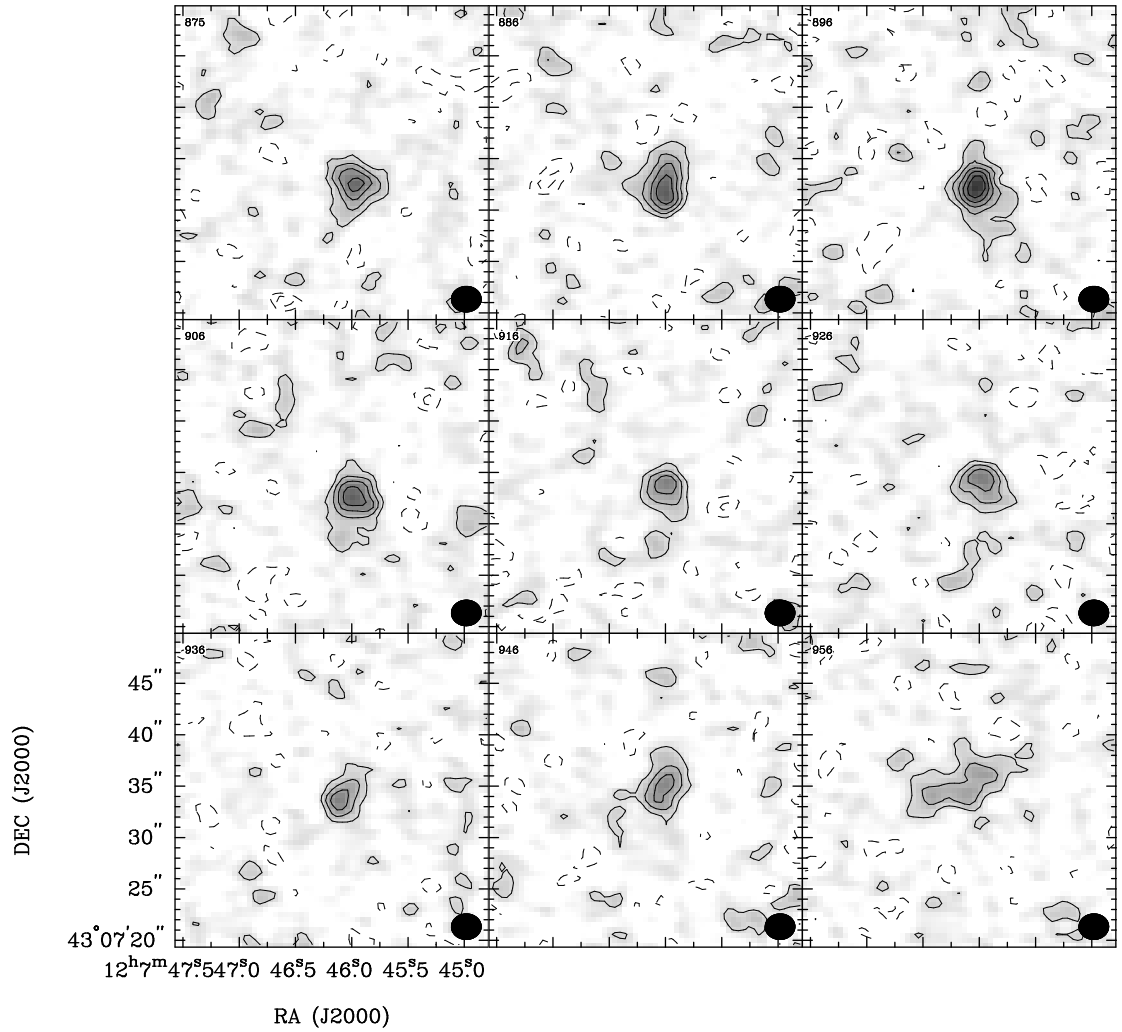


Figure 3.11: Channel maps of CO(1–0) emission (contours and greyscale) for NGC 4117. Contour levels are -3 , -1.5 , 1.5 , 3 , 4.5 , 6 , 7.5 times the rms in each channel ($8.5 \text{ mJy beam}^{-1}$). Heliocentric velocity of each panel in km s^{-1} is indicated in the upper left; the beam is shown in the lower right corner.

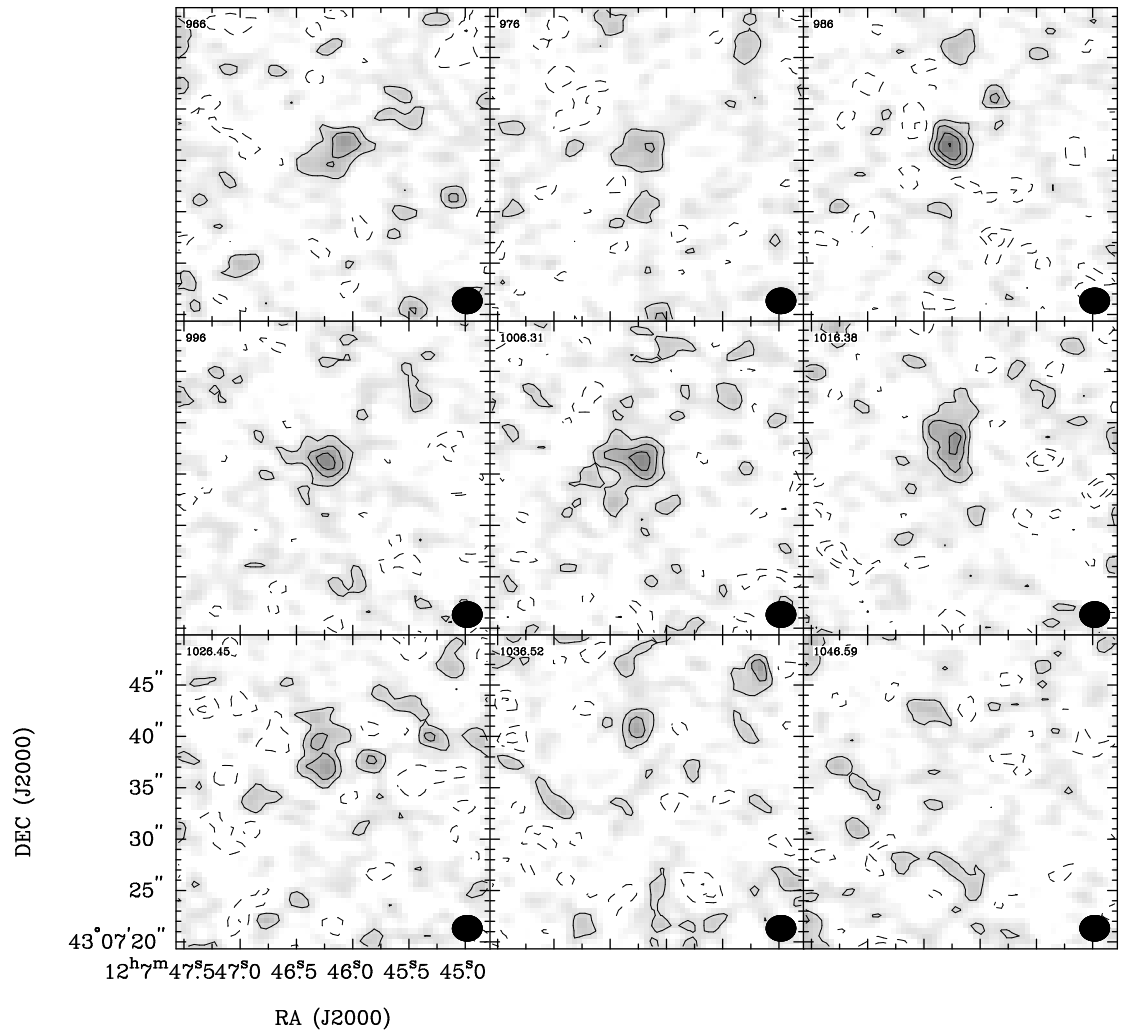


Figure 3.11: More CO(1–0) channel maps of NGC 4117.

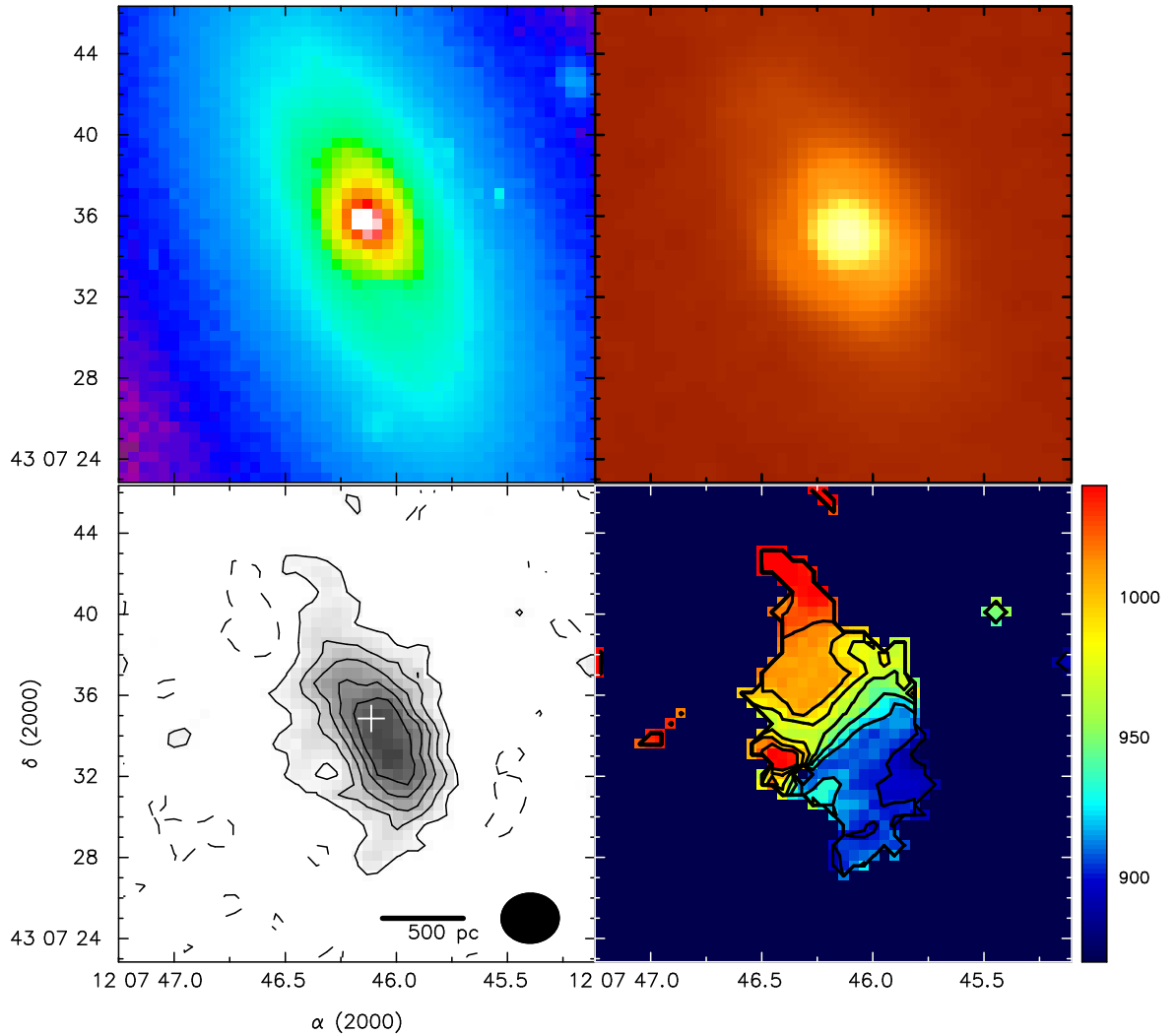


Figure 3.12: NGC 4117: (a) SDSS r -band image. (b) *Spitzer* IRAC $8\mu\text{m}$ image, with stellar emission subtracted following Pahre et al. (2004b). (c) Velocity-integrated CO(1–0) emission (contours and greyscale). Contour levels start at 2σ and are spaced in steps of 2σ ($\sigma = 0.3 \text{ Jy km s}^{-1}$); the cross marks the optical nucleus from SDSS. (d) CO(1–0) velocity field, with contours ranging from 880 to 1020 km s^{-1} at intervals of 20 km s^{-1} .

3.5.6 NGC 5173

NGC 5173 is an elliptical galaxy on the blue sequence. Kannappan & Fabricant (2001) identified the presence of counterrotating gas and stars in this galaxy. Based on asymmetries in stellar absorption line cross-correlation profiles for NGC 5173, KGB suggest that there may be an extended secondary stellar disk rotating with the gas, which may be the off-centered disk with blue condensations found by Vader & Vigroux (1991).

Based on its HI distribution, Knapp & Raimond (1984) suggest that NGC 5173 may have accreted its gas from a smaller satellite, which would explain the presence of counterrotating gas and stars in this galaxy. While much of the CO emission is regularly rotating (Figure 3.14d), there are asymmetries in the CO distribution that support the external accretion argument (Figure 3.14c).

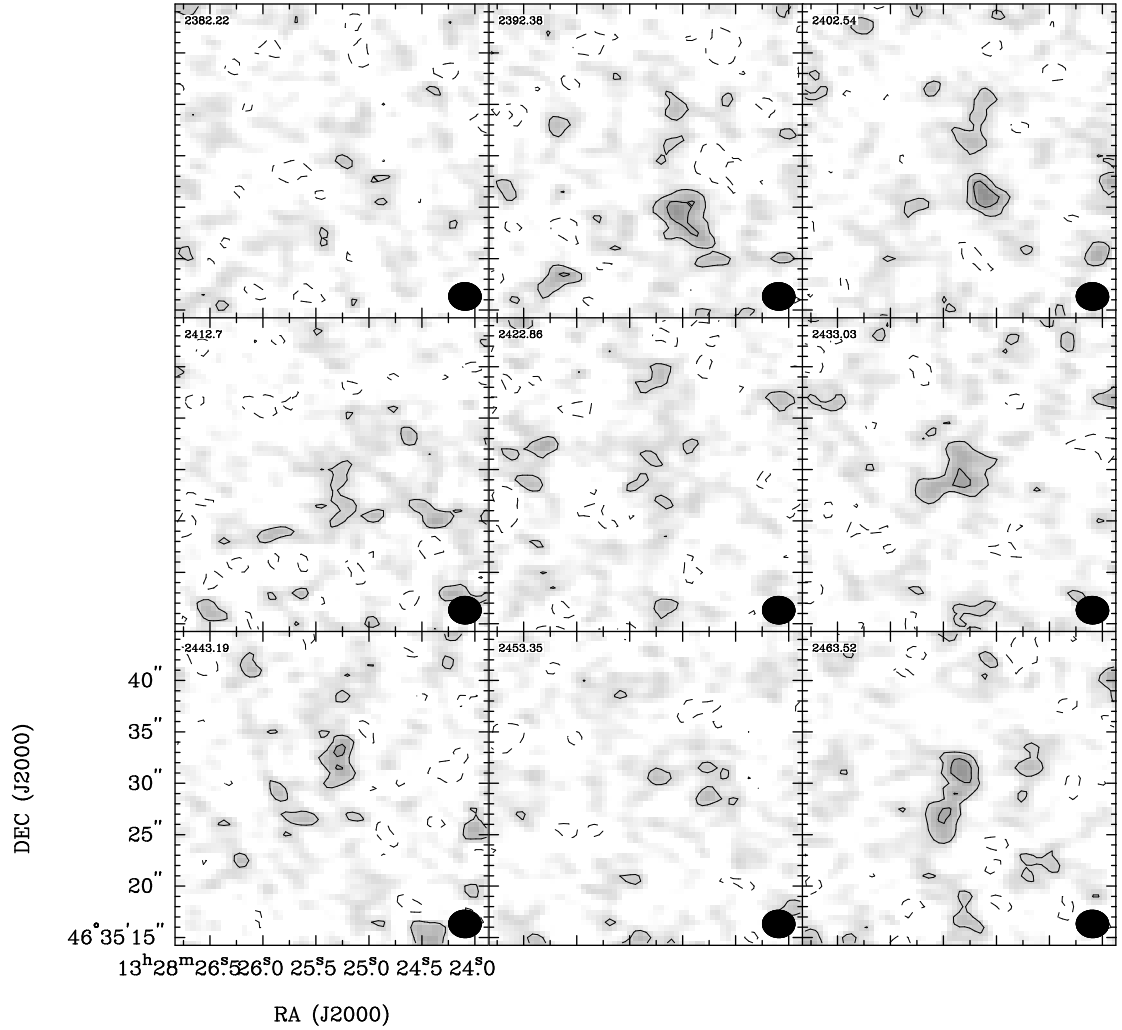


Figure 3.13: Channel maps of CO(1–0) emission (contours and greyscale) for NGC 5173. Contour levels are -3 , -1.5 , 1.5 , 3 times the rms in each channel ($7.3 \text{ mJy beam}^{-1}$). Heliocentric velocity of each panel in km s^{-1} is indicated in the upper left; the beam is shown in the lower right corner.

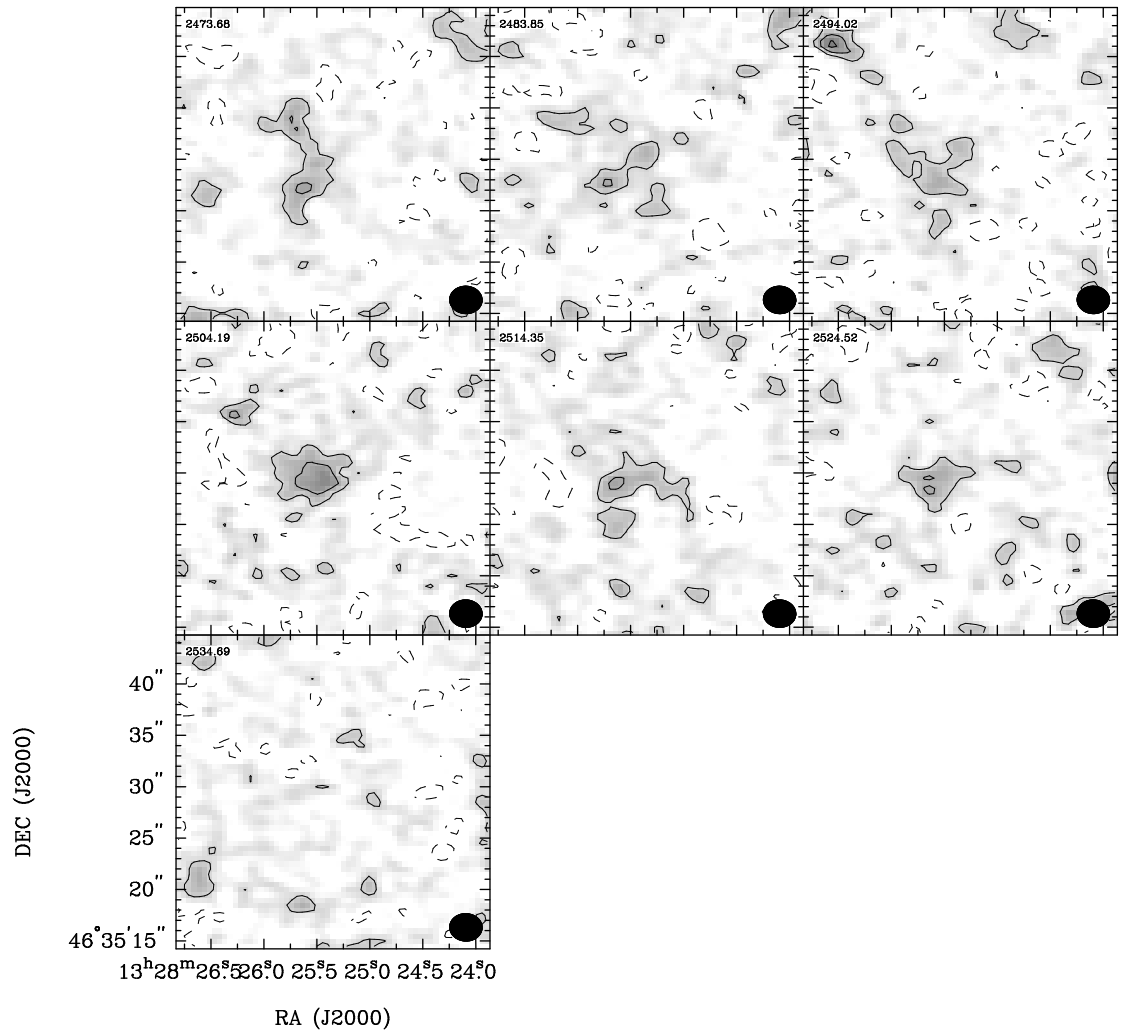


Figure 3.13: More CO(1–0) channel maps of NGC 5173.

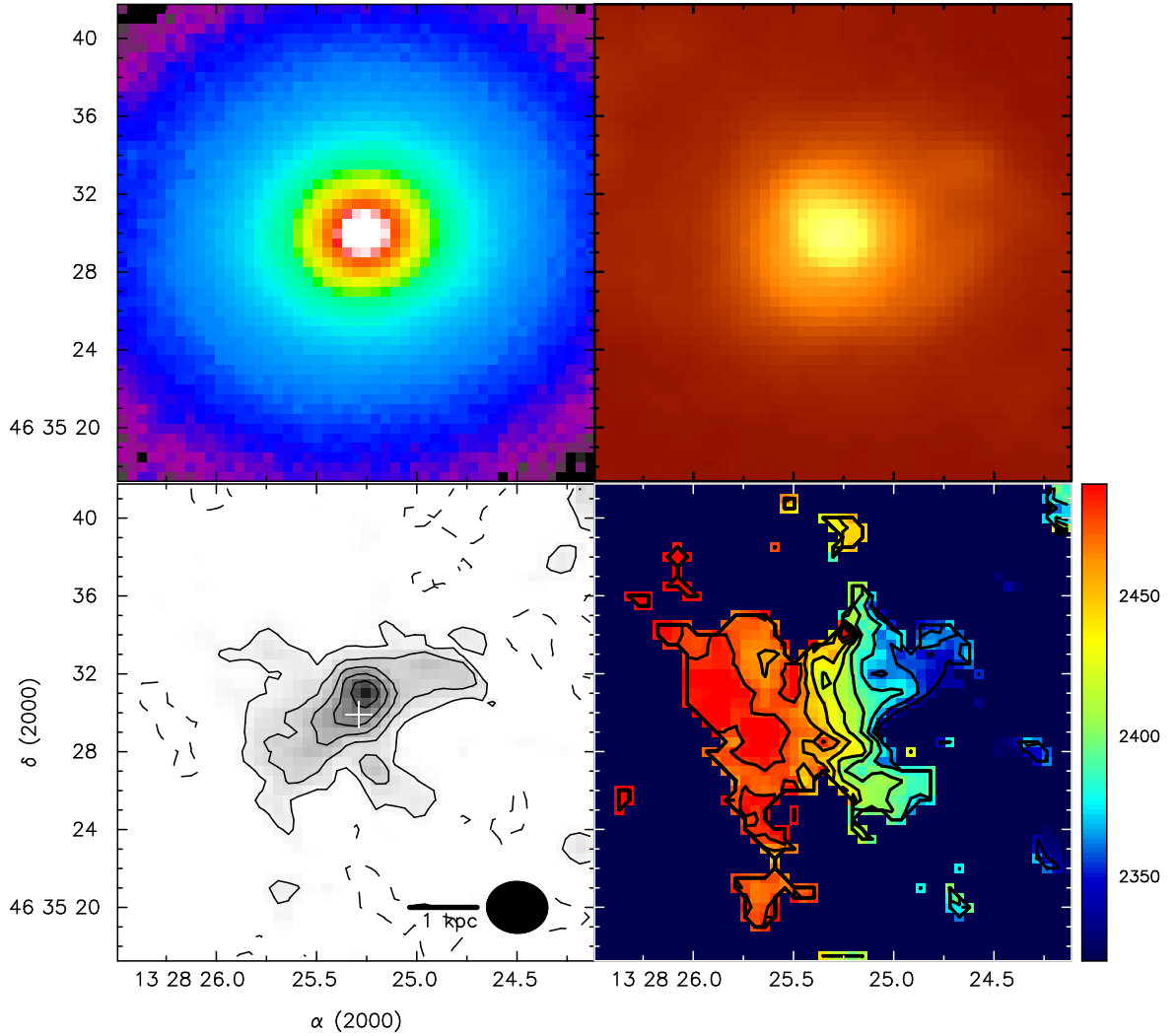


Figure 3.14: NGC 5173: (a) SDSS r -band image. (b) *Spitzer* IRAC $8\mu\text{m}$ image, with stellar emission subtracted following Pahre et al. (2004b). (c) Velocity-integrated CO(1–0) emission (contours and greyscale). Contour levels start at 2σ and are spaced in steps of 1σ ($\sigma = 0.25 \text{ Jy km s}^{-1}$); the cross marks the optical nucleus from SDSS. (d) CO(1–0) velocity field, with contours ranging from 2340 to 2480 km s^{-1} at intervals of 20 km s^{-1} .

3.5.7 NGC 5338

NGC 5338 is a red-sequence S0 that might actually be an extremely dust-obscured, star-forming early-type galaxy. It has surprisingly high metallicity ($12 + \log(\text{O}/\text{H}) = 8.94$; Peeples et al. 2008) for its mass ($M_* = 7.2 \times 10^8 M_\odot$), and Erwin & Sparke (2003) detected dust lanes as well as complex, asymmetric blue regions at its center using *HST* WFPC2 F606W imaging. The CO(1–0) emission (Figure 3.16d) is fairly regular and appears well correlated with the optical and $8\mu\text{m}$ PAH emission (Figure 3.16a, b), although the optical and CO central peaks are offset by $\sim 2''$. The CO(1–0) velocity map shows little regular rotation (Figure 3.16d).

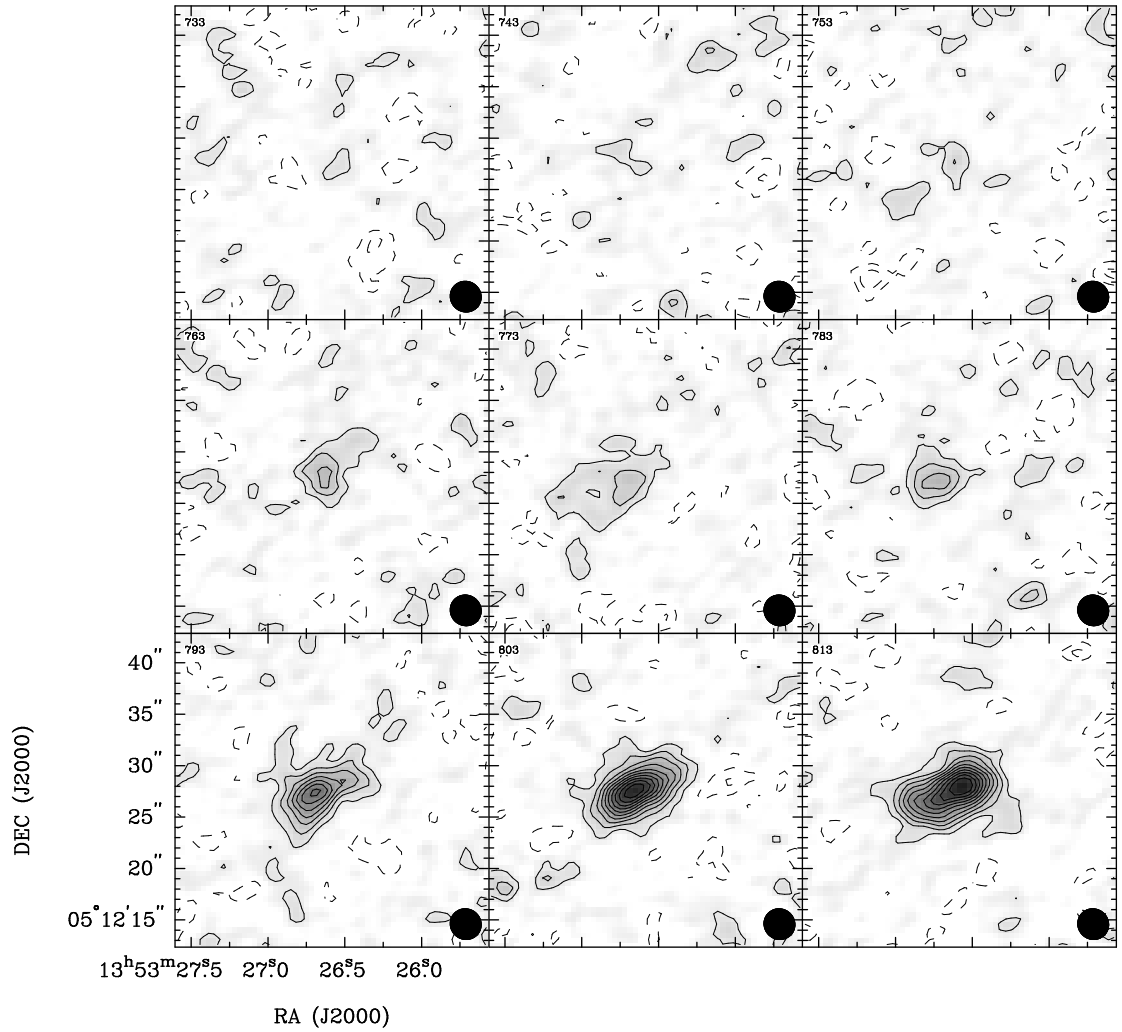


Figure 3.15: Channel maps of CO(1–0) emission (contours and greyscale) for NGC 5338. Contour levels are $-3, -1.5, 1.5, 3, 4.5, 6, 7.5, 9, 10.5, 12, 13.5$ times the rms in each channel ($7.8 \text{ mJy beam}^{-1}$). Heliocentric velocity of each panel in km s^{-1} is indicated in the upper left; the beam is shown in the lower right corner.

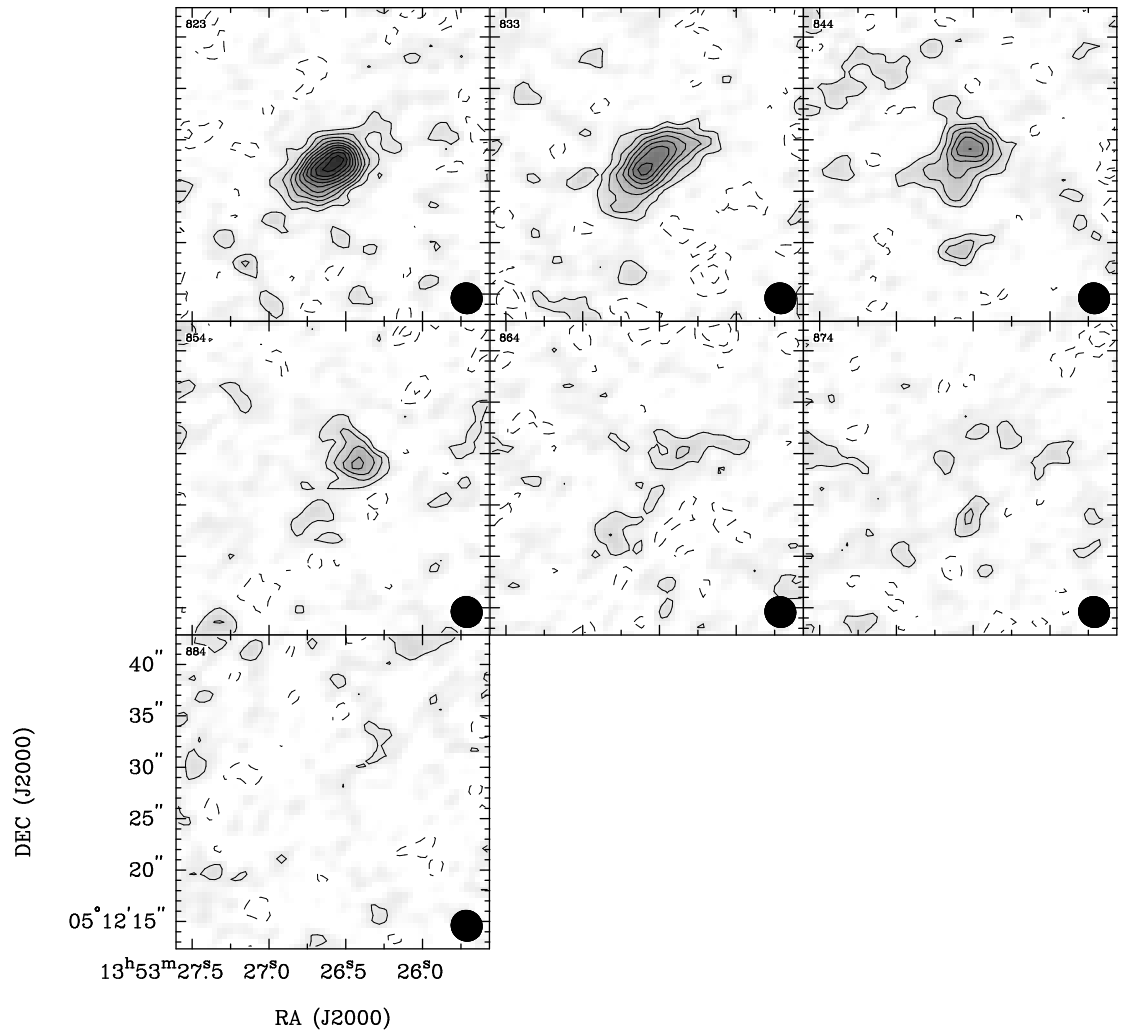


Figure 3.15: More CO(1–0) channel maps of NGC 5338.

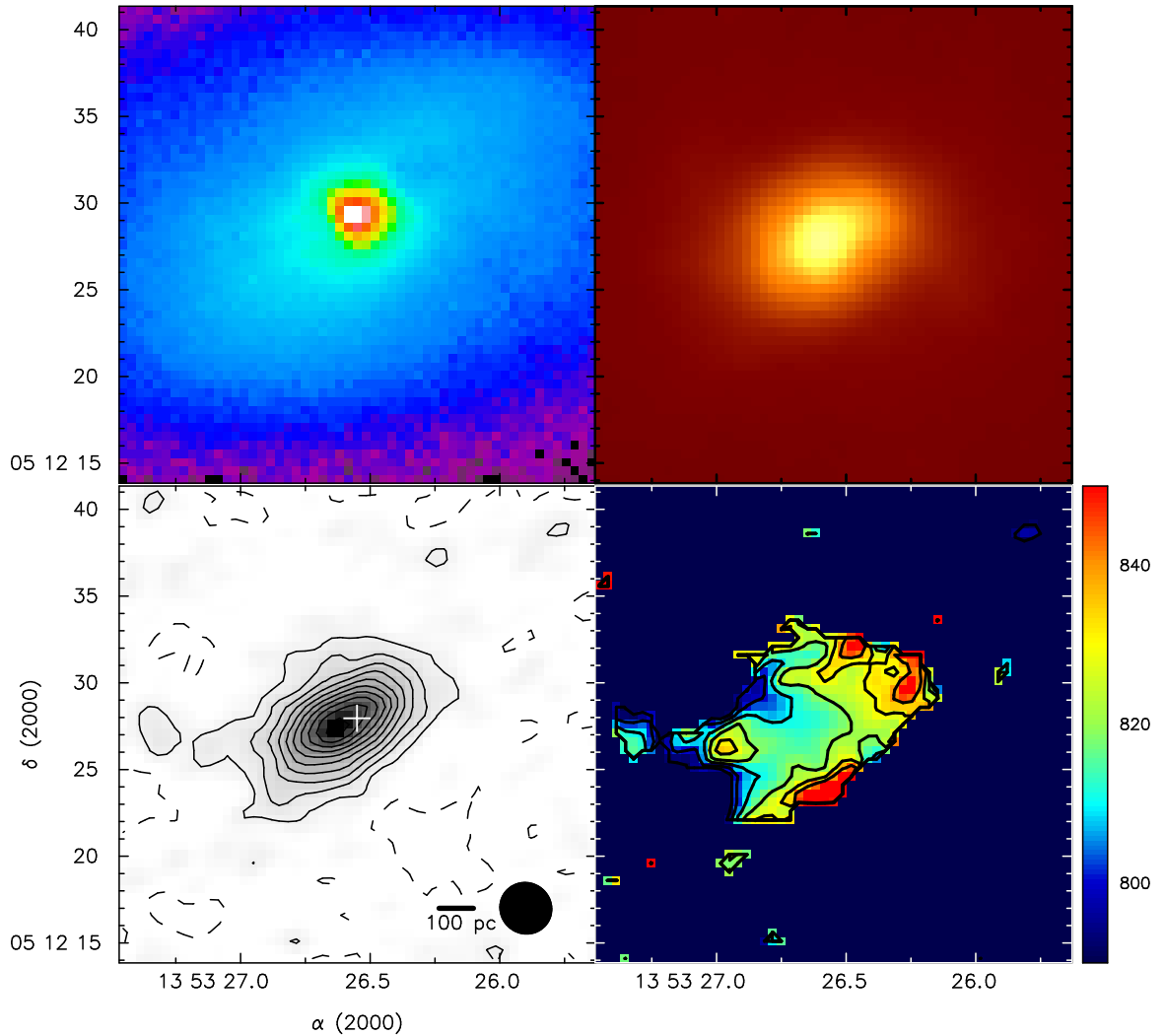


Figure 3.16: NGC 5338: (a) SDSS r -band image. (b) *Spitzer* IRAC $8\mu\text{m}$ image, with stellar emission subtracted following Pahre et al. (2004b). (c) Velocity-integrated CO(1–0) emission (contours and greyscale). Contour levels start at 3σ and are spaced in steps of 3σ ($\sigma = 0.23 \text{ Jy km s}^{-1}$); the cross marks the optical nucleus from SDSS. (d) CO(1–0) velocity field, with contours ranging from 790 to 850 km s^{-1} at intervals of 10 km s^{-1} .

3.5.8 UGC 12265N

UGC 12265N is a blue-sequence S0 galaxy that is perhaps in the process of merging with its companion, UGC 12265S (1' away). A preliminary VLA HI map for these two galaxies indicates that the smaller companion contains 3/4 of the total HI for the system. The companion is just outside the 100'' half-power beam width of the 6-meter antennas, and we do detect some CO(1–0) emission from UGC 12265S at the edge of the map (outside the field displayed in Figure 3.18). The CO in UGC 12265N appears to be a regularly rotating disk that is well-correlated with the 8 μ m PAH emission (Figure 3.18b, d).

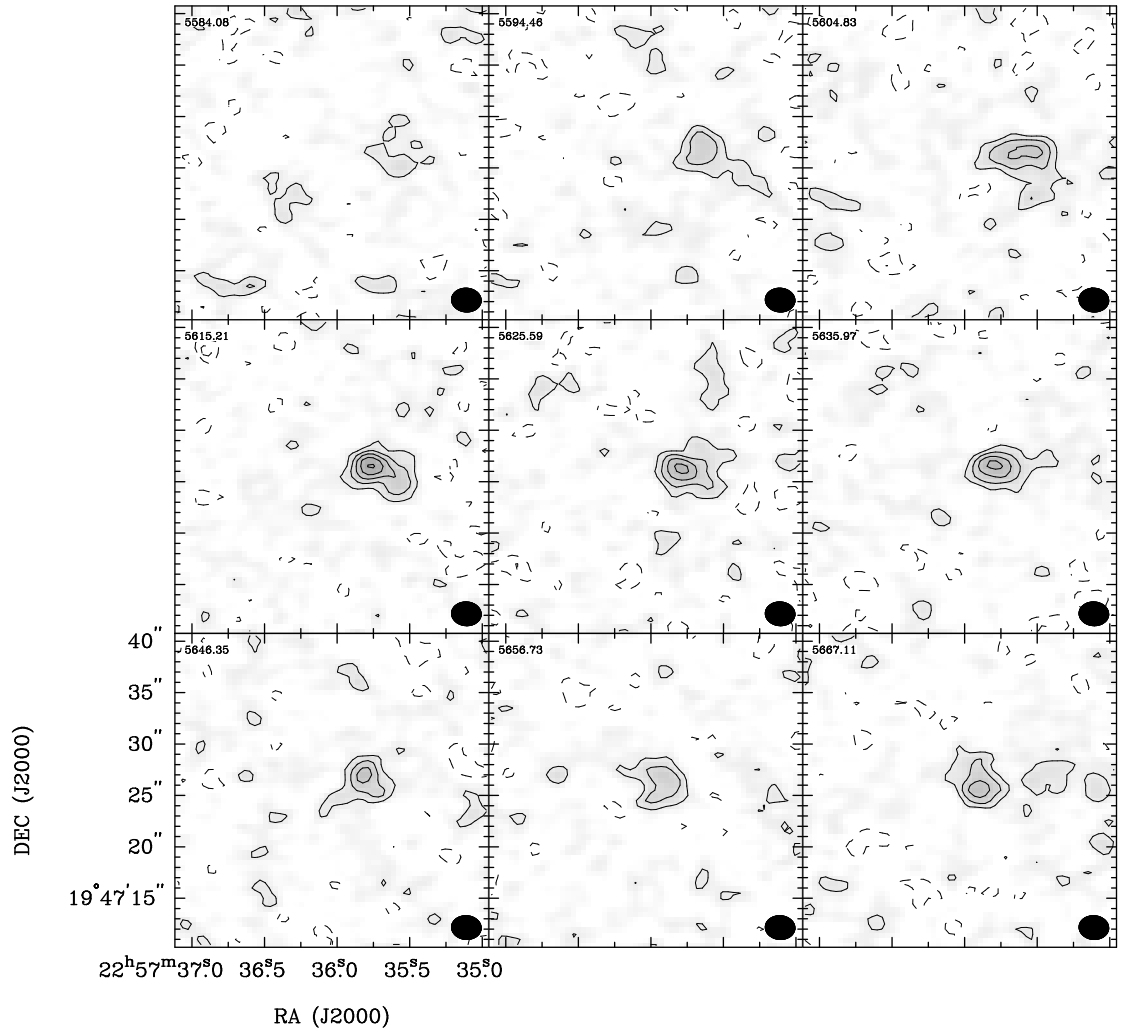


Figure 3.17: Channel maps of CO(1–0) emission (contours and greyscale) for UGC 12265N. Contour levels are -3 , -1.5 , 1.5 , 3 , 4.5 , 6 times the rms in each channel ($7.8 \text{ mJy beam}^{-1}$). Heliocentric velocity of each panel in km s^{-1} is indicated in the upper left; the beam is shown in the lower right corner.

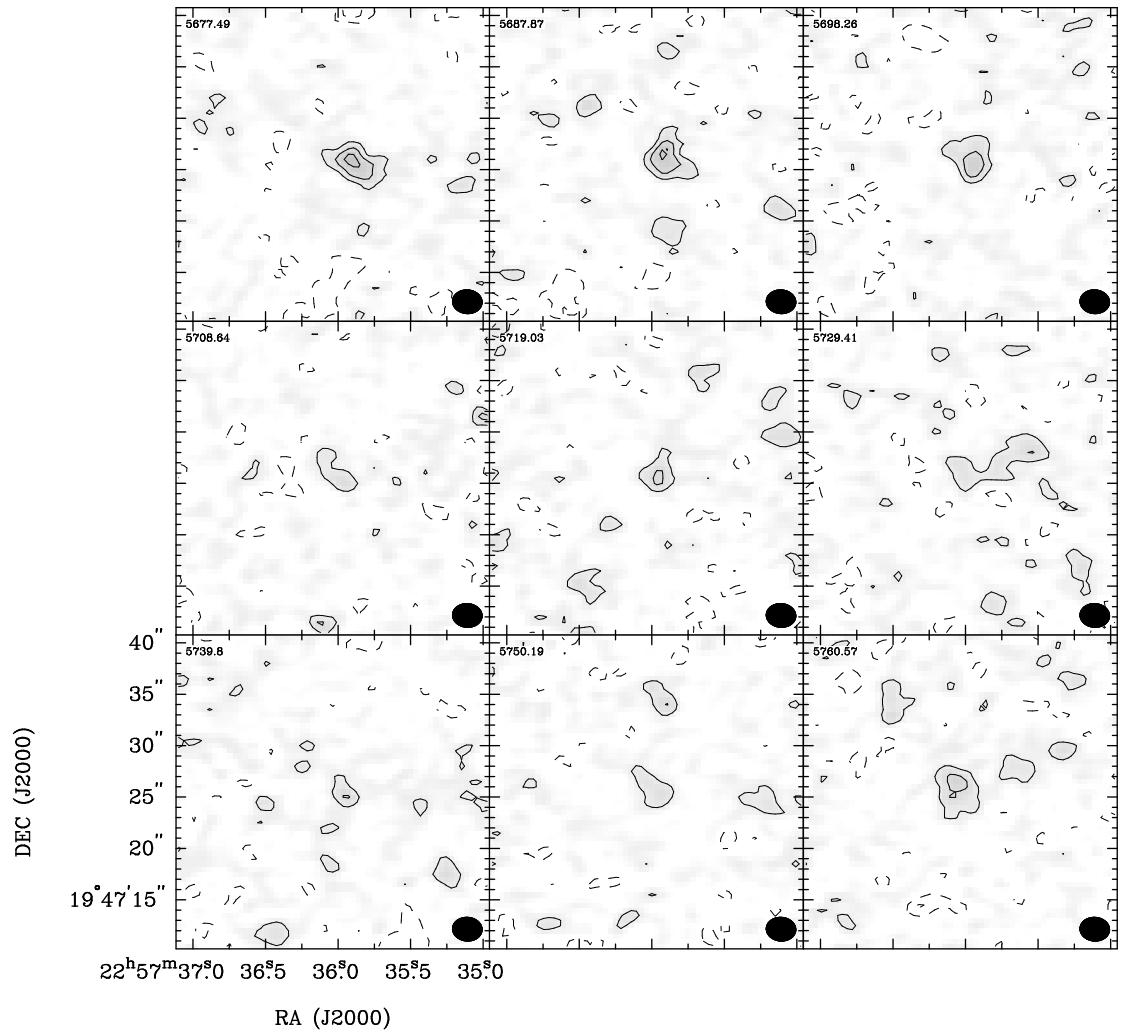


Figure 3.17: More CO(1–0) channel maps of UGC 12265N.

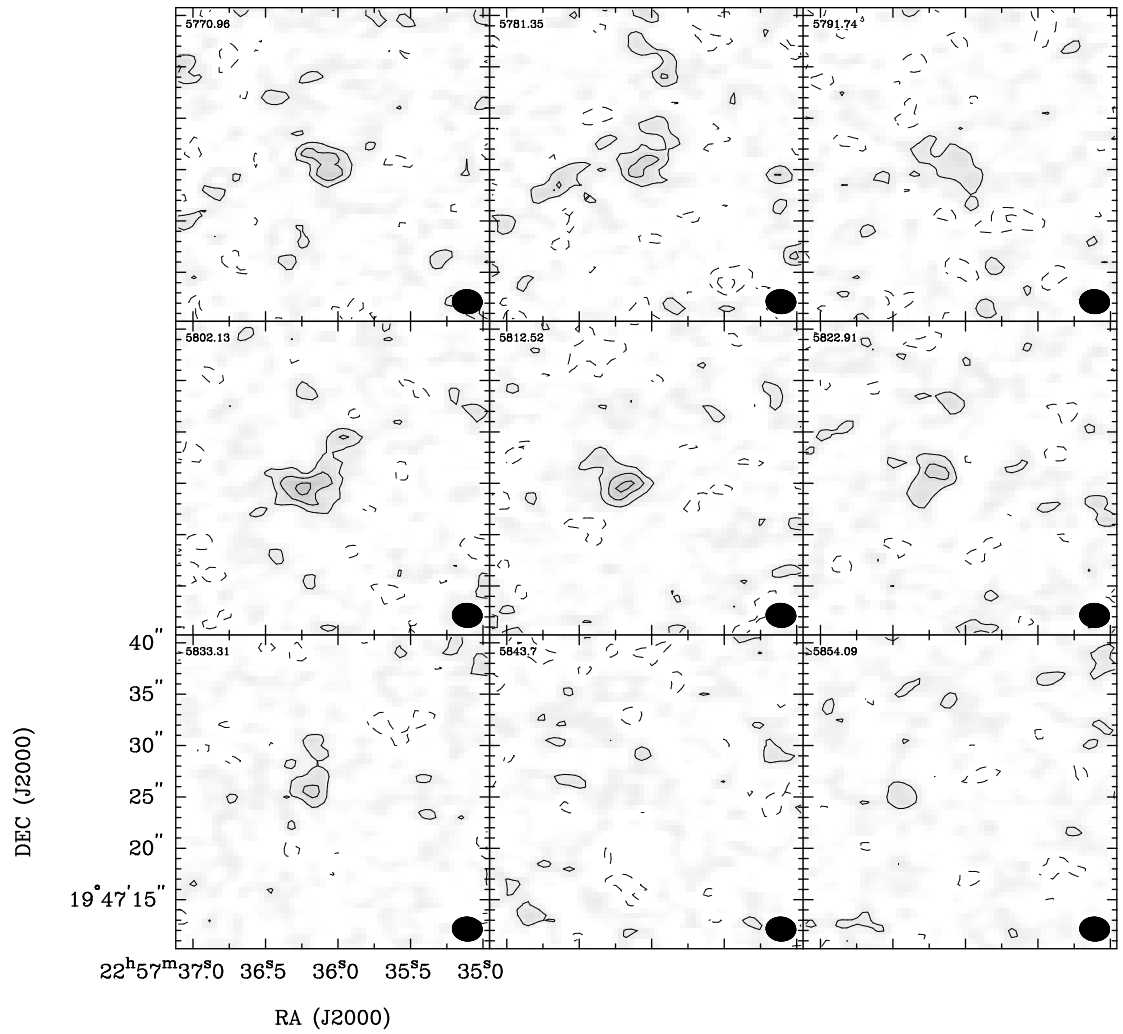


Figure 3.17: More CO(1-0) channel maps of UGC 12265N.

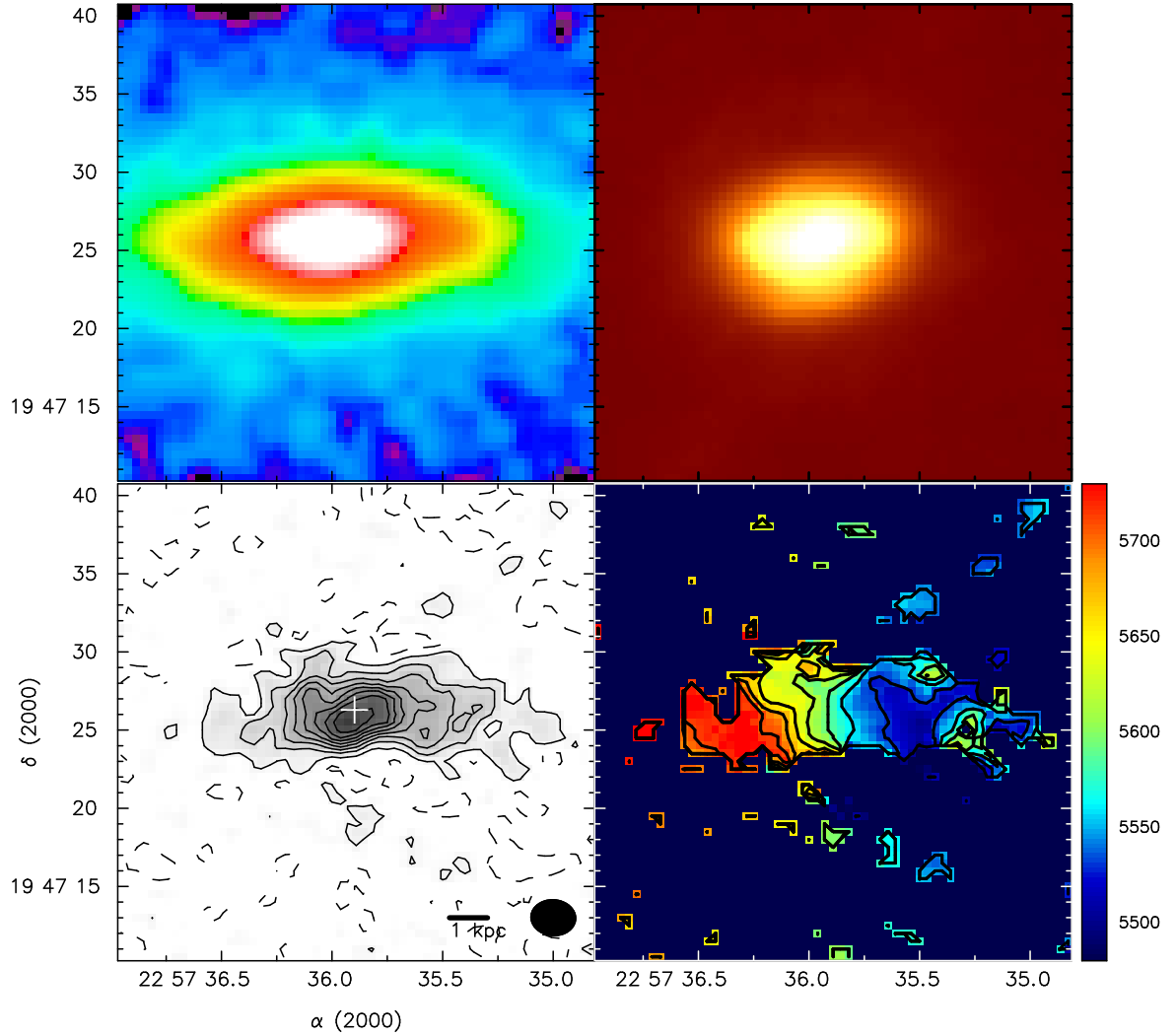


Figure 3.18: UGC 12265N: (a) DSS *R*-band image (no SDSS observations were available). (b) *Spitzer* IRAC $8\mu\text{m}$ image, with stellar emission subtracted following Pahre et al. (2004b). (c) Velocity-integrated CO(1–0) emission (contours and greyscale). Contour levels start at 2σ and are spaced in steps of 3σ ($\sigma = 0.13 \text{ Jy km s}^{-1}$); the cross marks the optical nucleus from DSS. (d) CO(1–0) velocity field, with contours ranging from 5500 to 5710 km s^{-1} at intervals of 30 km s^{-1} .

3.5.9 UGC 6003

UGC 6003 is a blue-sequence S0/a galaxy with a central starburst. The CO(1–0) emission observed by CARMA is very centrally concentrated – within $0.25R_{25}$ (Figure 3.20c). The velocity map shows very little rotation in the CO (Figure 3.20d).

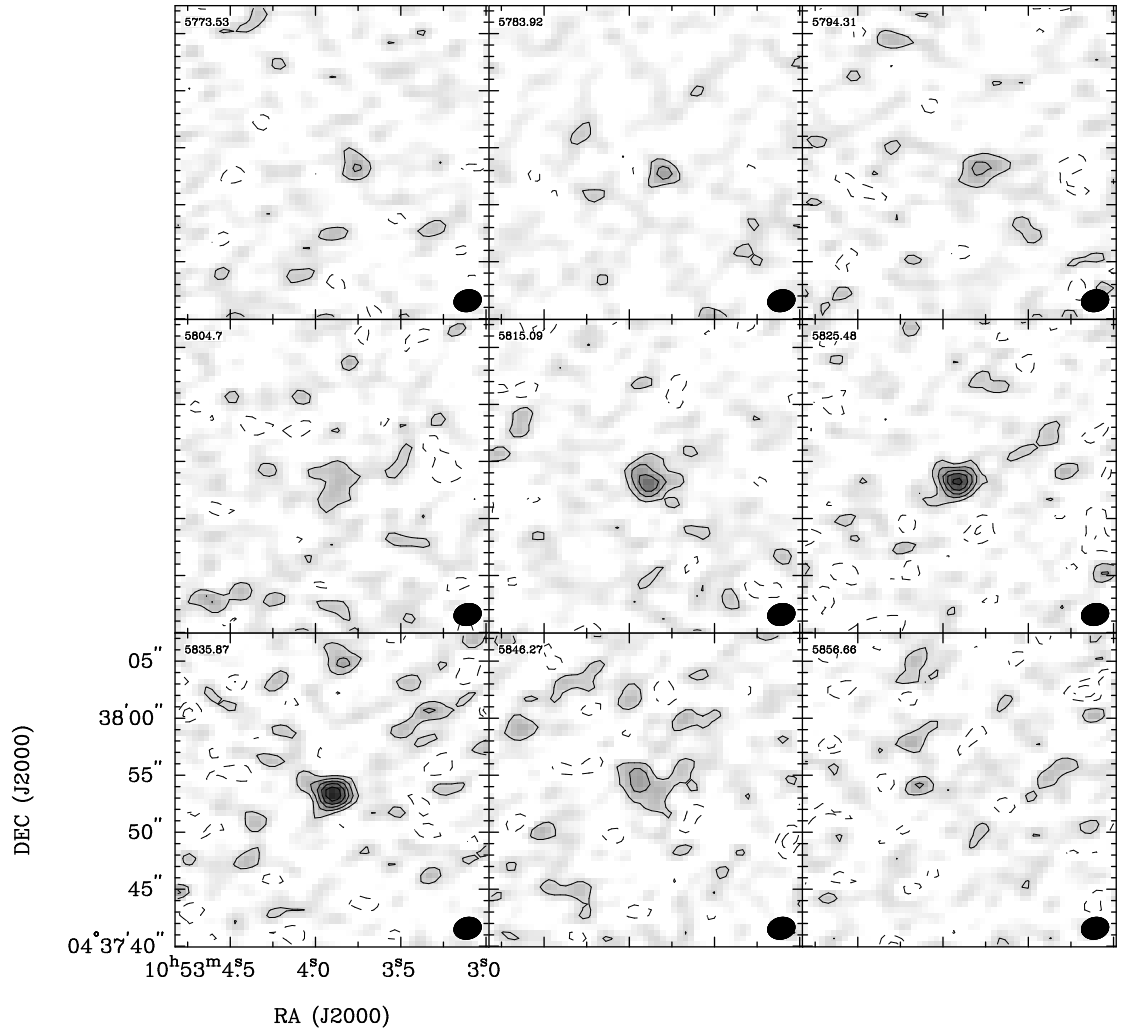


Figure 3.19: Channel maps of CO(1–0) emission (contours and greyscale) for UGC 6003. Contour levels are -3 , -1.5 , 1.5 , 3 , 4.5 , 6 , 7.5 times the rms in each channel $7.8 \text{ mJy beam}^{-1}$). Helio-centric velocity of each panel in km s^{-1} is indicated in the upper left; the beam is shown in the lower right corner.

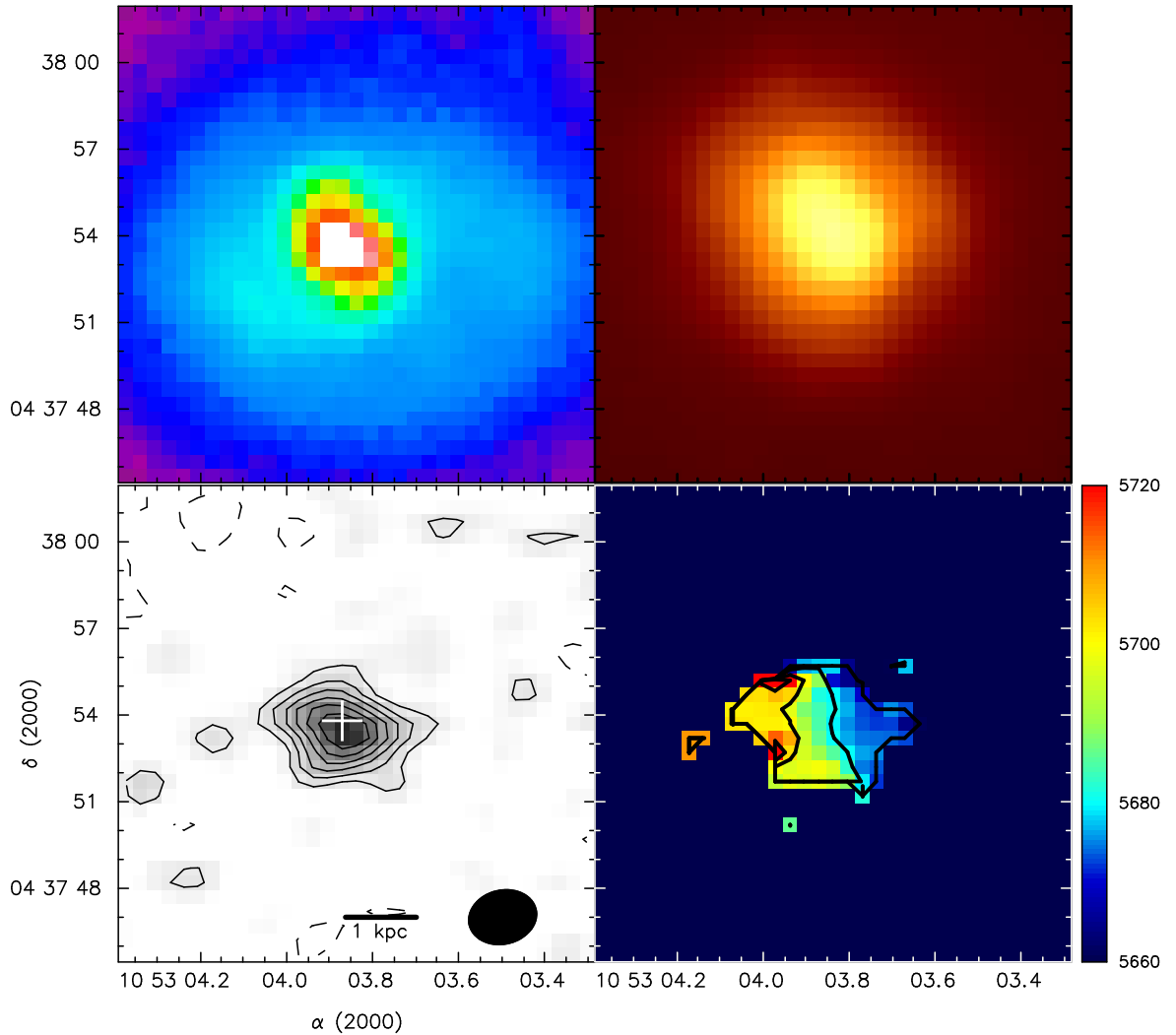


Figure 3.20: UGC 6003: (a) SDSS r -band image. (b) *Spitzer* IRAC $8\mu\text{m}$ image, with stellar emission subtracted following Pahre et al. (2004b). (c) Velocity-integrated CO(1–0) emission (contours and greyscale). Contour levels start at 2σ and are spaced in steps of 1σ ($\sigma = 0.34 \text{ Jy km s}^{-1}$); the cross marks the optical nucleus from SDSS. (d) CO(1–0) velocity field, with contours ranging from 5660 to 5720 km s^{-1} at intervals of 20 km s^{-1} .

3.5.10 UGC 6570

UGC 6570 is a mid-sequence S0/a galaxy identified by Kannappan & Fabricant (2001) as having counterrotating gas and stars in different planes. Of the four counterrotating gas/star E/S0s studied by KGB, UGC 6570 is the only one that shows no sign of a secondary stellar component. KGB argue that the stellar absorption line cross-correlation profiles show signs of a strong warp/distortion, suggesting that the gas has not had time to form stars after a recent interaction.

The CO(1–0) emission from UGC 6570 (Figure 3.22c) is very centrally concentrated. There is no evidence for regular rotation (Figure 3.22d), consistent with the hypothesis that the gas arrived recently and has not had time to settle and form stars. Higher resolution and higher signal-to-noise CO observations are needed to confirm our findings.

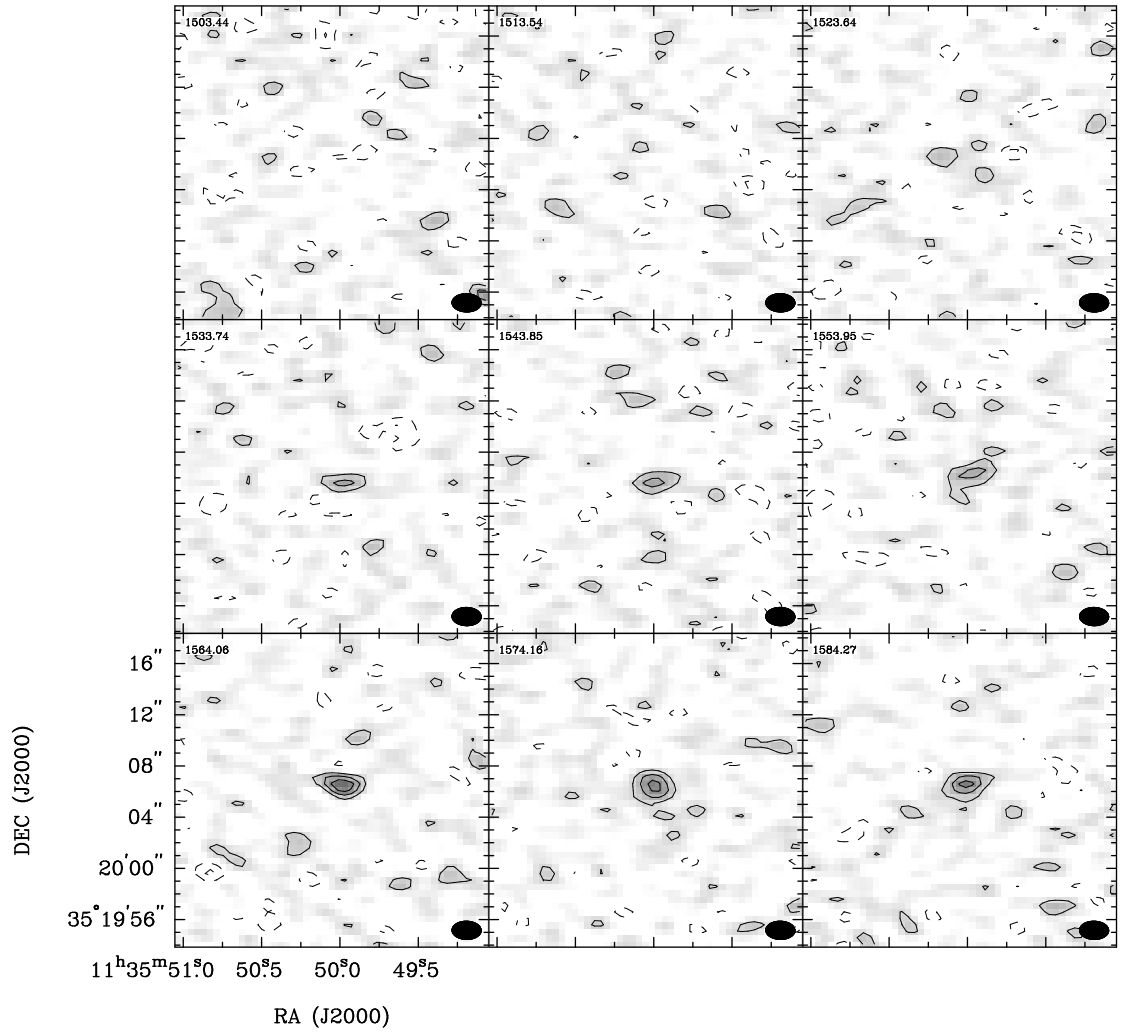


Figure 3.21: Channel maps of CO(1–0) emission (contours and greyscale) for UGC 6570. Contour levels are -3 , -1.5 , 1.5 , 3 , 4.5 , 6 times the rms in each channel ($14.4 \text{ mJy beam}^{-1}$). Heliocentric velocity of each panel in km s^{-1} is indicated in the upper left; the beam is shown in the lower right corner.

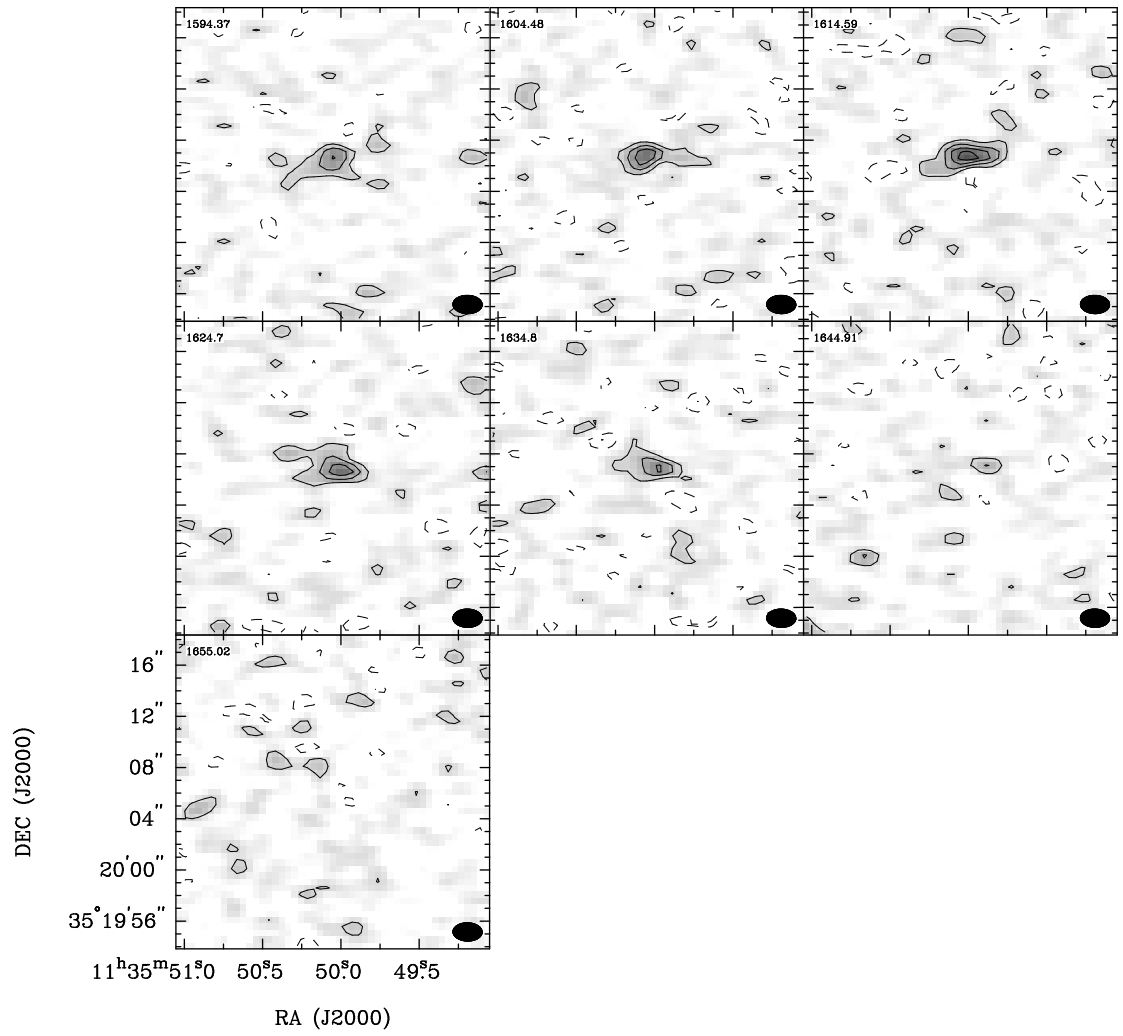


Figure 3.21: More CO(1-0) channel maps of UGC 6570.

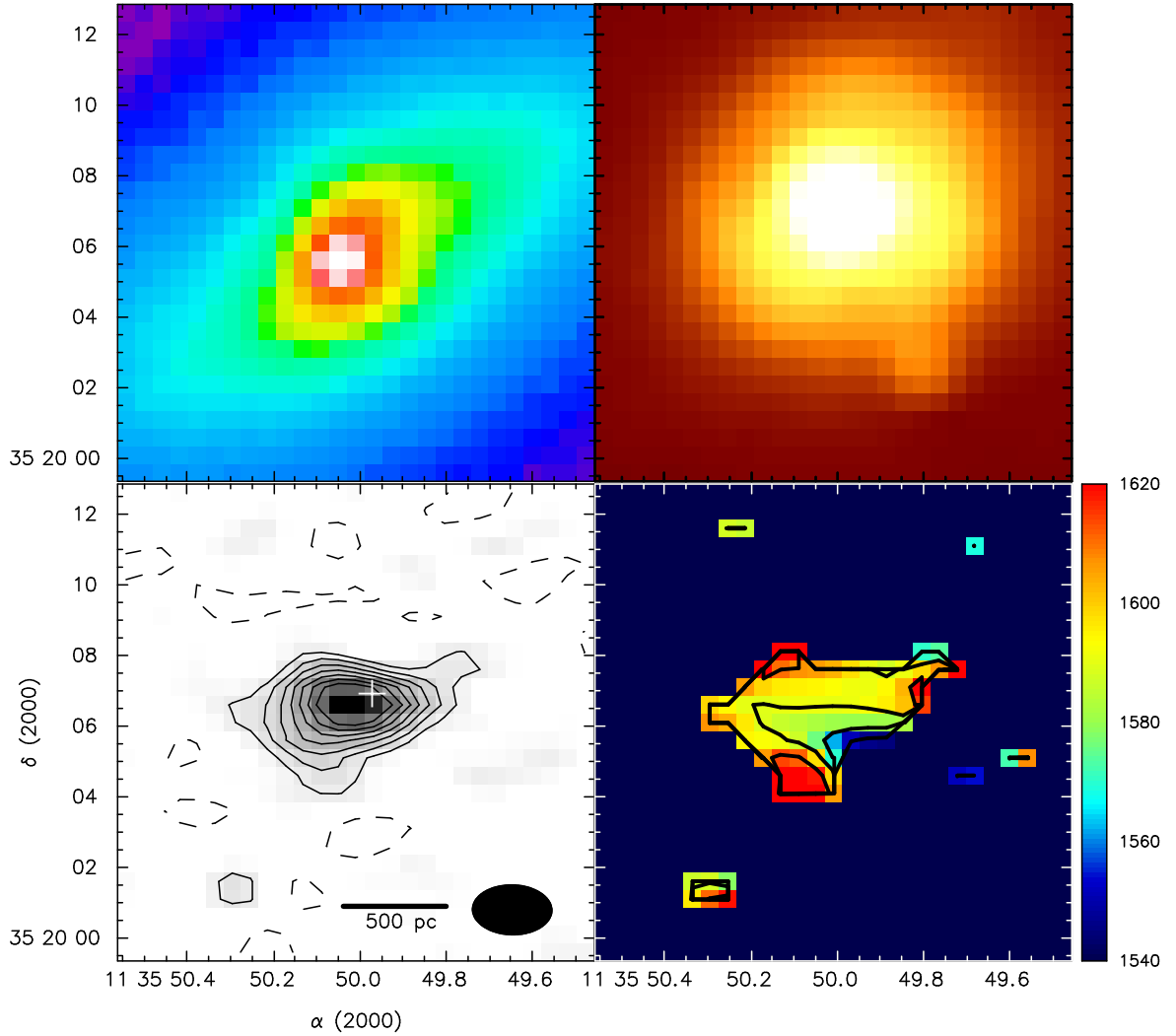


Figure 3.22: UGC 6570: (a) SDSS r -band image. (b) *Spitzer* IRAC $8\mu\text{m}$ image, with stellar emission subtracted following Pahre et al. (2004b). (c) Velocity-integrated CO(1-0) emission (contours and greyscale). Contour levels start at 2σ and are spaced in steps of 1σ ($\sigma = 0.65 \text{ Jy km s}^{-1}$); the cross marks the optical nucleus from SDSS. (d) CO(1-0) velocity field, with contours ranging from 1550 to 1610 km s^{-1} at intervals of 20 km s^{-1} .

3.5.11 UGC 6805

UGC 6805 is an S0 galaxy on the blue sequence. It appears to have two nuclei in the SDSS *R*-band image, but otherwise the light distribution is quite regular. Based on the distribution and velocity field of the CO(1–0) emission (Figure 3.24c, d), the gas appears to be in a rotating ring around the center of the galaxy, although the far side of the ring is not detected in CO. This structure is quite different from the $8\mu\text{m}$ PAH emission, which has similar resolution and a light distribution like the optical image. The double nuclei in the optical image correspond to the depression in the CO “ring.” This galaxy may be a merger remnant based on its optical double nuclei, but the regularity of the CO rotation suggests that it is fairly settled.

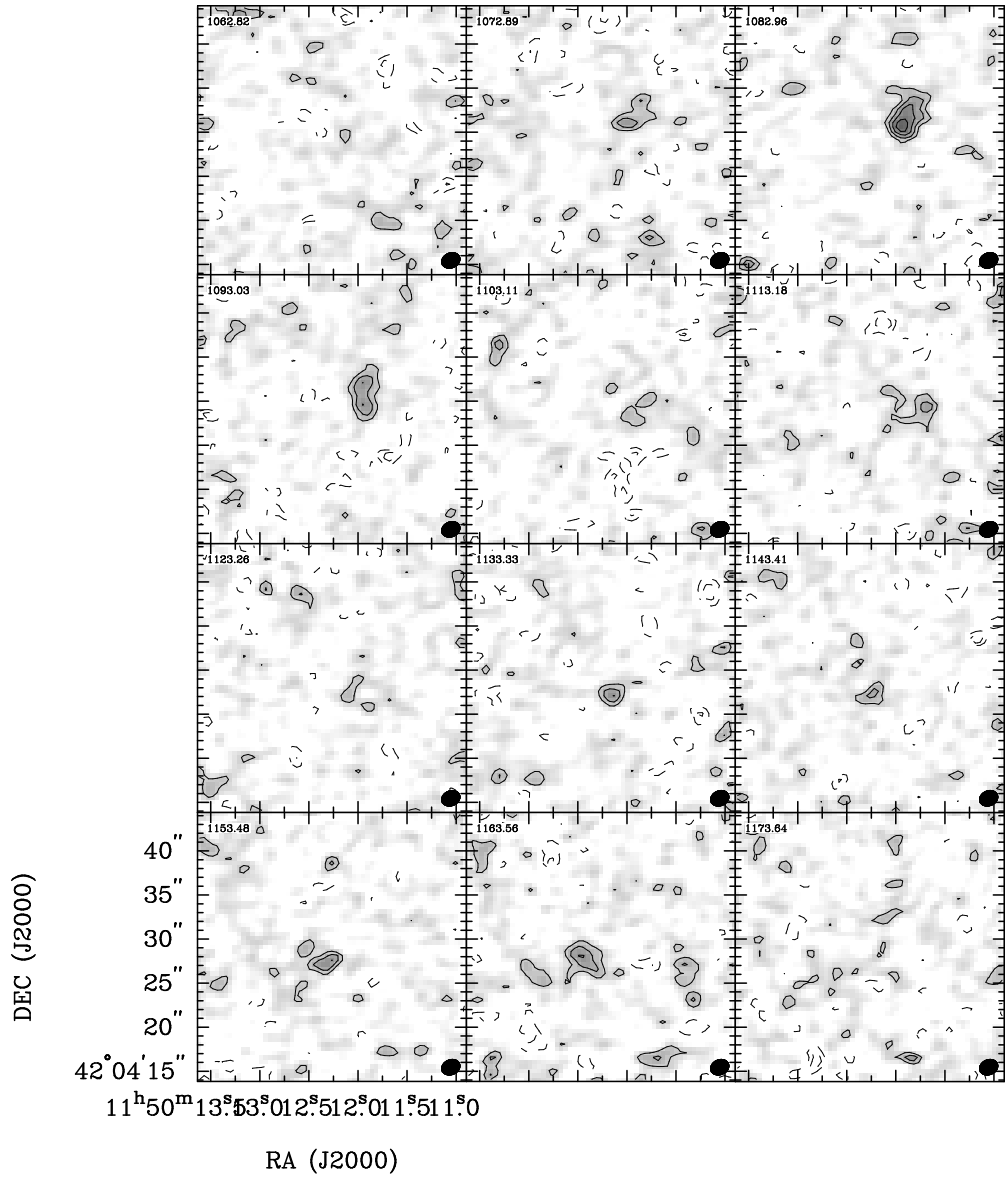


Figure 3.23: Channel maps of CO(1–0) emission (contours and greyscale) for UGC 6805. Contour levels are -2.5 , -1.5 , 1.5 , 2.5 , 3.5 , 4.5 , times the rms in each channel $9.5 \text{ mJy beam}^{-1}$). Heliocentric velocity of each panel in km s^{-1} is indicated in the upper left; the beam is shown in the lower right corner.

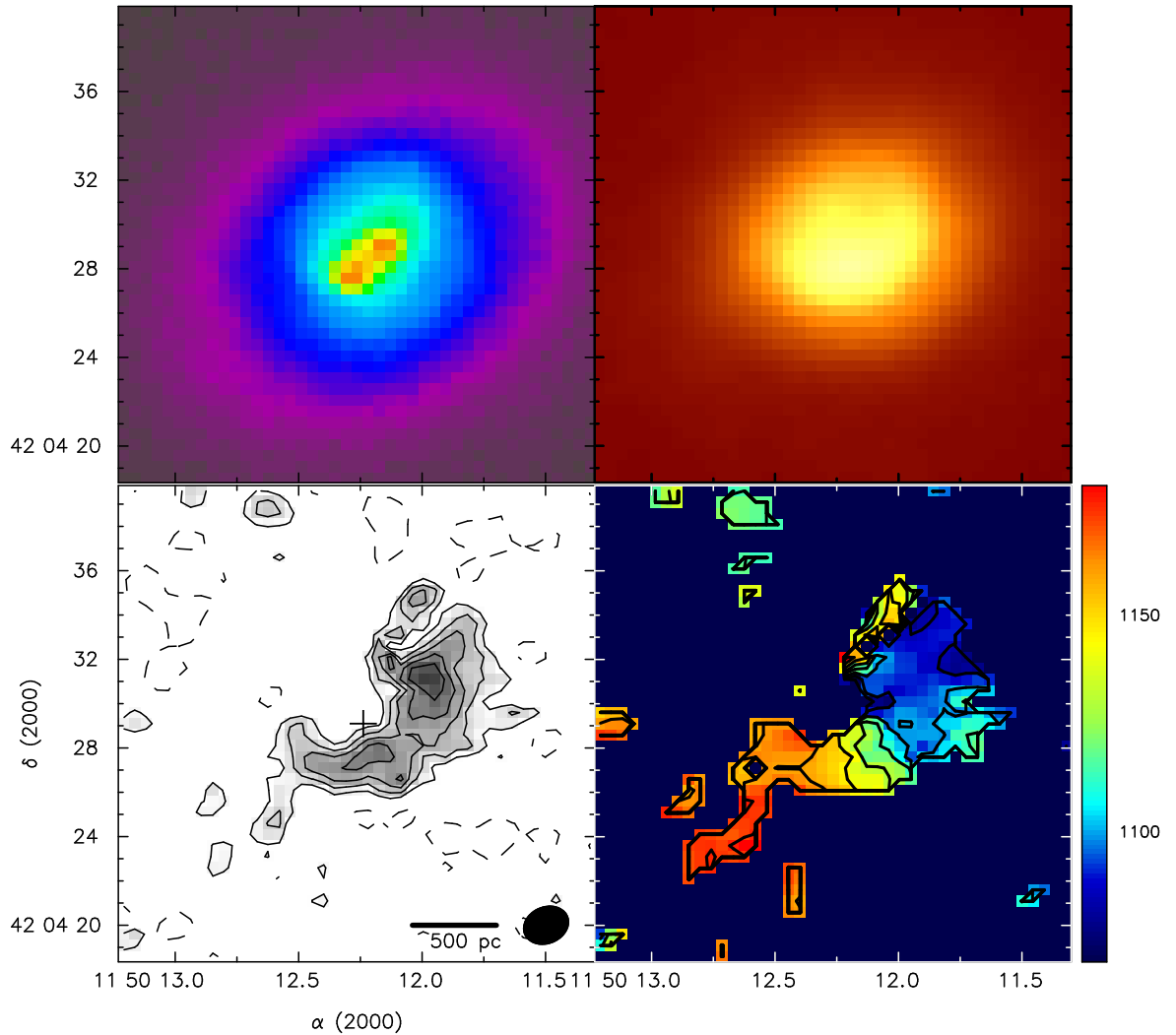


Figure 3.24: UGC 6805: (a) SDSS r -band image. (b) *Spitzer* IRAC $8\mu\text{m}$ image, with stellar emission subtracted following Pahre et al. (2004b). (c) Velocity-integrated CO(1–0) emission (contours and greyscale). Contour levels start at 2σ and are spaced in steps of 1σ ($\sigma = 0.20 \text{ Jy km s}^{-1}$); the cross marks the optical nucleus from SDSS. (d) CO(1–0) velocity field, with contours ranging from 1550 to 1610 km s^{-1} at intervals of 20 km s^{-1} .

3.5.12 UGC 7020A

UGC 7020A is a mid-sequence S0 galaxy that appears to be undergoing an interaction with a small companion. This is evidenced by the CO(1–0) emission, which is perpendicular to the major axis of the galaxy while still following the general rotation of the galaxy (Figure 3.26c, d). The CO(1–0) emission corresponds well to a blue streak across the center of the galaxy, ending in the south-western corner where the companion appears to be. The CO emission is well matched to the $8\mu\text{m}$ PAH emission. One possible explanation for the distribution of the CO may be that the interaction with the small companion compressed the atomic gas and triggered the star formation along the orbit of the companion, perpendicular to the plane of the galaxy.

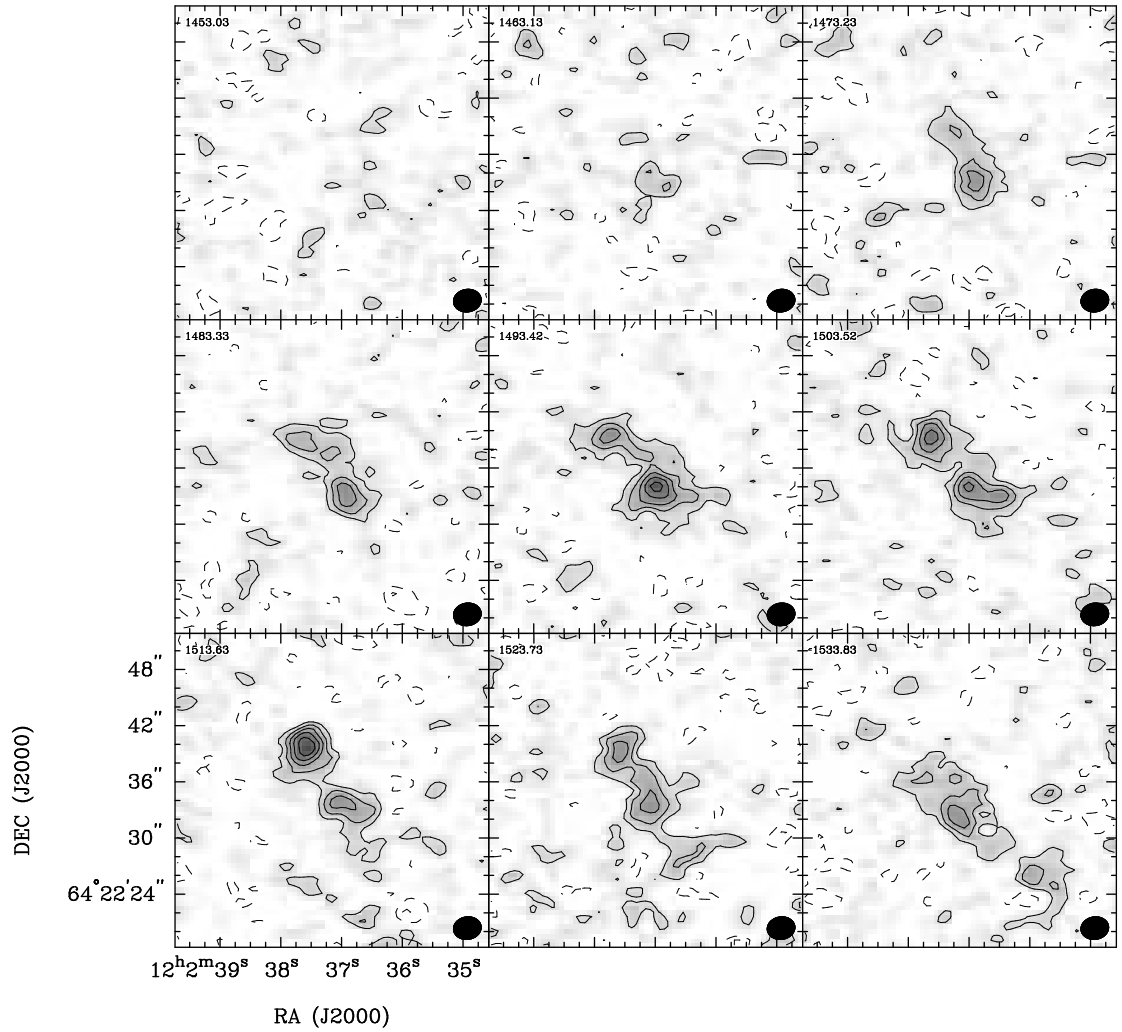


Figure 3.25: Channel maps of CO(1–0) emission (contours and greyscale) for UGC 7020A. Contour levels are -3 , -1.5 , 1.5 , 3 , 4.5 , 6 , 7.5 times the rms in each channel $9.3 \text{ mJy beam}^{-1}$). Heliocentric velocity of each panel in km s^{-1} is indicated in the upper left; the beam is shown in the lower right corner.

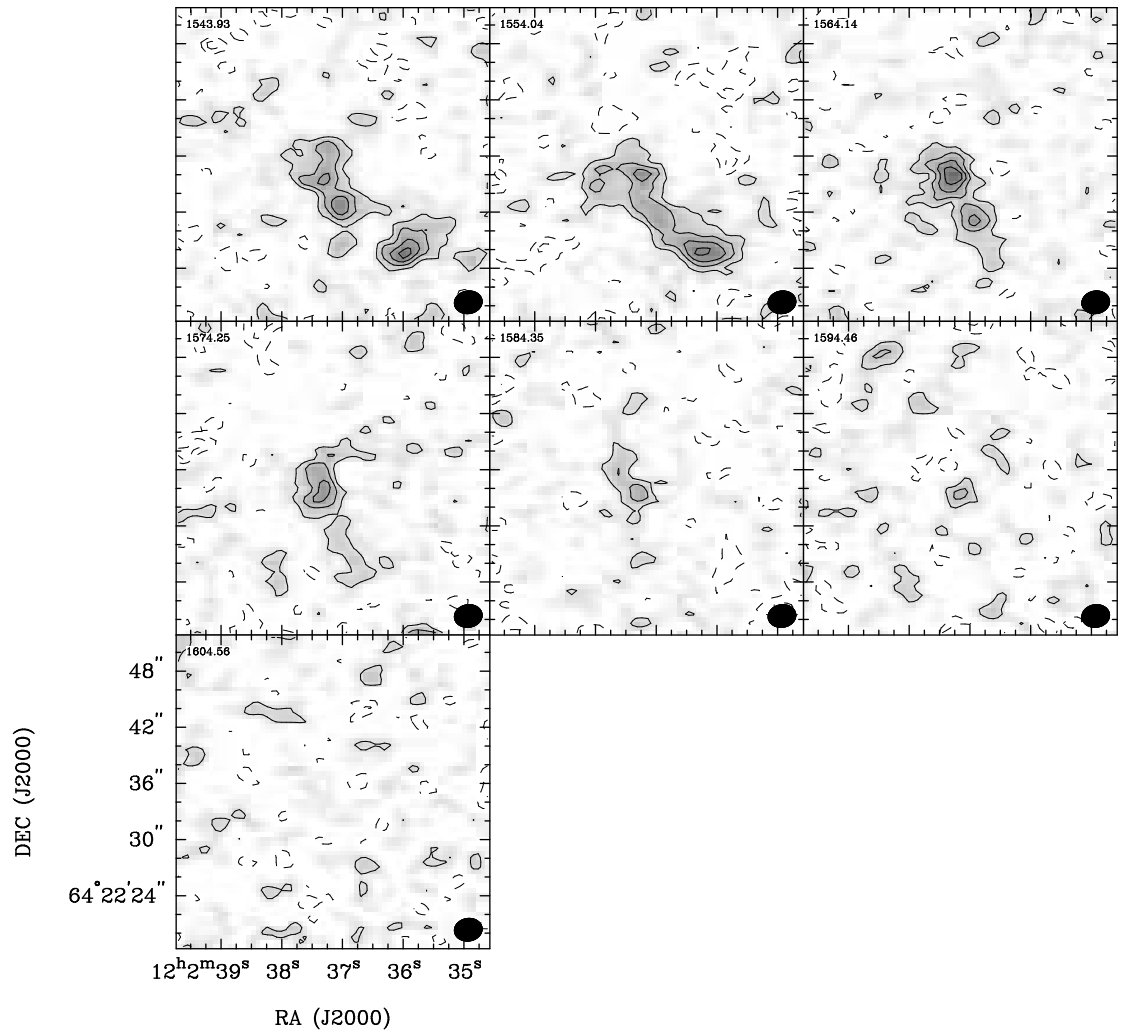


Figure 3.25: More CO(1-0) channel maps of UGC 7020A.

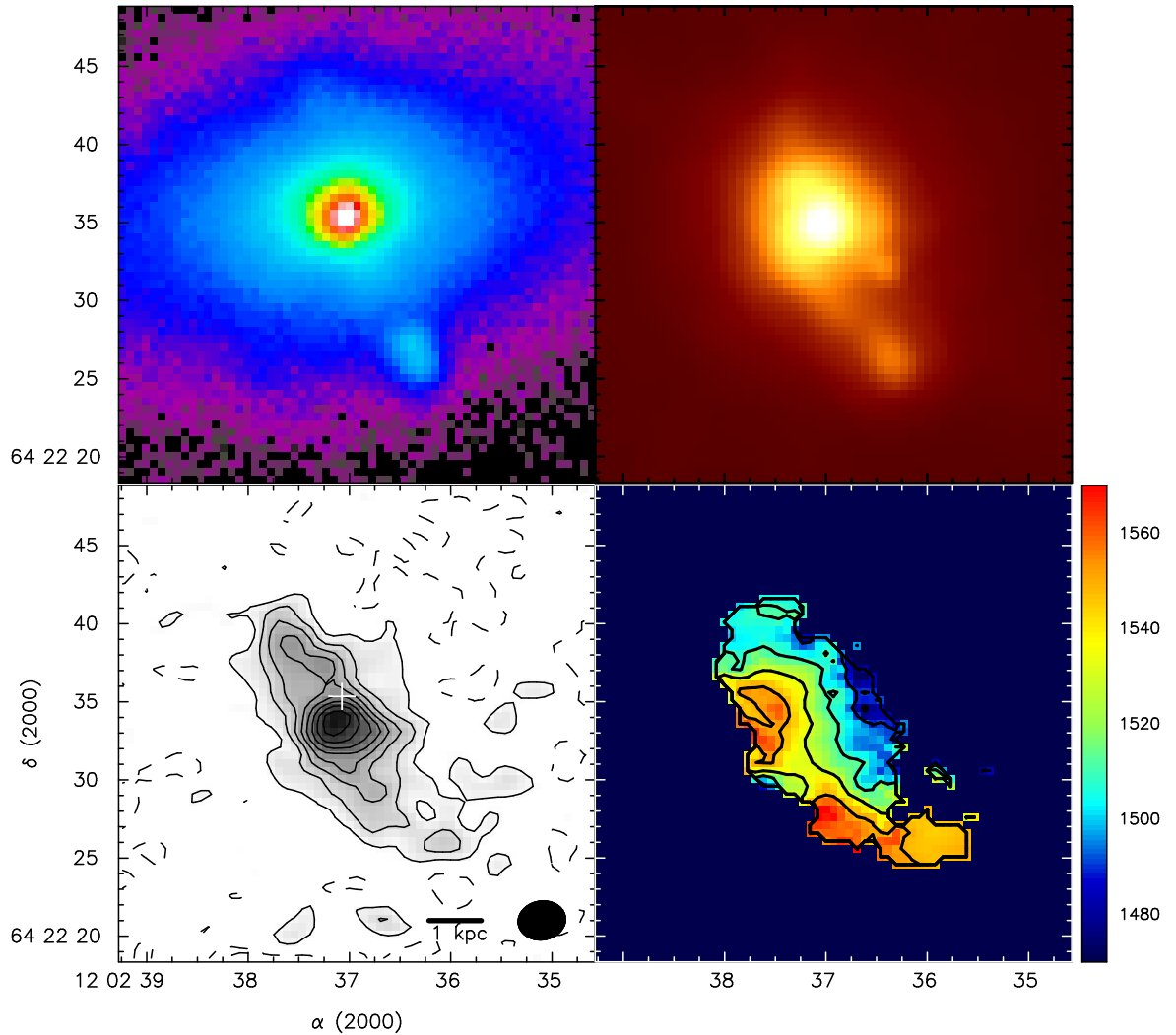


Figure 3.26: UGC 7020A: (a) SDSS r -band image. (b) *Spitzer* IRAC $8\mu\text{m}$ image, with stellar emission subtracted following Pahre et al. (2004b). (c) Velocity-integrated CO(1–0) emission (contours and greyscale). Contour levels start at 2σ and are spaced in steps of 2σ ($\sigma = 0.31 \text{ Jy km s}^{-1}$); the cross marks the optical nucleus from SDSS. (d) CO(1–0) velocity field, with contours ranging from 1470 to 1550 km s^{-1} at intervals of 20 km s^{-1} .

3.6 Summary

In this Chapter we have presented CARMA CO(1–0) observations of two red-, two mid-, and eight blue-sequence E/S0s with $M_* \leq 4 \times 10^{10} M_\odot$. Similar to CO observations of spiral galaxies, we find the CO emission in our E/S0s to be centrally concentrated, typically within $\sim 0.3 R_{25}$. While the majority of our galaxies show evidence of recent or ongoing mergers/interactions (NGC 3032, NGC 3773, NGC 4117, NGC 5173, UGC 6570, UGC 6805, UGC 7020A, UGC 12265N), nonetheless many appear to be have settled disks of molecular gas that are regularly rotating and well correlated with the $8\mu\text{m}$ PAH emission.

Chapter 4

The Relationship Between Molecular Gas and Star Formation

4.1 Introduction

Much progress has been made in recent decades in understanding the relationship between star formation rate (SFR) surface density (Σ_{SFR}) and gas surface density (Σ_{gas}) in nearby star-forming spiral galaxies, and this work has been used to infer the physical basis of the star formation law (e.g., Krumholz et al. 2009; Murray 2009). Studies relating the two observables with a power law of the form

$$\Sigma_{\text{SFR}} = a\Sigma_{\text{gas}}^N, \quad (4.1)$$

typically find power-law indices N ranging from 1 to 3 (e.g., Kennicutt 1998; Wong & Blitz 2002; Kennicutt et al. 2007; see Bigiel et al. 2008 for a review of previous work). In a spatially resolved study of HI and H₂ in star-forming spirals, Bigiel et al. (2008) find a linear ($N \sim 1$) relation between Σ_{SFR} and molecular-gas surface density (Σ_{H_2}), but little to no correlation between Σ_{SFR} and HI surface density.

In contrast, less is known about the connection between Σ_{gas} and star formation in early-type galaxies. The good correlation between the morphologies of molecular gas, $24\ \mu\text{m}$ emission, and radio continuum in local E/S0s hints that there is a relationship between Σ_{H_2} and Σ_{SFR} (Young et al. 2009). In a single-dish survey of CO emission in SAURON E/S0s, Combes et al. (2007) find that their galaxies follow the $N = 1.4$ disk-averaged power law, characteristic of spirals (Kennicutt 1998). Using multiple star-formation tracers, Crocker et al. (2010) find a similar result for a sample of 12 E/S0s, although possibly at lower total-gas star formation efficiencies ($\text{TSFE} \equiv \text{SFR}/M_{\text{HI}+\text{H}_2+\text{He}}$). Shapiro et al. (2010) update the Combes et al. results with spatially resolved maps, localizing both CO emission and star formation in the central regions of the galaxies and finding Σ_{SFR} , Σ_{H_2} , and molecular-gas star formation efficiency ($\text{MSFE} \equiv \text{SFR}/M_{\text{H}_2+\text{He}}$) values similar to those of spirals. However, spatially resolved studies of the H_2 -star formation relation at sub-kpc resolution similar to the analyses of Kennicutt et al. (2007) and Bigiel et al. (2008) have yet to be done for E/S0s.

Recent work has identified a local population of star-forming E/S0s that reside alongside spirals on the blue sequence in color vs. stellar mass space (Kannappan, Guie, & Baker 2009, hereafter KGB). The fraction of E/S0s on the blue sequence increases with decreasing mass, from $\gtrsim 5\%$ at stellar mass $M_* \sim 3 \times 10^{10} M_\odot$, up to $\gtrsim 20 - 30\%$ for $M_* \lesssim 5 \times 10^9 M_\odot$ (2% and 5% , respectively, of all galaxies in these mass ranges; KGB). Low-mass blue-sequence E/S0s, in contrast, appear more settled, occupying low-density field environments where gas accretion is likely (KGB). This population may reflect the transformation of “red and dead” E/S0s into spirals via inner- and outer-disk regrowth (KGB). KGB argue that many blue-sequence E/S0s occupy a “sweet spot” in M_* and stellar concentration index, characterized by abundant gas and bursty, efficient (when time-averaged over multiple bursts)

star formation, which may enable efficient disk building (see also §4.5). Chapter 2 (Wei et al. 2010a) confirm that blue-sequence E/S0s have fractionally large atomic gas reservoirs, comparable to those of spirals (0.1–1.0, relative to M_*). The ongoing star formation and large gas reservoirs of these galaxies make them easy targets for probing the spatially resolved relationship between Σ_{H_2} and Σ_{SFR} in E/S0s, offering unique insight into whether/how some E/S0s may be actively evolving via bursty, efficient star formation.

4.2 Sample & Data

Our parent sample of 32 galaxies consists of all E/S0s (14 blue-, 2 mid-, and 11 red-sequence) with $M_* \leq 4 \times 10^{10} M_\odot$ from the Nearby Field Galaxy Survey (NFGS, Jansen et al. 2000b), and an additional five blue-sequence E/S0s in the same mass range with HI maps available from the literature (see KGB). The sample was defined for *Spitzer* and *GALEX* programs GO-30406 and GI3-046012 (PI Kannappan), so all galaxies have new or archival FUV and $24\mu\text{m}$ data for SFR estimation. Of the parent sample, we observed 23 E/S0s in CO(1–0) with the Combined Array for Research in Millimeter-Wave Astronomy (CARMA), detecting 12 of 23. In this Letter, we focus on the 12 E/S0s with CARMA detections and 7 additional E/S0s with IRAM 30 m observations (five detections, two limits) in CO(1–0). These 19 E/S0s sample a large range (Table 4.1) in color and stellar mass (Figure 4.1), H_2/HI mass ratio (0.006–3.2), and total gas-to-stellar mass ratio (0.07–3.4).

The CARMA observations were taken between 2006–2009 in the C and D configurations, with typical resolution of $2''$ – $4''$. Velocity coverage ranges from 300 to 450 km s^{-1} , with resolution of $\sim 2.5 \text{ km s}^{-1}$. We reduced the data with the MIRIAD package (Sault et al. 1995), using natural weighting. For galaxies showing fairly

Table 4.1. Aperture-averaged properties for CARMA & IRAM 30 m E/S0s

Galaxy	Seq.	D_{maj} ($''$)	Dist. (Mpc)	M_* ($\log M_{\odot}$)	M_{HI} ($\log M_{\odot}$)	$M_{\text{H}_2, \text{C}}$ ($\log M_{\odot}$)	$M_{\text{H}_2, \text{S}}$ ($\log M_{\odot}$)	R_{ap} ($''$)	inclin. ($^{\circ}$)	Σ_{H_2} ($M_{\odot} \text{pc}^{-2}$)	Σ_{SFR} ($M_{\odot} \text{yr}^{-1} \text{kpc}^{-2}$)	τ_{dep} (Gyr)
NGC 3011	B	0.8	25.7	9.4	8.3		<7.0	12.1	27	<1.2	0.007±0.001	<0.22
NGC 3032	B	1.3	25.2	9.6	8.3	8.6	8.6 ^a	10.6	26	61.1±2.0	0.048±0.002	1.74±0.10
NGC 3073	B	1.1	21.1	9.1	8.5		7.0 ^b	10.6	31	3.0±0.6	0.004±0.001	0.91±0.27
UGC 6003	B	0.6	84.2	10.1	9.4	8.6	8.7	7.5	19	15.1±1.4	0.087±0.003	0.24±0.02
IC 692	B	0.8	21.4	8.9	8.4		6.8	12.1	42	1.0±0.3	0.006±0.001	0.22±0.08
UGC 6570*	M	1.2	28.6	9.6	8.4	8.0	8.0	7.5	62	10.1±0.8	0.066±0.001	0.21±0.02
UGC 6637*	B	0.9	31.5	9.2	8.6		7.3	12.1	66	0.7±0.2	0.004±0.001	0.25±0.07
NGC 3773	B	1.1	10.5	8.6	7.9	6.6		10.6	44	4.7±0.6	0.058±0.004	0.11±0.02
NGC 3870	B	1.0	14.5	8.8	8.4	6.9	7.2 ^c	12.1	41	3.3±0.5	0.038±0.003	0.12±0.02
UGC 6805	B	0.7	20.3	8.9	7.6	7.6	7.4	9.0	45	10.5±0.9	0.015±0.001	0.96±0.12
UGC 7020A	M	1.1	26.7	9.3	8.6	8.3	8.2	7.5	62	20.3±1.2	0.048±0.002	0.57±0.04
NGC 4117	R	1.8	19.0	9.7	8.3	7.7		7.5	72	8.4±0.6	0.005±0.000	2.35±0.25
NGC 5173	B	1.2	41.2	10.3	9.3	8.2		10.6	39	5.5±0.6	0.006±0.001	1.30±0.23
NGC 5338	R	1.9	10.3	8.9	7.3	7.3	7.4 ^d	7.5	57	19.0±1.2	0.011±0.001	2.27±0.26
UGC 9562	B	0.9	25.2	8.9	9.3		7.0	12.1	68	0.9±0.3	0.003±0.001	0.37±0.15
IC 1141	B	0.7	68.0	10.4	9.3	9.2		7.5	26	54.7±2.7	0.078±0.002	0.95±0.06
NGC 7077*	B	0.9	18.9	8.8	8.2		7.1	10.6	40	3.3±0.5	0.013±0.002	0.35±0.07
NGC 7360	B	1.2	67.9	10.5	9.6		<7.8	12.1	67	<0.5	0.001±0.000	<0.55
UGC 12265N	B	0.6	82.8	10.1	9.4	8.9	8.9	7.5	42	16.9±1.3	0.049±0.001	0.47±0.04

*Inclination assumed in calculating Σ_{H_2} and Σ_{SFR} is uncertain.

Note. — Optical major axis (D_{maj}), M_* , and distance data are from KGB. HI data are from Wei et al. (2010a) and references therein. $M_{\text{H}_2, \text{C}}$ is estimated from CARMA CO(1–0) data, and $M_{\text{H}_2, \text{S}}$ from single-dish data (central pointings only) from Kannappan et al., in prep. and Stark et al., in prep., except as marked: (a) Thronson et al. (1989), (b) Sage et al. (2007), (c) Welch & Sage (2003), (d) Leroy et al. (2005). $\tau_{\text{dep}} \equiv M_{\text{H}_2 + \text{He}} / \text{SFR}$.

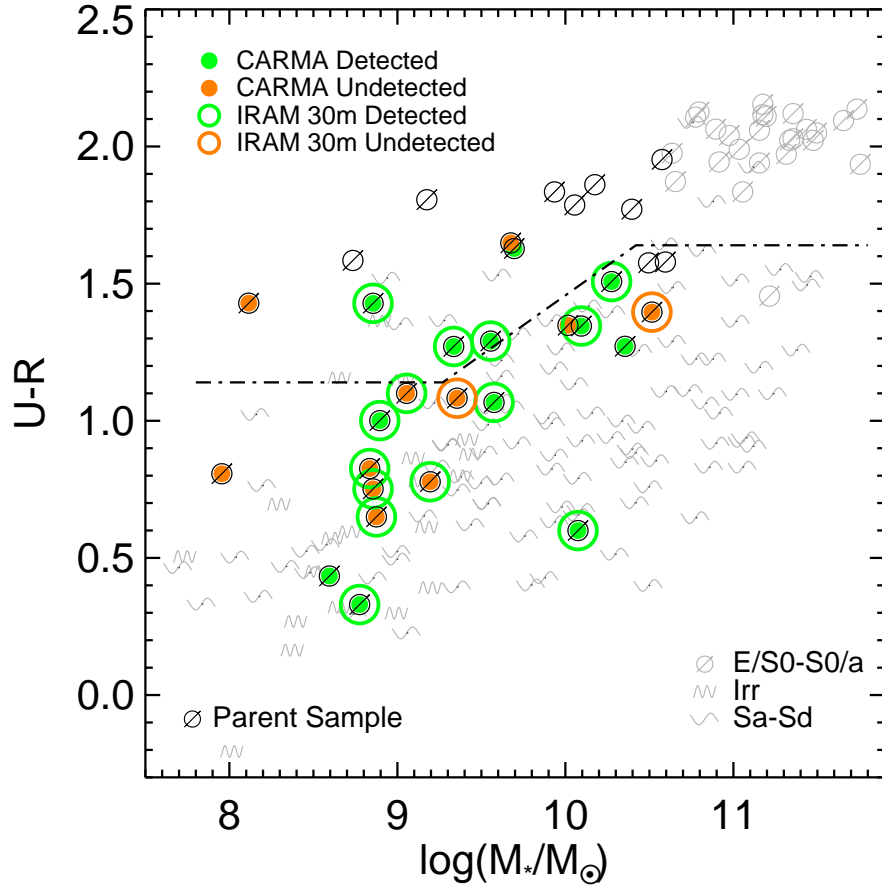


Figure 4.1: $U - R$ color vs. stellar mass for galaxies in the Nearby Field Galaxy Survey (Jansen et al. 2000b), plus five additional E/S0s from the literature. Symbols denote morphological types (KGB). The red sequence, i.e. the main locus of traditional red E/S0s, lies above the dashed line (with two borderline “mid-sequence” E/S0s boxed, see KGB), while the blue sequence (typically populated by spirals) lies below. Dark symbols denote the 32 galaxies in the parent sample; the rest of the NFGS is shown in light grey.

regular CO rotation, we fit velocity maps with model rotation curves and created masks from adaptive windows around the model velocity fields to make integrated-velocity maps. The four galaxies (NGC 3773, NGC 5338, UGC 6003, UGC 6570) without regular rotation in CO were masked in velocity based on their HI velocity profiles. A more detailed description of the CARMA data reduction is given in Chapter 3. IRAM 30 m CO(1–0) observations are from S. Kannappan et al. 2010, in preparation, and D. Stark et al. 2010, in preparation, with additional literature data as noted in Table 4.1. We consider central pointings only, so the 23'' IRAM beam probes inner disks (relative to $\sim 0'.6$ – $1'.9$ optical diameters). Comparison between CARMA and IRAM 30 m fluxes suggests that little flux is resolved out by the interferometric observations.

We use the pipeline 24 μ m mosaics from the *Spitzer* archive, and the background-subtracted pipeline-processed FUV data from the *GALEX* archive. The CARMA and *GALEX* data sets were convolved with a kernel that reproduce the MIPS 24 μ m PSF (FWHM $\sim 6''$; Gordon et al. 2008) exactly in the CARMA/*GALEX* images, including the Airy ring, which is $< 1\%$ of the $I_{24,\text{peak}}$. For our pixel-to-pixel analysis in §4.3, we further convolve our data to a resolution of 750 pc ($6.1''$ – $15.3''$) for comparison with Bigiel et al. (2008). All maps are at least Nyquist-sampled.

We estimate Σ_{H_2} and Σ_{SFR} following Leroy et al. (2008):

$$\frac{\Sigma_{\text{H}_2}}{M_\odot \text{ pc}^{-2}} = 4.4 \cos i \frac{I_{\text{CO}(1-0)}}{\text{K km s}^{-1}} \quad (4.2)$$

$$\frac{\Sigma_{\text{SFR}}}{M_\odot \text{ kpc}^{-2} \text{ yr}^{-1}} = \cos i \frac{8.1 \times 10^{-2} I_{\text{FUV}} + 3.2 \times 10^{-3} I_{24}}{\text{MJy sr}^{-1}}. \quad (4.3)$$

Equation 4.2 assumes a CO-to-H₂ conversion factor (X_{CO}) of $2 \times 10^{20} \text{ cm}^{-2} (\text{K km s}^{-1})^{-1}$.

Our estimates of Σ_{H_2} do not include helium; however, helium is included in estimates of molecular gas depletion time. Equation 4.3 uses the broken power law

initial mass function given by Kroupa (2001). Our procedures for calculating Σ_{H_2} and Σ_{SFR} are identical to those of Bigiel et al. (2008) after their conversion from CO(2–1) to CO(1–0) ($I_{\text{CO}(2-1)}/I_{\text{CO}(1-0)} = 0.8$), ensuring a fair comparison between the two data sets.

AGN contamination is not an issue for the 750 pc resolution analysis, as any AGN contribution in the infrared would be contained within the central resolution element. NGC 4117 and IC 1141 are known AGN hosts, and optical line diagnostics from Kewley et al. (2006b) identify NGC 5173 as a candidate host. However, IRAC color-color diagnostics (Sajina et al. 2005) suggest that (possible) AGN contributions to the integrated infrared emission in our galaxies are relatively weak, as the removal of the central resolution element does not significantly affect their positions in the infrared color-color diagram. Following Temi et al. (2007), we estimate possible $24 \mu\text{m}$ emission contamination from passively evolving stellar populations to be $< 8\%$ for our E/S0s.

4.3 The Resolved Star Formation Relation at 750 pc Resolution

Figure 4.2 plots the pixel-to-pixel relationship between Σ_{SFR} and Σ_{H_2} for the eight of our 19 galaxies resolved on 750 pc scales. We also include the 750 pc resolution data for the seven spirals observed by Bigiel et al. (2008) as light blue dots. The vertical dashed lines demarcate the three different star formation regimes discussed by Bigiel et al. (2008): HI-dominated, giant molecular cloud (GMC)/disk, and starburst. Figure 4.2 shows that all but two of the eight galaxies have some regions that fall within the GMC/disk regime, with two blue- and one mid-sequence E/S0s (NGC 3032, UGC 6570, and UGC 7020A) having the majority of their points in

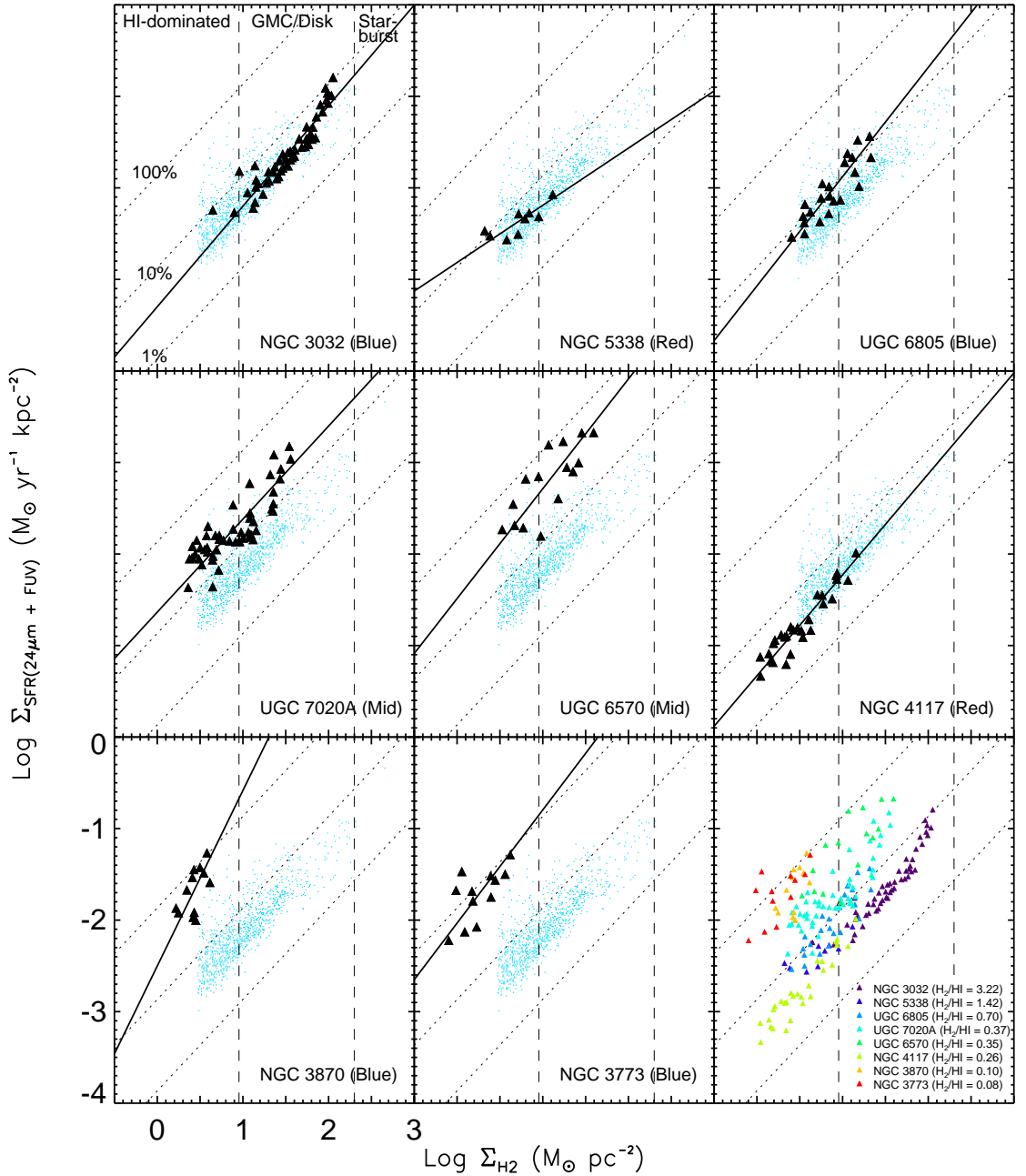


Figure 4.2: Σ_{SFR} vs. Σ_{H_2} at 750 pc resolution. Points for the seven spirals from Bigiel et al. (2008) are plotted in light blue. Black triangles show our eight E/S0s resolved in CO(1–0) with CARMA. Vertical dashed lines demarcate the three different regimes of star formation discussed in Bigiel et al. (2008), and dotted lines mark constant MSFE, corresponding (from top to bottom) to the depletion of 100%, 10%, and 1% of the molecular gas (including helium) within 10^8 yr, or equivalently to molecular gas depletion timescales of 0.1, 1, and 10 Gyr. Solid black lines represent OLS bisector fits. The color sequence (blue/mid/red) is noted at the bottom of each panel. The last panel combines the points for all eight galaxies, color-coded by $M_{\text{H}_2}/M_{\text{HI}}$, illustrating variations in MSFE with power-law index N and $M_{\text{H}_2}/M_{\text{HI}}$ (see §4.3 and §4.5).

this regime.

We fit the Σ_{H_2} - Σ_{SFR} relationship with a power-law of the form

$$\Sigma_{\text{SFR}} = a \left(\frac{\Sigma_{\text{H}_2}}{b M_{\odot} \text{pc}^{-2}} \right)^N \quad (4.4)$$

in log-log space using the ordinary least-squares (OLS) bisector method (solid line in Figure 4.2) and list the fit parameters in Table 4.2, using coefficient $A = \log_{10}(a/M_{\odot} \text{kpc}^{-2} \text{yr}^{-1})$. Note that we set the intercept of our fit at $\log_{10}(b)$, where b is the median Σ_{H_2} for each galaxy, to lessen the effect of the covariance between N and A . The power-law index N ranges from 0.62 to 1.92, with a median of ~ 1.2 . It is evident that the majority of E/S0s in Figure 4.2 exhibit a power-law relation between Σ_{H_2} and Σ_{SFR} , all the way down to the HI-dominated regime.

Figure 4.2 also plots (dotted) lines of constant MSFE with $N = 1$, defined as the inverse of the molecular gas depletion time $M_{\text{H}_2+\text{He}}/\text{SFR}$, and illustrates variations in N and $M_{\text{H}_2}/M_{\text{HI}}$. For blue- and mid-sequence E/S0s, we find that as MSFE increases, N seems to steepen and $M_{\text{H}_2}/M_{\text{HI}}$ seems to decrease. We find a wider range of MSFEs (4%–70%) compared to the 3%–8% found by Bigiel et al. (2008). We discuss whether MSFE truly measures molecular-gas star formation *efficiency* in §4.5.

4.4 The Global Star Formation Relation

In Figure 4.3, we show the 1–8 kpc aperture-averaged relationship between Σ_{H_2} and Σ_{SFR} for the eight E/S0s of Figure 4.2 plus 11 more blue-sequence E/S0s with CARMA detections and/or IRAM observations, as well as for normal spiral-disk and starburst galaxies (Kennicutt 1998) and SAURON E/S0s (Shapiro et al. 2010). With the exception of Kennicutt’s normal disk points, all the other points in Figure 4.3

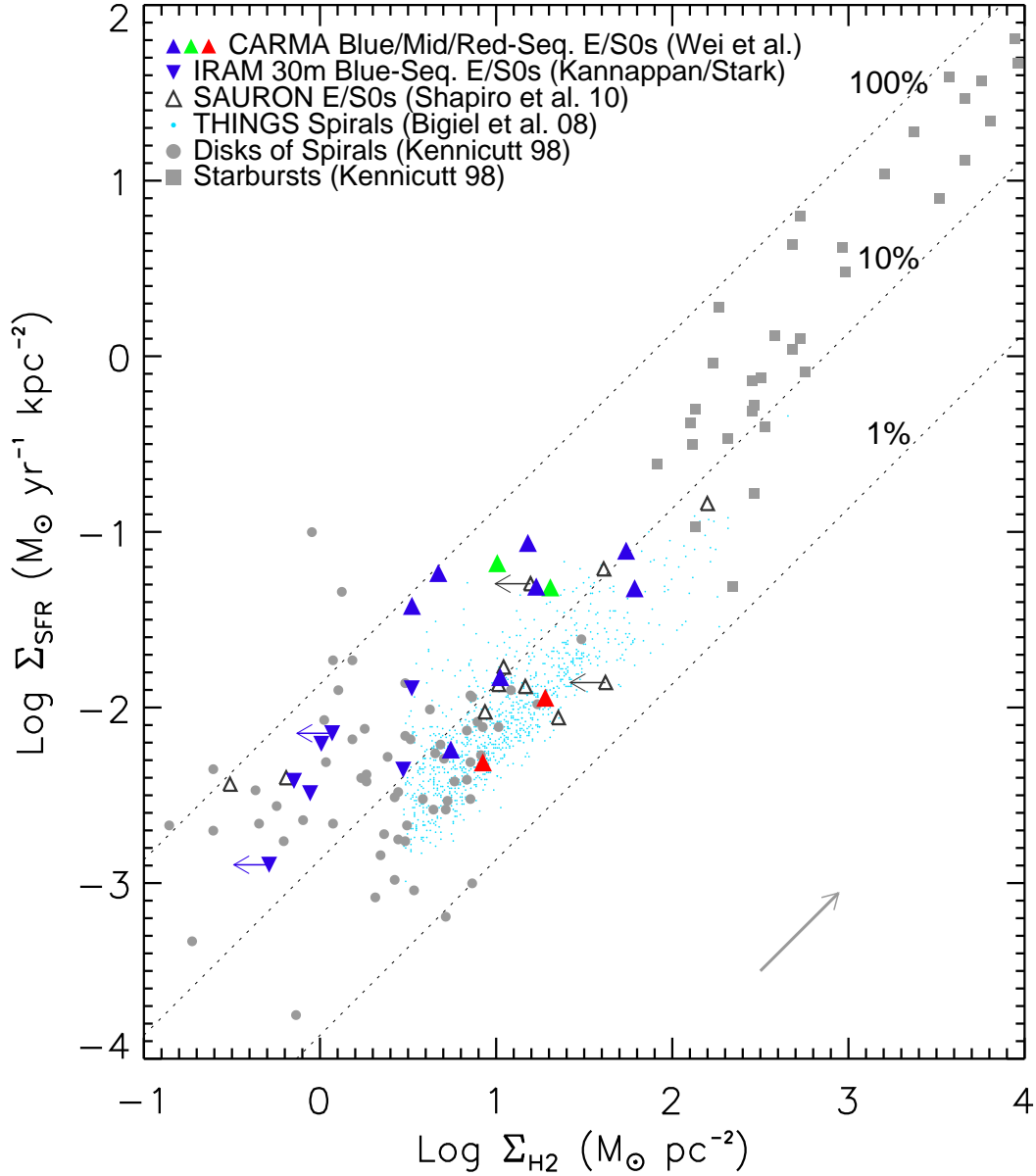


Figure 4.3: Aperture-averaged Σ_{SFR} vs. Σ_{H_2} for normal disk and nuclear starburst galaxies from Kennicutt (1998), SAURON E/S0s from Shapiro et al. (2010), and E/S0s from this Letter. The 750 pc resolution points from Bigiel et al. (2008) are also plotted in the background for comparison. Dotted lines mark the same lines of constant MSFE as in Figure 4.2. Grey arrow in the lower right shows typical shift of spiral disk points from Kennicutt (1998) if averaged over $0.6 r_{25}$ instead of r_{25} .

Table 4.2. Star formation relation fit parameters

Galaxy	b ($M_{\odot} \text{pc}^2$)	Coeff. A	Index N	RMS (dex)
Blue Seq.:				
NGC 3032	33.7	-1.62 ± 0.02	1.10 ± 0.08	0.12
NGC 3773	1.7	-1.75 ± 0.07	1.24 ± 0.16	0.20
NGC 3870	2.7	-1.67 ± 0.06	1.92 ± 0.35	0.23
UGC 6805	7.1	-2.06 ± 0.03	1.19 ± 0.10	0.18
Mid Seq.:				
UGC 6570	11.7	-1.21 ± 0.06	1.20 ± 0.14	0.23
UGC 7020A	7.7	-1.73 ± 0.03	1.02 ± 0.08	0.21
Red Seq.:				
NGC 4117	3.0	-2.81 ± 0.02	1.10 ± 0.06	0.13
NGC 5338	5.2	-2.37 ± 0.03	0.62 ± 0.11	0.09
Median	7.1	-1.73	1.19	

show the surface densities within regions of star formation or molecular gas. The starbursts were averaged over “the radius of the starburst region” determined from CO/infrared imaging (Kennicutt 1998), and the SAURON E/S0s were averaged over the extent of the star-forming region defined by $8 \mu\text{m}$ PAH emission (Shapiro et al. 2010). For our 19 E/S0s, we average M_{H_2} and SFR over an area with radius (R_{ap}) twice the scale length of the $24 \mu\text{m}$ emission, where the flux drops by e^{-2} from the peak. This area encompasses most of the flux in CO, $24 \mu\text{m}$, and FUV, and corresponds well to the visual impression of the extent of CO emission for most galaxies. Note that the dots from Bigiel et al. (2008) plotted in the background for reference are *local* (750 pc) measures of Σ_{H_2} and Σ_{SFR} as in Figure 4.2.

In contrast, the Kennicutt (1998) spiral disk points are averaged over r_{25} , which may dilute the values of Σ_{H_2} and Σ_{SFR} . We infer this from radial profiles of normal spirals in Bigiel et al. (2008), which indicate that H_2 typically extends out to only $\sim 0.6 r_{25}$. Thus the surface densities calculated by Kennicutt (1998) for spiral disks

should for consistency move up along lines of constant MSFE by ~ 0.62 dex (grey arrow in Figure 4.3).

Comparison of these data sets reveals that the aperture-averaged Σ_{H_2} and Σ_{SFR} for our 19 E/S0s overlap the range spanned by spiral disks, with six of the CARMA-detected E/S0s having sufficiently high surface densities to occupy the same space where Kennicutt (1998) finds the *centers* of spirals lie — between normal disks and starburst galaxies (not shown in Figure 4.3, as Kennicutt tabulates only combined HI+H₂ data for galaxy centers). Our E/S0s also appear to span the same range as the typically more massive SAURON E/S0s.

Figure 4.3 also shows a similarly large spread in aperture-averaged MSFEs as seen for local MSFEs in §4.3, with over half of the CARMA-detected and all of the 30 m-observed E/S0s (all blue- or mid-sequence) offset towards apparently higher MSFEs ($>10\%$) compared to the typical spirals from Bigiel et al. (2008). Equivalently, the molecular gas depletion times for our E/S0s range from 2.3 down to 0.1 Gyr, with a median of 0.5 Gyr — lower than that of the Bigiel et al. spirals. Additionally, the offset towards apparently higher MSFEs is seen in both the CARMA and IRAM 30 m galaxies in Figure 4.3, so it is not specific to interferometric data.

4.5 Discussion

We have shown above that the relationship between molecular gas and star formation in low-mass E/S0s ($M_* \lesssim 4 \times 10^{10} M_\odot$) resolved at 750 pc is similar to that for spirals, with a roughly linear correlation between Σ_{H_2} and Σ_{SFR} all the way down to the HI-dominated regime. This suggests that star formation occurs in H₂ and not HI, similar to what Bigiel et al. (2008) find for spirals. One intriguing difference is the apparently elevated MSFEs of our E/S0s compared to the MSFEs of the Bigiel

spirals. *Star formation efficiency*, however, may be a misnomer in some cases, as other factors may contribute to the observed offsets.

One possible cause for apparently elevated MSFEs is that the CO may not trace all of the H₂ in these galaxies, as many are low-mass systems where X_{CO} may be variable (e.g., Maloney & Black 1988; Pak et al. 1998; Pelupessy & Papadopoulos 2009). Kennicutt (1998) finds a similar scatter in MSFEs for low-luminosity ($L_B < 10^{10} L_\odot$) disk galaxies, which he attributes to variation in X_{CO} , possibly due to low metallicities. Recent *Herschel* results support this, finding evidence for excess cold dust that is not well-traced by CO in low-mass galaxies (O’Halloran et al. 2010; Kramer et al. 2010). However, metallicity measurements (available for 5/6 CARMA-detected and 3/7 IRAM-observed galaxies offset towards higher MSFEs) indicate that these galaxies are well within the range ($\gtrsim 1/4 Z_\odot$) where much work suggests that X_{CO} is similar to that assumed here (e.g., Rosolowsky et al. 2003; Leroy et al. 2006; Wolfire et al. 2010).

A second explanation is that some of these galaxies are advanced, H₂-depleted starbursts, where the delay between H₂ exhaustion and fading of star-formation tracers associated with young, massive stars gives the *appearance* of elevated MSFEs. Thus the possible correlation between elevated MSFE, lower $M_{\text{H}_2}/M_{\text{HI}}$, and steeper (higher N) slopes in the Schmidt-Kennicutt relation found in §4.3 may reflect the depletion of H₂ in the later stages of star formation, in good agreement with simulations that predict steeper Schmidt-Kennicutt relations and higher MSFEs as the molecular gas fraction decreases (Robertson & Kravtsov 2008). This is consistent with studies of NGC 1569, a post-starburst dwarf irregular (e.g., Angeretti et al. 2005) that also appears to have an elevated MSFE (Leroy et al. 2006).

A third possibility is that the observed offsets may reflect truly enhanced MSFEs. Kannappan & Wei (2008), updating Kannappan (2004), find that the fractional gas

content of galaxies abruptly rises below a gas-richness threshold mass of $M_* \sim 3\text{--}5 \times 10^9 M_\odot$, roughly corresponding to internal velocities of $\sim 120 \text{ km s}^{-1}$ (see also KGB). This is the same velocity threshold below which the physics of star formation may change due to possibly increased gas accretion, outflow, and metal loss from shallower potentials (Dalcanton et al. 2004; Garnett 2002; Dalcanton 2007). While the *total* SFEs of dwarf galaxies are low compared to those of normal star-forming spirals (e.g., Hunter & Elmegreen 2004; Dalcanton et al. 2004; Dalcanton 2007; Robertson & Kravtsov 2008), recent simulations suggest that gas-rich and/or lower metallicity galaxies deviate from the Schmidt-Kennicutt relationship towards higher *molecular* SFEs (Pelupessy & Papadopoulos 2009). These predictions are supported by observations of local dwarfs, which find high MSFEs in IC 10 and M33 compared to nearby spirals (Leroy et al. 2006; Gardan et al. 2007). This phenomenon could contribute to the scatter in MSFEs observed by Kennicutt (1998), as $L_B \sim 10^{10} L_\odot$ roughly corresponds to the gas-richness threshold mass. Similarly, the two SAURON E/S0s in Figure 4.3 with the highest MSFEs are low-luminosity systems with $L_B < 10^{10} L_\odot$.

Unlike previous studies of star formation in blue E/S0s, our sample focuses on galaxies below the gas-richness threshold mass (13 of our 19 E/S0s). At higher stellar masses, AGN and strong starbursts are observed to dominate the blue E/S0 population (e.g., Schawinski et al. 2009; Lee et al. 2010), which is not inconsistent with the nature of our six higher-mass E/S0s (three known/candidate AGNs and two likely starbursts¹).

¹UGC 12265N & UGC 6003 do not appear in the starburst regime of Figure 4.3 due to their large distances and the resulting poor resolution of the central region, but their nuclear EW(H α) emission measurements (86 and 76 Å, respectively) and very blue-centered color gradients suggest recent/ongoing central starbursts.

Our results suggest that (possibly milder) bursts likely play a key role for lower-mass E/S0s as well. The variation of MSFE in this scenario has implications for our understanding (and theoretical simulations) of low-mass galaxy evolution. The dynamical timescales for gas inflow typical for our sample (0.06–0.4 Gyr; Wei et al. 2010a) are short compared to the molecular gas consumption times we find here (0.1–2.3 Gyr), which suggests that refueling of H_2 from the HI reservoir to sustain star formation is limited only by the frequency of minor mergers/interactions that trigger gas inflow. If apparently elevated MSFEs reflect advanced, H_2 -depleted bursts, the fact that 15 of our 19 E/S0s have $\text{MSFE} > 10\%$ suggests that low-mass E/S0s may experience frequent small starbursts (with the caveat that we have sampled the most strongly star-forming examples by favoring blue-sequence E/S0s detected in CO). Therefore the TSFEs of lower-mass galaxies, when time-averaged over many bursts, may be elevated — consistent with the KGB finding that the concentration indices in blue-sequence E/S0s are similar to those identified by Kauffmann et al. (2006) as optimal for peak time-averaged TSFE. Our results support the picture of KGB and Wei et al. (2010a) that many blue-sequence E/S0s are in a “sweet spot” with abundant gas and bursty star formation enabling efficient disk building.

Chapter 5

Star Formation as Traced by $8\ \mu\text{m}$ PAH Emission

5.1 Introduction

Historically, early-type galaxies have been considered to be red and dead — the end result of galaxy evolution after all the gas has been consumed or expelled and star formation has been quenched. Work over the past several decades, however, suggests that this is not the case. In addition to having non-negligible amounts of atomic (e.g., Hawarden et al. 1981; Knapp et al. 1985; Wardle & Knapp 1986; Sadler et al. 2000; Oosterloo et al. 2002; Morganti et al. 2006) and molecular (e.g., Wiklind & Henkel 1992; Inoue et al. 1996; Wiklind et al. 1997; Young 2002; Welch & Sage 2003; Okuda et al. 2005; Sage et al. 2007; Young et al. 2008, 2009) gas, some early-type galaxies appear to be actively forming stars, albeit at lower rates than spiral galaxies (Yi et al. 2005; Combes et al. 2007; Schawinski et al. 2009; Young et al. 2009; Shapiro et al. 2010; Crocker et al. 2010). The focus of these studies is on massive ellipticals and lenticulars, and although these galaxies have small amounts

of gas and star formation, most studies agree that they will eventually consume their fuel and evolve passively.

Recent work, however, has identified a population of low-mass ($M_* \lesssim \text{few} \times 10^{10} M_\odot$) E/S0 galaxies found on the blue sequence in color vs. stellar mass space, where spiral galaxies typically reside (Kannappan, Guie, & Baker 2009, hereafter KGB). These galaxies have substantial fractional HI reservoirs, comparable to those of spiral galaxies and capable of sustaining star formation for a few Gyr at the current rate of star formation (KGB; Chapter 2, Wei et al. 2010a). Many of these galaxies overlap with the disks and centers of spirals in the molecular gas Schmidt-Kennicutt relation, with a roughly linear correlation between molecular gas and star formation surface densities and possible evidence of enhanced star formation efficiency (Chapter 4, Wei et al. 2010b).

The sample in Chapter 4 (Wei et al. 2010b) is biased towards the most strongly star-forming galaxies among the low-mass E/S0 population, since it includes mostly blue-sequence E/S0s. Additionally, the use of MIPS $24 \mu\text{m}$ and FUV data limits the study to a resolution of $\sim 6''$ (0.3–2.5 kpc), which blurs interesting features that may be associated with star formation. While interferometric observations of CO(1–0) in these galaxies can resolve molecular gas structures correlated with star formation, it would be costly in observing time to fully map a significant sample of low-mass early types, especially including a control sample of low-mass red-sequence E/S0s with only trace amounts of gas and star formation.

The *Spitzer Space Telescope*, and more specifically the $\leq 2''$ resolution InfraRed Array Camera (IRAC; Fazio et al. 2004), may remedy this situation. For nearby galaxies, the $7.7 \mu\text{m}$ polycyclic aromatic hydrocarbon (PAH) emission, thought to arise from the absorption of UV/optical light from young massive stars by small dust grains, dominates the IRAC Channel 4 centered at $8 \mu\text{m}$. PAH emission is typically

found surrounding HII regions (Giard et al. 1994; Helou et al. 2004), although not inside HII regions as carriers are dissociated by harder radiation fields (i.e., Helou et al. 2001; Laurent et al. 2000). Wu et al. (2005) calibrate the $8\mu\text{m}$ PAH emission of star-forming galaxies from the *Spitzer* First Look Survey against $\text{H}\alpha$ and radio luminosity to obtain star formation rates for these galaxies, and many subsequent studies have used the $8\mu\text{m}$ flux as a star formation indicator (e.g., Jackson et al. 2006; Shapiro et al. 2010).

In this Chapter, we use the $8\mu\text{m}$ PAH emission as a star-formation tracer for a sample of E/S0s that spans large ranges in both color and stellar mass to investigate the nature of star formation in early-type galaxies, with emphasis on lower-mass E/S0s. We also consider the relationship of $8\mu\text{m}$ PAH emission with CO emission for select galaxies where resolved CO maps are available, examining the spatial relationship between the two tracers. Finally, we consider the correlations between global $8\mu\text{m}$ PAH emission and measures of star formation as well as with global atomic and molecular gas masses.

5.2 Sample, Observations, and Data Reduction

Our full IRAC sample consists of all 15 blue-sequence E/S0s from the Nearby Field Galaxy Survey (NFGS, Jansen et al. 2000b), as well as 2 mid-sequence and 10 red-sequence E/S0s with similar stellar masses¹. We include an additional five blue-sequence E/S0s (NGC 3032, NGC 3073, NGC 3419, NGC 3773, NGC 3870) in the same mass range with HI maps available from the literature, for a total of 32 E/S0s. We plot the distribution of our sample in $U - R$ color vs. stellar mass space in

¹The 25 high-mass ($M_* \gtrsim 3 \times 10^{10} M_\odot$) red-sequence E/S0s from the NFGS were not included in this sample.

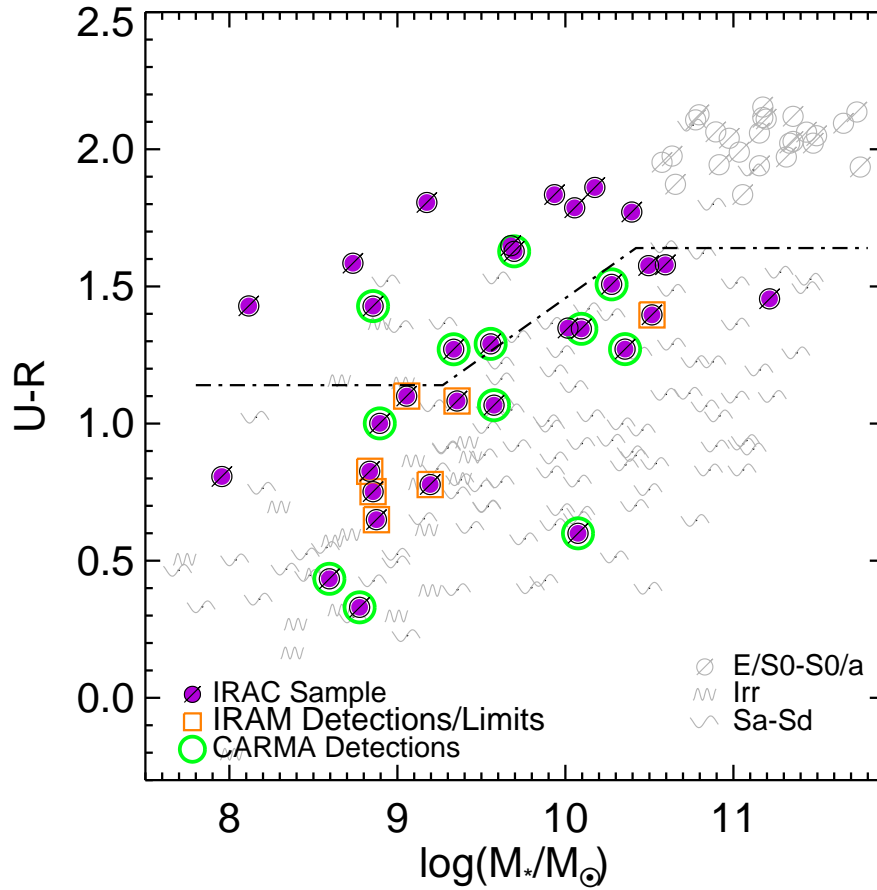


Figure 5.1: $U - R$ color vs. stellar mass for galaxies in the Nearby Field Galaxy Survey (Jansen et al. 2000b), plus five additional E/S0s from the literature. Symbols denote morphological types based on monochrome B or g band images (KGB). The red sequence (the main locus of high-mass and/or cluster E/S0s) lies above the dashed line, while the blue-sequence (typically populated by spiral galaxies) lies below (KGB). Dark symbols denote the 32 galaxies in our sample with *Spitzer* IRAC observations; the 12 galaxies with CARMA CO(1–0) detections are circled in green; the 7 galaxies with IRAM 30 m CO(1–0) observations are boxed in orange.

Figure 5.1, also noting the 12 galaxies with resolved CARMA CO(1–0) detections; the other NFGS galaxies are plotted for comparison.

Table 5.1. IRAC image properties

Galaxy	α_{2000} (J2000)	δ_{2000} (J2000)	3.6 μm Sky (Var.) (kJy sr $^{-1}$)	4.5 μm Sky (Var.) (kJy sr $^{-1}$)	8.0 μm Sky (Var.) (MJy sr $^{-1}$)
IC 1141	15:49:46.9	+12:23:57	27(4)	29(3)	2.00(0.03)
IC 1144	15:51:21.7	+43:25:04	10(3)	4(3)	0.39(0.03)
IC 1639	01:11:46.5	-00:39:52	73(2)	144(3)	6.36(0.04)
IC 195	02:03:44.6	+14:42:33	129(4)	358(4)	11.94(0.05)
IC 692	11:25:53.5	+09:59:15	91(3)	206(3)	7.94(0.04)
NGC 3011	09:49:41.2	+32:13:16	82(3)	262(4)	8.06(0.04)
NGC 3032	09:52:08.2	+29:14:10	44(3)	80(4)	4.12(0.04)
NGC 3073	10:00:52.1	+55:37:08	15(3)	53(6)	1.89(0.06)
NGC 3419	10:51:17.7	+13:56:46	06(2)	303(4)	10.30(0.04)
NGC 3499	11:03:11.0	+56:13:18	30(2)	93(3)	2.45(0.03)
NGC 3522	11:06:40.4	+20:05:08	92(3)	270(4)	8.86(0.04)
NGC 3605	11:16:46.6	+18:01:02	56(9)	105(17)	4.75(0.15)
NGC 3773	11:38:12.9	+12:06:43	40(3)	65(5)	4.15(0.06)
NGC 3870	11:45:56.6	+50:11:59	14(3)	50(3)	1.84(0.03)
NGC 4117	12:07:46.1	+43:07:35	26(3)	100(3)	2.94(0.03)
NGC 4308	12:21:56.8	+30:04:28	77(6)	203(3)	5.85(0.04)
NGC 516	01:24:08.1	+09:33:06	96(2)	208(4)	8.36(0.05)
NGC 5173	13:28:25.3	+46:35:30	27(2)	105(3)	2.46(0.04)
NGC 5338	13:53:26.5	+05:12:28	78(3)	263(3)	8.50(0.03)
NGC 5596	14:22:28.7	+37:07:20	12(2)	12(3)	1.08(0.03)
NGC 7077	21:29:59.6	+02:24:51	43(2)	108(2)	4.56(0.08)
NGC 7360	22:43:33.9	+04:09:04	54(2)	70(3)	3.71(0.04)
UGC 12265N	22:57:36.0	+19:47:26	49(2)	106(3)	4.19(0.04)
UGC 5923	10:49:07.6	+06:55:02	109(3)	316(4)	11.06(0.05)
UGC 6003	10:53:03.8	+04:37:54	117(2)	305(4)	10.35(0.05)
UGC 6570	11:35:49.1	+35:20:06	48(3)	157(3)	4.73(0.04)
UGC 6637	11:40:24.8	+28:22:26	71(2)	203(4)	6.18(0.04)
UGC 6655	11:41:50.6	+15:58:26	125(2)	379(3)	11.24(0.05)
UGC 6805	11:50:12.3	+42:04:28	27(2)	97(3)	3.06(0.04)
UGC 7020	12:02:37.6	+64:22:35	29(3)	64(3)	1.53(0.03)
UGC 8876	13:56:58.0	+45:58:24	30(2)	13(3)	0.38(0.03)
UGC 9562	14:51:14.4	+35:32:32	24(2)	65(3)	1.84(0.03)

5.2.1 *Spitzer* IRAC Data

Most of the galaxies in our sample were observed as part of in the *Spitzer* program GO-30406 (PI Kannappan). The galaxies were observed in a 16-position medium-scale cycling dither pattern in 16 \times 30 s exposure sequences for a total of 480 s on source in all four channels with IRAC. We used *Spitzer* archival data for the remaining galaxies (NGC 3073, NGC 3773, NGC 5338, NGC 7077). Most were observed with the same setup; the one exception was NGC 3605, which was observed in a 8 \times 12 s pattern, resulting in poorer signal to noise compared to the rest of the sample. The basic calibrated data (bcd) from the *Spitzer* archive were run through

a specialized pipeline to register the images, and then mosaiced using the “drizzle” method, resulting in improved resolution and a pixel scale of $0.75''$. See Regan et al. (2006) for a detailed description of the data pipeline.

The 3.6 and $4.5\ \mu\text{m}$ images were convolved with kernels (Gordon et al. 2008) designed to match the $8\ \mu\text{m}$ PSF. Following Regan et al. (2006), we estimated the background flux level by choosing four star-free regions in each channel image. We fitted the distribution of pixel intensities for each region with a Gaussian and subtracted the peak value of the Gaussian from each image. The median sky level is $50\ \text{kJy sr}^{-1}$ at $3.6\ \mu\text{m}$, $106\ \text{kJy sr}^{-1}$ at $4.5\ \mu\text{m}$, and $4.4\ \text{MJy sr}^{-1}$ at $8\ \mu\text{m}$. Within individual images, the sky variance at $3.6\ \mu\text{m}$ ranges from 2 to $9\ \text{kJy sr}^{-1}$, with a median of $3\ \text{kJy sr}^{-1}$; the sky variance at $4.5\ \mu\text{m}$ ranges from 2 to $17\ \text{kJy sr}^{-1}$, with a median of $3\ \text{kJy sr}^{-1}$; and the sky variance at $8\ \mu\text{m}$ ranges from 26 to $150\ \text{kJy sr}^{-1}$, with a median of $40\ \text{kJy sr}^{-1}$. We adopt the variance of the four sky background fits in each image as the error in our radial profile analysis (§5.3.3), since this dominates other sources of error.

The stellar emission in the $8\ \mu\text{m}$ channel is modeled following Pahre et al. (2004b) by scaling the 3.6 and $4.5\ \mu\text{m}$ channels to match the colors of M0 III stars expressed in magnitude units as:

$$[3.6] - [4.5] = -0.15 \tag{5.1}$$

$$[4.5] - [5.8] = +0.11 \tag{5.2}$$

$$[5.8] - [8.0] = +0.04 \tag{5.3}$$

and taking the average of the $3.6\ \mu\text{m}$ and $4.5\ \mu\text{m}$ channels. For this Chapter, we refer to $8\ \mu\text{m}$ flux from which stellar emission has been subtracted as “ $8\ \mu\text{m}$ PAH emission”.

5.2.2 Supplementary Data

Chapter 3 contains a description of CARMA CO(1–0) observations and data reduction for select E/S0s in our sample. IRAM 30 m CO(1–0) observations are from S. Kannappan et al. 2010 (in preparation) and D. Stark et al. 2010 (in preparation). We assume a CO-to-H₂ conversion factor (X_{CO}) of $2 \times 10^{20} \text{cm}^{-2} (\text{K km s}^{-1})^{-1}$.

Stellar masses were estimated by KGB by fitting stellar population models to *UBRJHK* photometry and integrated spectrophotometry. We also use star formation rates calculated by KGB from extinction-corrected H α spectral line data, integrated by scanning the slit across each galaxy and calibrated against IRAS-based star formation rates (SFRs) following Kewley et al. (2002).

5.2.3 Radial Profiles

Radial profiles of the 3.6 μm , 8 μm PAH, and CO(1–0) surface brightnesses ($\langle I_{3.6} \rangle_R$, $\langle I_{8.0 \text{ PAH}} \rangle_R$, and $\langle I_{\text{CO}(1-0)} \rangle_R$) were derived by azimuthally averaging the emission in rings using the ELLIPSE task in IRAF. We provided initial guesses for position angle and ellipticity, and allowed the task to vary the parameters while fitting the stellar light at 3.6 μm in steps of 0.75'' inward and outward starting from a semi-major axis of 10''. To ensure accurate comparison between the different tracers, we used the ellipse parameters estimated from fits to the 3.6 μm distribution to calculate the elliptical annuli used for 3.6 μm , 8 μm PAH, and CO(1–0) emission.

5.3 $8\ \mu\text{m}$ PAH Emission and Stellar Emission

5.3.1 Tracers of the Stellar and Star Formation Distributions

In §5.1, we presented the $8\ \mu\text{m}$ PAH emission as a star formation tracer. This assumption should be examined critically, as studies have shown that PAH emission is strongly dependent on local radiation field strength and metallicity, resulting in larger dispersions in $8\ \mu\text{m}$ luminosity at fixed SFR than at $24\ \mu\text{m}$ (e.g., Dale et al. 2005; Engelbracht et al. 2005; Wu et al. 2006; Smith et al. 2007; Calzetti et al. 2007). Regan et al. (2006) argue that the $8\ \mu\text{m}$ PAH emission is better used as a tracer of the ISM based on the good spatial correlation and constant ratio between the radial flux distributions of CO(1–0) and PAH emission. Regardless, the $8\ \mu\text{m}$ PAH emission allows us to probe star formation (or associated gas/dust content) with finer resolution (sub-kpc scales) compared to *Spitzer* $24\ \mu\text{m}$ and *GALEX* FUV emission, as well as superior signal to noise compared to interferometric CO(1–0) observations, for a large sample of E/S0s. In this Chapter, we assume that the $8\ \mu\text{m}$ PAH emission approximately traces the star formation distributions in our E/S0s, although we acknowledge that uncertainties remain as to the factors that contribute to emission at this wavelength.

We compare with $3.6\ \mu\text{m}$ emission, which has been shown to trace both the young and old low-mass stellar populations (K–M stars; Pahre et al. 2004a). Because this wavelength is virtually unaffected by extinction, the $3.6\ \mu\text{m}$ emission is an excellent tracer of the stellar mass distribution.

5.3.2 Maps of Stellar and PAH Emission

We present maps of the IRAC emission in Figure 5.2 for our sample galaxies. The left column displays the $3.6\ \mu\text{m}$ stellar emission in false color, with contours of 0.25, 0.5, 1, 2, 4, 8, 16, and 32 MJy sr^{-1} . The right column displays the $8\ \mu\text{m}$ PAH emission in false color, with contours of 0.5, 1, 2, 4, 8, 16, 32, and 64 MJy sr^{-1} .

The color scale images are scaled to best display the emission at each wavelength, so the contour levels serve better to compare the brightness among galaxies, especially in the $8\ \mu\text{m}$ PAH images where the level of emission varies greatly from galaxy to galaxy. We compare the PAH content of our galaxies within our sample as well as with other surveys in §5.3.3. Overall, the distributions of $3.6\ \mu\text{m}$ and $8\ \mu\text{m}$ PAH emission appear very similar for most of the galaxies, although the $8\ \mu\text{m}$ PAH emission appears to be clumpier.

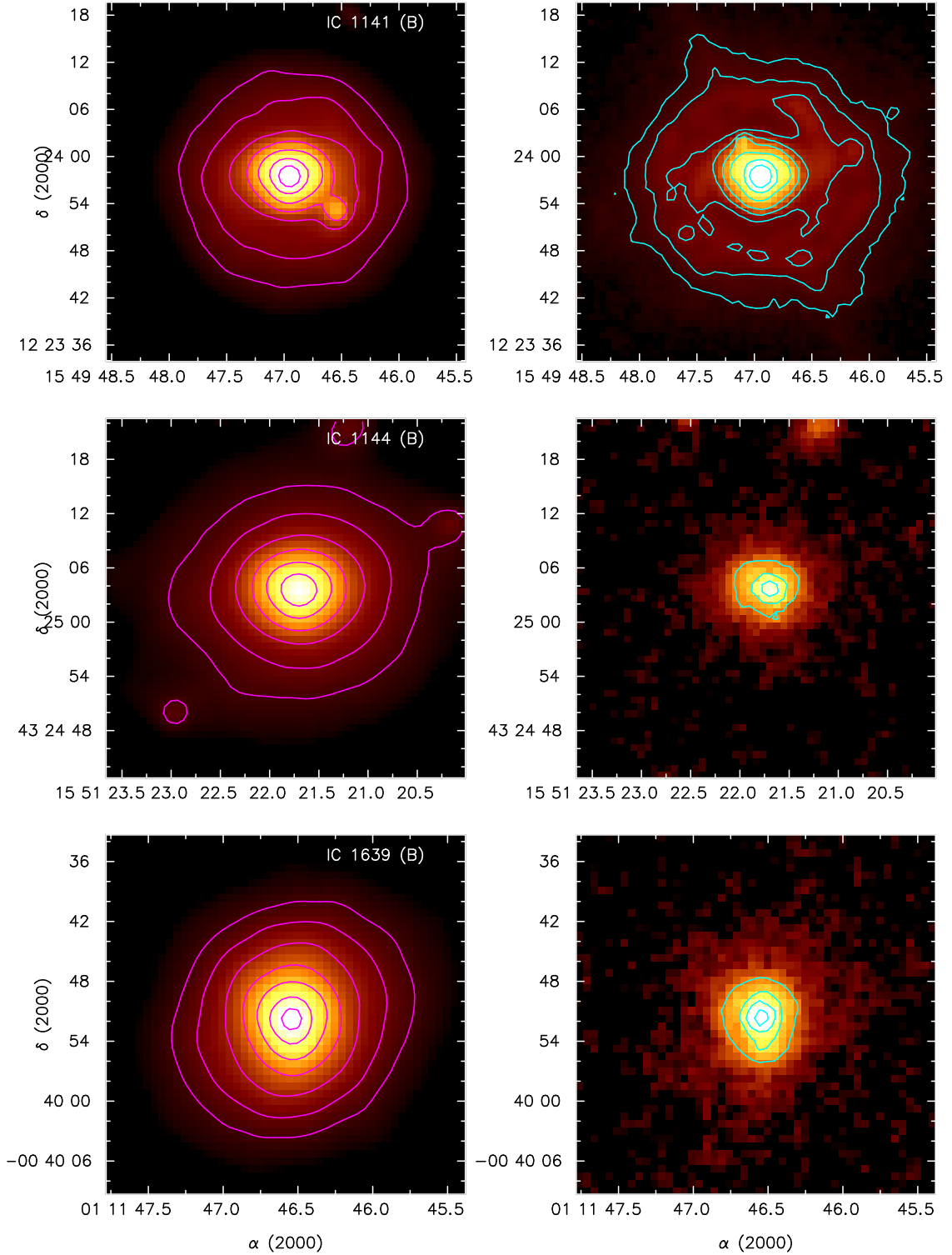


Figure 5.2: Comparison of $3.6\mu\text{m}$ and $8\mu\text{m}$ PAH emission for sample galaxies. Left: images of $3.6\mu\text{m}$ stellar emission, with contours at 0.25, 0.5, 1, 2, 4, 8, 16, and 32 MJy sr^{-1} . Galaxy name and color sequence association are noted in the upper right corner. Right: images of $8\mu\text{m}$ PAH emission for the same galaxies, with contours of 0.5, 1, 2, 4, 8, 16, 32, and 64 MJy sr^{-1} . Color scales have been adjusted individually for each galaxy to best display emission distributions.

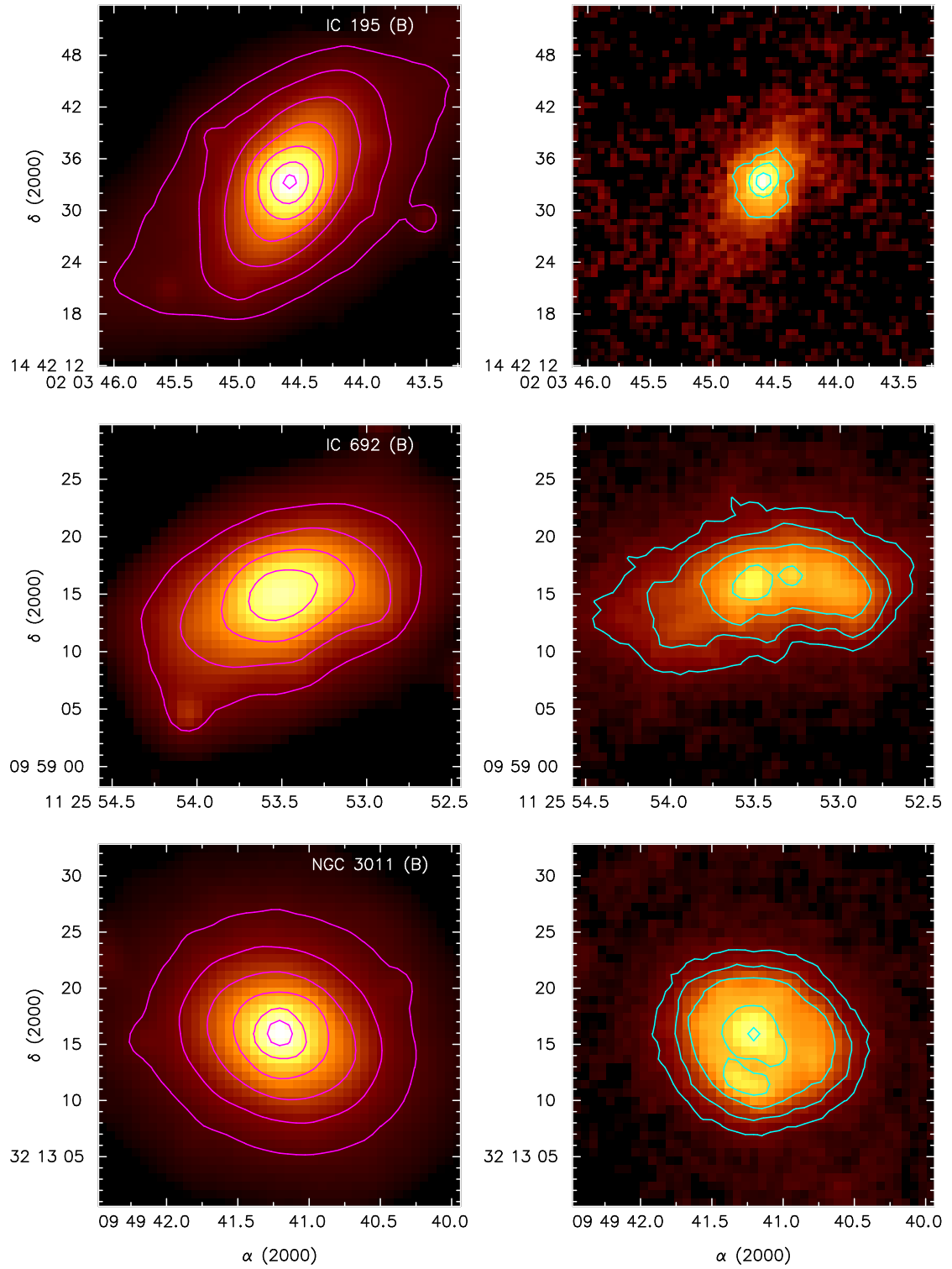


Figure 5.2: Comparison of 3.6 μm stellar (left) and 8 μm PAH (right) emission; see Figure 5.2a for details.

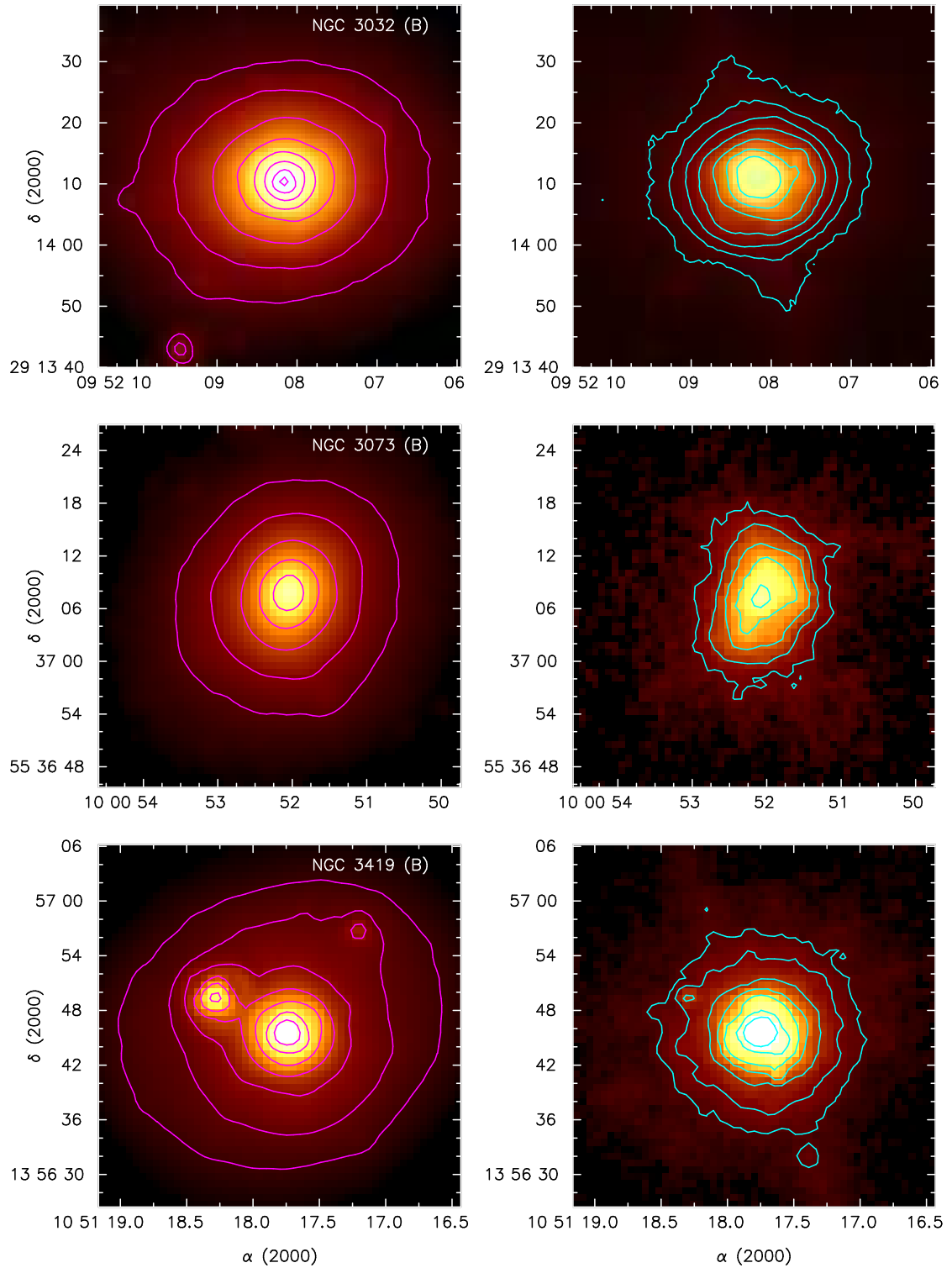


Figure 5.2: Comparison of 3.6 μm stellar (left) and 8 μm PAH (right) emission; see Figure 5.2a for details.

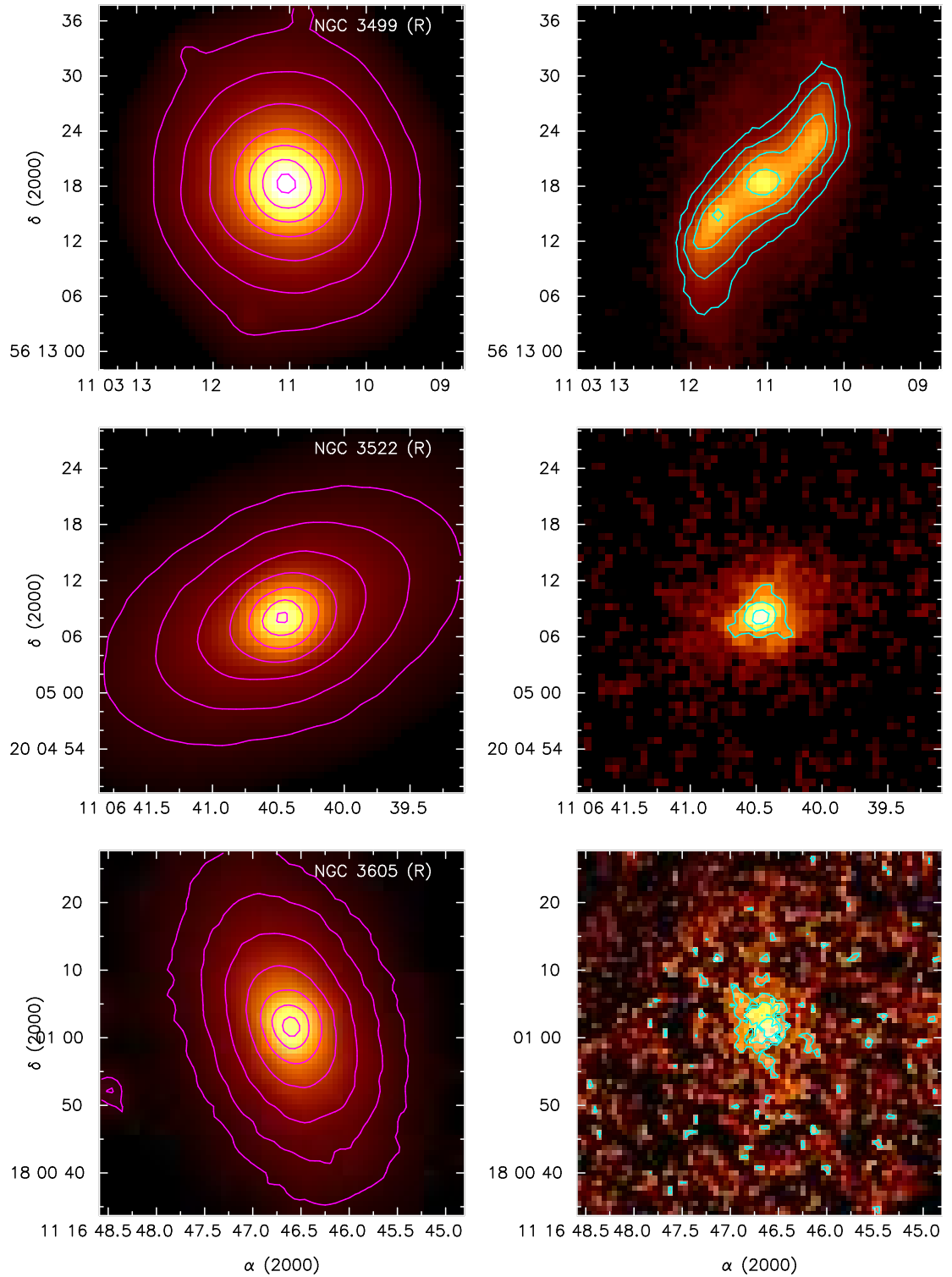


Figure 5.2: Comparison of 3.6 μm stellar (left) and 8 μm PAH (right) emission; see Figure 5.2a for details.

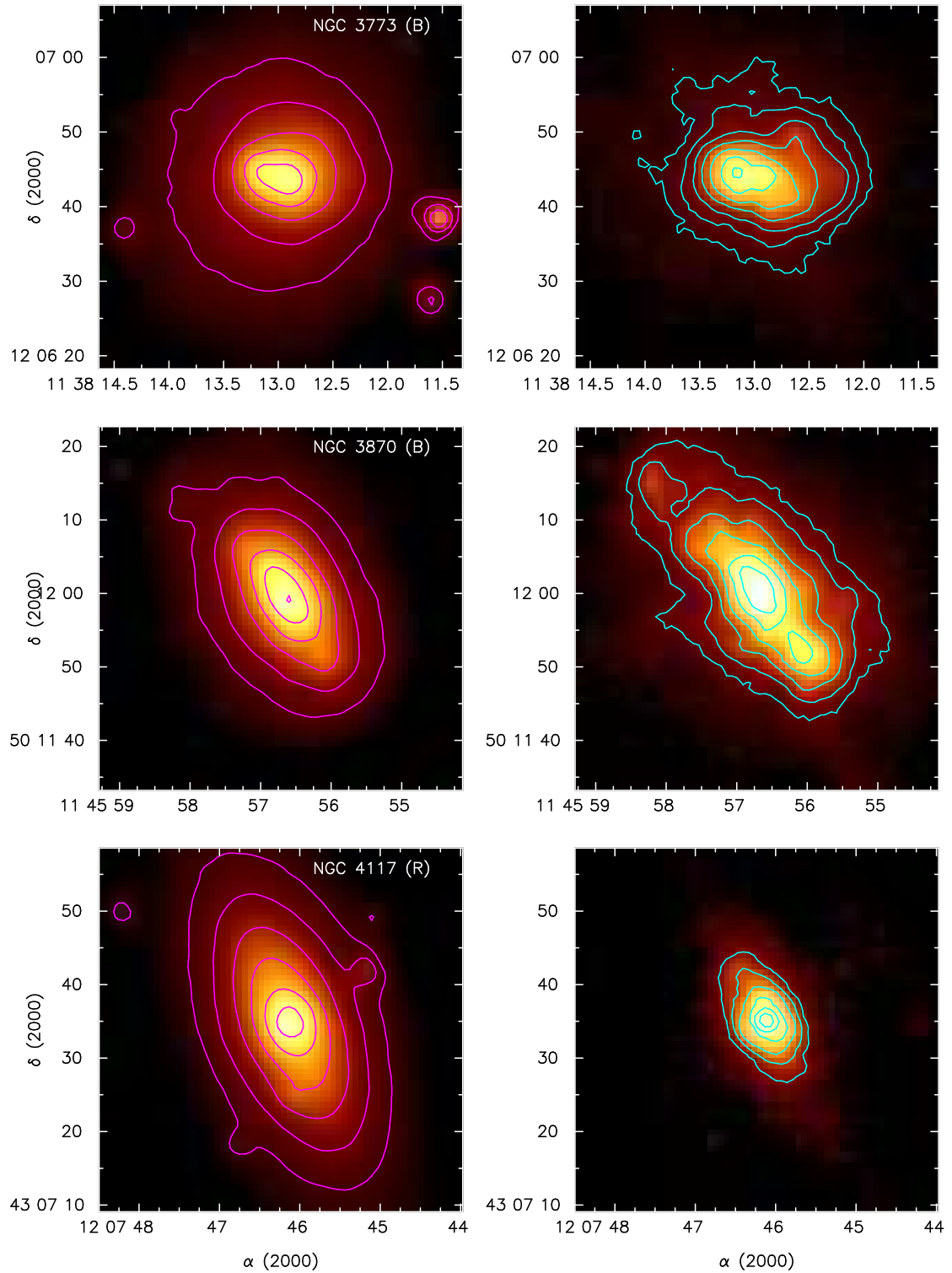


Figure 5.2: Comparison of 3.6 μm stellar (left) and 8 μm PAH (right) emission; see Figure 5.2a for details.

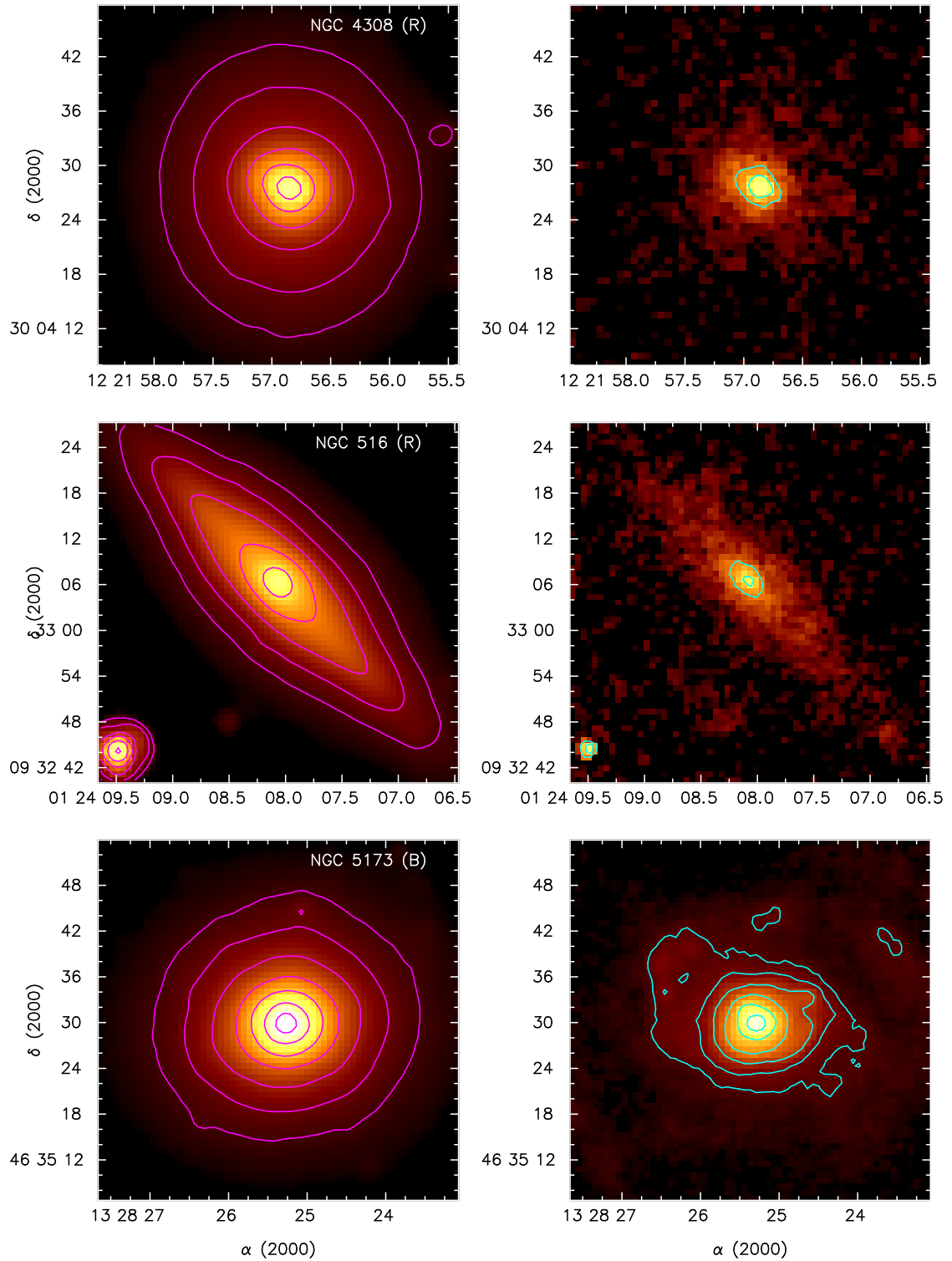


Figure 5.2: Comparison of 3.6 μm stellar (left) and 8 μm PAH (right) emission; see Figure 5.2a for details.

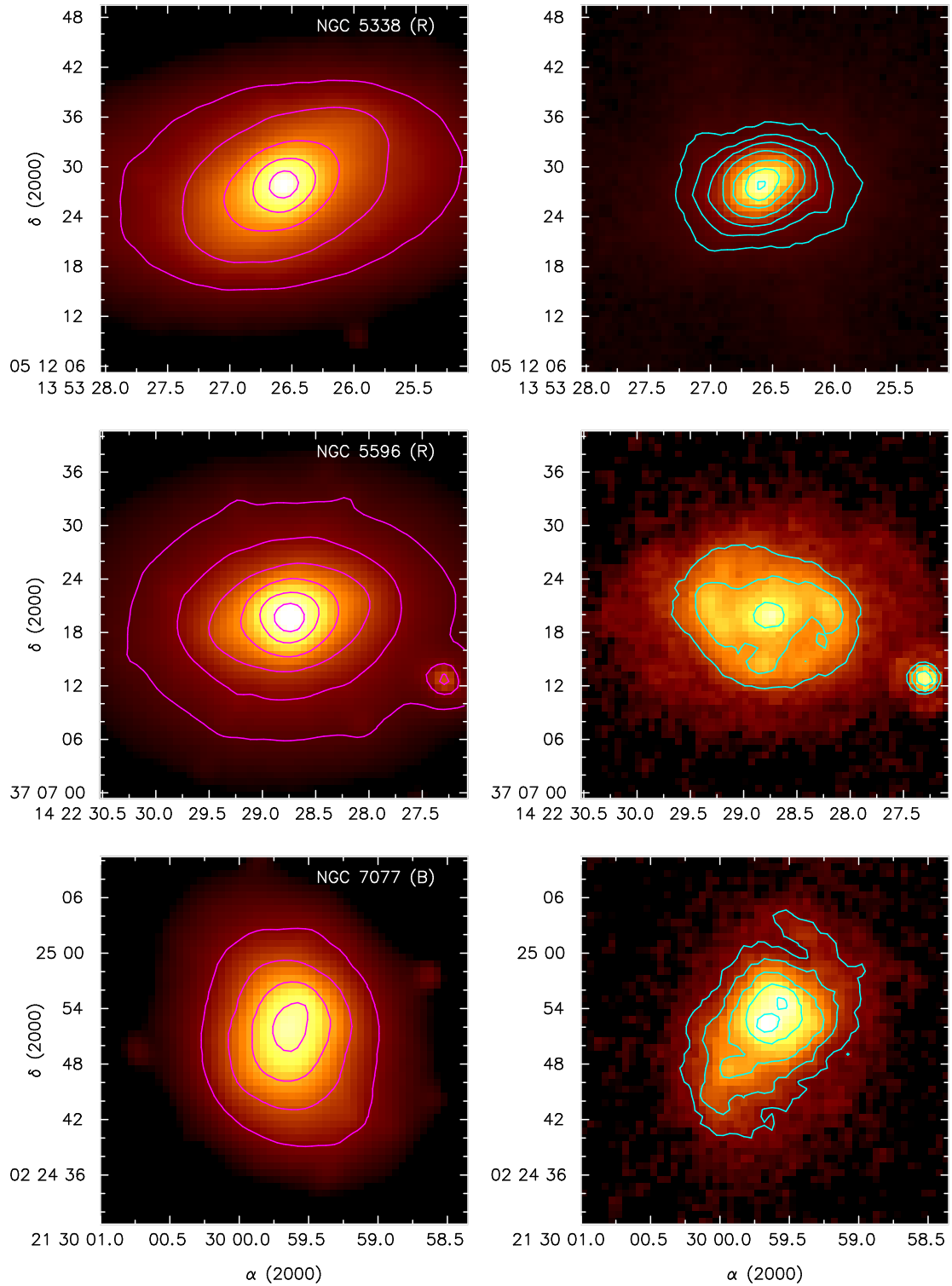


Figure 5.2: Comparison of 3.6 μm stellar (left) and 8 μm PAH (right) emission; see Figure 5.2a for details.

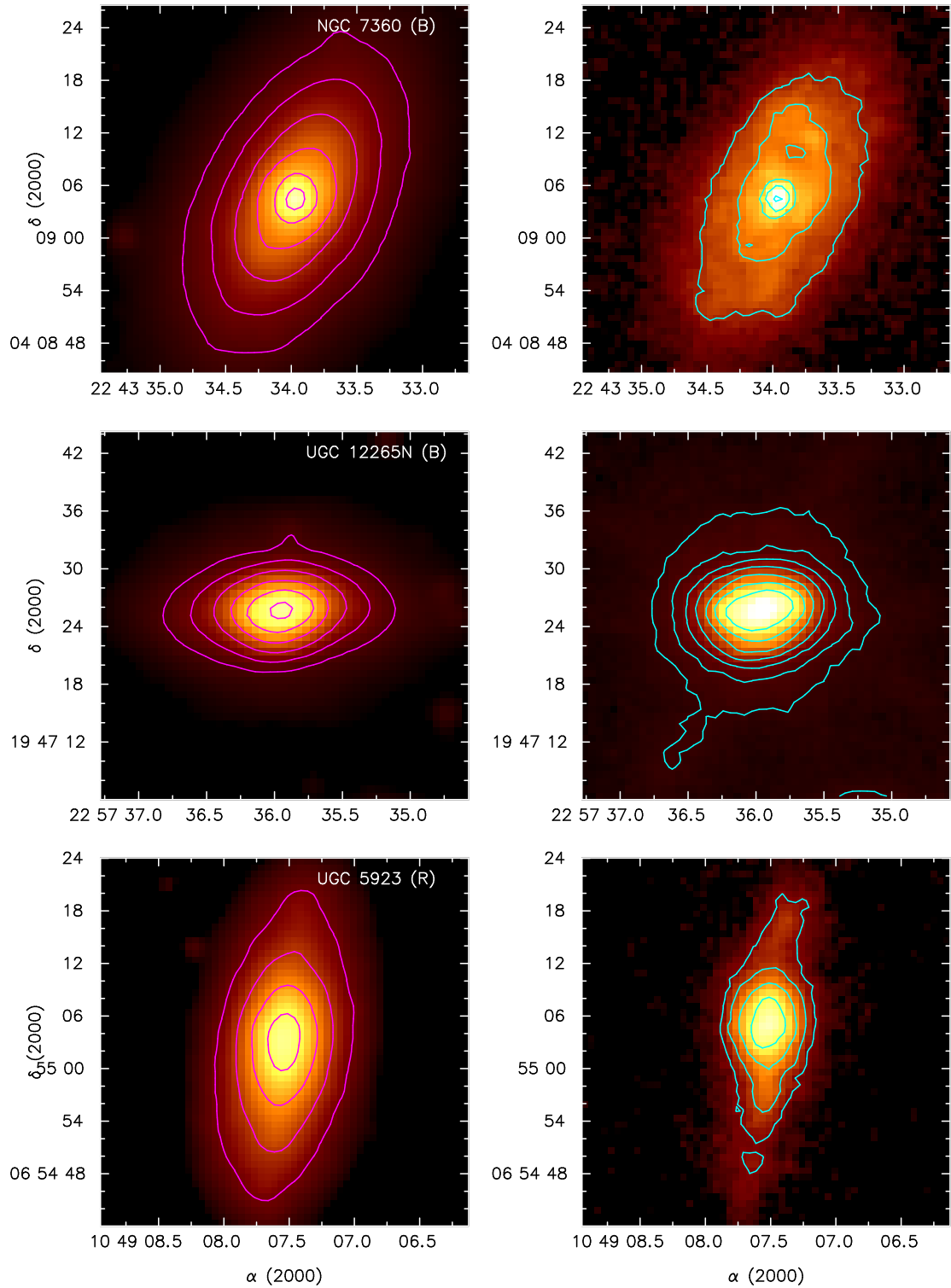


Figure 5.2: Comparison of 3.6 μm stellar (left) and 8 μm PAH (right) emission; see Figure 5.2a for details.

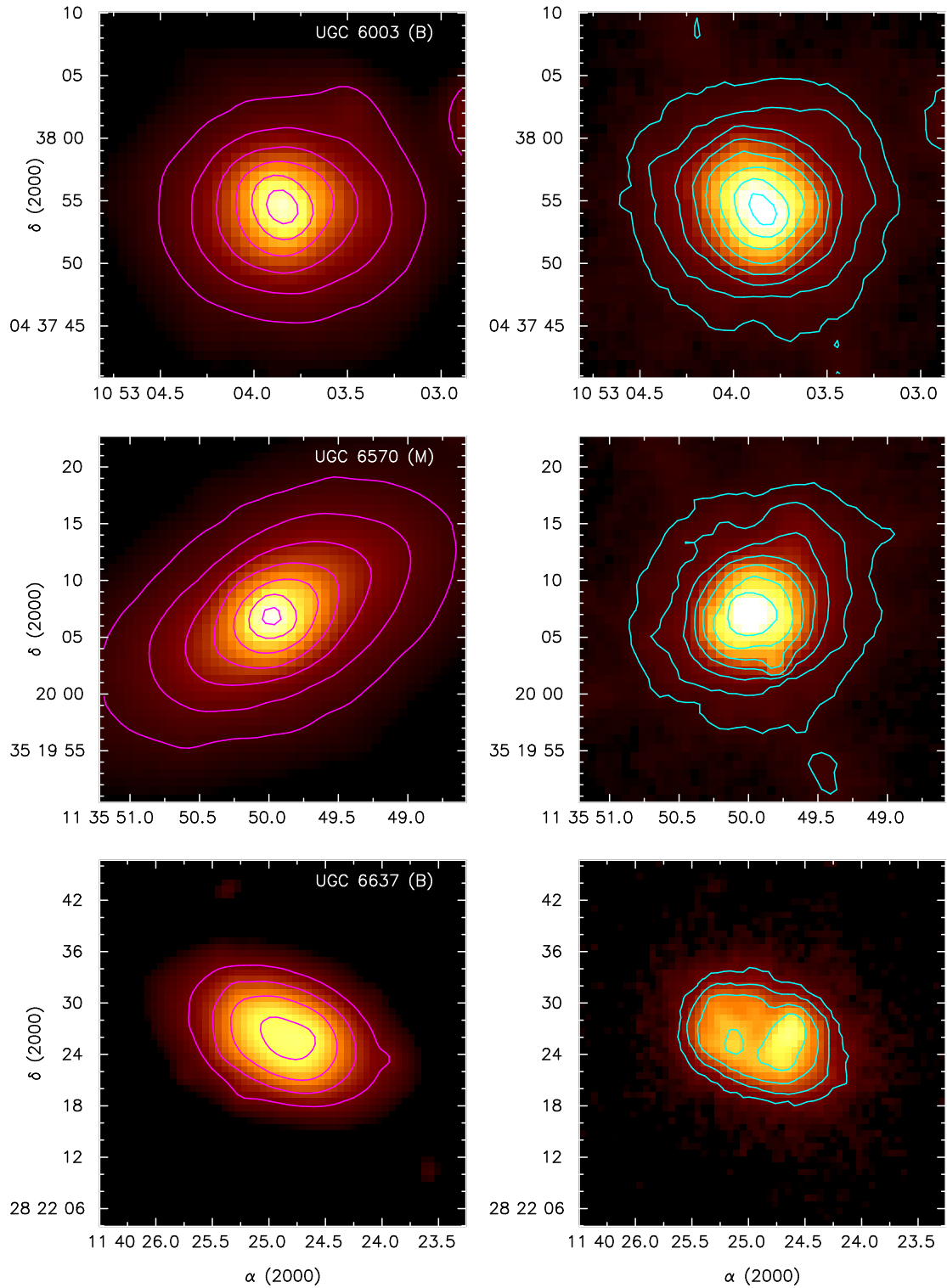


Figure 5.2: Comparison of $3.6\ \mu\text{m}$ stellar (left) and $8\ \mu\text{m}$ PAH (right) emission; see Figure 5.2a for details.

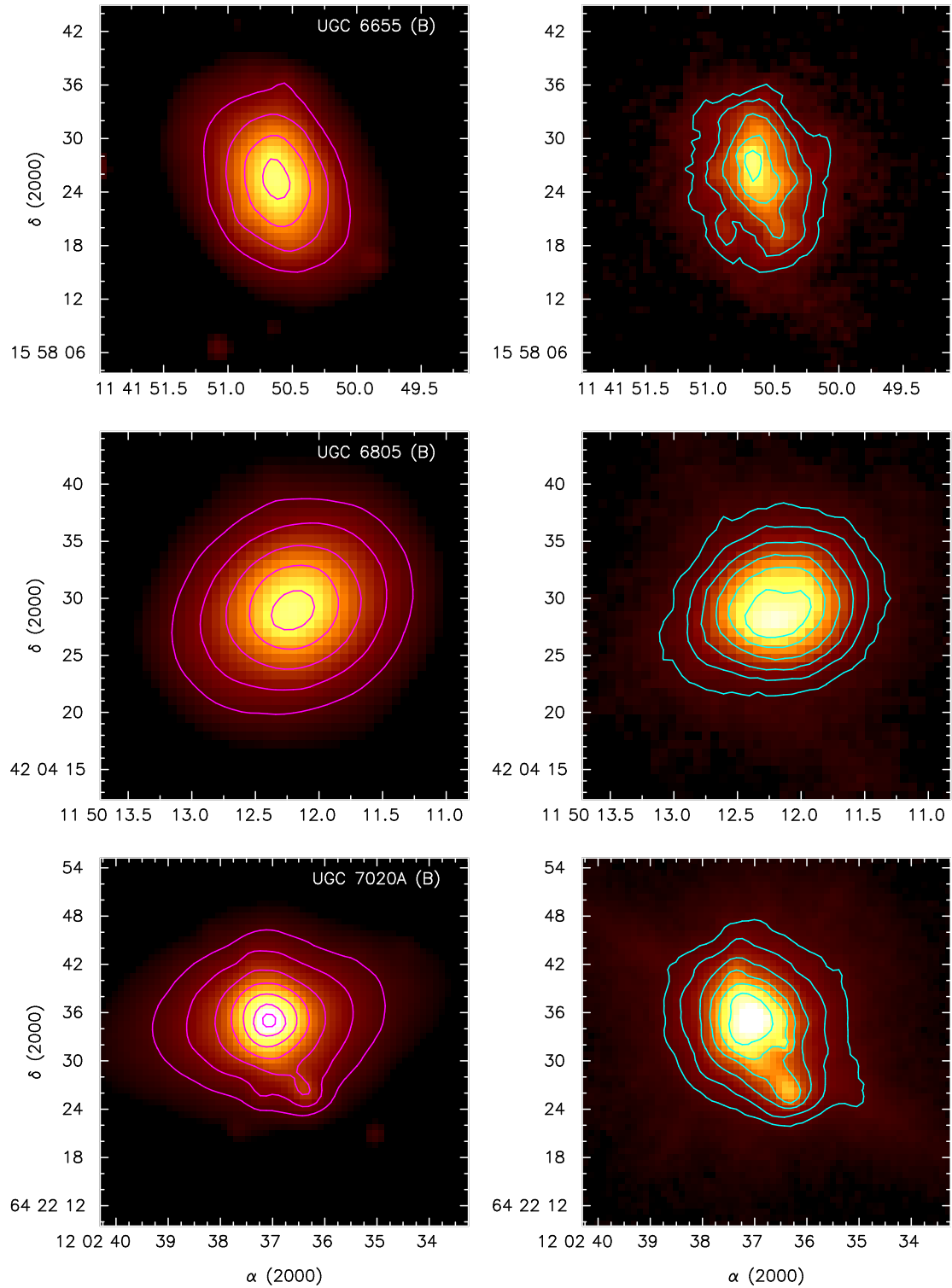


Figure 5.2: Comparison of 3.6 μm stellar (left) and 8 μm PAH (right) emission; see Figure 5.2a for details.

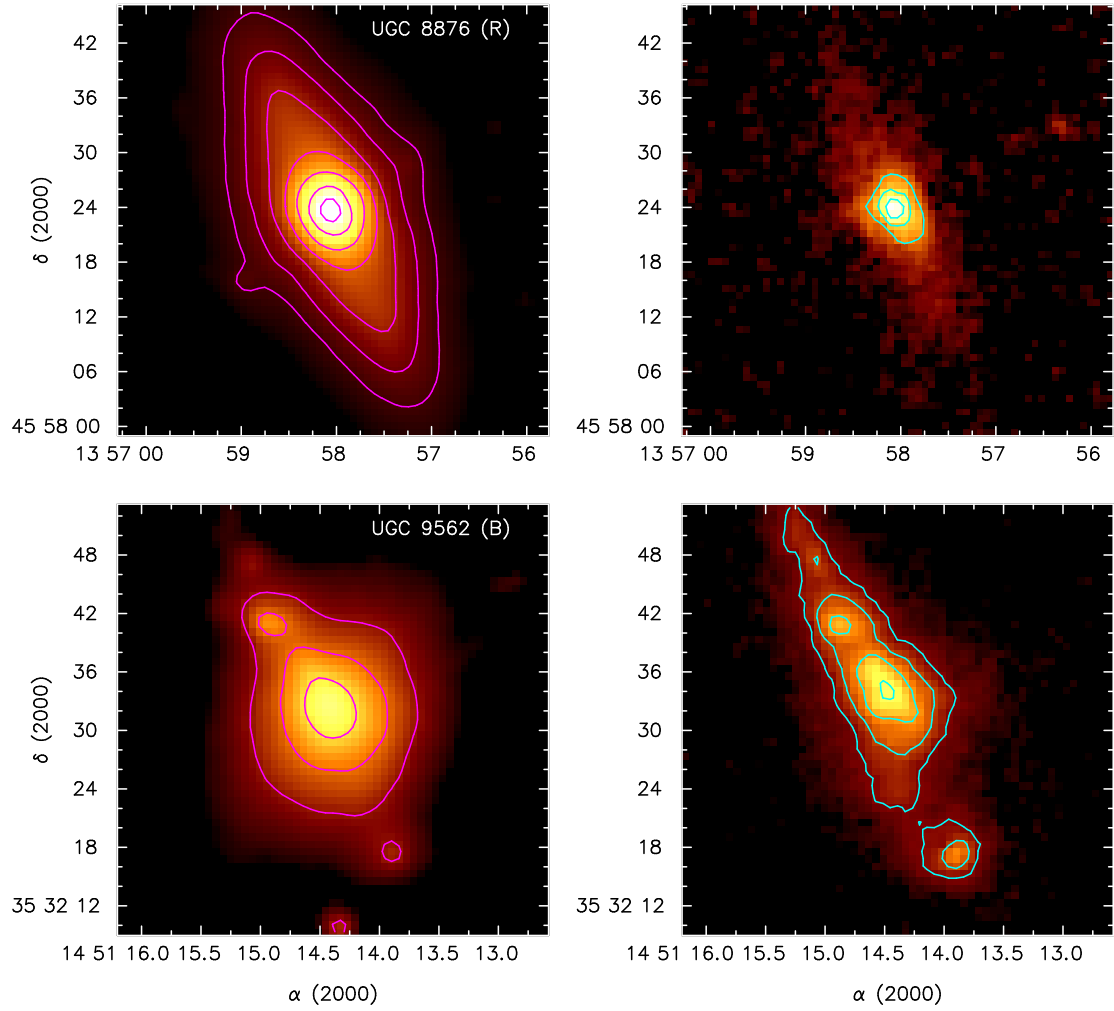


Figure 5.2: Comparison of 3.6 μm stellar (left) and 8 μm PAH (right) emission; see Figure 5.2a for details.

5.3.3 Stellar and PAH Radial Profiles

Profiles of $8\ \mu\text{m}$ PAH and $3.6\ \mu\text{m}$ surface brightness as a function of galactocentric radius (radial profiles) are presented in Figure 5.3 (right column). These were obtained by azimuthally averaging the surface brightness in concentric elliptical annuli as described in §5.2. The radial profiles are plotted over the same range in surface brightness for each galaxy to facilitate direct comparison. In each panel, we overplot the ratio of the two radial profiles — $\langle I_{8.0\text{PAH}} \rangle_R / \langle I_{3.6} \rangle_R$ — as green crosses; the galaxies are roughly ordered by decreasing $\langle I_{8.0\text{PAH}} \rangle_R / \langle I_{3.6} \rangle_R$. At large galactocentric radii, the surface brightness decreases to values comparable to or below the sky background level, and consequently the error bars become large.

We compare the $\langle I_{8.0\text{PAH}} \rangle_R / \langle I_{3.6} \rangle_R$ ratios for our E/S0s to those of star-forming spiral galaxies from the *Spitzer* Infrared Nearby Galaxies Survey (SINGS; Kennicutt et al. 2003). Figure 2 from Regan et al. (2006) shows that the $\langle I_{8.0\text{PAH}} \rangle_R / \langle I_{3.6} \rangle_R$ ratios² range from ~ 0.7 to 10 for most of their disk galaxies. We indicate this range (0.75–10) with shaded light blue backgrounds in Figure 5.3. About half of our E/S0s have values of $\langle I_{8.0\text{PAH}} \rangle_R / \langle I_{3.6} \rangle_R$ in the same range as spirals; these galaxies are primarily on the blue or mid sequence and include all but two of the 12 E/S0s we detect with CARMA in CO(1–0). Of the two red-sequence E/S0s with $\langle I_{8.0\text{PAH}} \rangle_R / \langle I_{3.6} \rangle_R \gtrsim 1.0$, one was detected in CO(1–0) (NGC 5338) and the other is the most HI-rich of our red-sequence E/S0s (UGC 5923, $M_{\text{HI}}/M_* \sim 0.5$; Chapter 2, Wei et al. 2010a).

In contrast, $\langle I_{8.0\text{PAH}} \rangle_R / \langle I_{3.6} \rangle_R$ ratios for the SAURON sample of more local, more massive E/S0s (de Zeeuw et al. 2002; Emsellem et al. 2004) span an almost completely different range. Figure 3 from Shapiro et al. (2010) shows that all but one

²Regan et al. presented $\langle I_{3.6} \rangle_R / \langle I_{8.0\text{PAH}} \rangle_R$, the inverse of the ratio used in this Chapter.

of their galaxies³ have azimuthally-averaged flux ratios ($\langle f_{8.0} \rangle_R / \langle f_{3.6} \rangle_R$) ranging from 0.3 to 1.0. This result roughly converts to $\langle I_{8.0\text{PAH}} \rangle_R / \langle I_{3.6} \rangle_R$ ratios of 0.04–0.75, after accounting for stellar emission in the $8\mu\text{m}$ channel. We shade this range in light red in Figure 5.3. The E/S0s with $\langle I_{8.0\text{PAH}} \rangle_R / \langle I_{3.6} \rangle_R$ ratios falling in this range appear to be mostly on the red sequence, with a few blue-sequence E/S0s in the mix. In the range $0.2 \lesssim \langle I_{8.0\text{PAH}} \rangle_R / \langle I_{3.6} \rangle_R \lesssim 0.75$, our E/S0s are typically blue- and red-sequence E/S0s with low amounts of gas and star formation, consistent with Shapiro et al. (2010) finding only small amounts of residual star formation in some E/S0s.

The eight galaxies with $\langle I_{8.0\text{PAH}} \rangle / \langle I_{3.6} \rangle \lesssim 0.2$ are shown in Figures 5.3i–5.3k; these are galaxies with very little PAH emission. Not surprisingly, the majority of these galaxies are red-sequence E/S0s (representing half of our red-sequence sample), consistent with the typical view of E/S0s being red and dead (i.e., containing very small amounts of gas, dust, and star formation). The three blue-sequence E/S0s in this category are the most massive of the 20 blue-sequence E/S0s in the sample ($M_* \geq 3 \times 10^{10} M_\odot$), in the range where KGB argue that blue-sequence E/S0s are major merger remnants destined to fade onto the red sequence. The deficiency of active star formation as traced by $8\mu\text{m}$ emission suggests that these blue-sequence E/S0s will quickly migrate onto the red sequence.

³NGC 3032, which is also one of our lower-mass, blue-sequence E/S0s detected in CO(1–0) by CARMA.

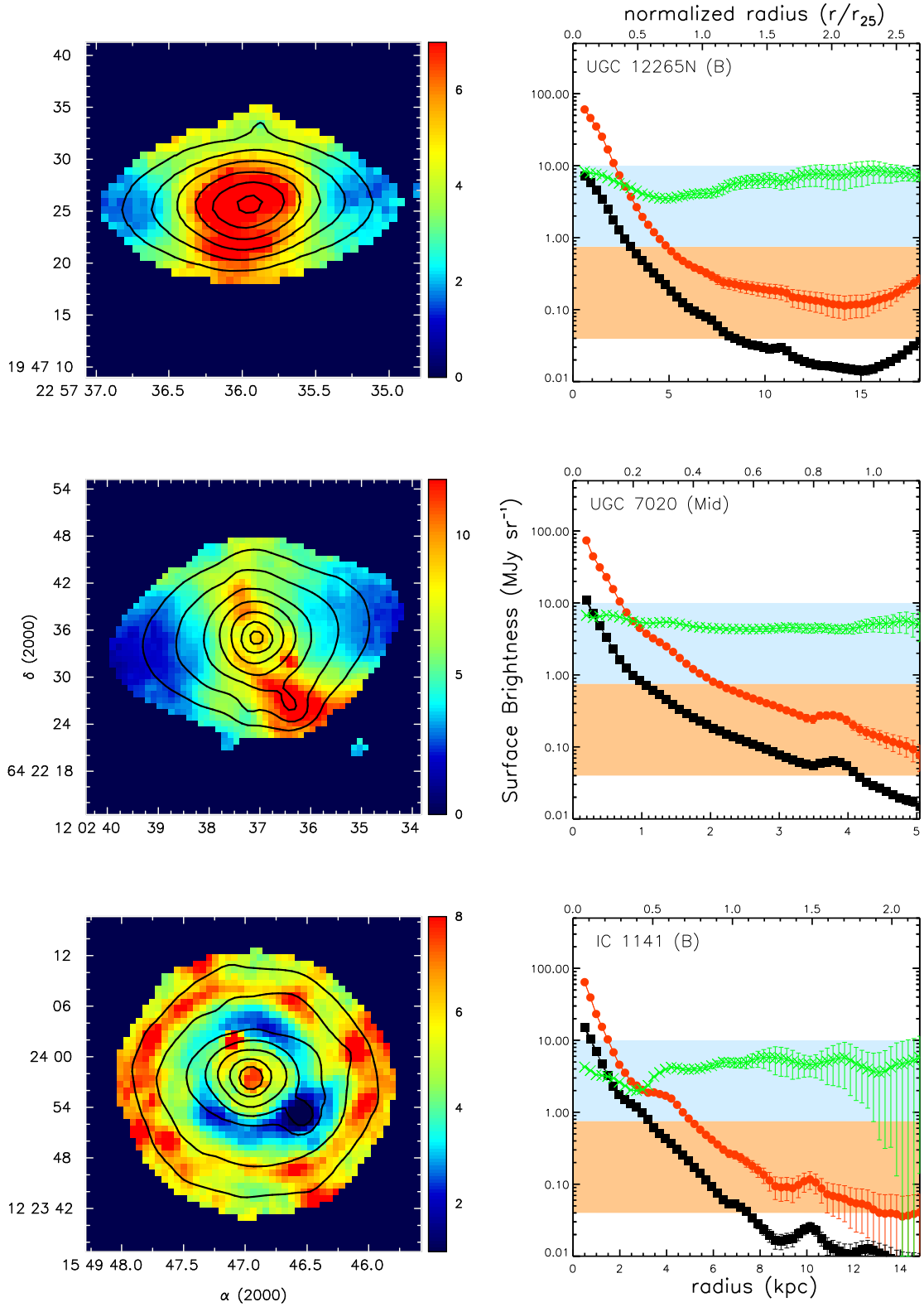


Figure 5.3: Left: Ratios of 8 μm PAH to 3.6 μm surface brightnesses, with contours of 3.6 μm emission overplotted. Images are masked at $I_{3.6} < 0.15 \text{ MJy sr}^{-1}$. Color bars indicate ratio scale. Right: Radial profiles of azimuthally-averaged surface brightnesses at 3.6 μm (black squares) and 8 μm PAH (red circles) as a function of galactocentric radius (bottom, kpc) and normalized radius (top, fraction of galaxy radius at the 25th mag isophote r_{25}) for the same E/SOs. Error bars are $\pm 1\sigma$ using the variance in sky brightness. Green crosses mark $\langle I_{8.0\text{PAH}} \rangle_R / \langle I_{3.6} \rangle_R$. We shade the region of $\langle I_{8.0\text{PAH}} \rangle_R / \langle I_{3.6} \rangle_R$ spanned by spiral galaxies (Regan et al. 2006) in light blue and the region of $\langle I_{8.0\text{PAH}} \rangle_R / \langle I_{3.6} \rangle_R$ spanned by SAURON E/SOs in light red (Shapiro et al. 2010).

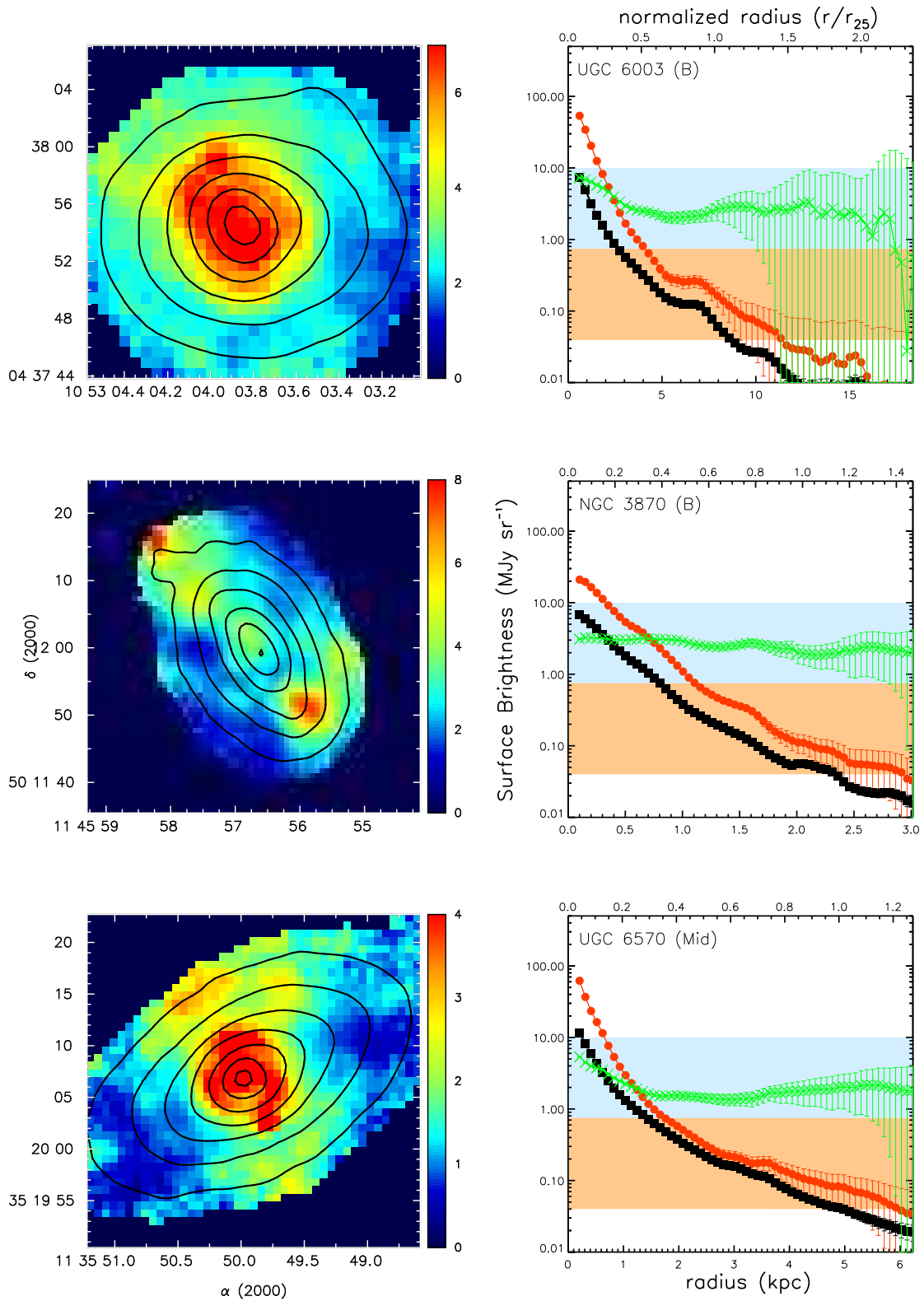


Figure 5.3: 8 μm PAH/3.6 μm ratio images (left) and radial profiles (right). See Figure 5.3a for details.

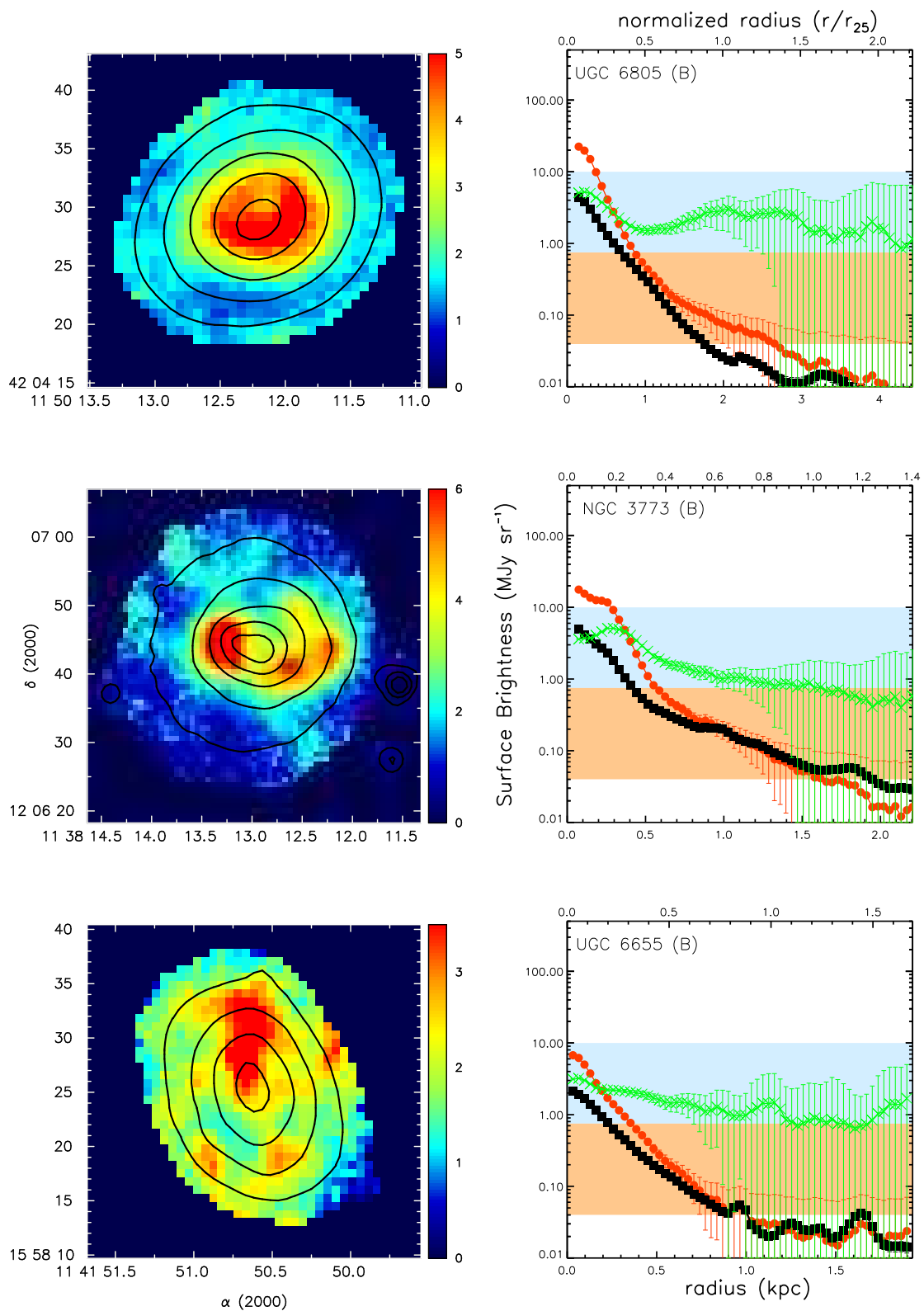


Figure 5.3: 8 μm PAH/3.6 μm ratio images (left) and radial profiles (right). See Figure 5.3a for details.

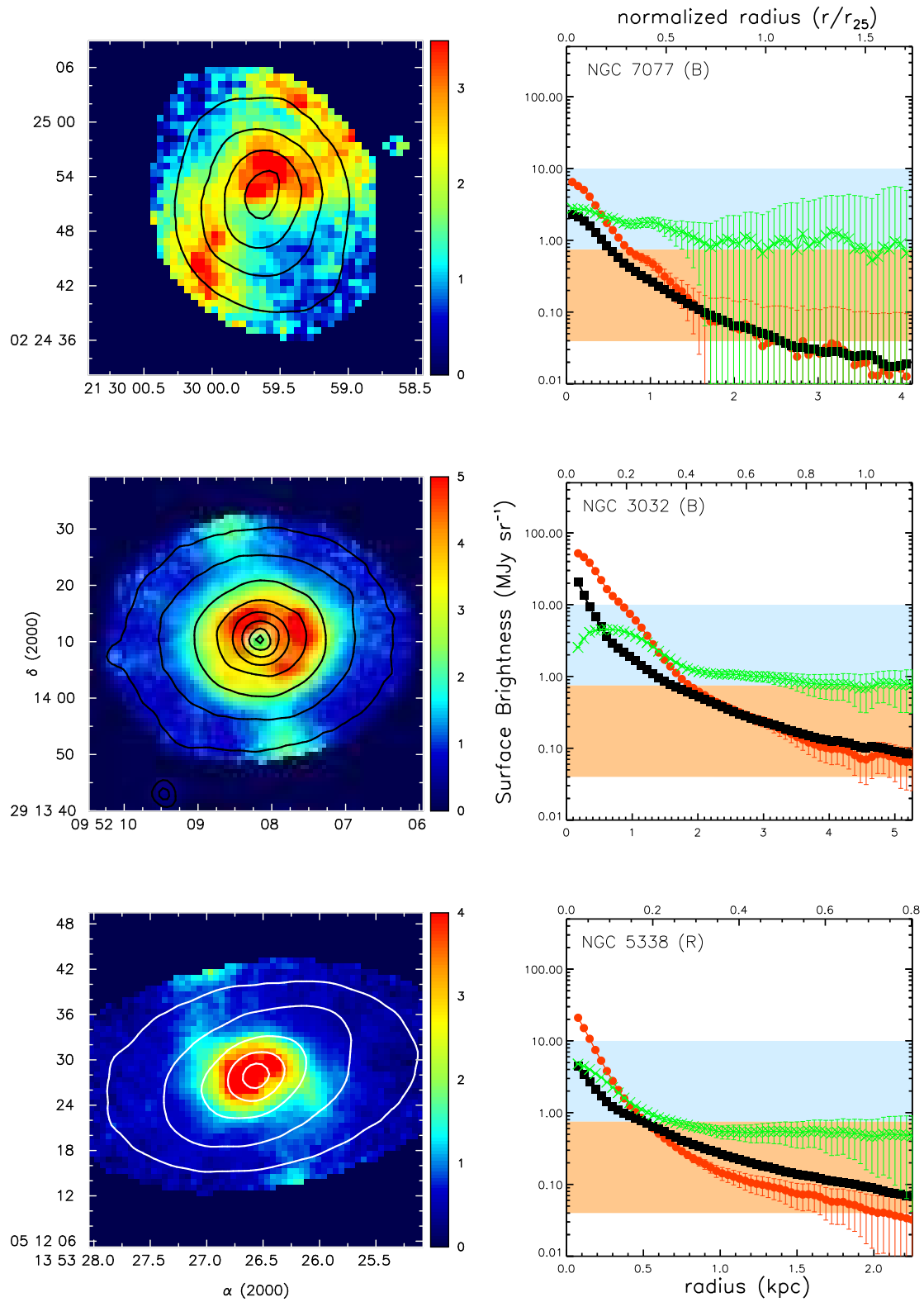


Figure 5.3: $8\ \mu\text{m}$ PAH/ $3.6\ \mu\text{m}$ ratio images (left) and radial profiles (right). See Figure 5.3a for details.

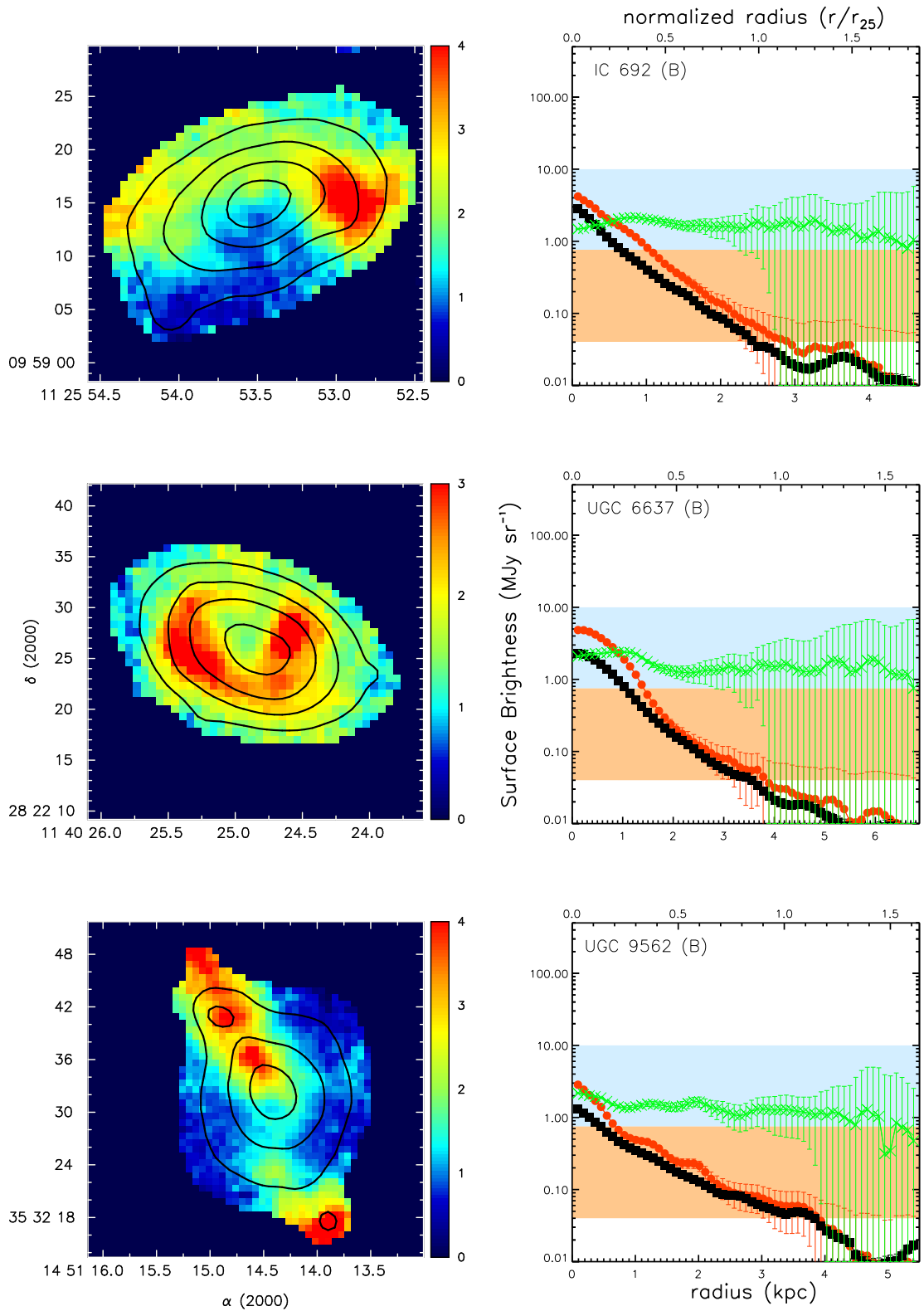


Figure 5.3: 8 μm PAH/3.6 μm ratio images (left) and radial profiles (right). See Figure 5.3a for details.

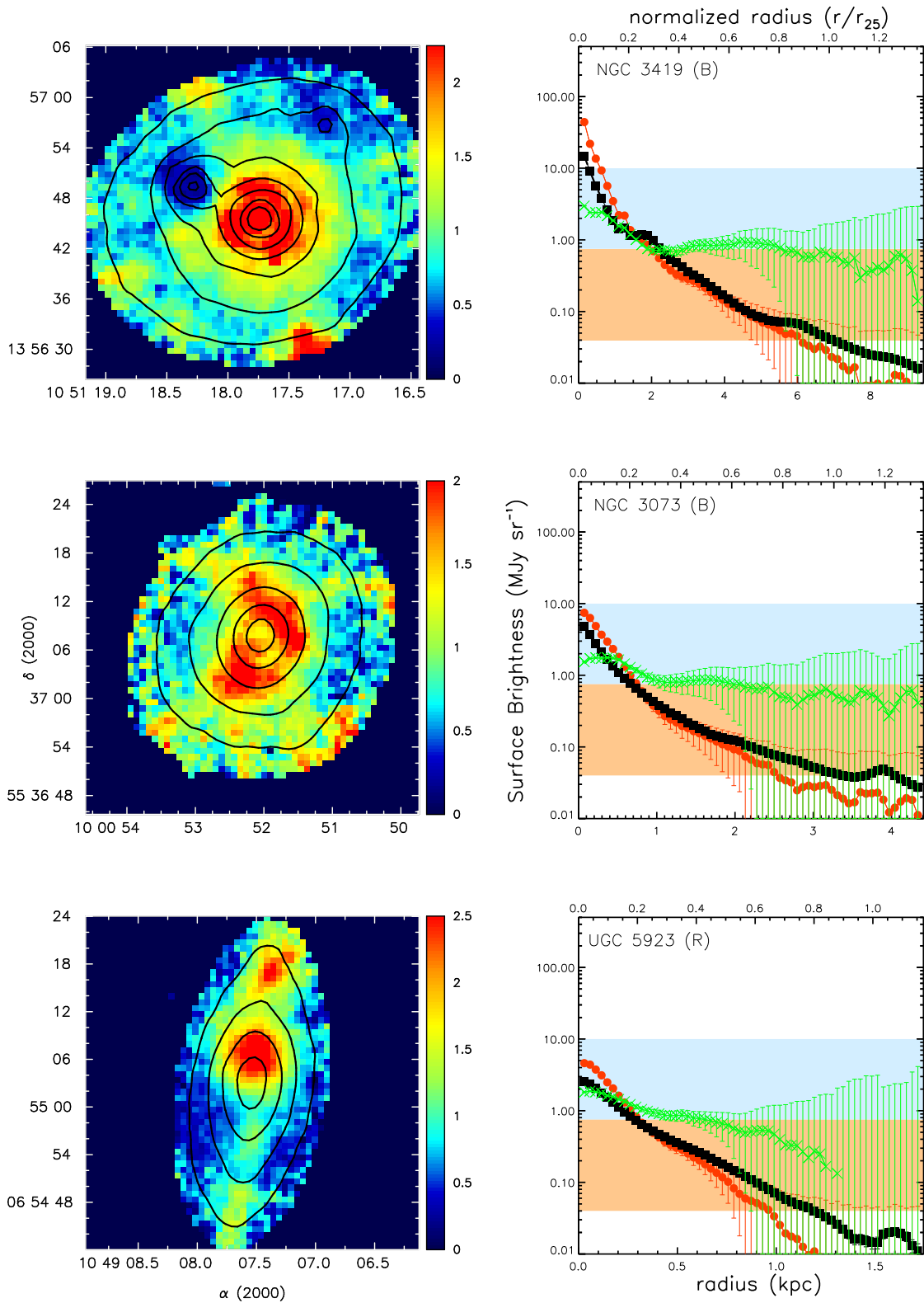


Figure 5.3: $8\ \mu\text{m PAH}/3.6\ \mu\text{m}$ ratio images (left) and radial profiles (right). See Figure 5.3a for details.

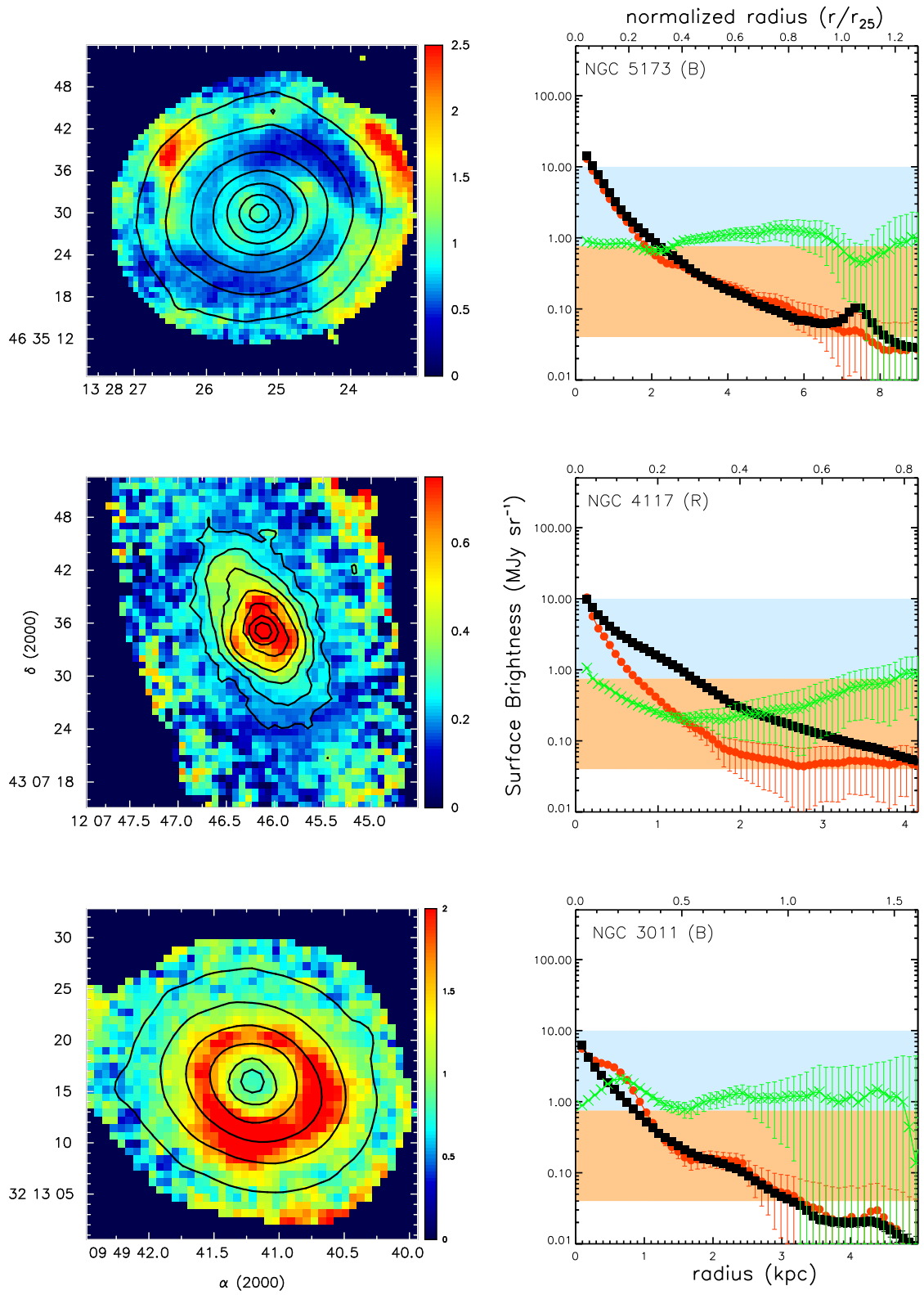


Figure 5.3: $8\ \mu\text{m}$ PAH/ $3.6\ \mu\text{m}$ ratio images (left) and radial profiles (right). See Figure 5.3a for details.

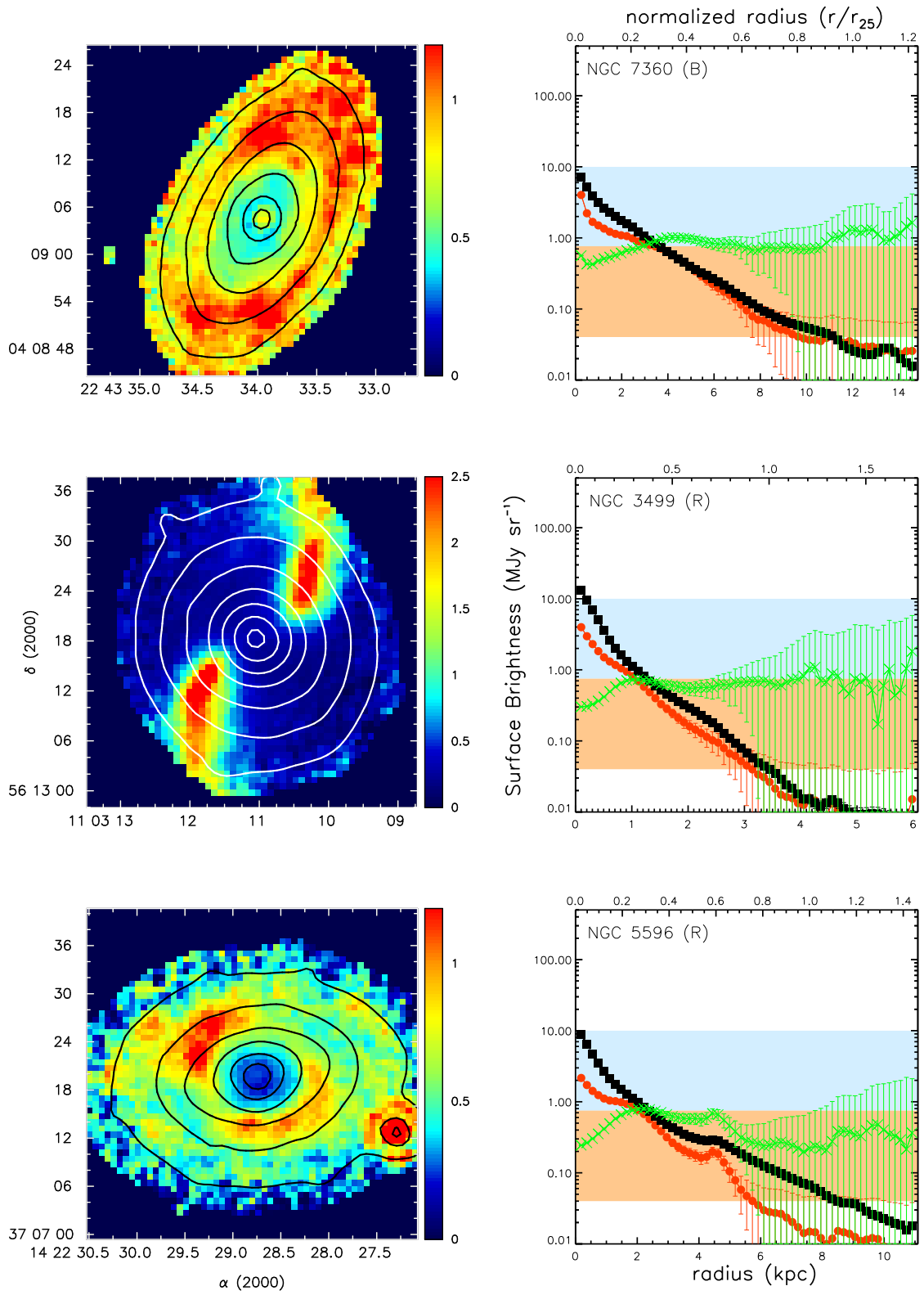


Figure 5.3: 8 μm PAH/3.6 μm ratio images (left) and radial profiles (right). See Figure 5.3a for details.

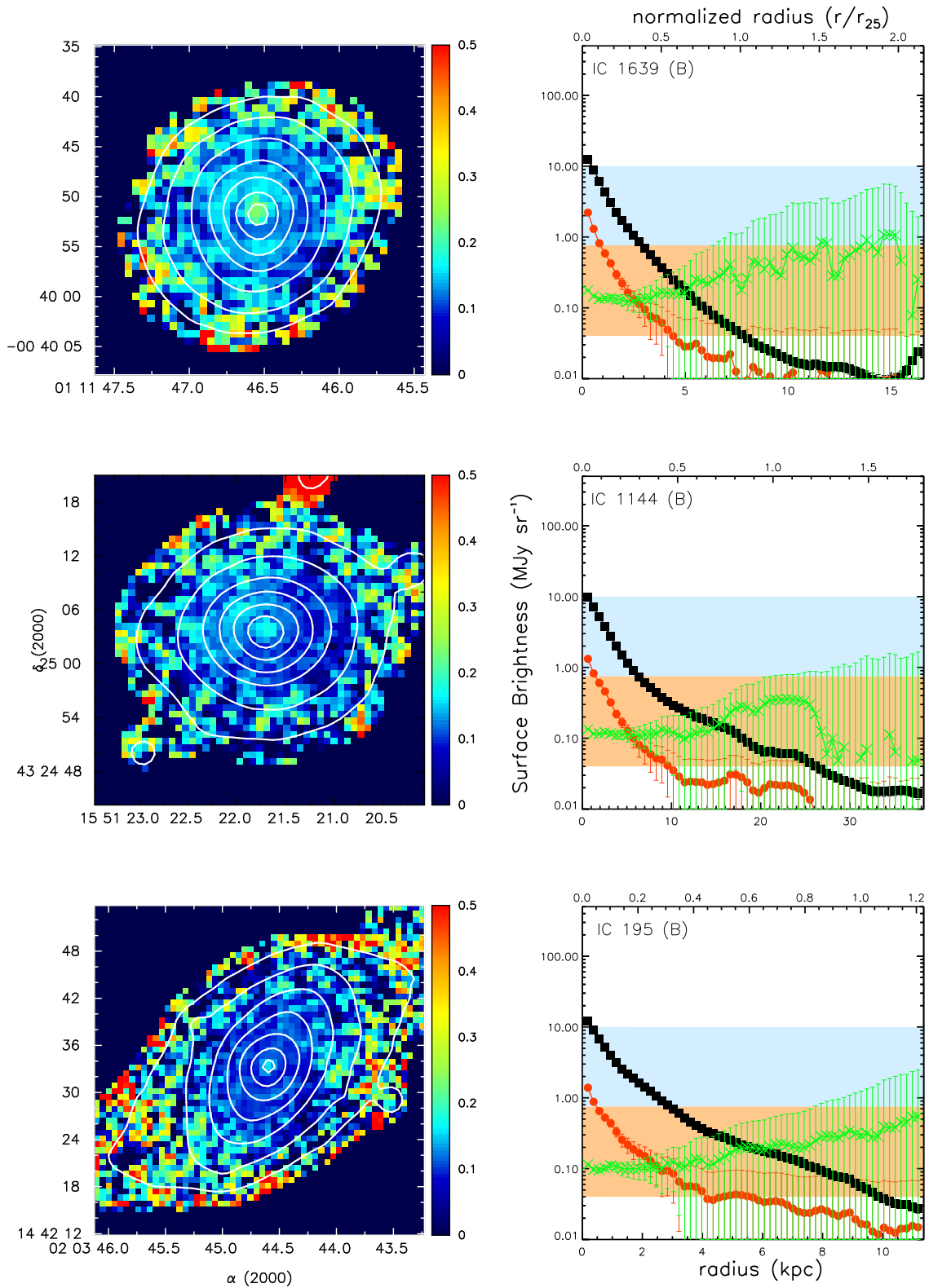


Figure 5.3: 8 μm PAH/3.6 μm ratio images (left) and radial profiles (right). See Figure 5.3a for details.

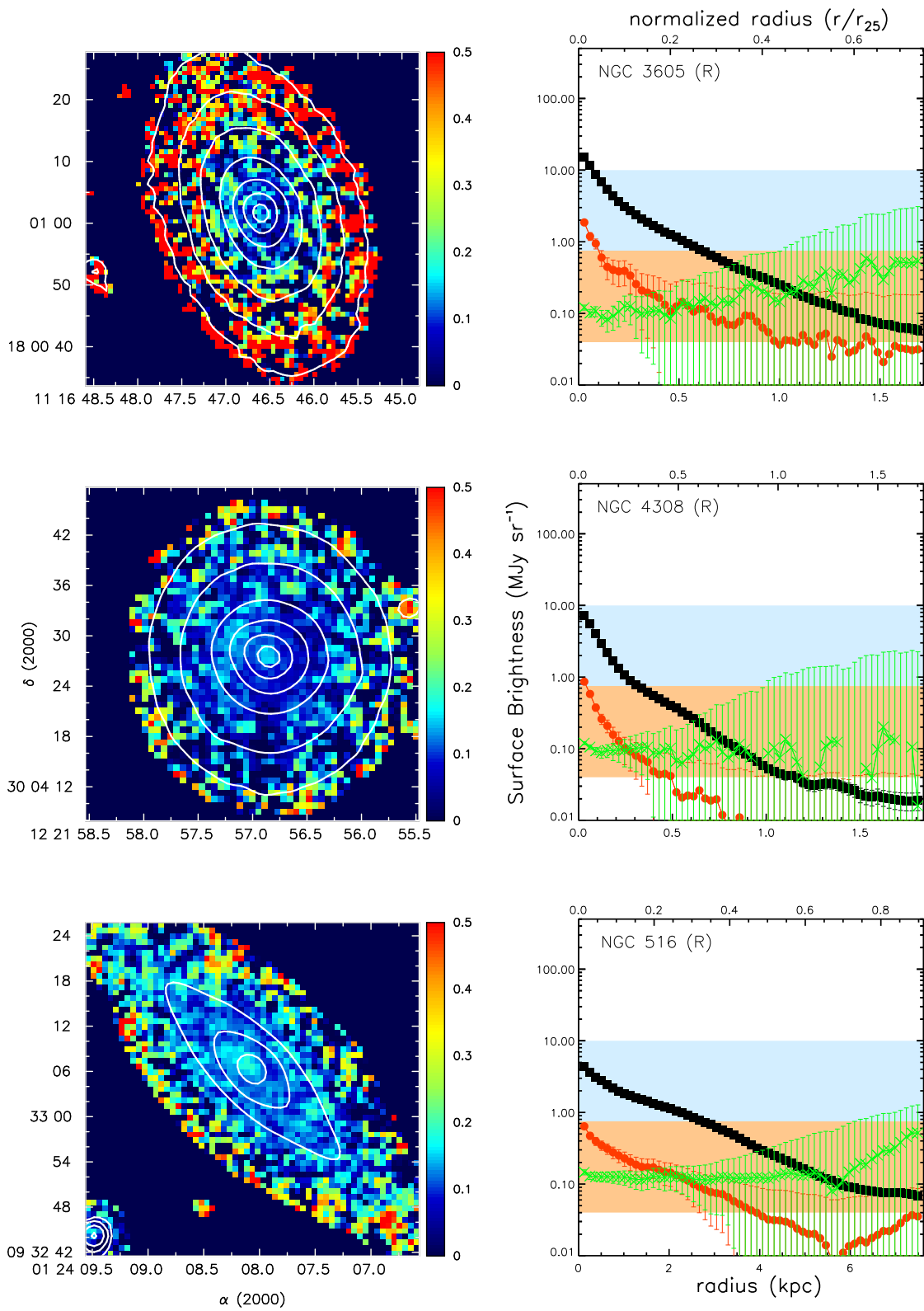


Figure 5.3: 8 μm PAH/3.6 μm ratio images (left) and radial profiles (right). See Figure 5.3a for details.

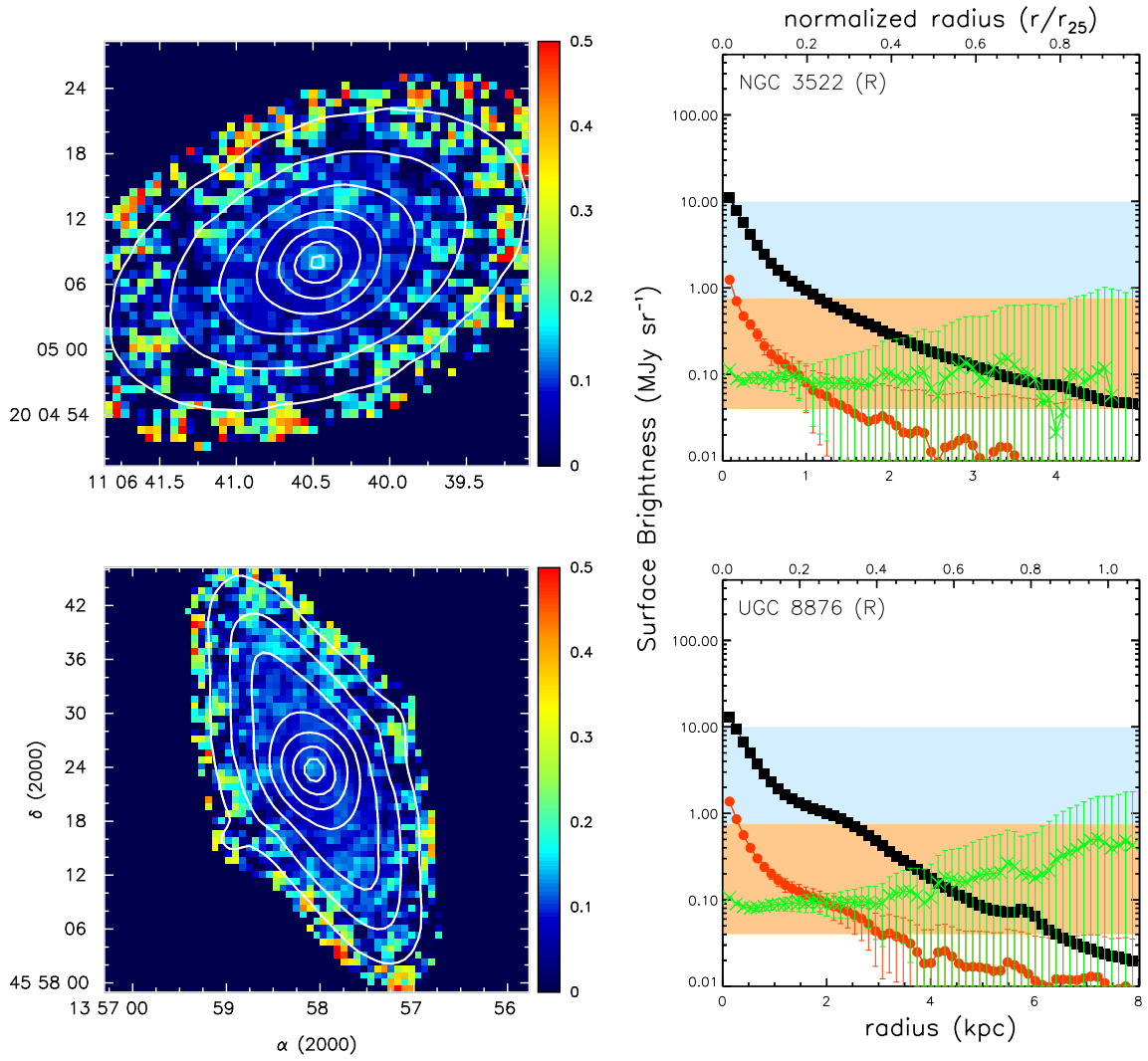


Figure 5.3: $8\ \mu\text{m}$ PAH/ $3.6\ \mu\text{m}$ ratio images (left) and radial profiles (right). See Figure 5.3a for details.

Table 5.2. Galaxy properties derived from IRAC data

Galaxy	Seq.	$\log M_*$ (M_\odot)	$f_{3.6}$ (Jy)	$f_{8.0, \text{PAH}}$ (Jy)	R (kpc)	H (kpc)	C	NA	W
	(1)	(2)	(3)	(4)	(5)	(6)	(7)	(8)	(9)
IC 1141	B	10.4	0.022	0.078	3.0*, 4.5				
IC 1144	B	11.2	0.020	0.002					×
IC 1639	B	10.6	0.020	0.002					×
IC 195	B	10.5	0.028	0.002					×
IC 692	B	8.9	0.009	0.014				×	
NGC 3011	B	9.4	0.015	0.017	0.7				
NGC 3032	B	9.6	0.054	0.135	0.7		×		
NGC 3073	B	9.1	0.019	0.016	0.4		×		
NGC 3419	B	10.0	0.016	0.045			×		
NGC 3499	R	9.9	0.028	0.013				×	
NGC 3522	R	9.7	0.025	0.001					×
NGC 3605	R	9.2	0.049	0.002					×
NGC 3773	B	8.6	0.023	0.054	0.35		×		
NGC 3870	B	8.8	0.021	0.061				×	
NGC 4117	R	9.7	0.030	0.011			×		
NGC 4308	R	8.7	0.021	0.001					×
NGC 516	R	10.1	0.021	0.001					×
NGC 5173	B	10.3	0.037	0.030	2.1*				
NGC 5338	R	8.9	0.019	0.027			×		
NGC 5596	R	10.4	0.024	0.009		2.25			
NGC 7077	B	8.8	0.011	0.015				×	
NGC 7360	B	10.5	0.020	0.012		4.5			
UGC 12265N	B	10.1	0.010	0.063			×		
UGC 5923	R	8.1	0.010	0.010				×	
UGC 6003	B	10.1	0.012	0.053			×		
UGC 6570	M	9.6	0.020	0.056			×		
UGC 6637	B	9.2	0.008	0.015	1.2		×		
UGC 6655	B	8.0	0.009	0.014				×	
UGC 6805	B	8.9	0.010	0.031	0.2		×		
UGC 7020A	M	9.3	0.018	0.106				×	
UGC 8876	R	10.2	0.027	0.002					×
UGC 9562	B	8.9	0.009	0.011				×	

* $I_{8.0 \text{ PAH}}/I_{3.6}$ rings are depressions as opposed to excesses.

Note. — Total 3.6 μm and 8 μm PAH fluxes ($f_{3.6}$, $f_{8.0, \text{PAH}}$) are estimated by summing over the region with surface brightness $>$ the sky variance in that channel. Columns 5–9 characterize the structures observed in $I_{8.0 \text{ PAH}}/I_{3.6}$ in Figure 5.3 as follows: (**R**) approximate distance to ring or ring-like structure from the center in kpc, (**H**) approximate radius of central depression in kpc, (**C**) centrally concentrated emission, (**NA**) non-axisymmetric emission, and (**W**) very weak 8 μm PAH emission.

5.3.4 Structure in the PAH Emission

Figures 5.2 and 5.3 suggest that there are small-scale differences between the distributions of 3.6 μm and 8.0 μm PAH emission. To help compare the distributions of these two tracers, we show the spatial distribution of the $I_{8.0 \text{ PAH}}/I_{3.6}$ ratios for our galaxies in the left column of Figure 5.3. To avoid displaying spurious high ratios,

we mask the images at pixels where $I_{3.6} < 0.15 \text{ MJy sr}^{-1}$. This cutoff corresponds to $\sim 0.5\text{--}1 \text{ MJy sr}^{-1}$ for the most $8 \mu\text{m}$ PAH-luminous E/S0s, down to the sky variance level for some red-sequence E/S0s, so no significant $8 \mu\text{m}$ PAH emission was masked (see Figure 5.2). The $3.6 \mu\text{m}$ emission is overplotted as contours to indicate the distribution of the stellar emission. While the surface brightness distributions at $3.6 \mu\text{m}$ and $8 \mu\text{m}$ PAH appear similar in many of our galaxies, the ratio images reveal interesting structures that are not easily seen in the original $8 \mu\text{m}$ PAH images. We classify the observed structures into different categories based on approximate descriptions of the $I_{8.0\text{PAH}}/I_{3.6}$ morphologies. The structures noted for each galaxy are listed in Table 5.2. The categories are described as follows:

Ring or Ring-Like (R): Several of our galaxies in Figure 5.3 appear to have ring or ring-like morphologies in the $I_{8.0\text{PAH}}/I_{3.6}$ images. As the distribution of $3.6 \mu\text{m}$ emission in our E/S0s is relatively smooth (as seen in Figure 5.2), the enhancements likely reflect excesses in the $8 \mu\text{m}$ PAH emission indicating regions of enhanced star formation. Note that for two of these galaxies (IC 1141, NGC 5173), the $I_{8.0\text{PAH}}/I_{3.6}$ ratios in the rings are *lower* than the average ratio for the rest of the galaxy, reflecting depressions instead of enhancements. These ring and ring-like enhancements or depressions are also seen in $\langle I_{8.0\text{PAH}} \rangle_R / \langle I_{3.6} \rangle_R$, appearing as bumps or dips as a function of galactocentric radius as noted in column 5 of Table 5.2.

Central Depressions (H): The $I_{8.0\text{PAH}}/I_{3.6}$ images for two of our E/S0s (NGC 7360, NGC 5596) exhibit ring or ring-like structures, but the radial profiles for these galaxies show central dips, implying that these galaxies have central depressions of $8 \mu\text{m}$ PAH emission. While NGC 7360 is on the blue sequence, it has a very low amount of star formation ($\sim 0.03 M_{\odot} \text{ yr}^{-1}$) and no detectable CO(1–0) emission. NGC 5596 is a red-sequence E/S0 and has no detectable H α emission. Thus, these central depressions may reflect the reduction of star formation in the galaxy center and the

inability of gas to reach and refuel the central star-forming regions.

Central Concentrations (C): The $I_{8.0\text{PAH}}/I_{3.6}$ images show central concentrations for several of our galaxies (column 7, Table 5.2). These central concentrations appear to be coincident with regions of changing ellipticity and position angle measured in the $3.6\text{ }\mu\text{m}$ surface brightness fits, suggesting the presence of a stellar bar. This bar may have driven recent gas inflow that may have triggered centrally concentrated star formation in many of these galaxies. The fact that all but two of the galaxies with central concentrations are on the blue sequence and that the two red-sequence E/S0s in this category are both detected in CO(1–0) by CARMA support this interpretation. Interestingly, about half of the galaxies with centrally concentrated $I_{8.0\text{PAH}}/I_{3.6}$ features also have ring or ring-like structures, which we discuss further below. Note that the large distances to two of these galaxies (UGC 6003, UGC 12265N) result in coarse linear resolutions (~ 1 kpc), which may have prevented us from resolving features such as rings.

Non-Axisymmetric (NA): Several of our galaxies (Table 5.2, column 8) have very mismatched $3.6\text{ }\mu\text{m}$ and $8\text{ }\mu\text{m}$ PAH distributions. The $8\text{ }\mu\text{m}$ PAH emission in these galaxies is often clumpy and offset from the center. The extreme asymmetry of these features suggests that the observed star formation may be triggered by interactions with nearby companions, fueled by external sources of gas. This is exemplified by the case of UGC 9562, where the peaks in the $I_{8.0\text{PAH}}/I_{3.6}$ image align well with the galaxy’s very blue polar ring — formed from recent interactions with its nearby companion UGC 9562 (KGB).

Weak PAH Emission (W): Eight of the 32 galaxies in our sample have only trace amounts of $8\text{ }\mu\text{m}$ PAH emission, so there is no clear structure in the ratio maps for these galaxies. These are the same galaxies discussed in §5.3.3 with $\langle I_{8.0\text{PAH}} \rangle_R / \langle I_{3.6} \rangle_R \lesssim 0.2$.

The fact that five of the seven E/S0s with ring or ring-like $I_{8.0\text{PAH}}/I_{3.6}$ excesses⁴ also have centrally peaked $I_{8.0\text{PAH}}/I_{3.6}$ ratios (suggesting central $8\ \mu\text{m}$ PAH excesses) is intriguing. In their spiral galaxy sample, Regan et al. (2006) observe both systems with $8\ \mu\text{m}$ PAH excesses and systems with $8\ \mu\text{m}$ PAH deficiencies in the central regions, with the former corresponding to barred galaxies and the latter to unbarred galaxies. Regan et al. (2006) argue that bars may be driving gas flows towards the centers of the galaxies resulting in central excesses of $8\ \mu\text{m}$ PAH emission that are consistent with observations of central CO excesses in barred spirals (Sakamoto et al. 1999; Sheth et al. 2005). Often, bars are accompanied by resonance rings of gas and star formation (e.g., Buta & Combes 1996).

We find that the identified ring and ring-like $\langle I_{8.0\text{PAH}} \rangle_R / \langle I_{3.6} \rangle_R$ excesses in the radial profiles correspond to large changes in the position angle ($\Delta\text{PA} > 10^\circ$) and ellipticity ($\Delta\epsilon > 0.1$) for the stellar emission in all seven galaxies. Although these changes do not meet the strict requirements for bar identification in spiral galaxies (e.g., Menéndez-Delmestre et al. 2007; Sheth et al. 2008, who require a monotonic increase of ϵ to > 0.2 and then a drop by > 0.1), it is possible that weak bars or resonances are present where we observe $8\ \mu\text{m}$ PAH excesses in the form of ring and ring-like structures in $\langle I_{8.0\text{PAH}} \rangle_R / \langle I_{3.6} \rangle_R$. This argument is especially compelling considering the correlation between rings and key properties: central $8\ \mu\text{m}$ PAH enhancements, blue colors, and CO(1–0) detections. Ringed galaxies are typically the most strongly star-forming E/S0s of the full sample. As bars occur predominantly in disk galaxies (e.g., Eskridge et al. 2000; Menéndez-Delmestre et al. 2007; Barazza et al. 2008), the presence of weak bars in our E/S0s is consistent with the disk-building scenario proposed by KGB.

Additionally, the possible existence of weak bars in these galaxies, as suggested

⁴We distinguish these from the ring depressions observed in IC 1141 and NGC 5173.

by the observed ring and ring-like excesses in the $I_{8.0\text{PAH}}/I_{3.6}$ ratios, may lead to gas inflow, resulting in enhanced central star formation (Elmegreen 1994; Knapen et al. 1995; Regan & Teuben 2004; Jogee et al. 2005; Sheth et al. 2005) which we observe in the $8\mu\text{m}$ PAH emission. The bar-driven gas inflow may also contribute to the growth of “pseudobulges” (Kormendy & Kennicutt 2004; Jogee et al. 2005; Debattista et al. 2006) in our E/S0s. As non-classical bulges, pseudobulges have exponential surface brightness profiles, blue colors, and/or rotationally supported dynamics (Kormendy & Kennicutt 2004). They occur in galaxies of all types, especially later-type spirals. Pseudobulges seem to form within and together with larger disks, as the sizes of the two components correlate (Courteau et al. 1996). Thus, if the enhanced central star formation we observe in the $8\mu\text{m}$ emission reflects pseudobulge growth from bar-driven gas inflow, it is likely that these galaxies are also building disks.

Another possibility is that the central $8\mu\text{m}$ PAH excesses result from external processes such as minor mergers/interactions with small companions instead of internal secular processes such as bar-driven inflow. Kannappan et al. (2004) find that central star formation enhancements correlate with morphological peculiarities and the presence of nearby companions, which suggest that external mechanisms may trigger gas inflow and result in the growth of pseudobulges. Thus the non-axisymmetric features we observe in the $I_{8.0\text{PAH}}/I_{3.6}$ ratios may reflect externally-triggered gas inflow and central star formation, which also supports the pseudobulge and disk growth scenario in our E/S0s.

5.4 $8\mu\text{m}$ PAH Emission vs. CO(1–0) Emission

We also compare $8\mu\text{m}$ PAH images with CO(1–0) maps for the 12 galaxies in our sample that have CARMA data. Note that as our CARMA-detected E/S0s are predominantly blue-sequence E/S0s detected in CO(1–0), we are here considering typically the most strongly star-forming E/S0s from the full sample of 32 galaxies.

5.4.1 Comparison of Spatial Distributions of PAH and CO(1–0) Emission

To examine how the CO(1–0) distribution, which traces the molecular component of the ISM, compares with the distribution of $8\mu\text{m}$ PAH emission, we provide two sets of images. Figure 5.4 compares the distributions of CO(1–0) emission (green contours) and $8\mu\text{m}$ PAH emission (black contours and false color). Since structures in the $8\mu\text{m}$ PAH images are subtle and difficult to discern, we also compare the CO emission (contours) with the $8\mu\text{m}$ PAH/ $3.6\mu\text{m}$ ratio images in Figure 5.5.

Figure 5.4 shows that for most galaxies, the overall correlation between large-scale structures in $8\mu\text{m}$ PAH and CO(1–0) is good, similar to what Regan et al. (2006) find for spirals. In IC 1141 (first panel of Figure 5.4a), both the CO and $8\mu\text{m}$ PAH emission trace the two spiral arms emerging from the east and west sides of the galaxy, although the arms appear fragmented in the CO distribution because of low signal to noise. Some notable exceptions where the $8\mu\text{m}$ PAH emission is not well-matched to the CO emission are UGC 6003, UGC 6570, and UGC 6805. Most of the differences between the two tracers, however, appear to be on smaller scales — manifesting as small (1–3'') offsets between emission peaks (e.g., NGC 3773, NGC 3870, NGC 4117), consistent with the finding of Bendo et al. (2010) that CO(3–2) and $8\mu\text{m}$ PAH are uncorrelated at spatial scales of \sim few hundred pc but

have the same global scale length in NGC 2408. These offsets may be an effect of the temporal delay between the consumption of molecular gas (as traced by CO(1–0)) and the star formation tracer.

Comparison between the $I_{8.0\text{PAH}}/I_{3.6}$ and CO(1–0) images (Figure 5.5) shows a correlation between small-scale structures for some galaxies. The CO(1–0) and $I_{8.0\text{PAH}}/I_{3.6}$ peaks match up very well in NGC 3773, NGC 3870, UGC 6003, and UGC 6805, and the CO ring in NGC 3032 appears in the $I_{8.0\text{PAH}}/I_{3.6}$ ratio image but not in the $8\ \mu\text{m}$ PAH image. So while the $8\ \mu\text{m}$ PAH emission correlates well on a global scale with CO(1–0), non-exponential disk structures such as rings, holes, and non-axisymmetric structures show up better in $I_{8.0\text{PAH}}/I_{3.6}$ images.

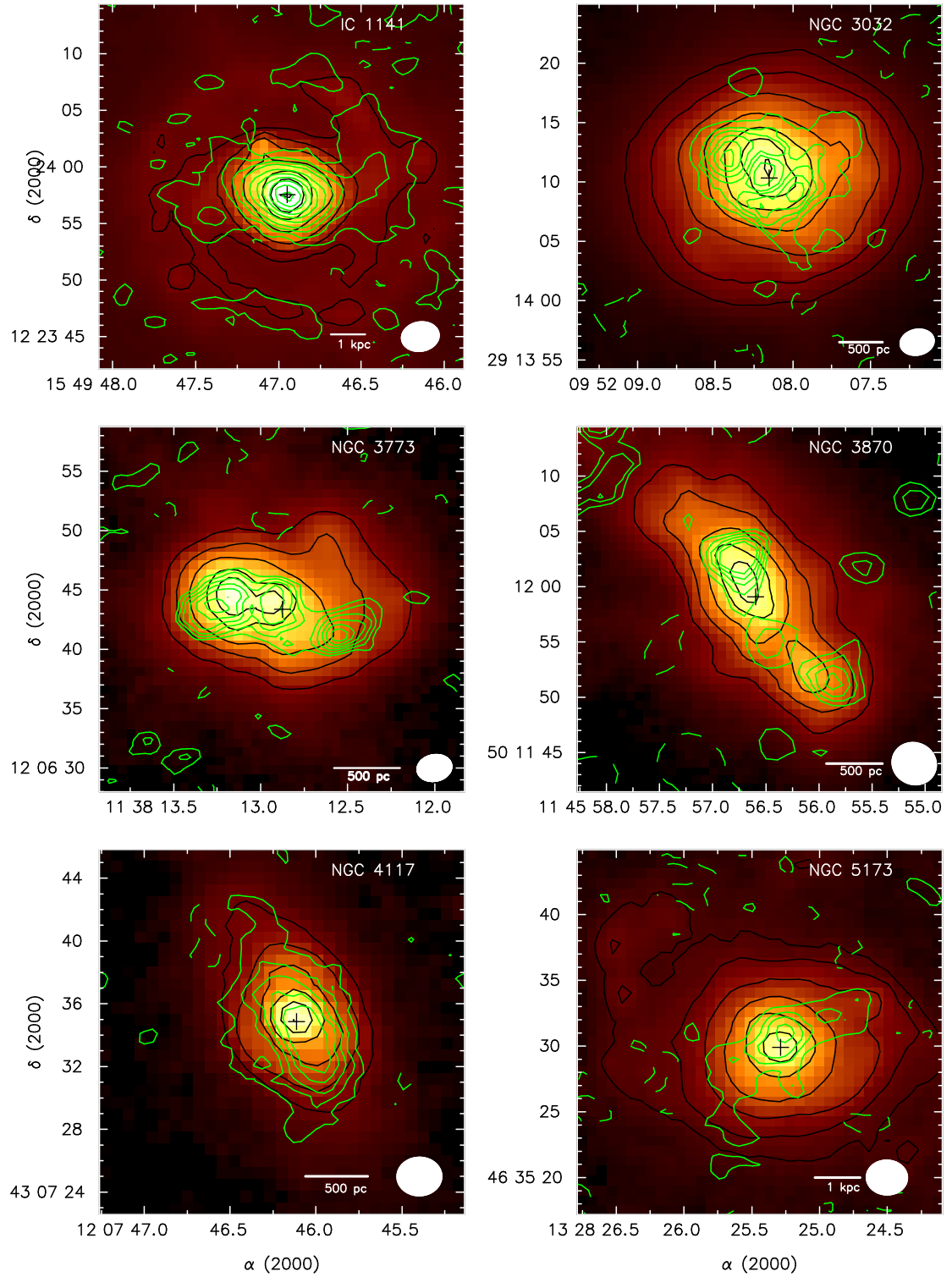


Figure 5.4: Color scale and black contours show 8 μm PAH emission (contours of 2, 4, 8, 16, 32, and 64 MJy sr⁻¹). Overplotted are green contours of CO(1-0) emission from CARMA at levels noted in Chapter 3.5, showing a correlation between the two wavelengths. CARMA beam size and linear scale are noted on the bottom right of each panel. SDSS (DSS for UGC 12265N) optical centers are marked with crosses.

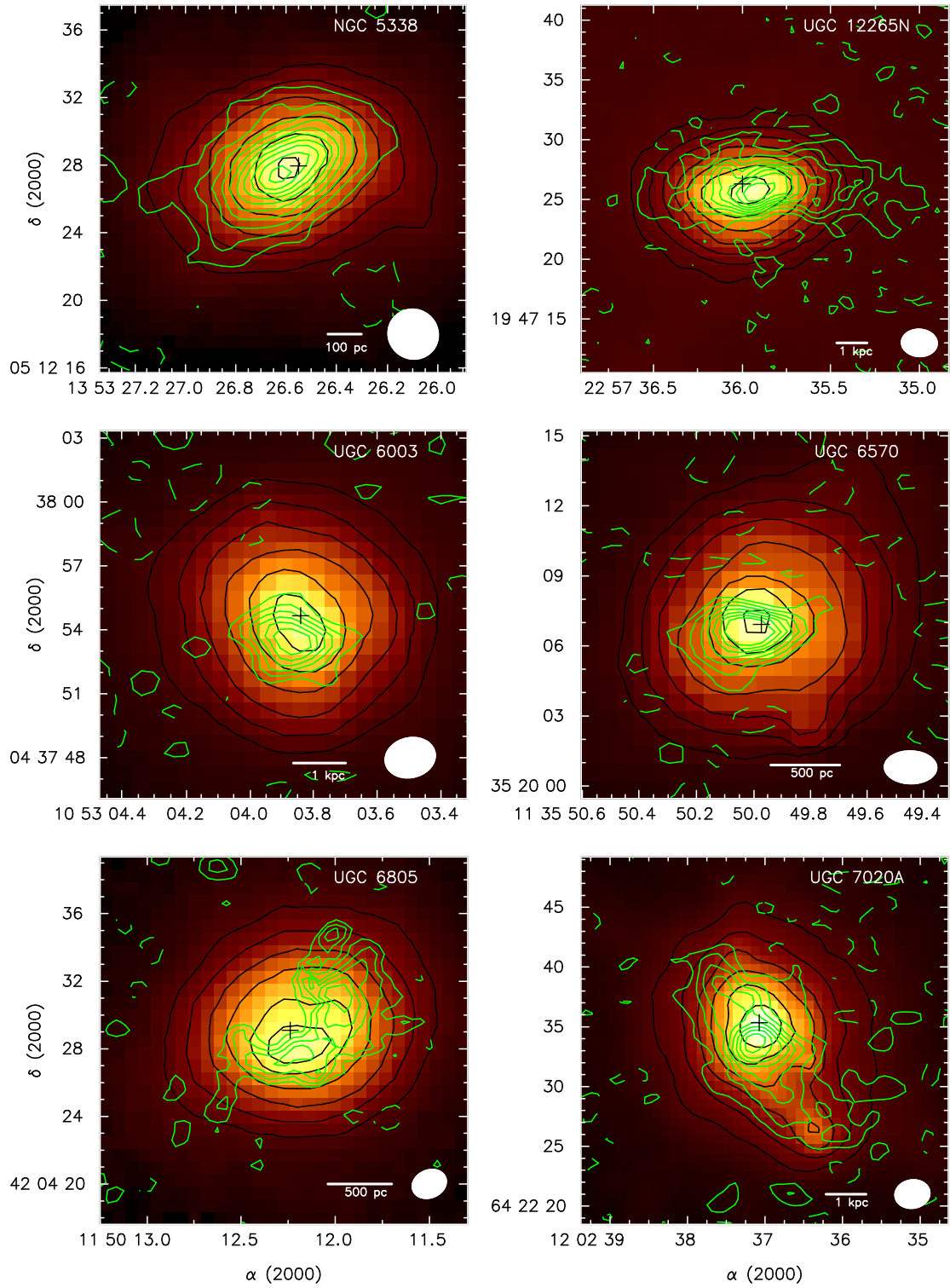


Figure 5.4: Images of 8 μm PAH emission with CO(1-0) contours overplotted in green. See Figure 5.4a for more details.

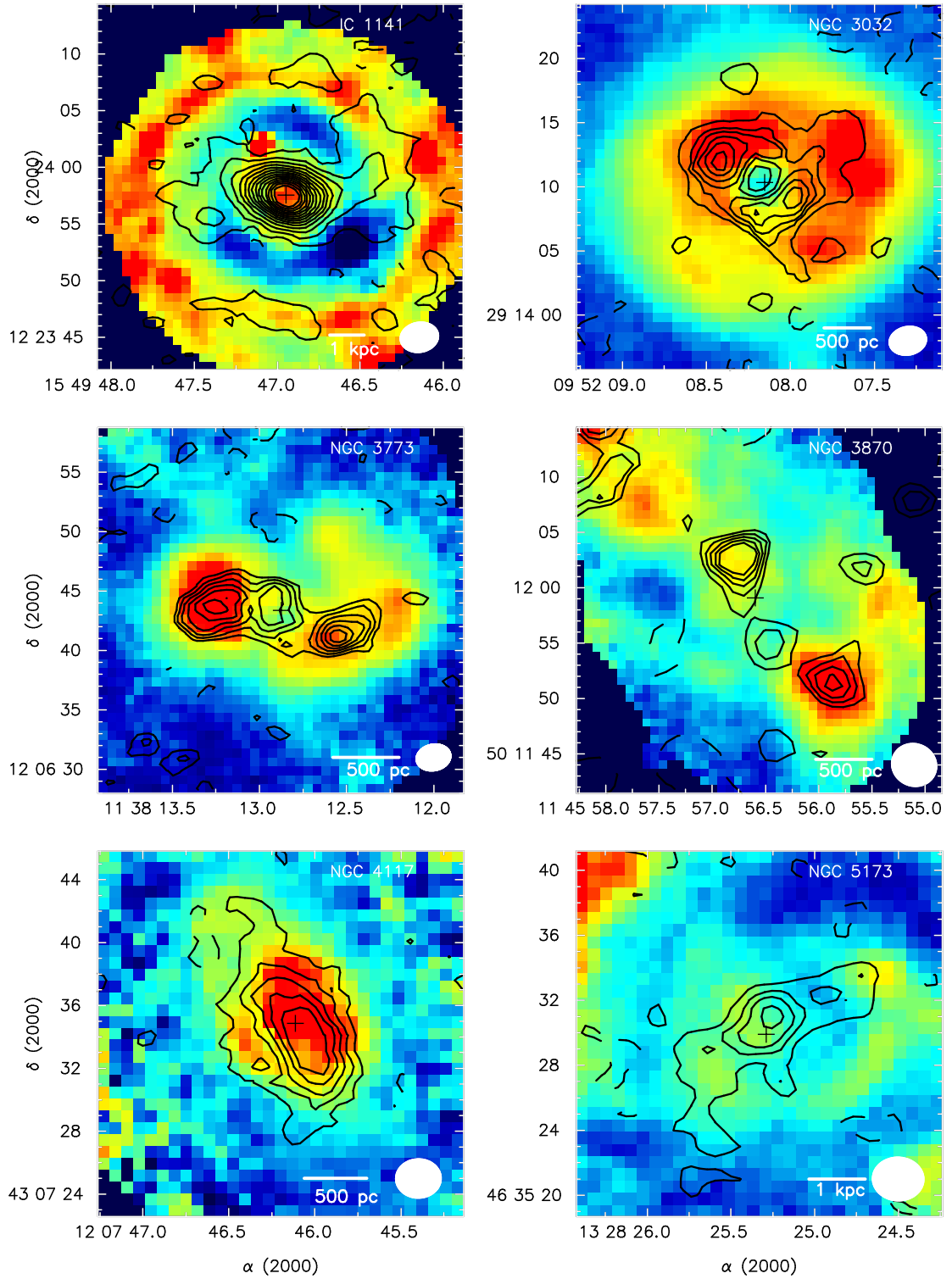


Figure 5.5: $I_{8.0\text{PAH}}/I_{3.6}$ ratios using same mask as Figure 5.3, with contours of CO(1-0) emission from CARMA overplotted at levels noted in Chapter 3.5, showing a correlation between the two. CARMA beam size and linear scale are noted on the bottom right of each panel. SDSS (DSS for UGC 12265N) optical centers are marked with crosses.

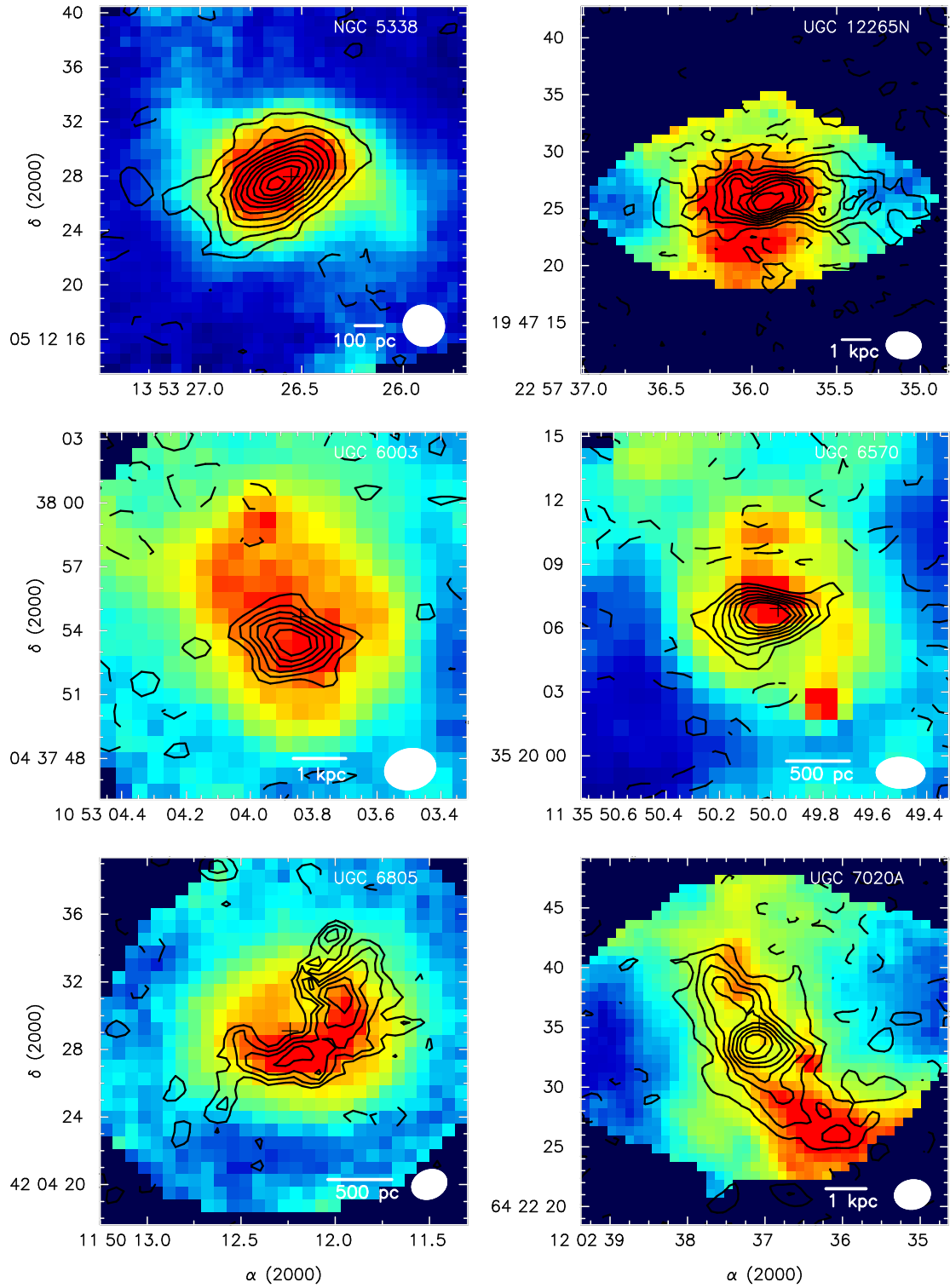


Figure 5.5: Images of $I_{8.0\text{PAH}}/I_{3.6}$ ratios with CO(1-0) contours overplotted.

5.4.2 Radial Distributions of PAH and CO(1–0) Emission

We plot the azimuthally-averaged $8\ \mu\text{m}$ PAH and CO(1–0) surface brightnesses — $\langle I_{8.0\text{PAH}} \rangle_R$ and $\langle I_{\text{CO}(1-0)} \rangle_R$ — of our 12 CARMA-detected E/S0s in Figure 5.6. Radially, the $8\ \mu\text{m}$ PAH profiles extend much further out than the CO(1–0) profiles, past $0.75\ r_{25}$ (galaxy radius at the 25th mag isophote) for most galaxies and beyond $1-2\ r_{25}$ for the E/S0s with the largest $I_{8.0\text{PAH}}/I_{3.6}$ ratios.

In contrast, the extent of CO(1–0) emission detected by our CARMA observations is much shorter, ranging from ~ 0.1 to $0.6\ r_{25}$ with a median of $0.3\ r_{25}$. We cannot rule out, however, the presence of weaker CO emission extending further out into the disk of the galaxy. If the molecular gas is distributed in an exponential disk, we expect that any missing emission does not constitute a large fraction of the total CO flux. Similar to our E/S0s, Regan et al. (2006) find the $8\ \mu\text{m}$ PAH emission can be seen out to 1.5 and in some cases beyond $2r_{25}$ for spiral galaxies, while the CO(1–0) emission of these galaxies extends out to less than half that distance.

Also similar to what Regan et al. (2006) find for spiral galaxies, we find that, in many cases, the shapes of the CO(1–0) radial profiles resemble those of the $8\ \mu\text{m}$ PAH profiles, with a roughly constant ratio between the two. The $\langle I_{\text{CO}(1-0)} \rangle_R / \langle I_{8.0\text{PAH}} \rangle_R$ ratios range from 0.3 to 5.3 for our 12 E/S0s, with a median value of 1.3 (orange asterisks in Figure 5.6). The two outliers towards the high end of the ratio, NGC 4117 and NGC 5338 ($\langle I_{\text{CO}(1-0)} \rangle_R / \langle I_{8.0\text{PAH}} \rangle_R \sim 5.3$ and 2.7 , respectively) both are red-sequence E/S0s. This divergence suggests that the use of $8\ \mu\text{m}$ PAH emission to trace CO(1–0) suggested by Regan et al. (2006) may be applicable only to strongly star-forming galaxies, though we emphasize that we have only limited data to support this hypothesis. Excluding the two red-sequence E/S0s, the $\langle I_{\text{CO}(1-0)} \rangle_R / \langle I_{8.0\text{PAH}} \rangle_R$ ratios range from 0.3 to 1.8, with a median of 1.0 and a variance of 0.5.

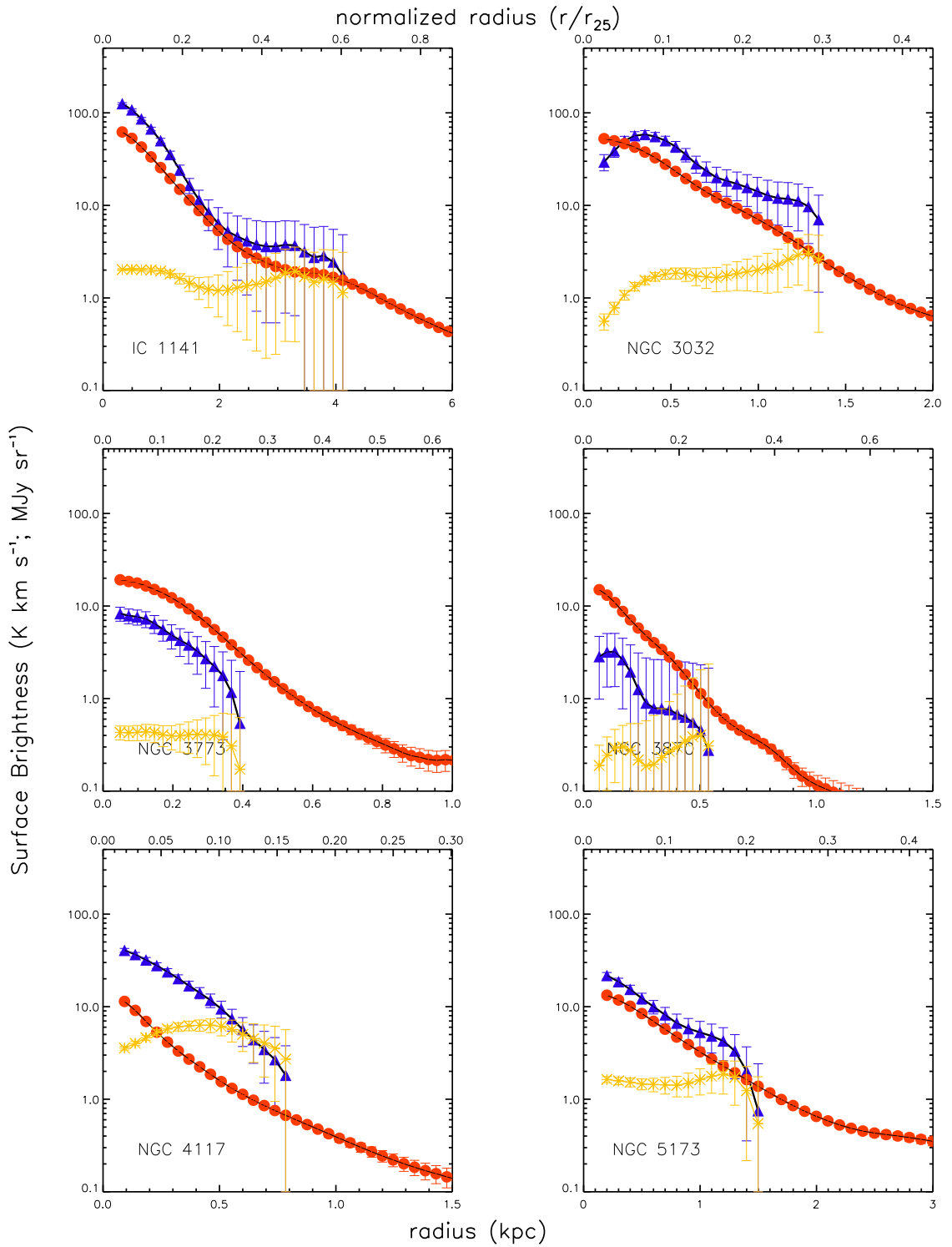


Figure 5.6: Comparison of CO(1-0) and 8 μ m PAH radial profiles. Radial profiles of azimuthally-averaged surface brightness of CO(1-0) emission (blue triangles), 8 μ m PAH emission (red circles), and the ratio of the two — $\langle I_{\text{CO}(1-0)} \rangle_R / \langle I_{8.0 \text{ PAH}} \rangle_R$ (orange asterisks) as a function of galactocentric radius (bottom, kpc) and normalized radius (top, fraction of galaxy radius at the 25th mag isophote r_{25}).

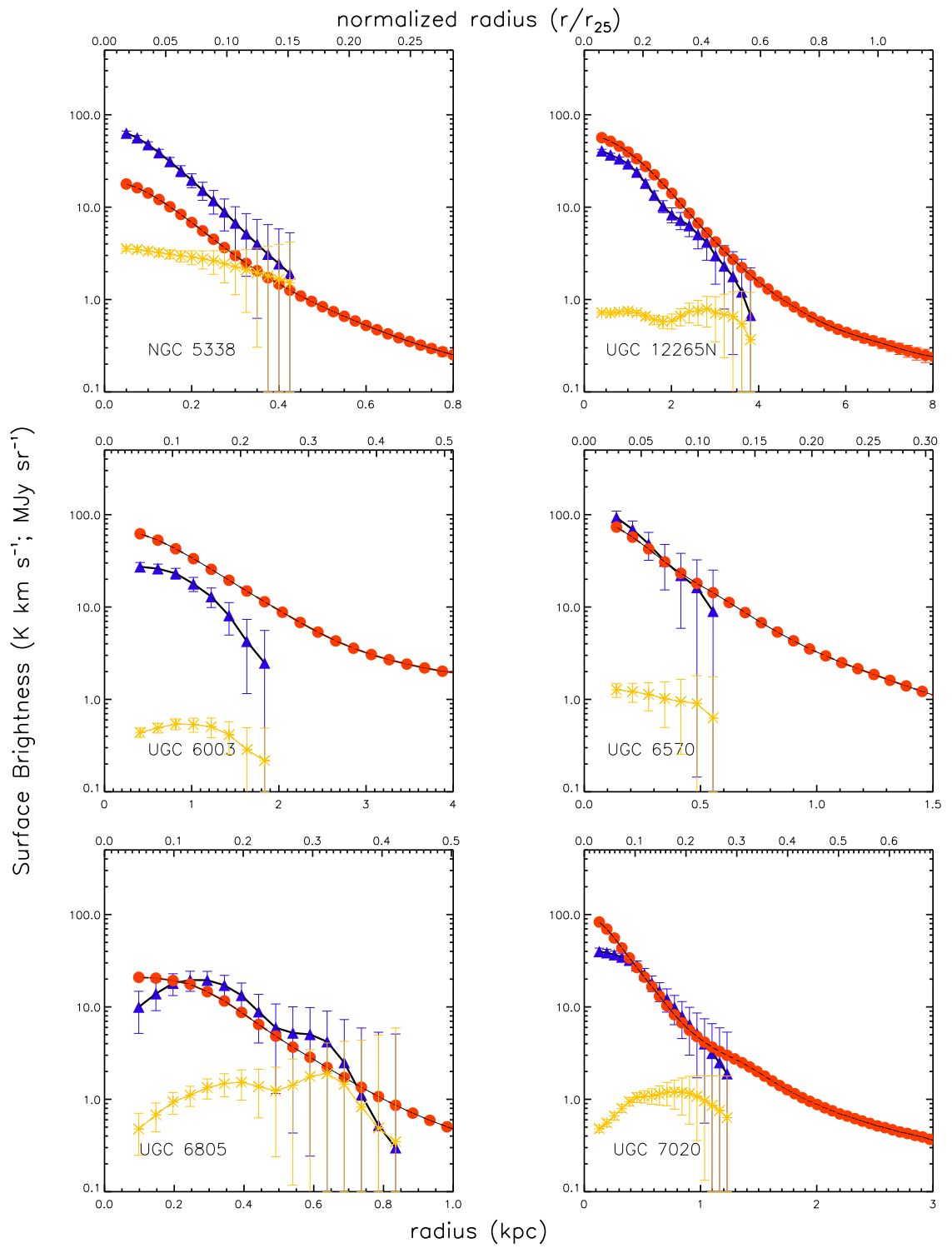


Figure 5.6: Radial profiles of azimuthally-averaged surface brightnesses for our E/S0s.

5.4.3 Correlations Between PAH, Gas, and Star Formation

The results of §5.3, §5.4.1, and §5.4.2 suggest that there is a close connection between $I_{8.0\text{PAH}}/I_{3.6}$ ratio, gas content, and star formation in E/S0 galaxies. This is perhaps not surprising, as $8\ \mu\text{m}$ PAH emission has been successfully used as a star formation tracer for spiral galaxies by various authors (e.g., Wu et al. 2005; Jackson et al. 2006), and gas content is intimately connected with star formation (e.g., Kennicutt 1998). In Figures 5.7 and 5.8, we compare specific star formation rate and various gas mass fractions (atomic, molecular, and total) against aperture-averaged $\langle I_{8.0\text{PAH}}/I_{3.6} \rangle$ ratios for our E/S0s. In this section we average the $3.6\ \mu\text{m}$ and $8\ \mu\text{m}$ PAH surface brightnesses over the area where the azimuthally-averaged surface brightness is above the sky variance of that image (Table 5.1).

We first plot the specific star formation rate ($\text{SSFR} \equiv \text{SFR}_{\text{H}\alpha}/M_*$) against $\langle I_{8.0\text{PAH}}/I_{3.6} \rangle$ in Figure 5.7. As previous studies find good agreement between $8\ \mu\text{m}$ emission and other star formation tracers (e.g., Wu et al. 2005; Jackson et al. 2006) and $3.6\ \mu\text{m}$ emission traces stellar mass, it is reasonable that we find a correlation between global $\langle I_{8.0\text{PAH}}/I_{3.6} \rangle$ and SSFR.

Figure 5.8a plots $\langle I_{8.0\text{PAH}}/I_{3.6} \rangle$ against atomic gas mass fraction (M_{HI}/M_* ; Chapter 2, Wei et al. 2010a). The points are color-coded by sequence association. Note that the three blue-sequence E/S0s with the lowest $\langle I_{8.0\text{PAH}}/I_{3.6} \rangle$ values are the massive merger remnants discussed in §5.3.3 destined to quickly fade onto the red sequence. Similar to what we find for the radial profile ratios in §5.3.3, the $\langle I_{8.0\text{PAH}}/I_{3.6} \rangle$ ratios distinguish quite well between the low-mass blue- ($\langle I_{8.0\text{PAH}}/I_{3.6} \rangle \sim 0.7\text{--}10$) and red-sequence E/S0s ($\langle I_{8.0\text{PAH}}/I_{3.6} \rangle \sim 0.1\text{--}0.7$). In Chapter 2 (Wei et al. 2010a), we find the blue- and red-sequence E/S0s also span different ranges in M_{HI}/M_* ; thus, comparison of the two quantities shows a corre-

lation between atomic gas mass fractions and $\langle I_{8.0\text{PAH}}/I_{3.6} \rangle$ separating the blue, star-forming E/S0s from the red, quiescent E/S0s.

We plot the correlation between the molecular gas mass fraction⁵ (M_{H_2}/M_*) and $\langle I_{8.0\text{PAH}}/I_{3.6} \rangle$ ratios in Figure 5.8b. Compared to Figure 5.8a, the correlation with M_{H_2}/M_* appears to be much tighter for blue-sequence E/S0s. Similar to the direct comparison between the CO(1–0) and $8\ \mu\text{m}$ PAH radial profiles in §5.4.2, we find the two red-sequence E/S0s are the outliers in this relationship. The paucity of H_2 data for red-sequence E/S0s, however, prevents us from determining whether there is a bimodal relation or these are just anomalous galaxies. As $8\ \mu\text{m}$ traces star formation and CO traces the molecular gas that stars form from, it is reasonable that there is a good correlation between the two. The correlation between $\langle I_{8.0\text{PAH}}/I_{3.6} \rangle$ and M_{H_2}/M_* for blue-sequence E/S0s and similarity in structure of CO(1–0) and $8\ \mu\text{m}$ PAH emission suggests, similar to Regan et al.’s conclusion for spirals, that $8\ \mu\text{m}$ PAH emission may be used as a *rough* tracer of the central H_2 content of star-forming galaxies.

Combining the atomic and molecular gas masses, Figure 5.8c plots $\langle I_{8.0\text{PAH}}/I_{3.6} \rangle$ (averaged over the extent of the $8\ \mu\text{m}$ PAH emission) ratios against $M_{\text{HI}+\text{H}_2}/M_*$. This correlation appears to be tighter than the comparison of $\langle I_{8.0\text{PAH}}/I_{3.6} \rangle$ with just the atomic gas mass fraction in Figure 5.8a, but not as tight as the relationship between $\langle I_{8.0\text{PAH}}/I_{3.6} \rangle$ and molecular gas mass fraction for blue-sequence E/S0s.

⁵Note that interferometric and/or single-dish CO data are available for only 19 of our 32 E/S0s, which are predominantly on the blue sequence, so any analysis including molecular gas is biased towards star-forming blue-sequence E/S0s.

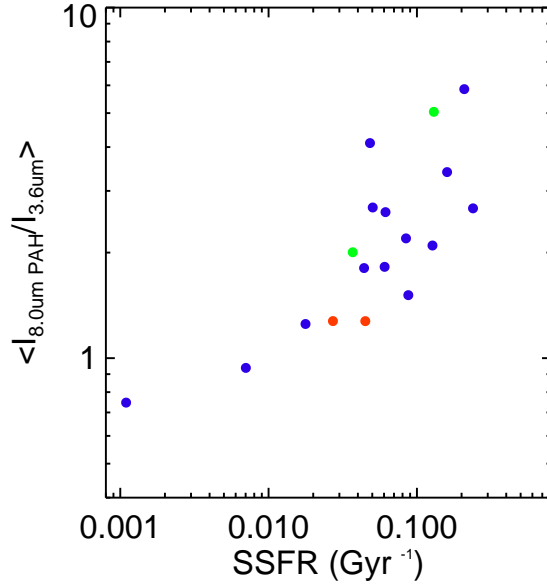


Figure 5.7: $\langle I_{8.0\text{PAH}}/I_{3.6} \rangle$, averaged over the extent of $8\mu\text{m}$ emission, vs. specific star formation rate (SSFR) estimated from $\text{H}\alpha$ emission (KGB). Galaxies are color-coded by sequence association (blue/green (mid)/red).

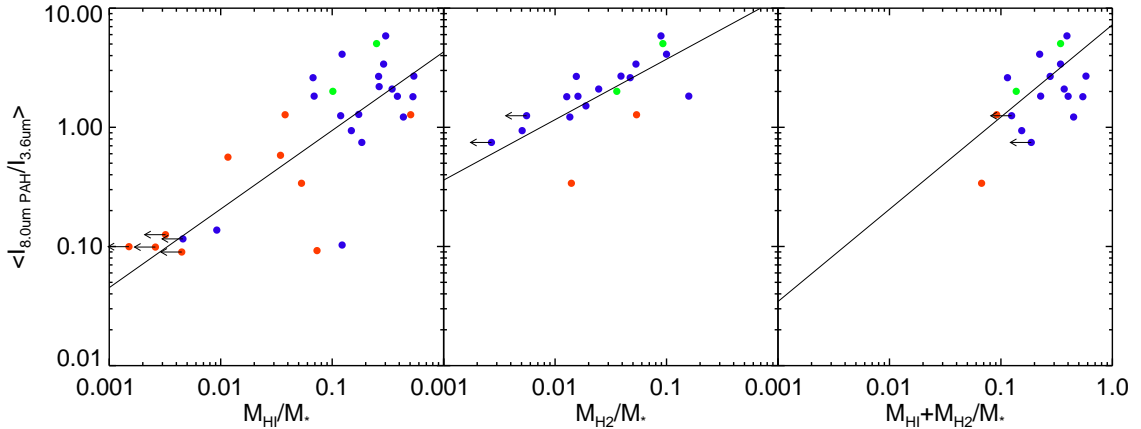


Figure 5.8: $\langle I_{8.0\text{PAH}}/I_{3.6} \rangle$ vs. (a) HI-to-stellar mass ratio, (b) H_2 -to-stellar mass ratio, (c) total gas ($\text{HI}+\text{H}_2$) to stellar mass ratio for blue-, mid-, and red-sequence E/S0s (blue/green/red circles). All panels span the same x-range. Galaxies lacking H_2 data (primarily red-sequence E/S0s) are not included in panels (b) and (c). Solid lines show bisector fits to the data points: $\log \langle I_{8.0\text{PAH}}/I_{3.6} \rangle = 0.66 \log(M_{\text{HI}}/M_*) + 0.63$; $\log \langle I_{8.0\text{PAH}}/I_{3.6} \rangle = 0.51 \log(M_{\text{H}_2}/M_*) + 1.07$; $\log \langle I_{8.0\text{PAH}}/I_{3.6} \rangle = 0.77 \log(M_{\text{HI}+\text{H}_2}/M_*) + 0.86$.

5.5 Conclusions

In this Chapter, we consider the $8\mu\text{m}$ PAH emission in low-mass E/S0s, with a focus on blue-sequence E/S0s with resolved CO maps. Based on comparisons with typical star-forming spirals from SINGS and massive E/S0s from SAURON, the $\langle I_{8.0\text{PAH}} \rangle_R / \langle I_{3.6} \rangle_R$ ratio allows us to distinguish the blue, gas-rich, star-forming galaxies from E/S0s that are either red and dead or in the process of becoming so in our sample. About half of our E/S0s, predominantly on the blue sequence and detected in CO(1–0), have $\langle I_{8.0\text{PAH}} \rangle_R / \langle I_{3.6} \rangle_R$ ratios similar to those of star-forming spirals. The other half of our sample, typically massive blue-sequence E/S0s or red-sequence E/S0s, have $\langle I_{8.0\text{PAH}} \rangle_R / \langle I_{3.6} \rangle_R$ ratios in the range spanned by the higher-mass SAURON E/S0s, showing only trace amounts of PAH emission.

While the spatial distribution of the $8\mu\text{m}$ PAH emission in our E/S0s appears fairly similar to that of stellar emission at $3.6\mu\text{m}$, the ratio of the two ($I_{8.0\text{PAH}}/I_{3.6}$) reveals intriguing ring- and ring-like structures in many of our galaxies, suggestive of the presence of bars in disks that may drive gas inwards and result in central $8\mu\text{m}$ PAH excesses, fueling pseudobulge growth. Since bars in spirals are often driven by interactions, the bars in our E/S0s may also result from interactions with small companions. The non-axisymmetric features in the $I_{8.0\text{PAH}}/I_{3.6}$ ratios may be more direct evidence for interaction — supporting the externally-triggered gas inflow scenario, which may also result in pseudobulge building (Kannappan et al. 2004).

Comparison between the CO(1–0) and $8\mu\text{m}$ PAH emission distributions shows good agreement globally, although there are offsets between emission peaks suggestive of a delay between molecular gas consumption and the star formation tracer. On smaller scales, the correlation between the $I_{8.0\text{PAH}}/I_{3.6}$ ratio and CO(1–0) ap-

pears better for most galaxies, implying that $I_{8.0\text{PAH}}/I_{3.6}$ may better trace rings, holes, and non-axisymmetric structures.

Consistent with previous studies of $8\ \mu\text{m}$ PAH emission, we find the $8\ \mu\text{m}$ PAH emission to be a good star formation indicator, showing a correlation between aperture-averaged $\langle I_{8.0\text{PAH}}/I_{3.6} \rangle$ ratios and specific star formation rates for our star-forming galaxies. We also find the aperture-averaged $\langle I_{8.0\text{PAH}}/I_{3.6} \rangle$ ratio to correlate with the fractional HI, H₂, and total (HI+H₂) gas mass fraction, with the correlation between $\langle I_{8.0\text{PAH}}/I_{3.6} \rangle$ and M_{H_2}/M_* being the best of the three.

Chapter 6

Summary and Future Work

6.1 Overview

Low-mass blue-sequence E/S0s are an intriguing population of galaxies with many characteristics that are in between those of typical red and dead E/S0s and blue, star-forming spirals, suggesting that these E/S0s may provide an evolutionary link between the two traditional classes. These galaxies appear on the blue sequence alongside spiral and irregular galaxies in color vs. stellar mass space, with increasing frequency below $M_* \sim 3 \times 10^{10} M_\odot$ (Kannappan, Guie, & Baker 2009). The mass-radius and mass- σ values for blue-sequence E/S0s fall in between those of spirals and red-sequence E/S0s; while high-mass blue-sequence E/S0s often resemble young merger or interaction remnants likely to fade to the red sequence, many low-mass blue-sequence E/S0s appear to be building disks and/or pseudobulges (KGB). For this dissertation, we set out to understand these low-mass blue-sequence E/S0s from the perspective of cold gas and star formation in order to determine whether these galaxies are in fact the population of early-type galaxies actively evolving to late type via disk regrowth as predicted by simulations of hierarchical galaxy formation and evolution.

In Chapter 2, we presented new single-dish HI observations of E/S0s on both sequences obtained with the Green Bank Telescope, as well as a complete tabulation of archival HI data for other galaxies in the Nearby Field Galaxy Survey. Normalized to stellar mass, the atomic gas masses for most blue-sequence E/S0s range from 0.1 to >1.0 , demonstrating that morphological transformation is possible if the detected gas can be converted into stars. These gas-to-stellar mass ratios are comparable to those of spiral and irregular galaxies, with similar dependence on stellar mass. Red-sequence E/S0s in the same stellar mass range, on the other hand, typically have gas-to-stellar mass ratios < 0.1 , insufficient for morphological transformation. Assuming that the HI is accessible for star formation, we found that many of our blue-sequence E/S0s can increase in stellar mass by 10–60% in 3 Gyr in both constant and exponentially declining star formation scenarios. We observe a relationship between blue-centeredness and enhanced specific star formation, suggesting that star formation in these galaxies is bursty and likely involves externally triggered gas inflows.

We presented CO(1–0) channel maps, velocity-integrated emission maps, and velocity fields for select blue- and red-sequence E/S0s from the Combined Array for Millimeter-wave Astronomy (CARMA) in Chapter 3. Comparison between CO(1–0) fluxes derived from our CARMA interferometric observations and single-dish spectra suggests that we neither resolved out nor failed to detect more extended emission. The distribution of CO appears to be centrally concentrated, similar to what is seen in CO observations of spiral galaxies; velocity fields show fairly regular rotation in some of the E/S0 galaxies.

In Chapter 4, we considered the relationship between molecular-gas and star-formation surface densities for a subsample of E/S0s located predominantly on the blue sequence. For a sample of eight E/S0s whose CARMA CO(1–0), *Spitzer* Multi-

band Imaging Photometer (MIPS) $24\ \mu\text{m}$, and *GALEX* Far-UV emission distributions are spatially resolved on a $750\ \text{pc}$ scale, we found roughly linear relationships between molecular-gas and star-formation surface densities within all galaxies with power law indices $N = 0.6\text{--}1.9$, with a median of 1.9. Globally, most of our blue-sequence E/S0s have aperture-averaged molecular-gas surface densities overlapping the range spanned by the disks and centers of spiral galaxies. While many of our E/S0s fall on the same Schmidt-Kennicutt relation as local spirals, $\sim 80\%$ are offset towards apparently higher molecular-gas star formation efficiency. Possible interpretations of the elevated efficiencies include bursty star formation similar to that in local dwarf galaxies, H_2 depletion in advanced starbursts, or simply a failure of the CO(1–0) emission to trace all of the molecular gas.

In Chapter 5, we considered the spatial distribution of star formation in blue- and red-sequence E/S0s as traced by $8\ \mu\text{m}$ PAH emission from the *Spitzer* InfraRed Array Camera (IRAC). Considering azimuthally-averaged surface brightness profiles, we found that the ratios of $8\ \mu\text{m}$ PAH to $3.6\ \mu\text{m}$ emission for most of our blue-sequence E/S0s are similar to those of local spirals from the *Spitzer* Infrared Nearby Galaxies Survey (SINGS), while the ratios for most of our red-sequence E/S0s are more similar to those of typical massive, local E/S0s from the SAURON Survey. While the spatial distribution of the $8\ \mu\text{m}$ PAH emission appears fairly similar to that of the stellar emission at $3.6\ \mu\text{m}$, ratio images of the two wavelengths reveals interesting ring and ring-like structures in some of our blue-sequence E/S0s. These structures could reflect the presence of weak bars or non-axisymmetric distortions due to interactions that can drive gas inwards to fuel central star formation. Comparison between the CO(1–0) and $8\ \mu\text{m}$ PAH emission distributions shows good global agreement, although structures such as rings and holes in the CO emission are better traced by the $8\ \mu\text{m}$ PAH/ $3.6\ \mu\text{m}$ ratio images. Finally, we find correlations between the

aperture-averaged $8\ \mu\text{m}$ PAH/ $3.6\ \mu\text{m}$ ratios and the HI-, H₂-, and total gas-to-stellar mass ratios, reflecting the fact that gas content and star formation are closely related.

In summary, we find that the cold gas and star formation properties of blue-sequence E/S0s are more similar to those of spiral galaxies than typical red-sequence E/S0s. Given that, in many cases, low-mass blue-sequence E/S0s have fractionally large atomic gas reservoirs, relatively settled molecular gas disks, star formation levels comparable to those of spirals, and a mechanism for driving gas inwards, it is quite possible that these galaxies constitute a transitional population between spiral and red-sequence E/S0s, evolving towards later-type morphologies via disk regrowth.

6.2 Future Work

One outstanding question is the extent of the cold gas that is available for disk regrowth. In this dissertation, we found that the molecular gas in many blue-sequence E/S0s appears to be regularly rotating and fairly settled, but as in spirals, it is often centrally concentrated. Thus it is difficult to estimate the size of the future stellar disk and quantify the amount of morphological transformation that is possible. Analysis of HI observations with the Very Large Array will allow us to look for extended gas disks and more accurately assess the potential for evolution towards later-type morphology in these galaxies. We will also look for settled gas structures indicative of morphological transformation on larger scales than our CO observations.

Other follow-up work includes the study of the kinematics of the gas and stars. We will compare predictions from simulations of disk (re)growth with the angular momentum distributions traced by the gas and stellar kinematics. Differences be-

tween atomic gas, molecular gas, and stellar kinematics may reveal the source of cold gas in these galaxies. Additionally, the VLA HI maps along with deep optical imaging will allow us to search for small companions and/or evidence of interactions (tidal tails, streams, etc.) to test our externally triggered star formation hypothesis.

A longer-term follow-up to this dissertation would be the search for high-redshift analogues of the blue-sequence E/S0s examined in this dissertation, as some of these analogues at lower masses may evolve into the large spiral galaxies we observe today. As the next generation of telescopes (ALMA, SKA, etc.) come online, we will be able to probe deeper and further into the past in search of the progenitors of present-day spirals. The results of this dissertation may help with the interpretation of gas and star formation data from high-redshift early-type galaxies.

Appendix A

Notes on GBT Observations

A.0.1 GBT Flux Measurements and Comparison with Literature Fluxes

Figure A.1 plots our new GBT HI fluxes against literature fluxes compiled in HyperLeda (Paturel et al. 2003), showing good agreement between the two. Notes on individual galaxies are as follows:

For many galaxies (UGC 6655, UGC 7020A, NGC 3011, IC 1141, UGC 6570) the GBT HI profiles have much stronger S/N than those from the literature, hence any differences in flux measurements between GBT and literature are likely to be attributed to the noisy profiles of the literature data. This can be seen in the error bars in Figure A.1.

NGC 5596: the literature flux is very noisy and has a velocity width of $> 500 \text{ km s}^{-1}$, so it makes sense that our flux measurement is smaller considering we measure a smaller velocity width.

NGC 4117: the literature data are also of poorer quality and suffer from confusion with a nearby companion NGC 4118 ($1.5'$ and 643 km s^{-1}). We separate out the companion by using the width of the ionized gas from $850\text{--}1050 \text{ km s}^{-1}$, which also

agrees with our preliminary CO data for this galaxy.

UGC 12265N: this galaxy is one member of a pair; its HI is completely blended in with its smaller companion, UGC 12265S, only $1'$ and $\sim 70 \text{ km s}^{-1}$ away (see Figure 2.3). Preliminary VLA HI data suggest that UGC 12265N contains about 1/4 of the total HI within the GBT beam, so we use this fraction of the total HI flux for our analysis.

NGC 3522: the HI spectrum from Lake & Schommer (1984) seems to have comparable S/N to our GBT spectrum, due to our rather short integration time. The $\sim 3'$ beam of the Arecibo Telescope used by Lake & Schommer (1984), however, could be missing some extended HI flux, which would explain the higher flux measurement on our part.

IC 1639, IC 195: both have known companions within the beam of the GBT. Because these galaxies do not have ionized-gas rotation information, we measure the HI fluxes within the ranges of stellar rotation ($5344\text{--}5444 \text{ km s}^{-1}$ and $3498\text{--}3798 \text{ km s}^{-1}$, respectively).

NGC 1029: does not have ionized-gas or stellar rotation data, so we exclude the companion by measuring the HI flux within a width given by Arecibo HI observations of this galaxy. The smaller $3'$ beam of the Arecibo Telescope does not detect the companion and finds a W_{20} of 353 km s^{-1} (Springob et al. 2005).

The following galaxies are classified as undetected, although HI emission was detected in velocity ranges corresponding to nearby galaxies. For these three galaxies, we give both the HI upper limit for the target galaxy as well as the HI flux from the nearby galaxy.

NGC 4308: The measured HI velocity suggests that the flux belongs to a nearby companion, UGC 7438 ($\sim 5'$, 699 km s^{-1}), although this is not certain. Assigning the gas to NGC 4308 does not change any results since the measured atomic gas

mass is still extremely low, $< 1\%$ of the stellar mass of the galaxy.

IC 1144: The measured HI velocity suggests that the flux belongs to a nearby companion, SDSS J155124.19+432506.8 ($\sim 0.5'$, 12225 km s^{-1}).

UGC 12835: Based on the measured HI velocity, the HI flux clearly belongs to a companion in the beam, and the target galaxy is undetected.

A.0.2 GBT HI Profiles of Sub- M_b E/S0s

We examine and discuss the HI profiles of red- and blue-sequence E/S0s, grouping them by different types of velocity profiles while noting the sequence each belongs to (B, mid-sequence, and R).

Galaxies with flat velocity profiles: NGC 3011(B), NGC 1552(R), NGC 3522(R), and NGC 3499(R) all have HI profiles that are reminiscent of a gas disk extending either slightly into or well beyond the flat part of the rotation curve. These profiles are not as sharply peaked as the typical double-horned profile, suggesting that the gas disk does not extend too far into the flat part of the rotation curve. None of these galaxies have large companions within the beam of the GBT, although all of these profiles seem to have slight asymmetries, suggesting there may be distortions in the gas disk.

Galaxies with rising velocity profiles: UGC 6003(B), UGC 6655(B), UGC 6570(Mid), UGC 7020A(Mid), and NGC 5338(R) have sharply peaked HI profiles, which are indicative of gas disks that are still in the rising part of the rotation curve. Most of these are relatively symmetric and do not have any known large companions within the beam of the GBT.

Galaxies in between the first two cases: UGC 6805(B), IC 1141(B), and UGC 5923(R) have HI profiles that seem to be a combination of the previous two cases — their HI profiles all have a single peak like the rising rotation curve case, but there is a slight

flattening suggesting that the gas is reaching the flat part of the rotation curve. UGC 6805 seems to have a gas disk with rotation in the rising part of the curve; although the center seems slightly flattened, it is hard to tell given the noise in the HI profile. IC 1141 and UGC 5923, on the other hand, seem to have centers that are much more flattened, suggesting that the gas disk may extend a little further into the flat part of the rotation curve. These galaxies also do not have any known large companions.

Galaxies with known companions: NGC 4117(R), UGC 12265N(B), IC 1639(B), and IC 195(B) all have optically confirmed companions. NGC 4117 has an asymmetric double horn profile between 800 and 1100 km s⁻¹, and a companion (NGC 4118) 1.5' and 643 km s⁻¹ away. UGC 12265N is actually a galaxy pair with UGC 12265S, and its HI profile is completely blended in since the two are less than 100 km s⁻¹ apart in velocity space. The larger peak in the HI profile for IC 1639 is actually its larger companion, IC 1640; IC 1639 is the smaller peak at 2581 km s⁻¹. IC 195 has two companions: IC 196, which is 2.2' away, but only about 15 km s⁻¹ apart in velocity space (so it is completely blended in), and Arp 290, which probably contributes to the HI profile at 3509 km s⁻¹, located 1.1' away.

Non-detections: UGC 130(R), NGC 516(R), NGC 3179(R), NGC 3605(R), NGC 4308(R), UGC 8876(R), IC 1144(B), and UGC 12835(R).

Miscellaneous: NGC 5596(R) and NGC 1298 (R) are both detections, but the S/N of their spectra are too poor to allow us to categorize their HI profiles.

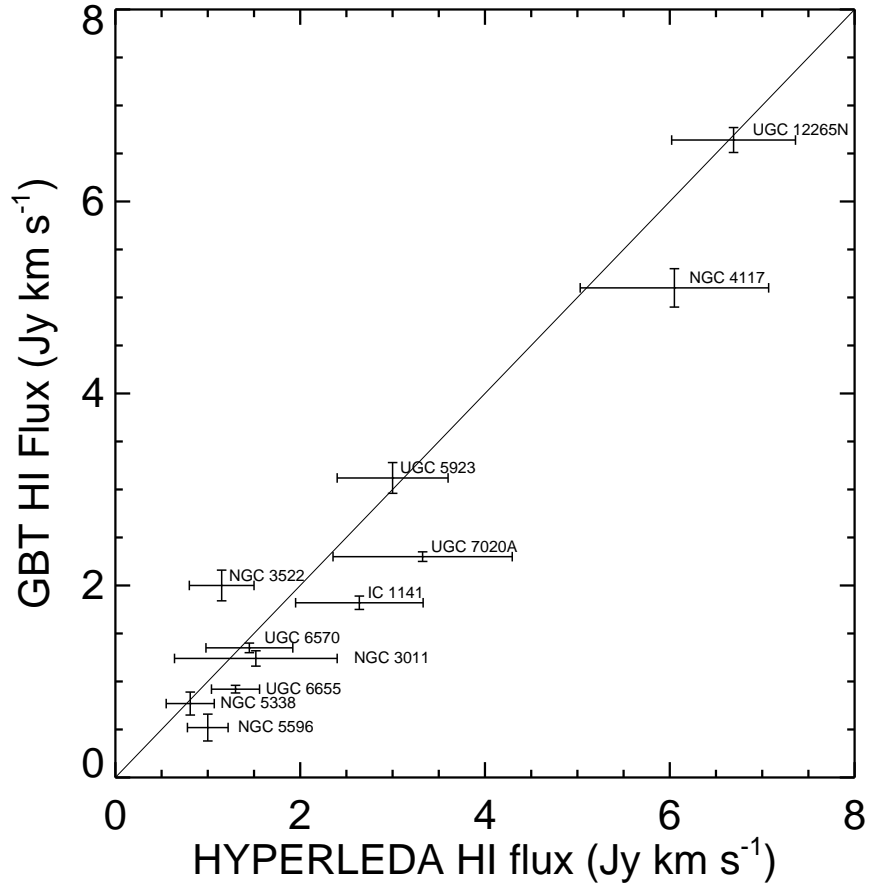


Figure A.1: Comparison of HI fluxes between our new GBT observations and HyperLeda homogenized data.

Appendix B

Bandpass Calibration for CARMA

B.1 Introduction

There are many components of an array which can affect the phase of interferometric observations – the signals from astronomical sources pass through many mixers, amplifiers, and filters before reaching the correlator. These components affect the delay, phase, and spectral shape of the astronomical signals. To calibrate out such effects in the bandpass, we ideally would like to have observations of a strong astronomical source with a flat spectrum. Though this calibration method works for the wider correlator bands¹ (500 MHz and 62 MHz), there is usually not enough signal-to-noise in the narrower bands (31 MHz and below) to calibrate the bandpass astronomically in a reasonable amount of time. In this memo we describe different methods of bandpass calibration for different bands.

¹In this document we often use the word “band”, not to be confused with “spectral window” — CARMA currently has 3 bands, each corresponds to 2 spectral windows, one in the upper sideband and one in the lower sideband. Band 1 = Windows 1 & 4, Band 2 = Windows 2 & 5, Band 3 = Windows 3 & 6. When we do calibrations in Miriad, we use `select=win(#)` to select the spectral window we wish to process.

B.2 The Signal Path

Figure B.1 shows the major components in the signal path. After passing through the atmosphere and telescope optics the signal reaches the cooled low noise double sideband mixer. This mixer converts the radio frequency (RF) signals down to the 1–5 GHz intermediate frequency (IF). Signals in the range from 1–5 GHz below and above the first local oscillator frequency (LO1) show up in the IF. All of the components before this mixer, including the sky and telescope optics, contribute to the RF gain, $G_{RF,antA}(f_{RF})$. Note that the phase of LO1 is switched through a series of Walsh sequences so that the correlator can separate the upper sideband ($f_{RF} = LO1 + f_{IF}$) signals from the lower sideband ($f_{RF} = LO1 - f_{IF}$) signals. So each correlator band gives you two spectral windows in the CARMA data. All bands receive their signals from the same RF components and $G_{RF,antA}(f_{RF})$ depends only on the sky frequency, f_{RF} , and not on the particular band used.

The IF signals in the 1-5 GHz range pass through amplifiers and attenuators in the antenna, are converted to light and sent along fiber to the control building, converted back to microwaves, amplified and attenuated some more before reaching the second mixer. These are all broadband components and can be characterized by the IF gain, $G_{IF,antA,bandN}(f_{IF})$. Although many of the components in the IF path are in common across all bands, there are components like the second mixer in the down-converters which are separate for each band and each band will have its own gain function $G_{IF,antA,bandN}(f_{IF})$. The second mixer is a single sideband mixer in the down-converter modules. Its base band output contains either the upper sideband signals above the 2nd LO ($f_{IF} = LO1 + f_{BB}$) or the lower sideband ($f_{IF} = LO1 - f_{BB}$). This choice is determined by the `configband`² command but

²All miriad and scriptWriter commands in this document will be written in **this font**.

is normally set to LSB.

The baseband components include everything from the down-converter mixer to the actual cross-correlation calculated in the correlator FPGAs (programmable logic devices). The center of the baseband is 750 MHz. The gain for this set of components is $G_{BB,antA,bandN}(f_{BB})$. The correlated noise gets injected at the beginning of this chain of baseband components. The noise signal passes through all of the correlator configuration dependent components and filtering at the astronomical signals. In particular the selectable analog filters for 500 MHz and 62 MHz or narrower modes plus the finite impulse response (FIR) filtering that takes place in the digitizer cards are all measured by the noise source. The power measurement of P_{sys} used for the system noise temperature measurement is after the analog filters and before the automatic level control (ALC) amplifier which ensures that the digitizers operate at a constant level. Note that there are goblins and magic beyond the digitizer. The signal is shifted in frequency a couple of time but for the purposes of this memo, you can consider this as more baseband filtering. The baseband filters can have fine scale structures and it is more important to carefully determine $G_{BB,antA,bandN}(f_{BB})$.

B.3 Astronomical Bandpass Calibration

B.3.1 Observations

The default scriptWriter setup for bandpass calibration is 15 minutes on a calibrator that is > 4 Jy in flux. This is sufficient for astronomical bandpass calibration of 500 MHz and 62 MHz, and, in the case of a bright calibrator, 31 MHz. To achieve a specific signal-to-noise for a given correlator configuration, the observer can specify the on-source time for the bandpass calibrator in the observing script.

We estimate the integration times required to reach a signal-to-noise of 30 per

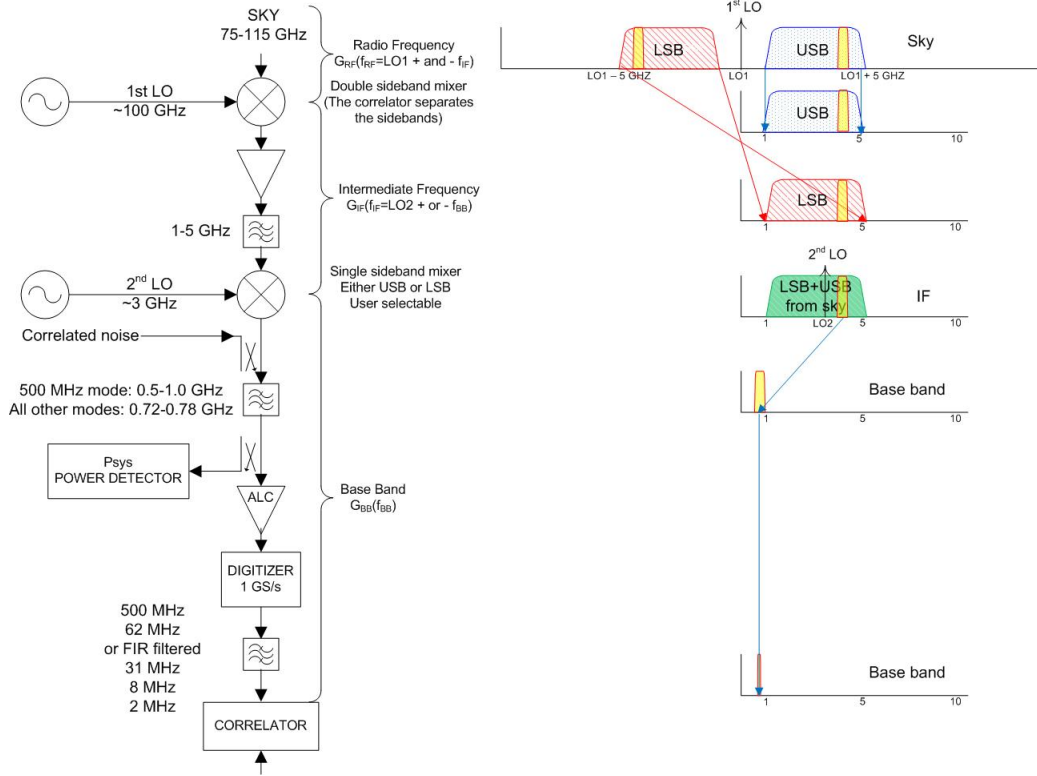


Figure B.1: **(Figure Credit: Dave Woody)** Signal path through the CARMA system.

channel, per antenna for 3mm observations at different bandwidths on a 4 Jy calibrator in Table B.1. A signal-to-noise level of 30 corresponds to phase errors $\sim 2^\circ$.³

Making some standard assumptions about the antenna gain of the two different telescopes (G_{10m}, G_{6m})⁴, the aperture efficiency ($\eta_{ap,10m}, \eta_{ap,6m}$), correlator efficiency (η_{cor}), system temperature ($T_{sys,10m}, T_{sys,6m}$), and atmospheric decorrelation (η_{atm}), we calculate the RMS per channel, per baseline as follows:

$$\sigma_{10m-10m} = \frac{G_{10m} \cdot T_{sys,10m}}{\sqrt{2} \cdot \eta_{ap,10m} \cdot \eta_{cor} \cdot \eta_{atm} \cdot \sqrt{BW \cdot \Delta t}} \quad (\text{B.1})$$

³In the case of strong signal, $S/N \sim 1/\sigma_\phi$ with σ_ϕ in radians.

⁴10m = the 10-meter OVROs, 6m = the 6-meter BIMAs

$$\sigma_{6m-6m} = \frac{G_{6m} \cdot T_{sys,6m}}{\sqrt{2} \cdot \eta_{ap,6m} \cdot \eta_{cor} \cdot \eta_{atm} \cdot \sqrt{BW} \cdot \Delta t} \quad (\text{B.2})$$

$$\sigma_{10m-6m} = \sqrt{\frac{G_{10m}}{\eta_{ap,10m}}} \sqrt{\frac{G_{6m}}{\eta_{ap,6m}}} \frac{\sqrt{T_{sys,10m} \cdot T_{sys,6m}}}{\sqrt{2} \cdot \eta_{cor} \cdot \eta_{atm} \cdot \sqrt{BW} \cdot \Delta t} \quad (\text{B.3})$$

Where the BW is the channel width in Hz, and Δt is the integration time in seconds. All the values we assumed are listed in Table B.2. Combining the baselines to get antenna-based noise per channel:

$$\sigma_{antenna} = \sqrt{\frac{1}{\frac{N_{10m-10m}}{\sigma_{10m-10m}^2} + \frac{N_{6m-6m}}{\sigma_{6m-6m}^2} + \frac{N_{10m-6m}}{\sigma_{10m-6m}^2}}} \quad (\text{B.4})$$

Since we want to calculate the integration time per channel, **per antenna**, we put in the appropriate number of baselines for each antenna. For each of the 10-meter antennas, there are 9 baselines with 6-meter antennas, and 5 baselines with the other 10-meter antennas. For each of the 6-meter antennas, there are 8 baselines with the other 6-meter antennas, and 6 baselines with the 10-meter antennas.

For the observer who wishes to calculate integration times for specific setups, we rewrite this equation to give the signal-to-noise per channel, per antenna as a function of integration time in seconds, flux of the bandpass calibrator in Jy, and channel width in Hz. Because the number of baselines with each type of antenna are different, we have two equations, one for the 6-meter antennas and one for the 10-meter antennas.

$$\frac{S}{N}(6m) = 3.22 \cdot 10^{-4} \cdot \text{Flux} \cdot \sqrt{BW} \cdot \Delta t \quad (\text{B.5})$$

$$\frac{S}{N}(10m) = 4.37 \cdot 10^{-4} \cdot \text{Flux} \cdot \sqrt{BW} \cdot \Delta t \quad (\text{B.6})$$

Bandwidth (MHz)	Channelwidth (MHz)	Int. Time (minutes)
500	31.25	0.3
62	0.977	9.3
31	0.488	18.5
8	0.122	74.2
2	0.0305	296.6

Table B.1: Estimated integration times for a 4 Jy bandpass calibrator for different correlator bandwidths at 3mm required to achieve a signal-to-noise of 30. Values are calculated using Equation B.5 and using the values listed in Table B.2. Please note that T_{sys} for both the 6- and 10-meter antennas are higher at CO, so the integration time needed to achieve a signal-to-noise of 30 would increase by about a factor of 4.

Variable		Value
10m Antenna Gain	G_{10m}	33 Jy/K
6m Antenna Gain	G_{6m}	96 Jy/K
10m Aperture Eff.	$\eta_{ap,10m}$	0.55
6m Aperture Eff.	$\eta_{ap,6m}$	0.65
Correlator Eff.	η_{cor}	0.87
10m Typical T_{sys}	$T_{sys,10m}$	140 K
6m Typical T_{sys}	$T_{sys,6m}$	110 K
Atm. Decorr.	η_{atm}	0.96

Table B.2: Typical CARMA values for antenna gains, aperture efficiency, correlator efficiency, and atmospheric decorrelation at 3mm. Note that T_{sys} at CO is slightly higher — 250 K for the 10-meters and 230 K for the 6-meters.

The observer then can easily solve for the variable of their choice using these equations. To calculate the integration time, we used Equation B.5 for the 6-meter antennas since the smaller collecting area requires longer integration time to achieve the same signal-to-noise as the 10-meter antennas.

B.3.2 Reduction: Bandpass of 500 MHz Band

Bandpass calibration in the wideband (500 MHz) is very straightforward since there is plenty of signal-to-noise in the wideband. To bandpass calibrate the wideband observations, use `mfcal` with a short interval on the bandpass calibrator at the beginning of the reduction process. For example:

```
mfcal vis=bpcal.mir interval=0.2 refant=9
```

`mfcal` solves for the bandpass response per frequency across each spectral window while simultaneously solving for the amplitude and phase correction over time. A short interval is necessary to avoid changes in the atmosphere, so the brighter the bandpass source, the better. Pick a reference antenna that's near the center of your array configuration with the best system temperature and size.

Once the bandpass solution is obtained, copy the bandpass gains table over to your phase calibrator and source and apply the solutions with `uvcat`:

```
gpcopy vis=bpcal.mir out=source.mir options=nocal  
uvcat vis=source.mir out=source.bp.mir options=nocal
```

The `options=nocal` is important because you don't want to apply the amplitude and phase calibrations calculated by the `mfcal`, you want to do that separately with the phase calibrator later on in the reduction.

Depending on the observing frequency, weather conditions, and the flux of the bandpass calibrator, there's usually enough signal-to-noise to bandpass calibrate the 62 MHz narrowband with the same method as the 500 MHz wideband provided that

one of the brighter calibrators can be observed.

B.3.3 Reduction: Bandpass of One 500 MHz + Two Narrower Bands

In some cases, it is useful to set up the correlator with two narrowbands and an overlapping wideband, which allows the observation of a fainter phase calibrator without changing correlator setups. In this scenario, we consider only narrowbands that can be bandpass calibrated astronomically (62 MHz and maybe 31 MHz if the bandpass calibrator is bright). The advantage of this kind of setup is a simpler reduction method, which involves only calculating the phase offset between the narrow and wideband using the astronomical bandpass calibrator. Please refer to Section B.3.1 for suggested integration times for the two narrowbands.

In this example, we have a 500 MHz wideband in band 1, and 62 MHz narrowbands in bands 2 and 3, and we're only interested in the upper side band (windows 4–6). Split up the data into different sources (bandpass calibrator, source, phase calibrator) but keep all three windows in the same Miriad file. After the appropriate flagging has been done, bandpass calibrate all three windows at the same time on an integration-by-integration basis to avoid temporal atmospheric effects:

```
mfcal vis=bpcal.mir interval=0.2 refant=9
```

Then copy and apply the bandpass gains table to your phase calibrator and source:

```
gpcopy vis=bpcal.mir out=source.mir options=nocal
```

```
uvcat vis=source.mir out=source.bp.mir options=nocal
```

The `uvcat` command applies the bandpass calibration, and like the example in the previous section, the `options=nocal` is important because we don't want to apply the phase calibrations calculated by the `mfcal`, you do that later with the phase calibrator. Running `mfcal` on all three windows at the same time calculates the offset between windows, which allows the observer to use the phase and amplitude solutions from the 500 MHz observations of the phase calibrator on the source data in the narrowbands. Extensive tests by Misty La Vigne and Jin Koda have found that this offset is constant over a period of a few days, so you only have to calculate this offset once in the track. For more information on phase/amplitude calibration, please see the CARMA cookbook.

B.4 Calibrating the Bandpass with the Noise Source

In the narrower bands, one runs into the problem of low signal-to-noise, which inhibits the use of an astronomical source for bandpass calibration. Hence we rely on the noise source, injected at the baseband, to relate the wideband astronomical passband to the narrowband. The theory is that we can still use wideband data to take out the RF and IF behavior, while the noise source takes out the baseband components.

B.4.1 Visibilities

A single antenna's contribution to the visibility of a point-like astronomical source is:

$$V_{astro,antA}(f_{RF}) = \sqrt{A_{astro}(f_{RF})} G_{RF,antA}(f_{RF}) G_{IF,antA,bandN}(f_{IF}) G_{BB,antA,bandN}(f_{BB}), \quad (\text{B.7})$$

where $f_{IF} = |f_{RF} - LO1|$ and $f_{BB} = |f_{IF} - LO2| = |f_{RF} - (LO1 \pm LO2)|$. The + sign in the last term is for the upper sideband signals from the down-converter and the - sign for the lower sideband. Signals with $f_{RF} > LO1$ are the upper sideband spectral windows in the Miriad data whereas signals with $f_{RF} < LO1$ are the lower sideband spectral windows. Note that the center of the final spectral band corresponds to $f_{BB} = 750$ MHz. The correlated noise source signal is injected into the base band and its single antenna component of the visibility is:

$$V_{noise,antA}(f_{BB}) = \sqrt{A_{noise}(f_{BB})} G_{BB,antA,bandN}(f_{BB}). \quad (\text{B.8})$$

The correlated noise source is designed to be wideband and have a reasonably flat spectrum. If LO1 and LO2 are kept at the same values as used for the astronomical observations then noise source visibilities will appear to come from the same sky frequencies, f_{RF} , as the astronomical observations. The noise source at baseband are phase switched to look like a lower sideband signal from the sky. A Miriad task is used to move a complex conjugate copy of the lower sideband spectral window to the upper sideband spectral window and hence the noise source appears to have both sidebands from the sky (see Section B.4.4 for more details).

B.4.2 Bandpass Calibration

Calibrating the astronomical visibilities of source X using the noise source observation is equivalent to dividing the astronomical visibilities by $V_{noise,antA}(f_{BB})$ giving:

$$V_{Ncal,astro,X,antA}(f_{RF}) = \sqrt{\frac{A_{astro} X_{RF}}{A_{noise}(f_{RF})}} G_{RF,antA}(f_{RF}) G_{IF,antA,bandN}(|f_{RF} - LO1|). \quad (\text{B.9})$$

This normalizes the astronomical observations to the correlated noise source and ideally removes the fine scale spectral features caused by the analog and FIR filters.

The normal procedure for bandpass calibrating astronomical data is to use a strong continuum astronomical source, X, to measure the bandpass in the same correlator configuration as the target, Y. This gives the bandpass calibrated signal:

$$V_{Xcal,astro,Y,antA}(f_{RF}) = \sqrt{\frac{A_{astro,Y}(f_{RF})}{A_{astro,X}(f_{RF})}}. \quad (\text{B.10})$$

if the same noise calibration had been previously applied to both X and Y, the noise calibration is effectively removed by the astronomical bandpass calibration.

The bandpass calibration source observed at wide resolution and the observation of the target source at narrow resolution can be linked using the correlated noise source. The trick is to normalize each astronomical observation by a noise source measurement with the **same** correlator configuration and with **same** LO1 and LO2 values for both sets of observations, i.e. only change the BW# in the “configband” command. The Miriad processing needs to be done in sky frequency or VLSR space so that Miriad can properly interpolate the wideband calibration onto the narrowband channels. The wideband observations are essentially giving the smoothed value for the gains and spectra. Over the RF frequency range of interest for the narrowband observations Equation (3) after noise calibration of the wideband observation of X becomes:

$$\overline{V_{Ncal,astro,X,antA}(f_{RF})} = \sqrt{\frac{A_{astro,X}(f_{RF})}{A_{noise}(f_{RF})}} \overline{G_{RF,antA}(f_{RF})G_{IF,antA,bandN}(|f_{RF} - LO1|)}. \quad (\text{B.11})$$

Applying astronomical bandpass calibration using noise calibrated wideband observations of source X to noise calibrated narrowband observations of source Y gives:

$$V_{N\&Xcal,astro,Y,antA}(f_{RF}) = \sqrt{\frac{A_{astro,Y}(f_{RF})\overline{A_{noise}(f_{RF})}}{A_{astro,X}(f_{RF})\overline{A_{noise}(f_{RF})}}} \frac{G_{RF,antA}(f_{RF})G_{IF,antA,bandN}(|f_{RF} - LO1|)}{G_{RF,antA}(f_{RF})\overline{G_{IF,antA,bandN}(|f_{RF} - LO1|)}} \quad (\text{B.12})$$

Over the bandwidth of the narrow spectral bands the RF and IF gains as well as the noise source spectrum should be smooth so that their fine scale spectra shapes divided by their averages is unity. Equation (6) then becomes:

$$V_{N\&Xcal,astro,Y,antA}(f_{RF}) = \sqrt{\frac{A_{astro,Y}(f_{RF})}{A_{astro,X}(f_{RF})}}. \quad (\text{B.13})$$

This has the benefit of calibrating the bandpass for narrowband target observations for high signal-to-noise wideband observations of the bandpass calibrator.

B.4.3 Writing an Observing Script

A quick step-by-step for implementing the noise bandpass calibration for narrowbands is outlined below, with the scriptWriter and Miriad steps associated with it.

The CARMA scriptWriter has an option to observe the source in all narrowband mode and the calibrator in all wideband mode. Note that the center of the 500 MHz band will be lined up in frequency with the center of the narrowband during astronomical and noise observations. To set up the observations, modify the 'reconfig' parameter in the observing script from None to od.CORR_BW500 like below:

```
# Correlator configuration for calibrators
# reconfig: Sets correlator configuration for calibration observations
# None : same as for science targets
# od.CORR_BW500L06: 500 MHz, non-overlapping bands in BIMA IF
# od.CORR_BW500L0 : 500 MHz, non-overlapping bands
# od.CORR_BW500 : change bands to 500 MHz without changing IF
# hybrid: Correlator configurations to calibrate band offsets.
# Needed only if all bands have width < 500 MHz.
```

```

# tintHybrid : integration time for each of the hybrid correlator modes
correlator = {
'reconfig' : od.CORR_BW500,
'hybrid' : None,
#'hybrid' : [ [BW500, BW62, BW62], [BW62, BW500, BW62] ],
'tintHybrid' : 5.0,
}

```

This will observe the bandpass calibrator and noise source in both the wideband and narrowband modes. Make sure you leave the noise source observations with its default settings.

B.4.4 Reduction

The calibrations should be done on a band-to-band basis, and it's best to split the spectral windows and sources (noise and astronomical) up to avoid confusion. In the example, we're only calibrating the lower sideband part of band 1 (= window 1), which we split up already. Please flag all your bad data before starting the bandpass calibration, otherwise the bandpass solution may not converge! **Note - it is critical not to do baseline or linelength corrections on the noise source - bad things will happen to the noise bandpass calibration if you do. It is recommended that you uvcat the noise data out before you apply the baseline and/or linelength corrections (if needed).**

1. Bandpass calibrate the 500 MHz wideband noise source. Figure B.2 shows the amplitude and phase of the noise source vs. channel in the 500 MHz band after noise bandpass calibration.

```
mfcal vis=noise500win1 refant=9 interval=0.2
```

2. Copy the noise bandpass from step (1) to the 500 MHz wideband astronomical calibrator, apply the solution, then bandpass calibrate the **astronomical** bandpass calibrator. Figure B.3 shows the amplitude and phase of the astronomical source (3c273) vs. channel after noise **and** astronomical bandpass calibration.

```
gpcopy vis=noise500win1 out=source500win1 options=nocal  
uvcat vis=source500win1 out=source500win1noise options=nocal  
mfcal vis=source500win1noise refant=9 interval=0.2
```

3. Bandpass calibrate the 31 MHz narrowband noise source. Figure B.4 shows the amplitude and phase of the noise source vs. channel in the narrowband after noise bandpass calibration.

```
mfcal vis=noise31win1 refant=9 interval=0.2
```

4. Copy the 31 MHz narrowband noise source to the narrowband **astronomical** source, apply.

```
gpcopy vis=noise31win1 out=source31win1 options=nocal  
uvcat vis=source31win1 out=source31win1noise options=nocal
```

5. Copy the 500 MHz wideband calibrations from step (2) to the narrowband **astronomical** source, apply. Figure B.5 shows the amplitude and phase of the astronomical source (3c273) vs. channel in the 31 MHz narrowband after all the bandpass calibrations have been applied.

```
gpcopy vis=source500win1noise out=source31win1noise options=nocal
uvcat vis=source31win1noise out=final options=nocal
```

The offset of phase from zero in Figure B.5 reflects the window-to-window offset between the narrow and wideband. This is ideally taken out by bandpass calibration on a bright astronomical calibrator, but we lack the signal-to-noise to do this in the narrowest bands. The offset can be calculated (after the bandpass calibration steps above) by doing a `selfcal` on the wideband astronomical source with `interval=0.2` to remove temporal atmospheric effects, copy and apply the gains to the corresponding narrowband observations of the bandpass calibrator, then carry out `selfcal` on the narrowband data with `interval=9999` to average over the entire bandpass observation (to maximize the signal-to-noise). The resulting gain solution contains the window-to-window offset. This offset can then be applied to the source data for that narrowband window. For more information please see the CARMA Cookbook.

Checking the Noise Bandpass Method

As a check, we do a final bandpass calibration on the narrowband astronomical source in the last step. **This is not a part of the reduction!** This is to check for differences between an astronomical bandpass calibration on a very bright source (the ideal way to do bandpass calibration, but it takes a lot of integration time and is too noisy for the narrower bands), and the noise bandpass technique described in the steps above. Figure B.6 shows the amplitude and phase vs. channel of the astronomical source — the very flat amplitude and phase imply that there isn't much difference between the two techniques.

Copying the Noise Source to the USB

If the data you want to work with is in the upper sideband (USB), where there is no noise source, the data will have to be conjugated into the USB in Miriad. One simple step does the trick:

```
uvcal vis=data.mir out=data.conj.mir options=noiseconj
```

B.4.5 Phase Calibration

The map quality is improved when a nearby astronomical point source calibrator is used to track the instrumental phase drifts and even some of the atmospheric delay changes. This usually results in using weaker phase calibrators which require as much correlated bandwidth as possible to get reliable phase measurements. The bandpass calibration described above uses the 500 MHz mode but with the same 2nd LO setting as used for the target observations. For narrow line observations this will result in large overlap among the three bands. The bands can be spread out to

cover more bandwidth by changing the 2nd LO in the `configband` command. This changes the band positions in the RF and IF bands. Another calibration step is required to link the RF and IF gains at the frequencies used for phase calibration to the target observation frequencies. This calibration is best done using the bandpass calibration source since the target observations are already linked to the bandpass source. Typically all bands and the phase calibrator observations will be calibrated relative to the wideband measurements of the bandpass source in band 1.

B.5 Calibration in the 62 MHz – CARMA Hybrid Mode

B.5.1 The Hybrid Method

Though the bandpass calibration technique utilizing the noise source discussed in the previous Section works well for the narrowbands (31 MHz and below), it introduces some unpleasant ripples in both amplitude ($\sim 10\%$) and phase ($\sim 10^\circ$). Though this may be ignored for some projects, PIs who wish to avoid introducing such noise into their maps should either bandpass calibrate the 62 MHz bands with a very bright astronomical source, or utilize the CARMA Hybrid Mode at the cost of longer bandpass calibrations (~ 30 minutes).

Though this document is focused on bandpass calibration, the main goal of the 62 MHz Hybrid mode is actually for observing a science source in 3 overlapping narrowband (62 MHz) modes, and observing the calibrator in 3 wideband (500 MHz) modes as discussed in the previous section. The wideband calibration observations will result in better signal-to-noise, which allows the PI to select fainter but closer calibrators. Hybrid passband observations are acquired during the track in the fol-

lowing correlator setups:

```
wide [BW500, BW500, BW500]
```

```
narrow [BW62, BW62, BW62]
```

```
hybrid [BW500, BW62, BW62]
```

```
hybrid [BW62, BW500, BW62]
```

in order to (1) calculate phase offsets between the wide and narrowband and (2) address atmospheric phase fluctuations. Differences in phase can be determined, in principle, when observations are made with (two) alternating wide and narrowband setups, but atmospheric phase fluctuations can introduce significant phase errors in the measured band offset which are in principle avoided by the hybrid approach.

B.5.2 Writing a Hybrid Observing Script

The CARMA scriptWriter is versatile and has been formatted with all of the tools necessary to observe a source with three 62 MHz bands.

In the example given below, the bands have been overlapped by 6 channels. The `chanoffset` variable defined by the observer, which is in GHz, is calculated as follows (add these lines to the scriptWriter generated observing script):

```
chanoffset = [bandwidth - ((#ofchannels_overlap + 0.5) * delta_nu)]/1000GHz  
bandwidth = 62.5 MHz #(= 62.5 MHz / 63 channels)  
delta_nu = 0.977 MHz
```

To overlap the Bands, set the tuning in the generated script as follows:

```

# Tuning options
tuning = {
  'restfreq' : linefreq('12CO(1-0)'), # Alternate way to specify rest frequency
# 'restfreq' : 95.0, # [GHz] Line rest frequency
  'sideband' : USB, # Sideband for first LO (LSB or USB)
  'IFfreq' : 1.79, # [GHz] IF frequency
}

# Correlator configuration for science target
chanoffset = 0.0560195
configband(1, BW62, tuning['restfreq']-chanoffset)
configband(2, BW62, tuning['restfreq'])
configband(3, BW62, tuning['restfreq']+chanoffset)

```

An observer can adjust the number of channels they wish to overlap with '# ofchannels_overlap'. The first 3 beginning and ending channels in the 62 MHz mode are known to have a large rms noise. Therefore, it is advisable to overlap at least 6 channels to be safe. The noisy channels should be flagged during reduction to avoid introducing more noise into the data. Furthermore, it is also advisable to overlap an even number of channels so that a symmetric number of channels/velocities are flagged later. As always, the correlator configuration should be checked using the Correlator Configuration Tool on the CARMA tools webpage.

To observe the calibrator in 3 wideband, 500 MHz modes, set `reconfig` to one of the three `od.CORR_BW500` options as shown below.

```

# Correlator configuration for calibrators

```

```

# reconfig: Sets correlator configuration for calibration observations
# None : same as for science targets
# od.CORR_BW500L06: 500 MHz, non-overlapping bands in BIMA IF
# od.CORR_BW500L0 : 500 MHz, non-overlapping bands
# od.CORR_BW500 : change bands to 500 MHz without changing IF
# hybrid: Correlator configurations to calibrate band offsets.
# Needed only if all bands have width < 500 MHz.
# tintHybrid : integration time for each of the hybrid correlator modes
correlator = {
  'reconfig' : od.CORR_BW500L06,
  #'hybrid' : None,
  'hybrid' : [ [BW500, BW62, BW62], [BW62, BW500, BW62] ],
  'tintHybrid' : 5.0,
}

```

If observing 3mm, `od.CORR_BW500L06` is the best option. To observe the pass-band source in the hybrid setup in addition to the wideband (for calibrator) and narrowband (for source) setups, uncomment the

```
'hybrid' : [ [BW500, BW62, BW62], [BW62, BW500, BW62] ],
```

command and comment out or delete the `'hybrid' : None,` option. The `'tintHybrid'` parameter sets the integration time for each of the the hybrid modes on the pass-band calibrator. I.e. For the setup above, you would get a total of 10 minutes for bandpass calibration, 5 minutes with setup `[BW500, BW62, BW62]` and 5 minutes with setup `[BW62, BW500, BW62]`.

Setting up Passband Observations:

```
Passband = {  
'doPassband' : True, # If True, observe passband calibrator  
'doPoint' : False, # Point up on passband calibrator if needed  
'forcePoint' : False, # Force pointing if source is available  
'tint' : 5.00, # [minutes] Passband calibrator integration time  
'minflux' : 4.00, # [Jy] Minimum flux density for passband cal  
'preferred' : '3c273,1058+015', # Preferred passband calibrator  
'middle' : False, # OK to observe in middle of phase/source cycle?  
'ncal' : 1, # Maximum number of calibrators to observe per track  
'interval' : None, # [hours] How frequently to perform passband cal  
}
```

An example setup for passband observations is given above. First, to observe a passband source, set `'doPassband'` to `True`. To set the integration time for the wide band and narrow band passband observations set `'tint'` to a value in minutes. It is important to set a minimum flux for the passband source with `'minflux'`, particularly if a preferred passband source is not set. It is possible to set multiple preferred passband sources as in the example given above; the script will first look to see if 3c273 is up and then 1058+015. To allow the passband source to be observed in the middle of a track, set `'middle'` to `True`. To point on the passband source if pointing is needed, set `'doPoint'` to `True`.

B.5.3 Reduction

Reduction of the 62 MHz Hybrid Mode is relatively complicated right now, and done by a C shell script calling various Miriad commands. Please see the CARMA Cookbook for more information.

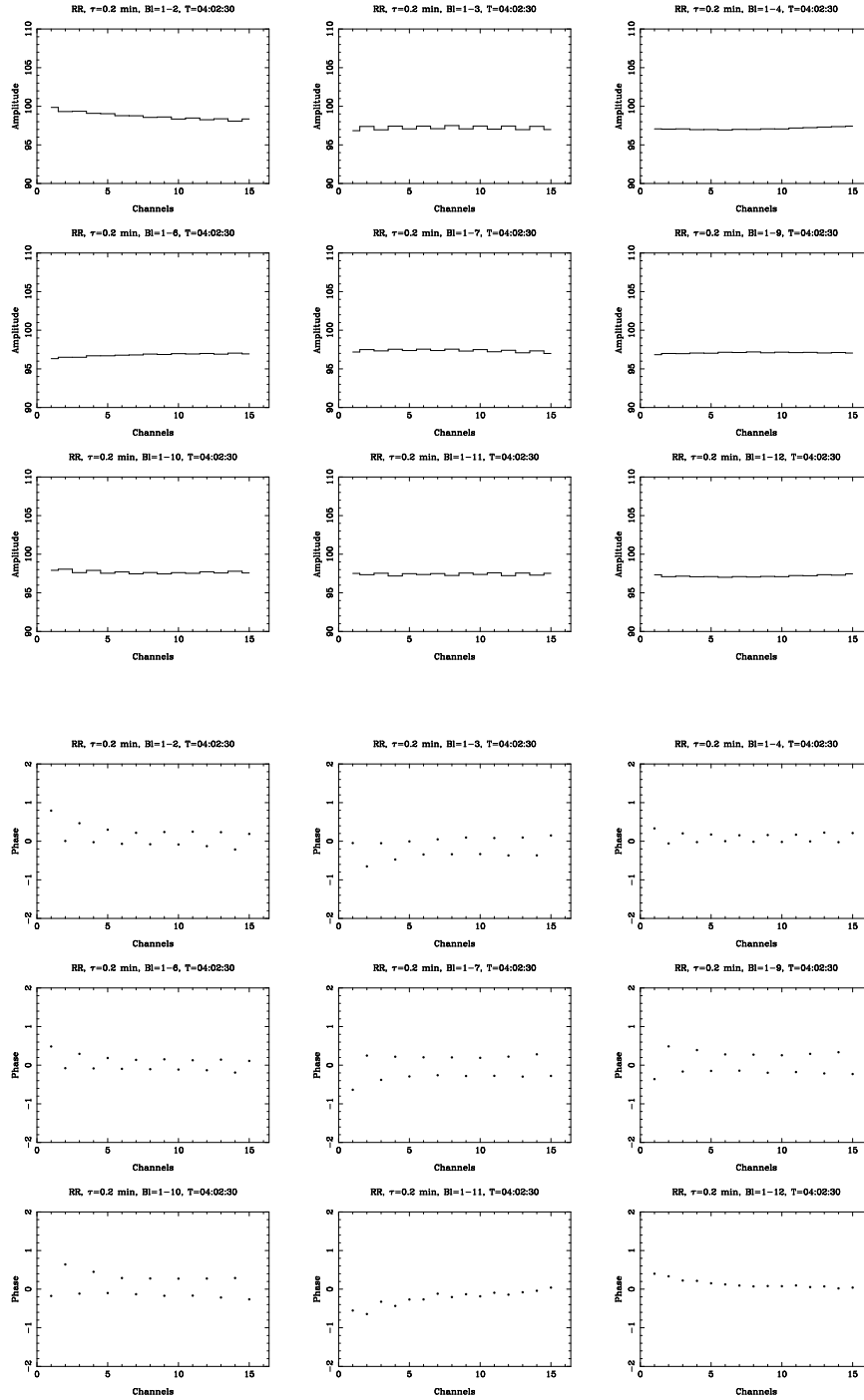


Figure B.2: Amplitude (top) and phase (bottom) of the noise source vs. channel in the 500 MHz band after noise bandpass calibration for baselines with Antenna 1. The bimodality in the phases are known and very small ($\sim 1^\circ$), and do not affect the bandpass calibration. The Miriad command used to make these plots is:

```
uvspec vis=visfilename device=visfile.ps/ps axis=channel,amp
```

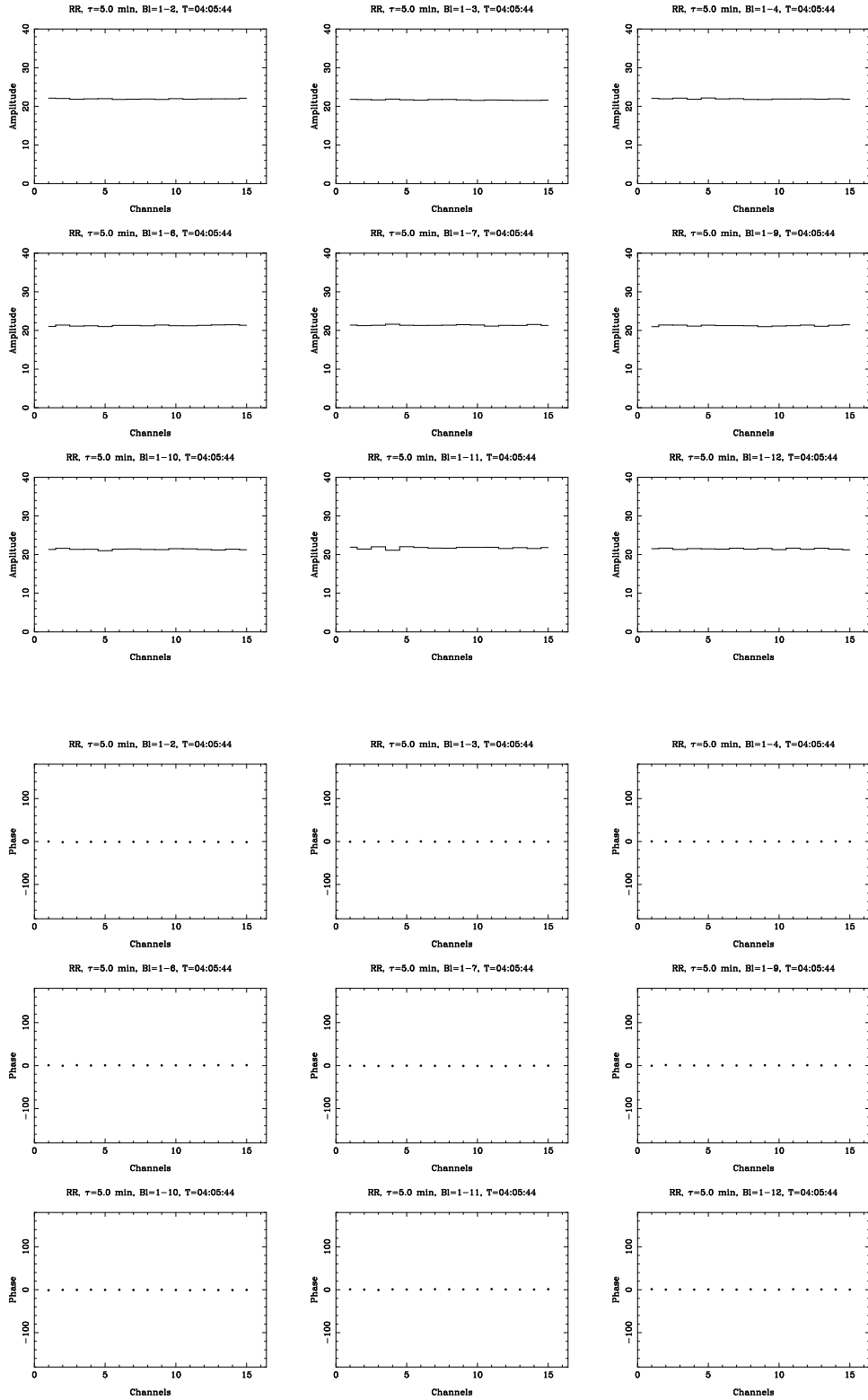


Figure B.3: Amplitude (top) and phase (bottom) of the astronomical source (3C273) vs. channel in the 500 MHz band after noise and astronomical bandpass calibration.

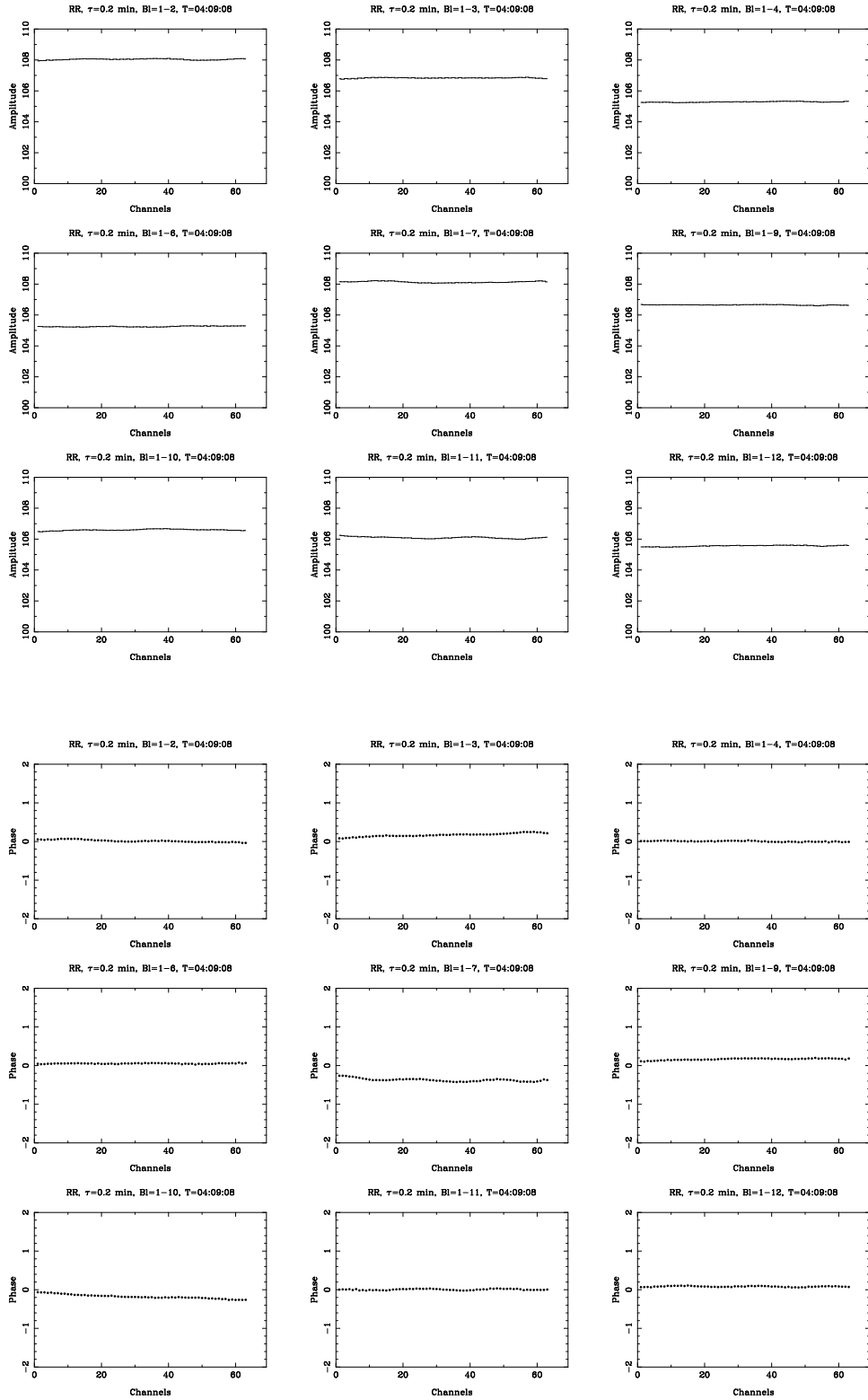


Figure B.4: Amplitude (top) and phase (bottom) of the noise source vs. channel in the 31 MHz narrowband after noise bandpass calibration.

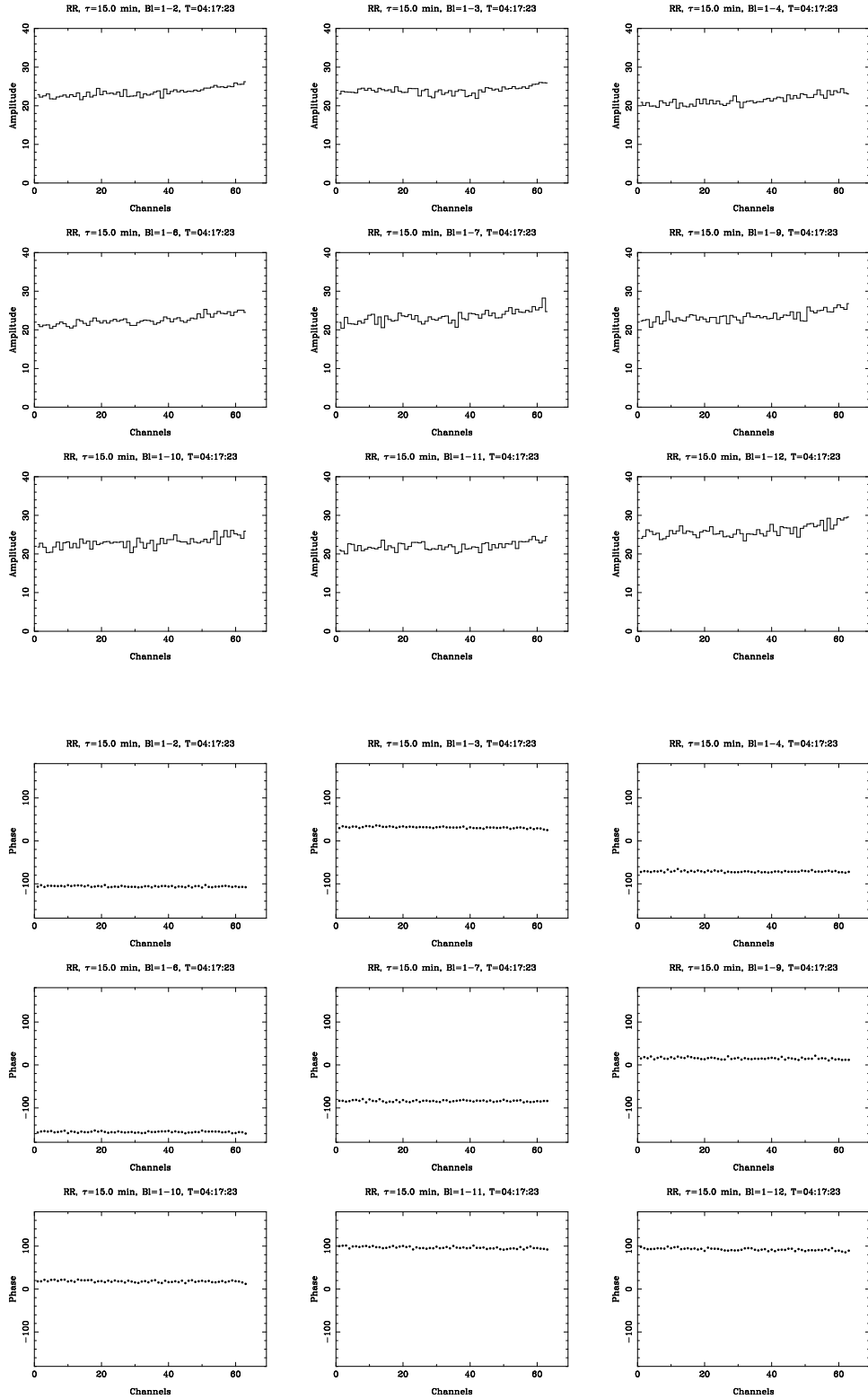


Figure B.5: Amplitude (top) and phase (bottom) of the astronomical source (3c273) vs. channel in the 31 MHz narrowband after all bandpass calibrations have been applied. Phase offsets from zero are corrected by the gain calibration later on in the reduction process.

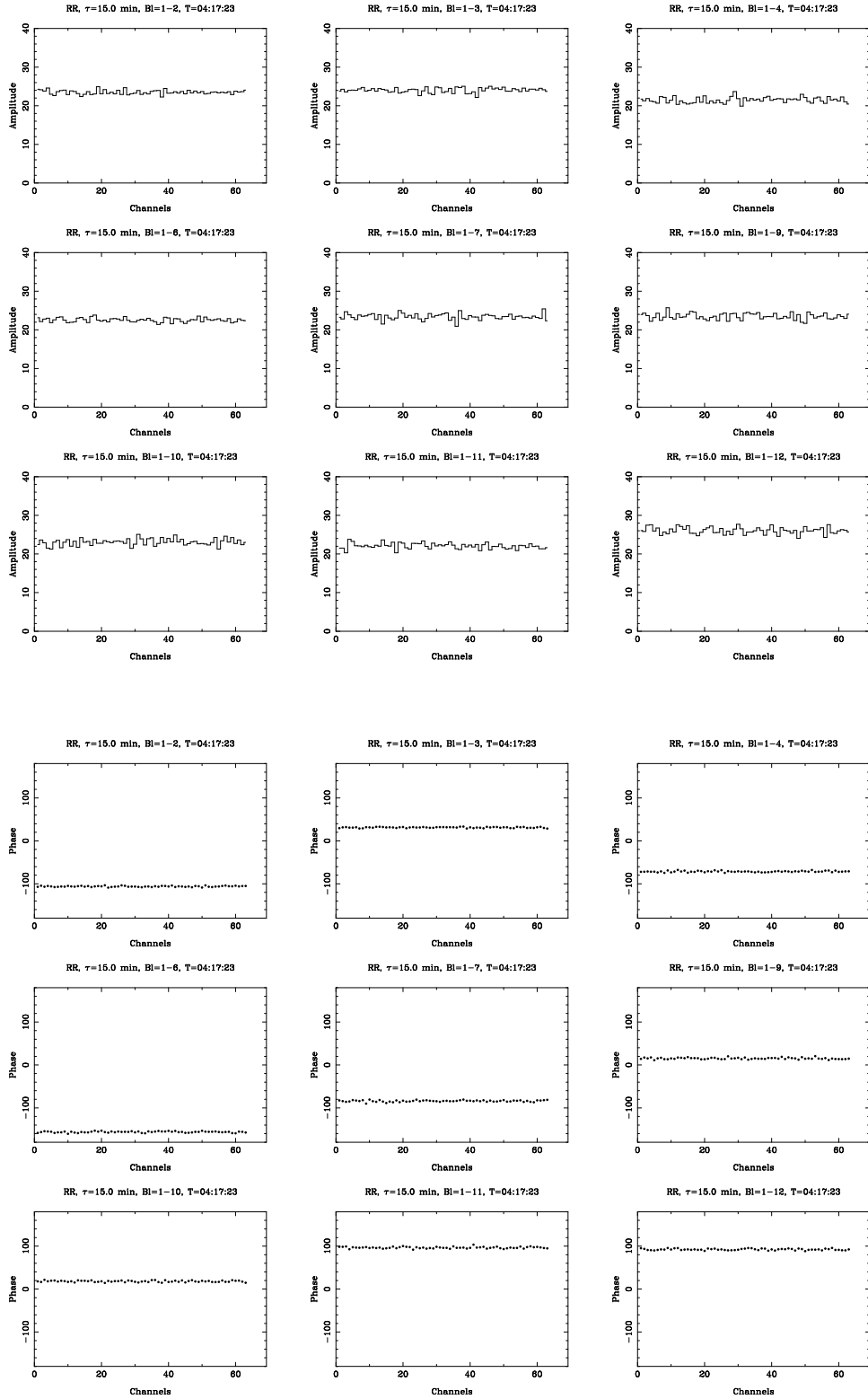


Figure B.6: Amplitude (top) and phase (bottom) of the calibrated 31 MHz astronomical source vs. channel after another astronomical bandpass — this is done as a check to look for differences between the noise bandpass calibration technique described in Section B.4.4 and a pure astronomical bandpass calibration. The flat amplitude and phase implies that there isn't much difference between the two techniques.

Appendix C

Glossary

Blue sequence – The region in color vs. stellar mass space typically occupied by young, star-forming spiral galaxies.

CARMA – Combined Array for Research in Millimeter-wave Astronomy, a millimeter interferometer located in Cedar Flat, California.

CO(1–0) – J=1–0 transition of carbon monoxide, used to trace molecular hydrogen in galaxies.

E/S0s – Elliptical and Lenticular galaxies, historically thought to be gas poor and passively evolving on the red sequence.

Early-Type Galaxies – Elliptical and Lenticular galaxies, historically thought to be gas poor and passively evolving on the red sequence.

FUV – Far-Ultraviolet radiation, as observed by *GALEX* detector centered on 1528Å.

GALEX – *Galaxy Evolution Explorer*, a space telescope in orbit around the Earth observing in ultraviolet wavelengths.

GBT – The Robert C. Byrd Green Bank Telescope, a 100-meter single-dish radio telescope located in Green Bank, West Virginia.

Gyr – 10^9 years.

H₂ – Molecular hydrogen.

HI – Atomic hydrogen.

IRAC – InfraRed Array Camera, an infrared camera on *Spitzer* that images at 3.6, 4.5, 5.8, and 8 μm .

KGB – Kannappan et al. (2009).

Late-Type Galaxies – Spiral galaxies, typically young, star-forming, and gas-rich.

M_b – bimodality mass ($M_* \lesssim 3 \times 10^{10} M_\odot$) discussed in KGB below which Kauffmann et al. (2003) finds star formation histories to be bursty.

MIPS – Multiband Imaging Photometer for Spitzer, a detector on *Spitzer* that observes at 24, 70, and 160 μm .

MSFE – Molecular star formation efficiency, or the % of molecular gas consumed in 10^8 years. Defined as $\text{SFR}/M_{\text{H}_2+\text{He}}$.

NFGS – Nearby Field Galaxy Survey, a catalog of ~ 200 nearby field galaxies (Jansen et al. 2000b).

PAH – Polycyclic Aromatic Hydrocarbons, large molecules found in the interstellar medium whose emission is used to trace star formation.

Red Sequence – The region in color vs. stellar mass space typically occupied by passive elliptical galaxies.

SFR – Star formation rate.

Spitzer – *Spitzer Space Telescope*, a space telescope in orbit around the Sun that observes in the infrared.

TSFE – Total-gas star formation efficiency, or the % of gas consumed in 10^8 years. Defined as $\text{SFR}/M_{\text{HI}+\text{H}_2+\text{He}}$.

X_{CO} – CO-to-H₂ conversion factor.

Bibliography

- Angeretti, L., Tosi, M., Greggio, L., Sabbi, E., Aloisi, A., & Leitherer, C. 2005, *AJ*, 129, 2203
- Baldry, I. K., Glazebrook, K., Brinkmann, J., Ivezić, Ž., Lupton, R. H., Nichol, R. C., & Szalay, A. S. 2004, *ApJ*, 600, 681
- Barazza, F. D., Jogee, S., & Marinova, I. 2008, *ApJ*, 675, 1194
- Barbieri, C., Bonoli, C., & Rafanelli, P. 1979, *A&AS*, 37, 541
- Barnes, D. G., Staveley-Smith, L., de Blok, W. J. G., Oosterloo, T., Stewart, I. M., Wright, A. E., Banks, G. D., Bhathal, R., Boyce, P. J., Calabretta, M. R., Disney, M. J., Drinkwater, M. J., Ekers, R. D., Freeman, K. C., Gibson, B. K., Green, A. J., Haynes, R. F., te Lintel Hekkert, P., Henning, P. A., Jerjen, H., Juraszek, S., Kesteven, M. J., Kilborn, V. A., Knezek, P. M., Koribalski, B., Kraan-Korteweg, R. C., Malin, D. F., Marquarding, M., Minchin, R. F., Mould, J. R., Price, R. M., Putman, M. E., Ryder, S. D., Sadler, E. M., Schröder, A., Stootman, F., Webster, R. L., Wilson, W. E., & Ye, T. 2001, *MNRAS*, 322, 486
- Barnes, J. E. 2001, in *Astronomical Society of the Pacific Conference Series*, Vol. 245, *Astrophysical Ages and Times Scales*, ed. T. von Hippel, C. Simpson, & N. Manset, 382
- Barnes, J. E. 2002, *MNRAS*, 333, 481
- Bekki, K. 1998, *ApJ*, 502, L133

- Bell, E. F., McIntosh, D. H., Katz, N., & Weinberg, M. D. 2003, *ApJS*, 149, 289
- Bendo, G. J., Wilson, C. D., Warren, B. E., Brinks, E., Butner, H. M., Chaniai, P., Clements, D. L., Courteau, S., Irwin, J., Israel, F. P., Knapen, J. H., Leech, J., Matthews, H. E., Mühle, S., Petitpas, G., Serjeant, S., Tan, B. K., Tilanus, R. P. J., Usero, A., Vaccari, M., van der Werf, P., Vlahakis, C., Wiegert, T., & Zhu, M. 2010, *MNRAS*, 402, 1409
- Bigiel, F., Leroy, A., Walter, F., Brinks, E., de Blok, W. J. G., Madore, B., & Thornley, M. D. 2008, *AJ*, 136, 2846
- Binney, J., & Merrifield, M. 1998, *Galactic Astronomy* (Galactic Astronomy : by James Binney and Michael Merrifield. Princeton, NJ : Princeton University Press, 1998. (Princeton series in astrophysics) QB857 .B522 1998)
- Binney, J., & Tremaine, S. 2008, *Galactic Dynamics: Second Edition* (Galactic Dynamics: Second Edition, by James Binney and Scott Tremaine. ISBN 978-0-691-13026-2 (HB). Published by Princeton University Press, Princeton, NJ USA, 2008.)
- Blanton, M. R., Eisenstein, D., Hogg, D. W., Schlegel, D. J., & Brinkmann, J. 2005, *ApJ*, 629, 143
- Blitz, L., & Rosolowsky, E. 2004, *ApJ*, 612, L29
- Bock, D., Bolatto, A. D., Hawkins, D. W., Kembell, A. J., Lamb, J. W., Plambeck, R. L., Pound, M. W., Scott, S. L., Woody, D. P., & Wright, M. C. H. 2006, in *Society of Photo-Optical Instrumentation Engineers (SPIE) Conference Series*, Vol. 6267, Society of Photo-Optical Instrumentation Engineers (SPIE) Conference Series
- Bournaud, F., Jog, C. J., & Combes, F. 2005, *A&A*, 437, 69
- Bower, R. G., Benson, A. J., Malbon, R., Helly, J. C., Frenk, C. S., Baugh, C. M., Cole, S., & Lacey, C. G. 2006, *MNRAS*, 370, 645

- Buta, R., & Combes, F. 1996, *Fund. Cosmic Phys.*, 17, 95
- Calzetti, D., Kennicutt, R. C., Engelbracht, C. W., Leitherer, C., Draine, B. T., Kewley, L., Moustakas, J., Sosey, M., Dale, D. A., Gordon, K. D., Helou, G. X., Hollenbach, D. J., Armus, L., Bendo, G., Bot, C., Buckalew, B., Jarrett, T., Li, A., Meyer, M., Murphy, E. J., Prescott, M., Regan, M. W., Rieke, G. H., Roussel, H., Sheth, K., Smith, J. D. T., Thornley, M. D., & Walter, F. 2007, *ApJ*, 666, 870
- Ciotti, L., D’Ercole, A., Pellegrini, S., & Renzini, A. 1991, *ApJ*, 376, 380
- Cole, S., Aragon-Salamanca, A., Frenk, C. S., Navarro, J. F., & Zepf, S. E. 1994, *MNRAS*, 271, 781
- Combes, F., Young, L. M., & Bureau, M. 2007, *MNRAS*, 377, 1795
- Cortese, L., & Hughes, T. M. 2009, *MNRAS*, 1412
- Courteau, S., de Jong, R. S., & Broeils, A. H. 1996, *ApJ*, 457, L73
- Crocker, A. F., Bureau, M., Young, L. M., & Combes, F. 2008, *MNRAS*, 386, 1811
- . 2010, ArXiv e-prints
- Dalcanton, J. J. 2007, *ApJ*, 658, 941
- Dalcanton, J. J., Yoachim, P., & Bernstein, R. A. 2004, *ApJ*, 608, 189
- Dale, D. A., Bendo, G. J., Engelbracht, C. W., Gordon, K. D., Regan, M. W., Armus, L., Cannon, J. M., Calzetti, D., Draine, B. T., Helou, G., Joseph, R. D., Kennicutt, R. C., Li, A., Murphy, E. J., Roussel, H., Walter, F., Hanson, H. M., Hollenbach, D. J., Jarrett, T. H., Kewley, L. J., Lamanna, C. A., Leitherer, C., Meyer, M. J., Rieke, G. H., Rieke, M. J., Sheth, K., Smith, J. D. T., & Thornley, M. D. 2005, *ApJ*, 633, 857
- Darg, D. W., Kaviraj, S., Lintott, C. J., Schawinski, K., Sarzi, M., Bamford, S., Silk, J., Andreescu, D., Murray, P., Nichol, R. C., Raddick, M. J., Slosar, A., Szalay, A. S., Thomas, D., & Vandenberg, J. 2009, ArXiv e-prints

- Dasyra, K. M., Tacconi, L. J., Davies, R. I., Genzel, R., Lutz, D., Naab, T., Burkert, A., Veilleux, S., & Sanders, D. B. 2006a, *ApJ*, 638, 745
- Dasyra, K. M., Tacconi, L. J., Davies, R. I., Naab, T., Genzel, R., Lutz, D., Sturm, E., Baker, A. J., Veilleux, S., Sanders, D. B., & Burkert, A. 2006b, *ApJ*, 651, 835
- . 2006c, *ApJ*, 651, 835
- de Zeeuw, P. T., Bureau, M., Emsellem, E., Bacon, R., Carollo, C. M., Copin, Y., Davies, R. L., Kuntschner, H., Miller, B. W., Monnet, G., Peletier, R. F., & Verolme, E. K. 2002, *MNRAS*, 329, 513
- Debattista, V. P., Mayer, L., Carollo, C. M., Moore, B., Wadsley, J., & Quinn, T. 2006, *ApJ*, 645, 209
- Dekel, A., & Birnboim, Y. 2006, *MNRAS*, 368, 2
- Dellenbusch, K. E., Gallagher, III, J. S., Knezek, P. M., & Noble, A. G. 2008, *AJ*, 135, 326
- Elmegreen, B. G. 1994, *ApJ*, 425, L73
- Emsellem, E., Cappellari, M., Krajnović, D., van de Ven, G., Bacon, R., Bureau, M., Davies, R. L., de Zeeuw, P. T., Falcón-Barroso, J., Kuntschner, H., McDermid, R., Peletier, R. F., & Sarzi, M. 2007, *MNRAS*, 379, 401
- Emsellem, E., Cappellari, M., Peletier, R. F., McDermid, R. M., Bacon, R., Bureau, M., Copin, Y., Davies, R. L., Krajnović, D., Kuntschner, H., Miller, B. W., & de Zeeuw, P. T. 2004, *MNRAS*, 352, 721
- Engelbracht, C. W., Gordon, K. D., Rieke, G. H., Werner, M. W., Dale, D. A., & Latter, W. B. 2005, *ApJ*, 628, L29
- Erwin, P., & Sparke, L. S. 2003, *ApJS*, 146, 299
- Eskridge, P. B., Frogel, J. A., Pogge, R. W., Quillen, A. C., Davies, R. L., DePoy, D. L., Houdashelt, M. L., Kuchinski, L. E., Ramírez, S. V., Sellgren, K., Terndrup, D. M., & Tiede, G. P. 2000, *AJ*, 119, 536

- Faber, S. M., & Gallagher, J. S. 1976, *ApJ*, 204, 365
- Fakhouri, O., & Ma, C.-P. 2008, *MNRAS*, 359
- Fazio, G. G., Ashby, M. L. N., Barmby, P., Hora, J. L., Huang, J., Pahre, M. A., Wang, Z., Willner, S. P., Arendt, R. G., Moseley, S. H., Brodwin, M., Eisenhardt, P., Stern, D., Tollestrup, E. V., & Wright, E. L. 2004, *ApJS*, 154, 39
- Fouque, P., Durand, N., Bottinelli, L., Gouguenheim, L., & Paturel, G. 1990, *A&AS*, 86, 473
- Fraternali, F., & Binney, J. J. 2008, *MNRAS*, 386, 935
- Gardan, E., Braine, J., Schuster, K. F., Brouillet, N., & Sievers, A. 2007, *A&A*, 473, 91
- Garnett, D. R. 2002, *ApJ*, 581, 1019
- Giard, M., Bernard, J. P., Lacombe, F., Normand, P., & Rouan, D. 1994, *A&A*, 291, 239
- Gordon, K. D., Engelbracht, C. W., Rieke, G. H., Misselt, K. A., Smith, J., & Kennicutt, Jr., R. C. 2008, *ApJ*, 682, 336
- Governato, F., Willman, B., Mayer, L., Brooks, A., Stinson, G., Valenzuela, O., Wadsley, J., & Quinn, T. 2007, *MNRAS*, 374, 1479
- Hawarden, T. G., Longmore, A. J., Goss, W. M., Mebold, U., & Tritton, S. B. 1981, *MNRAS*, 196, 175
- Haynes, M. P., & Giovanelli, R. 1984, *AJ*, 89, 758
- Helou, G., Malhotra, S., Hollenbach, D. J., Dale, D. A., & Contursi, A. 2001, *ApJ*, 548, L73
- Helou, G., Roussel, H., Appleton, P., Frayer, D., Stolovy, S., Storrie-Lombardi, L., Hurt, R., Lowrance, P., Makovoz, D., Masci, F., Surace, J., Gordon, K. D., Alonso-Herrero, A., Engelbracht, C. W., Misselt, K., Rieke, G., Rieke, M., Willner, S. P., Pahre, M., Ashby, M. L. N., Fazio, G. G., & Smith, H. A. 2004, *ApJS*,

154, 253

- Hibbard, J. E., & van Gorkom, J. H. 1996, *AJ*, 111, 655
- Hibbard, J. E., van Gorkom, J. H., Rupen, M. P., & Schiminovich, D. 2001, in *Astronomical Society of the Pacific Conference Series, Vol. 240, Gas and Galaxy Evolution*, ed. J. E. Hibbard, M. Rupen, & J. H. van Gorkom, 657
- Hopkins, P. F., Cox, T. J., Younger, J. D., & Hernquist, L. 2009, *ApJ*, 691, 1168
- Hubble, E. P. 1926, *ApJ*, 64, 321
- Huchtmeier, W. K., & Richter, O.-G. 1989, *A General Catalog of HI Observations of Galaxies. The Reference Catalog. (A General Catalog of HI Observations of Galaxies. The Reference Catalog. Huchtmeier, W.K., Richter, O.-G., pp. 350. ISBN 0-387-96997-7. Springer-Verlag Berlin Heidelberg 1989)*
- Hunter, D. A., & Elmegreen, B. G. 2004, *AJ*, 128, 2170
- Inoue, M. Y., Kamenno, S., Kawabe, R., Inoue, M., Hasegawa, T., & Tanaka, M. 1996, *AJ*, 111, 1852
- Jackson, D. C., Cannon, J. M., Skillman, E. D., Lee, H., Gehrz, R. D., Woodward, C. E., & Polomski, E. 2006, *ApJ*, 646, 192
- Jansen, R. A., Fabricant, D., Franx, M., & Caldwell, N. 2000a, *ApJS*, 126, 331
- Jansen, R. A., Franx, M., Fabricant, D., & Caldwell, N. 2000b, *ApJS*, 126, 271
- Jogee, S., Scoville, N., & Kenney, J. D. P. 2005, *ApJ*, 630, 837
- Kannappan, S. J. 2004, *ApJ*, 611, L89
- Kannappan, S. J., & Fabricant, D. G. 2001, *AJ*, 121, 140
- Kannappan, S. J., Fabricant, D. G., & Franx, M. 2002, *AJ*, 123, 2358
- Kannappan, S. J., & Gawiser, E. 2007, *ApJ*, 657, L5
- Kannappan, S. J., Guie, J. M., & Baker, A. J. 2009, *AJ*, 138, 579
- Kannappan, S. J., Jansen, R. A., & Barton, E. J. 2004, *AJ*, 127, 1371
- Kannappan, S. J., & Wei, L. H. 2008, in *American Institute of Physics Confer-*

- ence Series, Vol. 1035, The Evolution of Galaxies Through the Neutral Hydrogen Window, ed. R. Minchin & E. Momjian, 163
- Kannappan et al. 2010, in preparation
- Kauffmann, G., Heckman, T. M., De Lucia, G., Brinchmann, J., Charlot, S., Tremonti, C., White, S. D. M., & Brinkmann, J. 2006, MNRAS, 367, 1394
- Kauffmann, G., Heckman, T. M., White, S. D. M., Charlot, S., Tremonti, C., Peng, E. W., Seibert, M., Brinkmann, J., Nichol, R. C., SubbaRao, M., & York, D. 2003, MNRAS, 341, 54
- Kauffmann, G., White, S. D. M., & Guiderdoni, B. 1993, MNRAS, 264, 201
- Kennicutt, R. C., Hao, C., Calzetti, D., Moustakas, J., Dale, D. A., Bendo, G., Engelbracht, C. W., Johnson, B. D., & Lee, J. C. 2009, ApJ, 703, 1672
- Kennicutt, Jr., R. C. 1998, ApJ, 498, 541
- Kennicutt, Jr., R. C., Armus, L., Bendo, G., Calzetti, D., Dale, D. A., Draine, B. T., Engelbracht, C. W., Gordon, K. D., Grauer, A. D., Helou, G., Hollenbach, D. J., Jarrett, T. H., Kewley, L. J., Leitherer, C., Li, A., Malhotra, S., Regan, M. W., Rieke, G. H., Rieke, M. J., Roussel, H., Smith, J., Thornley, M. D., & Walter, F. 2003, PASP, 115, 928
- Kennicutt, Jr., R. C., Calzetti, D., Walter, F., Helou, G., Hollenbach, D. J., Armus, L., Bendo, G., Dale, D. A., Draine, B. T., Engelbracht, C. W., Gordon, K. D., Prescott, M. K. M., Regan, M. W., Thornley, M. D., Bot, C., Brinks, E., de Blok, E., de Mello, D., Meyer, M., Moustakas, J., Murphy, E. J., Sheth, K., & Smith, J. D. T. 2007, ApJ, 671, 333
- Kewley, L. J., Geller, M. J., & Barton, E. J. 2006a, AJ, 131, 2004
- Kewley, L. J., Geller, M. J., Jansen, R. A., & Dopita, M. A. 2002, AJ, 124, 3135
- Kewley, L. J., Groves, B., Kauffmann, G., & Heckman, T. 2006b, MNRAS, 372, 961

- Knapen, J. H., Beckman, J. E., Shlosman, I., Peletier, R. F., Heller, C. H., & de Jong, R. S. 1995, *ApJ*, 443, L73
- Knapp, G. R., Kerr, F. J., & Williams, B. A. 1978, *ApJ*, 222, 800
- Knapp, G. R., & Raimond, E. 1984, *A&A*, 138, 77
- Knapp, G. R., & Rupen, M. P. 1996, *ApJ*, 460, 271
- Knapp, G. R., Turner, E. L., & Cunniffe, P. E. 1985, *AJ*, 90, 454
- Kormendy, J., & Kennicutt, Jr., R. C. 2004, *ARA&A*, 42, 603
- Krajnović, D., Bacon, R., Cappellari, M., Davies, R. L., de Zeeuw, P. T., Emsellem, E., Falcón-Barroso, J., Kuntschner, H., McDermid, R. M., Peletier, R. F., Sarzi, M., van den Bosch, R. C. E., & van de Ven, G. 2008, *MNRAS*, 390, 93
- Kramer, C., Buchbender, C., Xilouris, E. M., Boquien, M., Braine, J., Calzetti, D., Lord, S., Mookerjee, B., Quintana-Lacaci, G., Relaño, M., Stacey, G., Tabatabaei, F. S., Verley, S., Aalto, S., Akras, S., Albrecht, M., Anderl, S., Beck, R., Bertoldi, F., Combes, F., Dumke, M., Garcia-Burillo, S., Gonzalez, M., Gratier, P., Güsten, R., Henkel, C., Israel, F. P., Koribalski, B., Lundgren, A., Martin-Pintado, J., Röllig, M., Rosolowsky, E., Schuster, K. F., Sheth, K., Sievers, A., Stutzki, J., Tilanus, R. P. J., van der Tak, F., van der Werf, P., & Wiedner, M. C. 2010, *A&A*, 518, L67
- Kroupa, P. 2001, *MNRAS*, 322, 231
- Krumholz, M. R., McKee, C. F., & Tumlinson, J. 2009, *ApJ*, 699, 850
- Lake, G., & Schommer, R. A. 1984, *ApJ*, 280, 107
- Laurent, O., Mirabel, I. F., Charmandaris, V., Gallais, P., Madden, S. C., Sauvage, M., Vigroux, L., & Cesarsky, C. 2000, *A&A*, 359, 887
- Lavalley, M. P., Isobe, T., & Feigelson, E. D. 1992, in *Bulletin of the American Astronomical Society*, Vol. 24, *Bulletin of the American Astronomical Society*, 839–840

- Lee, J. H., Hwang, H. S., Lee, M. G., Lee, J. C., & Matsuhara, H. 2010, *ApJ*, 719, 1946
- Lees, J. F., Knapp, G. R., Rupen, M. P., & Phillips, T. G. 1991, *ApJ*, 379, 177
- Leroy, A., Bolatto, A., Walter, F., & Blitz, L. 2006, *ApJ*, 643, 825
- Leroy, A., Bolatto, A. D., Simon, J. D., & Blitz, L. 2005, *ApJ*, 625, 763
- Leroy, A. K., Walter, F., Brinks, E., Bigiel, F., de Blok, W. J. G., Madore, B., & Thornley, M. D. 2008, *AJ*, 136, 2782
- Li, C., Kauffmann, G., Heckman, T. M., White, S. D. M., & Jing, Y. P. 2008, *MNRAS*, 385, 1915
- Li, Y., Mac Low, M.-M., & Klessen, R. S. 2006, *ApJ*, 639, 879
- Lin, D. N. C., & Tremaine, S. 1983, *ApJ*, 264, 364
- Maloney, P., & Black, J. H. 1988, *ApJ*, 325, 389
- Marganian, P., Garwood, R. W., Braatz, J. A., Radziwill, N. M., & Maddalena, R. J. 2006, in *Astronomical Society of the Pacific Conference Series*, Vol. 351, *Astronomical Data Analysis Software and Systems XV*, ed. C. Gabriel, C. Arviset, D. Ponz, & S. Enrique, 512
- Martini, P., Regan, M. W., Mulchaey, J. S., & Pogge, R. W. 2003, *ApJS*, 146, 353
- Menéndez-Delmestre, K., Sheth, K., Schinnerer, E., Jarrett, T. H., & Scoville, N. Z. 2007, *ApJ*, 657, 790
- Morganti, R., de Zeeuw, P. T., Oosterloo, T. A., McDermid, R. M., Krajnović, D., Cappellari, M., Kenn, F., Weijmans, A., & Sarzi, M. 2006, *MNRAS*, 371, 157
- Morganti, R., Sadler, E. M., Oosterloo, T., Pizzella, A., & Bertola, F. 1997, *AJ*, 113, 937
- Mundell, C. G., Ferruit, P., Nagar, N., & Wilson, A. S. 2009, *ApJ*, 703, 802
- Murray, N. 2009, *ApJ*, 691, 946
- Naab, T., Jesseit, R., & Burkert, A. 2006, *MNRAS*, 372, 839

- Noordermeer, E., van der Hulst, J. M., Sancisi, R., Swaters, R. A., & van Albada, T. S. 2005, *A&A*, 442, 137
- O'Halloran, B., Galametz, M., Madden, S. C., Auld, R., Baes, M., Barlow, M. J., Bendo, G. J., Bock, J. J., Boselli, A., Bradford, M., Buat, V., Castro-Rodriguez, N., Chanial, P., Charlot, S., Ciesla, L., Clements, D. L., Cormier, D., Cooray, A., Cortese, L., Davies, J. I., Dwek, E., Eales, S. A., Elbaz, D., Galliano, F., Gear, W. K., Glenn, J., Gomez, H. L., Hony, S., Isaak, K. G., Levenson, L. R., Lu, N., Okumura, K., Oliver, S., Page, M. J., Panuzzo, P., Papageorgiou, A., Parkin, T. J., Perez-Fournon, I., Pohlen, M., Rangwala, N., Rigby, E. E., Roussel, H., Rykala, A., Sacchi, N., Sauvage, M., Schulz, B., Schirm, M. R. P., Smith, M. W. L., Spinoglio, L., Srinivasan, S., Stevens, J. A., Symeonidis, M., Trichas, M., Vaccari, M., Vigroux, L., Wilson, C. D., Wozniak, H., Wright, G. S., & Zeilinger, W. W. 2010, *A&A*, 518, L58
- Okuda, T., Kohno, K., Iguchi, S., & Nakanishi, K. 2005, *ApJ*, 620, 673
- Oosterloo, T. A., Morganti, R., Sadler, E. M., Vergani, D., & Caldwell, N. 2002, *AJ*, 123, 729
- Pahre, M. A., Ashby, M. L. N., Fazio, G. G., & Willner, S. P. 2004a, *ApJS*, 154, 235
- . 2004b, *ApJS*, 154, 229
- Pak, S., Jaffe, D. T., van Dishoeck, E. F., Johansson, L. E. B., & Booth, R. S. 1998, *ApJ*, 498, 735
- Paturel, G., Theureau, G., Bottinelli, L., Gouguenheim, L., Coudreau-Durand, N., Hallet, N., & Petit, C. 2003, *A&A*, 412, 57
- Peeples, M. S., Pogge, R. W., & Stanek, K. Z. 2008, *ApJ*, 685, 904
- Pelupessy, F. I., & Papadopoulos, P. P. 2009, *ApJ*, 707, 954
- Regan, M. W., & Mulchaey, J. S. 1999, *AJ*, 117, 2676

- Regan, M. W., & Teuben, P. J. 2004, *ApJ*, 600, 595
- Regan, M. W., Thornley, M. D., Vogel, S. N., Sheth, K., Draine, B. T., Hollenbach, D. J., Meyer, M., Dale, D. A., Engelbracht, C. W., Kennicutt, R. C., Armus, L., Buckalew, B., Calzetti, D., Gordon, K. D., Helou, G., Leitherer, C., Malhotra, S., Murphy, E., Rieke, G. H., Rieke, M. J., & Smith, J. D. 2006, *ApJ*, 652, 1112
- Robertson, B. E., & Kravtsov, A. V. 2008, *ApJ*, 680, 1083
- Rosolowsky, E., Engargiola, G., Plambeck, R., & Blitz, L. 2003, *ApJ*, 599, 258
- Sadler, E. M., Oosterloo, T. A., Morganti, R., & Karakas, A. 2000, *AJ*, 119, 1180
- Sage, L. J., & Welch, G. A. 2006, *ApJ*, 644, 850
- Sage, L. J., Welch, G. A., & Young, L. M. 2007, *ApJ*, 657, 232
- Sage, L. J., & Wrobel, J. M. 1989, *ApJ*, 344, 204
- Sajina, A., Lacy, M., & Scott, D. 2005, *ApJ*, 621, 256
- Sakamoto, K., Okumura, S. K., Ishizuki, S., & Scoville, N. Z. 1999, *ApJ*, 525, 691
- Sancisi, R. 1992, in *Physics of Nearby Galaxies: Nature or Nurture?*, ed. T. X. Thuan, C. Balkowski, & J. Tran Thanh van, 31
- Sault, R. J., Teuben, P. J., & Wright, M. C. H. 1995, in *Astronomical Society of the Pacific Conference Series, Vol. 77, Astronomical Data Analysis Software and Systems IV*, ed. R. A. Shaw, H. E. Payne, & J. J. E. Hayes, 433
- Schawinski, K., Lintott, C., Thomas, D., Sarzi, M., Andreescu, D., Bamford, S. P., Kaviraj, S., Khochfar, S., Land, K., Murray, P., Nichol, R. C., Raddick, M. J., Slosar, A., Szalay, A., Vandenberg, J., & Yi, S. K. 2009, *MNRAS*, 396, 818
- Schiminovich, D., van Gorkom, J. H., van der Hulst, J. M., & Malin, D. F. 1995, *ApJ*, 444, L77
- Schneider, S. E., Helou, G., Salpeter, E. E., & Terzian, Y. 1986, *AJ*, 92, 742
- Schneider, S. E., Thuan, T. X., Magri, C., & Wadiak, J. E. 1990, *ApJS*, 72, 245
- Schweizer, F., & Seitzer, P. 1988, *ApJ*, 328, 88

- . 1992, *AJ*, 104, 1039
- Schweizer, F., van Gorkom, J. H., & Seitzer, P. 1989, *ApJ*, 338, 770
- Serra, P., Trager, S. C., van der Hulst, J. M., Oosterloo, T. A., Morganti, R., van Gorkom, J. H., & Sadler, E. M. 2007, *New Astronomy Review*, 51, 3
- Shapiro, K. L., Falcón-Barroso, J., van de Ven, G., de Zeeuw, P. T., Sarzi, M., Bacon, R., Bolatto, A., Cappellari, M., Croton, D., Davies, R. L., Emsellem, E., Fakhouri, O., Krajnović, D., Kuntschner, H., McDermid, R. M., Peletier, R. F., van den Bosch, R. C. E., & van der Wolk, G. 2010, *MNRAS*, 402, 2140
- Sheth, K., Elmegreen, D. M., Elmegreen, B. G., Capak, P., Abraham, R. G., Athanassoula, E., Ellis, R. S., Mobasher, B., Salvato, M., Schinnerer, E., Scoville, N. Z., Spalsbury, L., Strubbe, L., Carollo, M., Rich, M., & West, A. A. 2008, *ApJ*, 675, 1141
- Sheth, K., Vogel, S. N., Regan, M. W., Thornley, M. D., & Teuben, P. J. 2005, *ApJ*, 632, 217
- Skrutskie, M. F., Cutri, R. M., Stiening, R., Weinberg, M. D., Schneider, S., Carpenter, J. M., Beichman, C., Capps, R., Chester, T., Elias, J., Huchra, J., Liebert, J., Lonsdale, C., Monet, D. G., Price, S., Seitzer, P., Jarrett, T., Kirkpatrick, J. D., Gizis, J. E., Howard, E., Evans, T., Fowler, J., Fullmer, L., Hurt, R., Light, R., Kopan, E. L., Marsh, K. A., McCallon, H. L., Tam, R., Van Dyk, S., & Wheelock, S. 2006, *AJ*, 131, 1163
- Smith, J. D. T., Draine, B. T., Dale, D. A., Moustakas, J., Kennicutt, Jr., R. C., Helou, G., Armus, L., Roussel, H., Sheth, K., Bendo, G. J., Buckalew, B. A., Calzetti, D., Engelbracht, C. W., Gordon, K. D., Hollenbach, D. J., Li, A., Malhotra, S., Murphy, E. J., & Walter, F. 2007, *ApJ*, 656, 770
- Solomon, P. M., Rivolo, A. R., Barrett, J., & Yahil, A. 1987, *ApJ*, 319, 730
- Somerville, R. S., & Primack, J. R. 1999, *MNRAS*, 310, 1087

- Springob, C. M., Haynes, M. P., Giovanelli, R., & Kent, B. R. 2005, *ApJS*, 160, 149
- Stark et al. 2010, in preparation
- Steer, D. G., Dewdney, P. E., & Ito, M. R. 1984, *A&A*, 137, 159
- Steinmetz, M., & Navarro, J. F. 2002, *New Astronomy*, 7, 155
- Stewart, K. R., Bullock, J. S., Wechsler, R. H., & Maller, A. H. 2009, ArXiv e-prints
- Stewart, K. R., Bullock, J. S., Wechsler, R. H., Maller, A. H., & Zentner, A. R. 2008, *ApJ*, 683, 597
- Temi, P., Brighenti, F., & Mathews, W. G. 2007, *ApJ*, 660, 1215
- . 2009a, *ApJ*, 695, 1
- . 2009b, *ApJ*, 707, 890
- Thronson, Jr., H. A., Tacconi, L., Kenney, J., Greenhouse, M. A., Margulis, M., Tacconi-Garman, L., & Young, J. S. 1989, *ApJ*, 344, 747
- Toomre, A., & Toomre, J. 1972, *ApJ*, 178, 623
- Vader, J. P., & Vigroux, L. 1991, *A&A*, 246, 32
- van der Hulst, J. M., van Albada, T. S., & Sancisi, R. 2001, in *Astronomical Society of the Pacific Conference Series, Vol. 240, Gas and Galaxy Evolution*, ed. J. E. Hibbard, M. Rupen, & J. H. van Gorkom, 451
- van Dokkum, P. G. 2005, *AJ*, 130, 2647
- van Gorkom, J. H., Knapp, G. R., Raimond, E., Faber, S. M., & Gallagher, J. S. 1986, *AJ*, 91, 791
- Verheijen, M. A. W., & Sancisi, R. 2001, *A&A*, 370, 765
- Wardle, M., & Knapp, G. R. 1986, *AJ*, 91, 23
- Wei, L. H., Kannappan, S. J., Vogel, S. N., & Baker, A. J. 2010a, *ApJ*, 708, 841
- Wei, L. H., Vogel, S. N., Kannappan, S. J., Baker, A. J., Stark, D., & Laine, S. 2010b, *ApJL*, submitted
- Welch, G. A., & Sage, L. J. 2003, *ApJ*, 584, 260

- White, S. D. M., & Frenk, C. S. 1991, *ApJ*, 379, 52
- White, S. D. M., & Rees, M. J. 1978, *MNRAS*, 183, 341
- Wiklind, T., Combes, F., & Henkel, C. 1995, *A&A*, 297, 643
- Wiklind, T., Combes, F., Henkel, C., & Wyrowski, F. 1997, *A&A*, 323, 727
- Wiklind, T., & Henkel, C. 1989, *A&A*, 225, 1
- . 1992, *A&A*, 257, 437
- Wolfire, M. G., Hollenbach, D., & McKee, C. F. 2010, *ApJ*, 716, 1191
- Wong, T., & Blitz, L. 2002, *ApJ*, 569, 157
- Wu, H., Cao, C., Hao, C., Liu, F., Wang, J., Xia, X., Deng, Z., & Young, C. 2005, *ApJ*, 632, L79
- Wu, Y., Charmandaris, V., Hao, L., Brandl, B. R., Bernard-Salas, J., Spoon, H. W. W., & Houck, J. R. 2006, *ApJ*, 639, 157
- Yi, S. K., Yoon, S., Kaviraj, S., Deharveng, J., Rich, R. M., Salim, S., Boselli, A., Lee, Y., Ree, C. H., Sohn, Y., Rey, S., Lee, J., Rhee, J., Bianchi, L., Byun, Y., Donas, J., Friedman, P. G., Heckman, T. M., Jelinsky, P., Madore, B. F., Malina, R., Martin, D. C., Milliard, B., Morrissey, P., Neff, S., Schiminovich, D., Siegmund, O., Small, T., Szalay, A. S., Jee, M. J., Kim, S., Barlow, T., Forster, K., Welsh, B., & Wyder, T. K. 2005, *ApJ*, 619, L111
- Young, L. M. 2002, *AJ*, 124, 788
- . 2005, *ApJ*, 634, 258
- Young, L. M., Bendo, G. J., & Lucero, D. M. 2009, *AJ*, 137, 3053
- Young, L. M., Bureau, M., & Cappellari, M. 2008, *ApJ*, 676, 317
- Zaritsky, D., & Rix, H.-W. 1997, *ApJ*, 477, 118